The Effect of the GLP-1 Agonist, Liraglutide, on the Right Ventricle in Pulmonary Hypertension

Thesis submitted to Imperial College London
for the degree of
Doctor of Philosophy

by

Lin Zhao

2020

National Heart and Lung Institution,
Faculty of Medicine,
Imperial College London
Hammersmith Hospital, London, United Kingdom

Declaration of Originality

I declare that the work contained in this thesis is original and was conducted by myself. The contribution from others has been acknowledged within the text or appropriately referenced.

Declaration of Copyright

Acknowledgements

To begin with, I would like to thank Professor Lan Zhao who offered me day-to-day supervision and guidance. This work cannot be made possible without her constant instruction and her clear vision in science. I am also grateful that she has always been supportive and encouraging throughout the entire period of my PhD, giving me faith and leading me out through the frustrations in science. Thank you, professor.

My sincere thanks have to go to Professor Martin Wilkins and Dr. Timothy Dawes, for reviewing my work on a regular basis. Their feedbacks were constructive and helpful, which improved the study in many aspects.

The group members have worked tirelessly in cooperation for this work. Their contributions are considerable. I thank Dr. Ali Ashek, Dr. Nicoleta Baxan, and Dr. Chien-Nien Chen for their scientific expertise. I thank Olivier Dubois, Dr. Fu-Chiang Yeh, Marili Niglas, Chongyang Xie, Farah Sabrin, and Yiguan Chen for their full support.

I want to thank Professor Ardeschir Ghofrani and Professor Ralph Schermuly who gave me supervision and helped to plan the work. I sincerely acknowledge the dedication of the members in Giessen's group in Germany, as they conducted the mice study and offered expertise in echocardiography.

My thanks also must go to Dr. Christopher Rhodes who guided me into bioinformatic analysis. I thank Dr. Beata Wojciak-Stothard, Dr. Waheedah Abdul-Salam and Dr. John Wharton who offered valuable comments and put effort to make up the great research environment.

I would like to express my deep gratitude to Mr. Ma Iao Lai who generously provided financial supports to the research and to my living in London.

Above all, I dedicate this work to my loved ones. I thank my parents and families who supported me in every aspect and give me love without any reservation. I would like to express my greatest gratitude to my dear wife Yanghong who has stood at my side all the time from the very beginning.

Abstract

Right ventricular (RV) function is the major determinant of prognosis in pulmonary hypertension (PH) and dysregulated myocardial metabolism is a prominent feature of RV dysfunction. Glucagon-like peptide-1 (GLP-1) is one of the incretin hormones that potentiates insulin secretion and reduces glucagon release. Recent studies have shown that GLP-1 agonist liraglutide, an approved diabetes treatment, reduces the risk of heart failure in diabetes patients and improves pulmonary endothelial function in PH rats. My PhD project hypothesized that liraglutide is an emerging PH treatment, aiming to define its effects on RV function.

I established cardiac magnetic resonance imaging (MRI) as a key translational tool to characterize the RV functional and structural remodelling, especially the RV uncoupling features, employing monocrotaline (MCT) and Sugen hypoxia (SuHx) PH models, along the course of PH development, together with pathological and molecular assessment.

In both MCT and SuHx rats, treatment with liraglutide attenuated pulmonary artery pressure and pulmonary remodelling. Importantly, I demonstrated that liraglutide reversed the MCT or SuHx induced RV structural and functional remodelling by MRI cine, T1 mapping and gadolinium-enhanced scans. Moreover, pathological examination indicated that liraglutide reduced cardiac fibrosis and cardiomyocyte hypertrophy, as well as capillary rarefaction. Further study using the pulmonary artery banding mice validated and confirmed the direct effect of liraglutide on the RV.

I examined the molecular pathways involved in RV remodelling that are impacted by liraglutide using RNA sequencing. Data from the PAB and SuHx models indicated the important involvement of liraglutide in the regulation of PI3K-Akt and AMPK pathways.

My PhD project presented important preclinical evidence that liraglutide saves RV structural and functional remodelling in PH by modulating the cardiac metabolic homeostasis in addition to its pulmonary effects, supporting liraglutide as a potential future therapeutic option for PH patients.

Table of contents

Table of figures

List of tables

Glossary of abbreviations

Abbreviation	Full name
^{18}F-FDG	Fluorodeoxyglucose (18F)
3Rs	Replacement, Reduction and Refinement
6MWD	6-minute walk distance
AC	Adenylate cyclase
ADP	Adenosine diphosphate
AED	Animal equivalent dose
Akt	Protein kinase B
AMP	Adenosine monophosphate
AMPK	AMP-activated protein kinase
ANOVA	Analysis of variance
BCA	Bicinchoninic acid
BSA	Body surface area
CAD	Coronary artery disease
cAMP	Cyclic adenosine monophosphate
CCB	Calcium channel blockers
cDNA	Complementary DNA
cGMP	Cyclic guanosine monophosphate
CHF	Chronic heart failure
CI	Cardiac index (the cardiac output is standardised by BSA)
CMC	Carboxyl methylcellulose sodium
CO	Cardiac output
CT	Computed tomography
CTEPH	Chronic thromboembolic pulmonary hypertension
DCA	Dichloroacetate
DEG	Differentially expressed gene
DNA	Deoxyribonucleic acid
dNTP	Deoxynucleoside triphosphate
DPP-4	Dipeptidyl peptidase-4
DRP1	Dynamin-related protein-1
Ea	Arterial elastance
ECG	Electrocardiogram

Abbreviation	Full name
ECV	Extracellular volume
EDVI	End diastolic volume index (the volume is standardised by BSA)
Ees	End-systolic elastance
Ees/Ea	A parameter describing the ventricular-vascular coupling (VVC)
EF	Ejection fraction
eNOS	Endothelial nitric oxide synthase
ESV	End systolic volume
ESVI	End systolic volume index (the volume is standardised by BSA)
ET-1	Endothelin 1
ETC	Electron transport chain
EVG	Elastic van Gieson (staining)
FAO	Fatty acid β-oxidation
FDG	Fludeoxyglucose
FDR	False discovery rate
FITC	Fluorescein isothiocyanate
GDP	Guanosine diphosphate
GLP-1	Glucagon-like peptide 1
GLP-1R	Glucagon-like peptide 1 receptor
GSEA	Gene set enrichment analysis
GTP	Guanosine triphosphate
GTPase	GTP hydrolase enzyme
HE	Haematoxylin-eosin (staining)
HF	Heart failure
HIF-1	Hypoxia-inducible factors-1
HLA	Horizontal long axis
HRE	Hypoxic response element
HRP	Horseradish peroxidase
IP	Insertion point
IPAH	Idiopathic pulmonary arterial hypertension
ISCU	Iron-sulphur cluster assembly proteins

Abbreviation	Full name
IVS	Inter-ventricular septum
JNK	c-Jun N-terminal kinases
KEGG	Kyoto Encyclopaedia of Genes and Genomes
LGE	Late-gadolinium enhancement
LV	Left ventricle
LVEDV	Left ventricular end-diastolic volume
LVEF	Left ventricular ejection fraction
MCT	Monocrotaline
miRNA	microRNA
mPAP	Mean pulmonary arterial pressure
MR	Magnetic resonance
MRI	Magnetic resonance imaging
mTOR	The mammalian target of rapamycin
MV	Mitral valve
NGS	Next-generation sequencing
NO	Nitric oxide
NRF2	Nuclear factor erythroid 2-related factor 2
ORA	Over-representation analysis
PA	Pulmonary artery
PAAT	Pulmonary artery acceleration time
PAB	Pulmonary artery banding
PAEC	Pulmonary artery endothelial cell
PAH	Pulmonary arterial hypertension
PASMC	Pulmonary artery smooth muscle cell
PAWP	Pulmonary artery wedge pressure
PC	Principal component
PCA	Principal component analysis
PCR	Polymerase chain reaction
PDE	Phosphodiesterase
PDH	Pyruvate dehydrogenase
PDK	Pyruvate dehydrogenase kinase
PET	Positron emission tomography

Abbreviation	Full name
PET-CT	Positron emission tomography-computed tomography
PH	Pulmonary hypertension
PI3K	Phosphoinositide 3-kinase
PPARα	Peroxisome proliferator-activated receptor α
PVR	Pulmonary vascular resistance
qPCR	Quantitative real-time polymerase chain reaction
RCT	Randomized controlled trial
RHC	Right heart catheterization
RNA	Ribonucleic acid
RNAseq	RNA sequencing
RV	Right ventricle
RVEDP	Right ventricular end-diastolic pressure
RVEDV	Right ventricular end-diastolic volume
RVEF	Right ventricular ejection fraction
RVESV	Right ventricular end-systolic volume
RVF	Right ventricular failure
RVFAC	Right ventricular fractional area change
RVM	Right ventricular mass
RVSP	Right ventricular systolic pressure
RVSV	Right ventricular stroke volume
RVWT	Right ventricular wall thickness
S'RV	Right ventricular annular systolic excursion velocity
SBP	Systolic blood pressure
SERCA2	Sarcoplasmic reticulum Ca2+ ATPase 2
sGC	Soluble guanylate cyclase
SIRT1	Sirtuin 1
SMC	Smooth muscle cell
SNP	Single-nucleotide polymorphism
sSBP	Systolic systemic blood pressure
SuHx	SU5416 combined with hypoxia
SVI	Stroke volume index (the stroke volume is standardised by BSA)
T2DM	Type 2 diabetes mellitus

Abbreviation	Full name
TAPSE	Tricuspid annular plane systolic excursion
TBST	Tris-buffered saline with Tween 20 (0.1%)
TE	Echo time
TGF	Transforming growth factor
TI	Inversion times
TR	Repetition time
TSPO	Translocator protein
VEGF	Vascular endothelial growth factor
VENC	Velocity encoding
VLA	Vertical long axis
VMI	Ventricular mass index
WGA	Wheat germ agglutinin
WU	Wood unit

Chapter 1 Introduction

1. Pulmonary hypertension

1.1 Overview

Pulmonary hypertension (PH) is a devastating disease of the cardiopulmonary system. Before 2018, PH was defined as the increase of the mean pulmonary artery pressure (mPAP) to ≥ 25 mmHg at rest measured by right heart catheterisation (RHC).[1,2] This was a conservative definition and its limitation had been recognized. Patients with an mPAP of 21-24 mmHg have decreased exercise capacity and increased mortality.[3,4] An analysis of 1187 normal subjects from multiple studies concluded that the normal mPAP range is 14.0 ±3.3 mmHg, with an upper limit of 20 mmHg.[5] In 2018, the 6th World Symposium on Pulmonary Hypertension (Nice, France) scrutinized the existing evidence and announced an updated version of the haemodynamic definition of PH. The updated statement has therefore proposed to use mPAP >20 mmHg as the cut-off value for PH. It has also been addressed to use the cut-off value in combination with other observations in order to well characterize the clinical situation of PH.[6] In PH patients, the increase of pulmonary artery pressure causes the elevation of the afterload of the right ventricle (RV) and thus undermines the RV function. The dysfunction of the cardiopulmonary system and the impairment of RV performance are held accountable for the disease severity and clinical worsening. RV failure (RVF) is the main cause of death in patients with PH.[7]

PH can result from the excessive proliferation of pulmonary artery cells which increases the pulmonary vascular resistance (PVR), or/and the disease could also be a consequence of the increase in pulmonary venous pressure in left-sided heart diseases. The first condition is described as precapillary and the latter is postcapillary. With the increased mPAP > 20 as a prerequisite, precapillary PH can be confirmed if pulmonary artery wedge pressure (PAWP) ≤ 15 mmHg and the PVR ≥ 3 Wood Unit (WU). Isolated post-capillary PH (IpcPH) is defied by the concomitant presence of mPAP >20 mmHg, PAWP > 15 mmHg and PVR < 3 WU. If both the PAWP and the PVR increases (mPAP >20 mmHg, PAWP > 15 mmHg and PVR ≥ 3 WU), the PH is attributed to combined pre- and post-capillary (CpcPH).[6] Characterization of the PH condition is important to avoid misclassification and contraindicated treatments.

Symptoms of PH are non-specific and are usually raised from the progressive RV dysfunction. Symptoms such as breath shortness, dizziness, chest pain, and lower extremity oedema could be observed; however, there may not be noticeable clinical manifestation at the early stage. If there is a clinical suspicion of PH, a detailed inquiry of medical history, a careful physical examination, as well as targeted cardio-pulmonary inspections are required for diagnosis. The diagnosis of PH rests on RHC. RHC directly measures the pressures in the RV and pulmonary vasculature. It serves as the gold standard for the diagnosis and characterization of PH.

1.2 Classifications

PH can be idiopathic or be attributable to a wide spectrum of factors and conditions. Based on the aetiology, pathophysiology, and clinical management, PH has been subclassified into five groups.[6] In general, they are: arterial, venous, hypoxic, thromboembolic, and miscellaneous. Formal terms of the PH classifications are listed in *Table 1-1*. Group 1 PH, pulmonary arterial hypertension (PAH), is the most extensively studied one. PAH is characterized by the vasculopathy of multi-layer pulmonary arterioles, including cell proliferation, perivascular fibrosis, formation of plexiform lesions, and development of *in situ* thrombi.[8] The vasculopathy of PAH shares common features with the changes in the pulmonary vasculature of patients with other groups of PH as well.

Table 1-1 Clinical classification of PH

1 PAH

1.1 Idiopathic PAH (IPAH)

1.2 Heritable PAH

1.3 Drug- and toxin-induced PAH

1.4 PAH associated with:

1.4.1 Connective tissue disease

1.4.2 HIV infection

1.4.3 Portal hypertension

1.4.4 Congenital heart disease

1.4.5 Schistosomiasis

1.5 PAH long-term responders to calcium channel blockers

1.6 PAH with overt features of venous/ capillaries (PVOD/ PCH) involvement

1.7 Persistent PH of the new-born syndrome

2 PH due to left heart disease

2.1 PH due to heart failure with preserved LVEF

2.2 PH due to heart failure with reduced LVEF

2.3 Valvular heart disease

2.4 Congenital/acquired cardiovascular conditions leading to post-capillary PH

3 PH due to lung diseases and/or hypoxia

3.1 Obstructive lung disease

3.2 Restrictive lung disease

3.3 Other lung disease with mixed restrictive/ obstructive pattern

3.4 Hypoxia without lung disease

3.5 Developmental lung disorders

4 PH due to pulmonary artery obstructions

4.1 Chronic thromboembolic PH

4.2 Other pulmonary artery obstructions

5 PH with unclear and/or multifactorial mechanisms

5.1 Haematological disorders

5.2 Systemic and metabolic disorders

5.3 Others

5.4 Complex congenital heart disease

* PVOD: pulmonary veno-occlusive disease; PCH: pulmonary capillary haemangiomatous; LVEF: left ventricular ejection fraction.

** Table reproduced from 2019 Simonneau *et al*.[6]

1.3 Prevalence and prognosis

There is limited information on the global epidemiology of PH. Data on the prevalence of all the groups of PH are not widely available as well. Several major registries described the epidemiology of PAH (Group 1 PH). In Europe, the estimation of the overall prevalence of PAH is 26 cases per million.[9] In the United Kingdom, there is an estimated prevalence of 6.6 cases per million.[10] Registries in the United States reported a prevalence of around 10 per million.[11,12] The incidence of PAH ranges from 2.0 to 7.6 cases per million adults per year. Incidence of PAH in females is higher compared to males, but female PAH patients have better survival than males.[13]

The prognosis of PH has been significantly improved in the last decades. An early registry in the United States enrolled 194 primary PH patients (referred to as idiopathic PAH in current classification) during the years from 1981 to 1985 when there were no targeted treatment options. Reporting from this registry revealed an estimated median survival of 2.8 years in these patients, with the 1-, 3-, and 5-year survival rates of 68%, 48% and 34%, respectively.[14] A huge improvement of the survival was documented after the targeted treatment became clinically available. According to the REVEAL study (2006-2009 in the United States), the current median survival time of PAH patients rose to around 7 years. The 1-, 3-, 5-, and 7-year survival rates are 85%, 68%, 57%, and 49%, respectively.[15]

Among the top factors relevant to the survival of PH patients, RV function stands out as the most important. The progression of the disease is closely linked to RV performance. RV function is the key determinant of the survival and prognosis in patient with PH.[16]

2. The pathology of the pulmonary vasculature in PH

Pulmonary vascular remodelling can be observed in almost all the subgroups of PH. The vasculopathy in PAH has been documented intensively, because the pathologic changes in the pulmonary vasculature of PAH could serve as a distinctive feature of PH. Pulmonary vascular remodelling leads to the formation of various vascular lesions which obstruct the vascular lumen and the subsequent increase of PVR. The remodelling involves the alternation of all the cell types that comprise pulmonary vessels, as well as their interplay with inflammatory cells. The following paragraphs briefly introduce the pathological changes of the vessel layers of the pulmonary artery in PH condition.

2.1 Intima remodelling

The intima of normal pulmonary vessels is a single layer of endothelial cells. In severe cases of PAH, the intima fractional thickness could increase significantly. This could cause an obstruction and lead to an increase in pulmonary vascular resistance.[17] In the remodelled pulmonary arteries, the cells which make up the thickened intima could be endothelial-like, fibroblastic-like, or/and the collagen-predominated. The disordered proliferation of endothelial-like cells was observed in plexiform lesions, a featured vascular lesion in idiopathic PAH lungs.[17] The expression of angiogenesis markers, such as vascular endothelial growth factor (VEGF), was detected in a majority of the vascular lesions found in the lung of the PH.[18]

2.2 Media remodelling

Medial thickening is constantly observed in the pulmonary vascular remodelling. In the diseased condition, proliferated and hypertrophied pulmonary artery smooth muscle cells (PASMCs) dominantly occupies the medial layer of the remodelled arteries. The presence of the SMCs-like cells in distal non-muscularized vessels can also be observed.[19] Biological changes of the PASMCs has been characterized. When exposing to pathological stimuli, such as hypoxia, PASMC switches from quiescent to synthetic status. This switch enhances the production of chemokine and cytokine. PASMCs with the synthetic phenotype are also involved in the production and degradation of extracellular matrix protein.[20,21] Similar to the proliferation of

endothelial cells, the hyperplastic and phenotypic changes in PASMCs obliterate the vessel lumen.

2.3 Adventitia remodelling

Adventitia remodelling was noted in idiopathic PAH (IPAH) patients and PH experimental models.[22,23] The boundaries of the adventitia is not always clear, and the cell composition of the adventitia is not homogeneous. This makes it difficult to precisely analyse and compare the extent of adventitia remodelling. Accumulating experimental data indicates that the adventitial fibroblasts of pulmonary vessels act as the important regulator of inflammation, injury-sensing and hypoxia response.[24] The adventitial fibroblasts in PH condition (PH-Fibs) presented not only increased proliferation but also excessive pro-inflammatory activation. PH-Fibs are able to activate inflammatory cells, such as macrophage, and thus stimulates the secretion of chemokines, cytokines, and glycolytic metabolites.[25]

2.4 Perivascular inflammation

Perivascular infiltration of inflammatory cells is constantly observed in remodelled pulmonary arteries. Tuder *et al* reported the infiltration of macrophages and lymphocytes in PH patients lungs in 1994.[26] Perivascular mast cells were also observed in several types of PH, especially in PAH such as idiopathic PAH and congenital heart disease related PAH.[27] Dendritic cells have been found in the adventitia and media of the vascular lesions in idiopathic PAH.[28] In addition, increased cytokines and chemokines secreted from the *in situ* inflammatory cells and pulmonary vascular cells such as synthetic PASMC and PH-Fibs also contribute to pulmonary pathology in PH.[29,30] A higher plasma levels of cytokines and chemokines are found in PH patients.[31]

3. The RV remodelling in PH

3.1 The cardiopulmonary unit

The RV performance is of great importance as it is the key determinant of the outcome of the disease. It is closely linked to the state of the pulmonary vasculature. The concept of 'cardiopulmonary unit' has been proposed for a better and comprehensive understanding of the interaction between the RV and the pulmonary vasculature.[16] The two components of the cardiopulmonary unit, *i.e.* the RV and the pulmonary vasculature, have their own intrinsic characteristics (subsystem function). The integration of the intrinsic characteristics makes for the global functioning of the cardiopulmonary unit (system function). *Table 1-2* listed the major intrinsic and global parameters of the cardiopulmonary unit.

Table 1-2 Characterization of the cardiopulmonary unit

Component	**RV**	**Pulmonary circulation**
Depiction	Pressure–volume relationship	Pressure–flow relationship
Intrinsic characteristics	Heart rate Contractility (Ees) Relaxation Diastolic stiffness	Vascular resistance (PVR) Arterial compliance Arterial elastance (Ea)

Global functionality	**Pressures**	**Volumes**	**Flows**	**Coupling**
	RV pressures PAP PAWP	RV volumes Stroke volume Ejection fraction	Cardiac output Pulmonary flow	Ees/Ea

** Reproduced from 2019 Vonk Noordegraaf et al.[16]*

3.2 Characterisation of the cardiopulmonary performance

To characterize the intrinsic feature of the components of the cardiopulmonary unit, the elastance of the RV and the pulmonary vasculature needs to be measured. Analysis of the pressure-volume (P-V) relationship is required for the RV (*Figure 1-1*), and pressure-flow relationship is for the pulmonary vasculature. The ratio of RV end-systolic elastance (Ees) to the pulmonary artery elastance (Ea) describes the RV

adapting state, and it serves as the reference metric of the coupling of the cardiopulmonary unit.

$E\mathrm{es}$ can be defined as the ratio of the RV end-systolic pressure over the RV end-systolic volume (RVEDP/RVEDV).[32,33] $E\mathrm{es}$ value can be calculated from the P-V loops (or the P-V relationship of the RV, *Figure 1-1 A*). P-V loops are constructed by plotting the RV pressure against RV volume. The loop depicts one entire cardiac cycle with every point in the P-V loop reflect a unique ventricular status in the cardiac cycle. Ventricular elastance is changing all the time in the cardiac cycle and the peak value is often assumed equal to the value obtained at end-systole, *i.e.* the end-systolic elastance ($E\mathrm{es}$). $E\mathrm{es}$ is a load-independent (intrinsic) parameter that represents the RV contractility.[34,35] $E\mathrm{es}$ is determined by the myocardium mass and the contractile force of the cardiomyocyte. To characterize $E\mathrm{es}$, multiple P-V loops of a varying preload of the ventricle are required to construct the RV end-systolic pressure-volume relationship (ESPVR). This can be achieved, for example, by the obstruction of vena cava in animals or by Valsalva manoeuvre in human beings.[33] ESPVR, depicted by linking all the end-systolic points of the P-V loops, is an approximately linear relationship and its slope is $E\mathrm{es}$.

Arterial elastance ($E\mathrm{a}$) is a ventricular-independent measure that reflects vascular resistance and compliance. $E\mathrm{a}$ can be regarded as a measure of the total load of RV and it can be estimated from the P-V loops using the equation $E\mathrm{a} = P\mathrm{es}/\mathrm{SV}$, ($P\mathrm{es}$: end-systolic pressure; SV: stroke volume). In this formula, $P\mathrm{es}$ stands for end-systolic pressure, and SV is the stroke volume. To visualize $E\mathrm{a}$ in P-V loop plot, connect the ventricular end-systolic point and the max ventricular volume on the volume axis with a line and the slope of this line is $E\mathrm{a}$.[36]

The coupling of RV and PA (or the cardiopulmonary unit), *i.e.* the matching of contractility to afterload, is an important evaluation of the functioning of the cardiopulmonary unit. This coupling can be described as $E\mathrm{es}/E\mathrm{a}$. This ratio is closely linked to the severity and outcome of PH.[37,38] In the optimal state, $E\mathrm{es}/E\mathrm{a}$ is estimated to be 1.0 to 2.0.[39] Lower values of $E\mathrm{es}/E\mathrm{a}$ predict increased mortality in PAH, while the higher values imply that the RV output is properly coupled to the pulmonary circulation.[40,41]

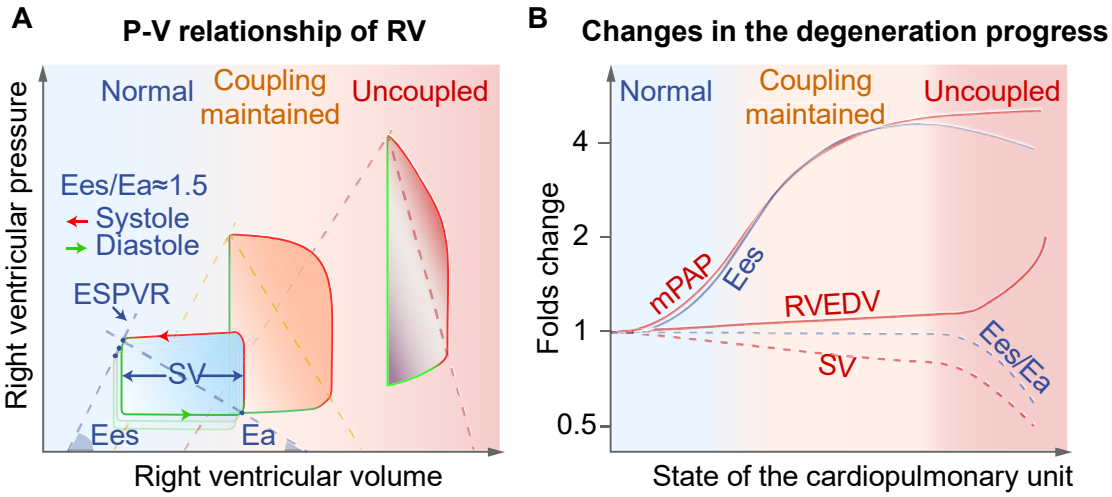

Figure 1-1 Demonstration of the decoupling progression of the cardiopulmonary in PH

(A) A sketch depicts the changes in the patterns of the P-V loops in different disease stages. End-systolic pressure-volume relationship (ESPVR) is derived from multiple PV loops with varied RV pre-load as depicted. A functioning RV has an Ees/Ea value of approximately 1.5. A failing/uncoupled RV has decreased Ees/Ea ratio that less than 1. (B) The changes of the featured parameters of the cardiopulmonary unit following the time course of the progression in PH condition. Figures reproduced with modification from 2017 Vonk Noordegraaf et al.[32] [Elsevier License Number: 1055050-1]

3.3 RV adaptive capacity in PH condition

Pulmonary vascular remodelling causes an increase in PVR. Increasing PVR leads to the elevation of right ventricular (RV) afterload, which initiates the RV pathological impairment.[42] *Figure 1-1* depicted the cardiopulmonary system in normal (left) and PH (right) condition. At the early stage, RV remodelling occurs in order to adapt to the increased afterload, *i.e.* the cardiopulmonary unit stay coupled. The RV function correlates with the capability of the RV to adapt to its increasing load. Through adaptive remodelling, such as RV hypertrophy, RV contractility (Ees) can increase to its 4-5 folds to remain functioning.[32] At the ultimate stage (*Figure 1-2* right-sided sketch) when the adaptive mechanism exhausted, RV decompensation develops and RV failure happens.[43]

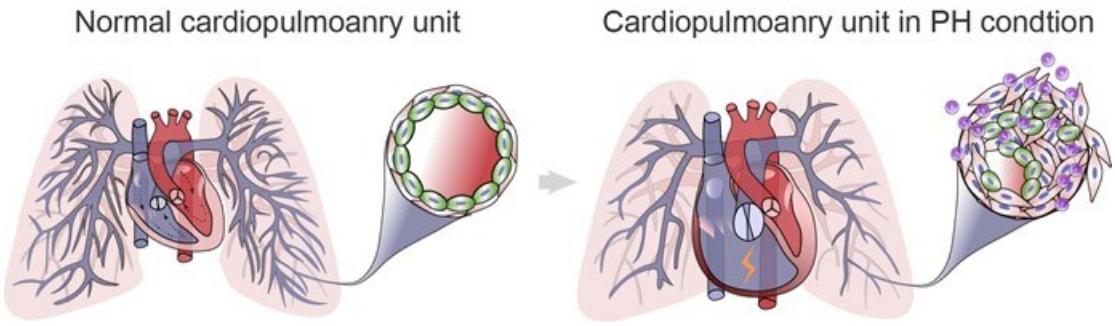

Figure 1-2 Diagram of the cardiopulmonary unit in normal and PH conditions

RV adaptation present different morphometrics and molecular features. Adaptive RV remodelling is characterized by concentric hypertrophy with minimal fibrosis.[43] Patients with adaptive RV remodelling, *e.g.* patients with Eisenmenger syndrome, can remain clinically stable with preserved RV function for a long time.[43] In contrast, maladaptive RV remodelling presents eccentric hypertrophy with excessive RV fibrosis and decreased cardiac output.[44] This pattern has usually been observed in idiopathic patients and patients with autoimmune diseases.[44] The determinants of the capability of RV adaptation are not fully documented and investigated. Tricuspid regurgitation and RV desynchrony have been reported to be markers of maladaptive RV remodelling.[43] Cardiac inflammation and fibrosis have a strong correlation to cardiac maladaptation.[44] The underlying mechanism of the transformation from adaptive RV remodelling to maladaptive configuration remains poorly understood.[45]

An important evaluation of the RV adapting status to the increased load is the ventriculoarterial coupling.[16] When the coupling is adequate, the RV is adapted to the haemodynamic changes and the function of the cardiopulmonary unit is preserved. On the contrary, once uncoupling happens, the cardiopulmonary unit is not able to maintain its function and RV failure develops. To describe the coupling state, parameters of intrinsic characteristics and systemic functionality need to be analysed, as will be discussed in the following part.

3.4 The transition from coupling to uncoupling state of the cardiopulmonary unit

The transition from coupling to uncoupling state of the cardiopulmonary unit is sequential. A comprehensive analysis of the haemodynamic and structural parameters helps to evaluate and define the coupling state (*Figure 1-1 B*). In the early

stage when the coupling persists, compensatory RV cardiomyocyte hypertrophy can be observed as a response to the pressure overload imposed on the RV. This cardiomyocyte hypertrophy increases $E\mathrm{es}$, indicating an increase in the contractility. The increase in PVR could promote the increase of $E\mathrm{a}$. The coupling is kept with the significantly increased RV contractility through hypertrophy, *i.e.* the $E\mathrm{es}/E\mathrm{a}$ ratio persisted.[32] Towards the late stage, the hypertrophic mechanism is exhausted. $E\mathrm{es}$ is no longer increased, however, the pulmonary vasculopathy keeps advancing ($E\mathrm{a}$ increases). This change leads to a decrease in the $E\mathrm{es}/E\mathrm{a}$ ratio. $E\mathrm{es}/E\mathrm{a}$ ratio serves as a reliable indicator of the coupling state.

The RV dilation, indicated by the increase of RV end-diastolic volume (RVEDV), has been regarded as an attempt to avoid the loss of stroke volume (SV). However, the RV contractility ($E\mathrm{a}$) could hardly be maintained when RV dilatation happens. Excessive cardiomyocyte hypertrophy promotes energy consumption and increases myocardium stiffness, leading to functional impairments of the RV.[46] As a consequence, SV could not be properly reserved and the RV coupling ($E\mathrm{es}/E\mathrm{a}$) is lost. With the hypertrophy mechanism exhausted, this is also the phase that the cardiomyocyte loss (ischemia) and replacement (fibrosis) start to dominate.[47]

RV microcirculation ischemia (decreased capillary density and perfusion) is a marker of RV decoupling.[48] Microcirculation ischemia causes cardiomyocyte loss, which not only damages the contractility but also facilitates fibrogenesis. RV fibrosis is a hallmark of RV decoupling.[49] It may prevent cardiomyocyte overstretch, but the fibrosis contributes to RV decoupling in many aspects, such as by increasing cardiac stiffness or causing electromechanical desynchrony.[50,51]

4. Prospect of the treatment options for PH and the RV dysfunction

4.1 Current treatment for PH

Current approved medications have only covered PH patients from group 1 and 4 (PAH and CTEPH), and they are all pulmonary vasculature targeted rather than RV-directed. The approved targeted medications comprise the mediators in three major pathways that involve in vasodilation and antiproliferation. Calcium channel blockers (CCBs) may benefit PAH patients who tested positive for pulmonary vasodilator test (*i.e.* vasodilators perfusion lead to a drop of mPAP by more than 10mmHg to reach the mPAP ≤40mmHg without cardiac output decrease).[52] *Figure 1-3* demonstrated the main mechanisms of the targeted PH medications.

Prostacyclin analogues act via the prostacyclin receptor which activates adenylate cyclase (AC) that increases the cyclic adenosine monophosphate (cAMP). The increased intracellular cAMP concentration leads to a downstream effect of vasodilation and anti-proliferation.[53]

One more pharmacotherapeutic option of PH is endothelin receptor antagonists (ERAs) that block the vasoconstriction effect of endothelin 1 (ET-1).[54] The side effect of ERAs is associated with liver toxicity, peripheral oedema, and haemoglobin decrease. ERAs showed little beneficial effect on other groups of PH.[55,56]

Another therapeutic targeted pathway involves endothelial nitric oxide (NO) and cyclic guanosine monophosphate (cGMP). With endothelial nitric oxide synthase (eNOS), pulmonary artery endothelial cells synthesize NO that activates the soluble guanylate cyclase (sGC) which subsequently converts guanosine triphosphate (GTP) to cGMP. The increase of cGMP results in vasodilation and anti-proliferation, and there are several types of phosphodiesterase (PDE) selectively hydrolyse intracellular cGMP such as PDE type 5 (PDE-5).[57] PH medications targeting this pathway include the sGC activator (Riociguat) and the PDE-5 inhibitors (Sildenafil and Tadalafil). The side effect of them has been commonly reported, including hypotension and myalgia.[58] The efficacy of PDE-5 inhibitors remains controversial in patients of group 2 and 3 PH.[59,60]

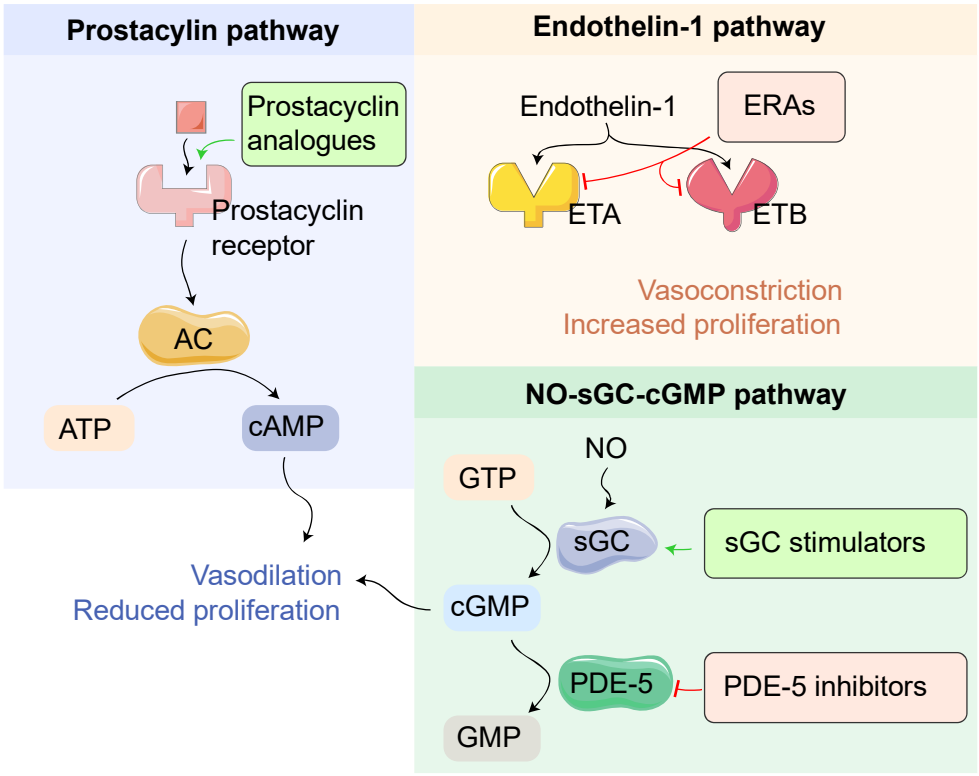

Figure 1-3 Summary of pathways targeted by current PAH therapies

Current PAH-specific medications reduce PVR and improve haemodynamic dysfunction, however, these medications showed less evidence to prevent the progressing RV deterioration.[61] The survival of patients remains a challenging problem in the clinic.[62] There is an urgent need for effective therapies that can afford PH patients with a better quality of life and longer survival.

4.2 Potential therapeutic options targeting the metabolism dysfunction of PH and the RV

Several key components in PH pathophysiology, including metabolic dysregulation and inflammation, have been revealed.[44] In PH patients, the dysfunction of the molecular and cellular processes involved in bioenergetic transformation and utilization has been closely associated with the development of uncontrolled vasoconstriction of the pulmonary circulation, as well as RV dysfunction, in patients with PH.[63] Moreover, evidence of the association between metabolic syndrome (*e.g.* obesity/ insulin resistance) and PAH has been extensively reported.[64] Based on the increasing knowledge that metabolic dysregulation contributes to the deterioration of

pulmonary vasculature and RV function, modulating the metabolic dysfunction potentially exerts therapeutic effects on the cardiopulmonary pathology in PAH (*Figure 1-4*).[65,66]

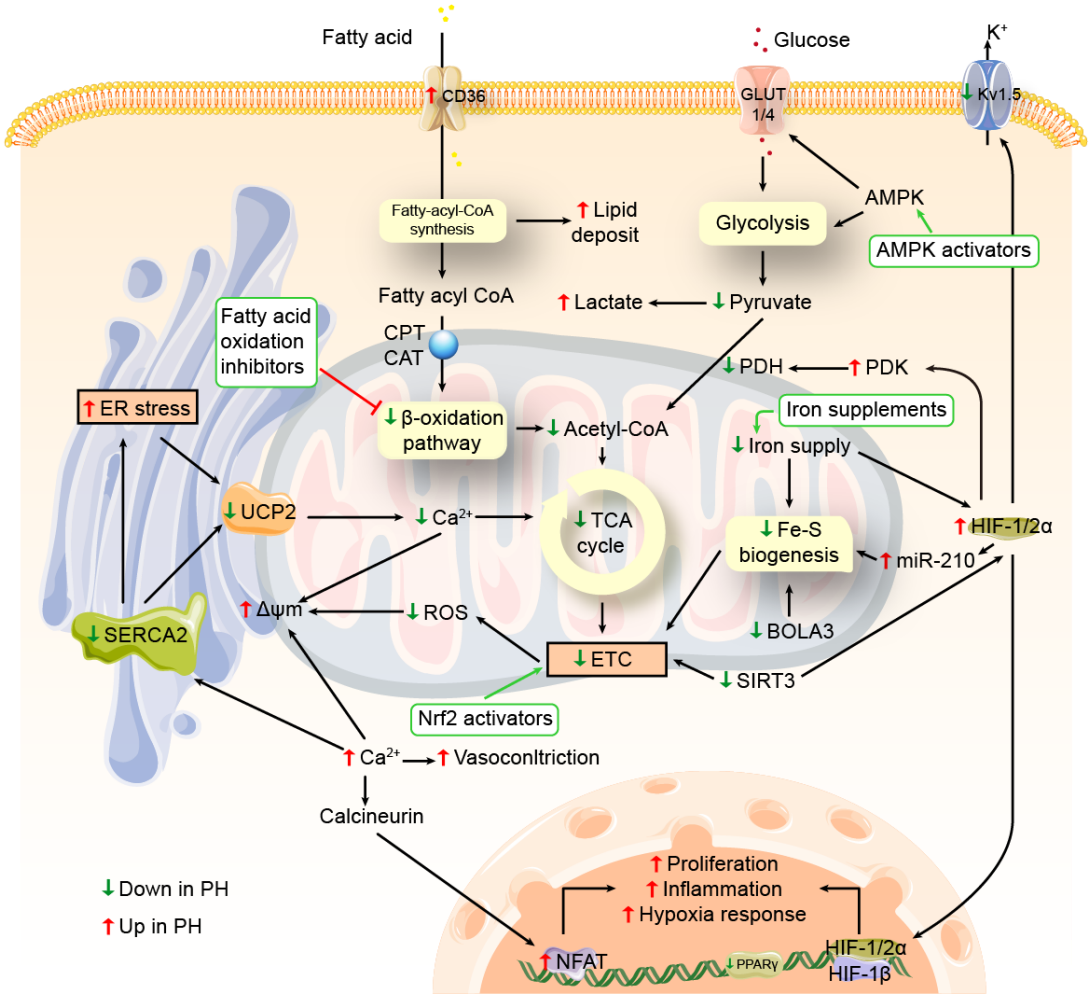

Figure 1-4 Sketching map of metabolic signalling and the potential intervention targets of the RV deterioration in PH

Figure extracted from the book chapter *Pathobiology of Pulmonary Hypertension* of the book *Reference Module in Biomedical Sciences*, with permission from the publisher.[67] [The figure was authored by myself; Elsevier License Number: 4885521299334.]

4.2.1 Modulators of glucose metabolism

In PH patients, the glucose metabolism of the pulmonary vascular cells, as well as the RV cardiomyocyte, can be shifted from glucose oxidisation to anaerobic glycolysis (known as 'glycolytic shift').[68,69] This metabolic change was firstly noted in

cancer biology as the *Warburg effect*, which has been linked to the malignant cellular phenotype.[70] Suppressed glucose oxidation implicated in the failing RV.[71] Dysregulation of the enzymes of the glycolytic pathway is implemented in the process of metabolic reprogramming.[72] Activation of hypoxia-inducible factors-1 (HIF-1), a transcription factor that consists of HIF-1α and HIF-1β subunits, impacts on the glycolytic pathway and inhibits glucose oxidation.[73] Hypoxic stimulus, or pathogenic signalling, can suppress the hydroxylation of HIF-1α subunit, leading to an increased formation of HIF-1 which binds to a hypoxic response element (HRE) and initiate the transcription of hypoxic-response genes facilitating the molecular and cellular process of PAH pathology.[74,75] Modulators targeting the regulation of HIF-1 and its downstream effectors show therapeutic potential in PH.

The gene encoding pyruvate dehydrogenase kinase (PDK) is one of the target genes of HIF-1. PDK phosphorylates the pyruvate dehydrogenase (PDH), the key enzyme that catalyses the oxidation of pyruvate into acetyl-CoA that goes into the Krebs cycle.[76] Phosphorylation of PDH suppresses the generation of acetyl-CoA in mitochondria and facilitates the transformation of pyruvate to lactate in the cytoplasm. This process can serve as a cytoprotective mechanism under hypoxic conditions to meet energy demand. However, in pathogenic conditions, such as chronic hypoxia, HIF-induced PDK expression can initiate the metabolism reprogramming that contributes to the deterioration of cellular phenotype.[74]

Dichloroacetate (DCA) is a small molecule that inhibits the phosphorylating activity of PDK and leads to activation of PDH, shifting the metabolic pattern to glucose oxidation.[77,78] Beyond the pharmacological effect on PDK, DCA has also been reported to interact with other HIF-controlled molecules.[75,79] DCA treatment ameliorates dysregulation of glucose utilization, vascular muscularization of pulmonary arteriole and perivascular inflammation in experiment PH models.[77,80,81] Administration of DCA in PAH models not only reverses the established pulmonary vascular remodelling, but also improves RV cardiac function and attenuate the RV hypertrophy by increase myocardium glucose oxidation.[65,75,77] The phase I clinical trial of DCA (NCT01083524) supports the efficacy of the inhibition of PDK with DCA in some IPAH patients with certain genetical background.[82] DCA increased mitochondrial respiration in *ex vivo* human PAH lungs. IPAH patients with oral DCA presented decreased mPAP and PVR,

and a potentially improved 6-minute walk distance (6MWD), however, an huge intra-group variance was observed. Lack of response was linked with inactivating mutations of *SIRT3* and *UCP2*.

4.2.2 Fatty acid oxidation inhibitors

Fatty acid β-oxidation (FAO) makes a major contribution to meet the myocardium energy demand. FAO produces citrate and acetyl-CoA, which suppress glucose oxidation. In the pathology of RV dysfunction, the suppression of glucose oxidation facilitates the metabolic reprogramming that favours glycolysis, which is responsible for the deterioration of RV function[83]. Inhibiting FAO with trimetazidine and ranolazine restored the glucose oxidation and improved RV performance in the pulmonary artery banding (PAB) model.[84] A phase III clinical trial with the FAO inhibitor ranolazine demonstrated that ranolazine improves exercise capacity and the WHO cardiac function class, as well as the RV cardiac index in PH patients.[85] However, this study described no improvement in pulmonary haemodynamic parameters. A recently completed phase IV study examined the effects of six-months ranolazine treatment in PH associated with LV diastolic dysfunction (NCT02133352). The available results on the registration website (ClinicalTrials.gov) have shown that six-month ranolazine administration in the LV-associated PH leads to a reduction of mPAP, PAWP and PVR, along with the improvement of 6MWD. The detailed results have not been published.[86] Among currently ongoing clinical studies, there is one trial (NCT01839110) that aims to exam the combined therapy of ranolazine and PH specific medications in improving the outcome of PH patients with RV dysfunction. There is another trial which assesses RV metabolic and structural changes in PH patients treated with or without ranolazine (NCT01917136). A phase II trial of trimetazidine has been started to investigate the therapeutic benefit of trimetazidine on RV function, RV myocardium remodelling, and miRNA expression (NCT02102672). In general, the currently available clinical evidence support that FAO inhibitors improve exercise capacity and PA haemodynamic.

4.2.3 AMPK activators

The pharmacologic intervention of AMP-activated protein kinase (AMPK) shows therapeutic potential to PH and the following RV dysfunction through mediating

cellular energy homeostasis and hypoxic response.[87] Activation of AMPK by nitrite or metformin in a left heart related PH animal model lead to the reversal of pulmonary vascular remodelling and pulmonary hypertension.[88] The anti-diabetic medication, metformin, also known as an activator of AMPK, has been extensively studied as a therapeutic potential for PH.[89] A clinical study to verify the metabolic effect of metformin in PAH patients (NCT01884051) was started in 2012 and the results will be released in 2022.

4.2.4 Mitochondrial-targeted agents

The biosynthesis and assembly of iron-sulphur (Fe-S) proteins are critical to mitochondrial function. Fe-S proteins are involved in the electron transport chain (ETC) of mitochondrial complexes and the operation of the kerbs cycle.[90] Iron deficiency has long been recognized in PAH patients and has been associated with clinical worsening and survival.[91] The rats with 4-week iron deficiency diet developed prominent pulmonary vascular remodelling, profound perivascular inflammation, and RV hypertrophy. Dysregulation of mitochondrial function and upregulation glycolytic genes were observed in these rats.[92] Clinical iron deficiency disturbed hypoxia signalling and predispose patients to hypoxia-induced hypertension, which can be reversed by ferric carboxymaltose administration.[93] Intravenous iron replacement in idiopathic PAH patients with iron deficiency improved the quality of life and the exercise capacity, while the RV cardiac function and 6MWD remained unchanged.[94] The iron-sulphur cluster assembly proteins (ISCU) assembles Fe-S clusters functioning in mitochondrial complex and kerbs circle.[90] ISCU can be downregulated by microRNA-210 (miR-210) and the latter is one of the transcriptional targets of activated HIF.[95,96] The enhancement of miR-210/ISCU singling facilitate the pathology of PH in a rodent model, and inhibition of this singling may be an alternative option to intervene iron-related dysregulation in PAH pathology.[96]

Mitochondria are continuously undergoing dynamic fission (division) and fusion (union). The mitochondrial dynamic is closely linked to cell apoptosis and proliferation. In the pathology of PH, the pulmonary vascular cells present hyperproliferative and apoptosis-resistant states and the upregulation of mitochondrial fission in the pulmonary vascular cells is necessary to sustain the mitosis. Excessive mitochondrial

fission caused by the activation of a GTPase, dynamin-related protein-1 (DRP1), is important in the pathology of PH and may serve as a therapeutic target.[97] Dysregulation of the DRP1 adapter proteins has also been found to promote pulmonary arterial hypertension through increasing mitotic mitochondrial fission.[98]

Nuclear factor erythroid 2-related factor 2 (NRF2) plays a crucial role in maintaining the structural and functional integrity of the mitochondria through affecting the mitochondrial membrane potential and ATP synthesis, impacting mitochondrial FAO.[99] The impaired mitochondrial function can benefit from the NRF2 activators.[99] In the hypoxia PH model, enhance the activity of NRF2 using pharmacological or genetical methods lead to a decrease of RV hypertrophy and pulmonary vascular remodelling.[100] A phase II clinical study in PAH patients testing the therapeutic potency of an NRF2 activator, bardoxolone methyl, is currently underway (NCT02036970).

4.3 GLP-1 agonists as a promising medication for PH

4.3.1 Biology of GLP-1 and its receptor

Glucagon-like peptide-1 (GLP-1) is one of the incretin hormones that potentiates insulin secretion and reduces glucagon release. GLP-1 is constantly released from enteroendocrine L cells, but food ingestion can induce its release to more than 2 folds. The primary active form of GLP-1 is GLP-1(7-36) amide, a 30-amino acid. GLP-1(7-36) acts on a canonical G-protein-coupled receptor (*i.e.* GLP-1R) to modulate the glucose metabolism. GLP-1R was originally found in islet β-cells, yet the expression of GLP-1R has been widely identified in a variety of tissues such as the lung, heart, kidney, and the nervous system.[101-103] GLP-1(7-36) is rapidly degenerated, by the ubiquitously expressed dipeptidyl peptidase-4 (DPP-4), into a 28-amino acid metabolite of GLP-1(9-36). The latter can be further cleaved by neutral endopeptidase (NEP24.11) into multiple smaller carboxyterminal peptides such as GLP-1(28–36). GLP-1(9-36) and GLP-1(28–36) have their own biological activity but they do not act on GLP-1R. They may be involved in biological processes such as the regulation of mitochondrial signalling pathways.[104]

4.3.2 GLP-1 agonists

GLP-1 agonists, which are resistant to the degeneration of DPP-4, have been developed as agents for anti-diabetes and weight-control purposes. GLP-1 agonists are becoming the dominating medication in the management of diabetes, with the well-tolerance and sustained efficacy on glycaemic control. The clinically approved GLP-1 agonist are listed in *Table 1-3*.

The first GLP-1 agonist being used in the clinic is Exenatide and it was developed from the Exendin-4, a 39-amino peptide isolated from the saliva of Gila monster. Exendin-4 shares sequence homology with human GLP-1 and it has increased resistance to human DPP-4 (half-life 2.4 hours). Exenatide is an identical synthetic of Exendin-4. Exenatide needs to be injected subcutaneously twice a day. Extended-release exenatide (exenatide microspheres) was developed, which decreased the injection frequency to once a week. Lixisenatide is a modified version of exenatide. Based on the structure of exenatide, a proline residue was deleted, and 6 lysine residues were added to the C-terminal, forming the Lixisenatide. The modification afforded Lixisenatide a higher resistance to DPP-4 (half-life 3 hours).[105] Lixisenatide is delivered once-daily subcutaneously.

Liraglutide is the first GLP-1 agonist that directly modified from the human GLP-1(7-36). It is a derivative of GLP-1(7-36) that modified with C16 free fatty acid and bound with albumin. These changes made liraglutide a stable GLP1-R agonist that has a plasma half-life up to 15 hours, making it the first GLP-1R with once-per-day administration.

There have been three GLP-1 agonists that were developed for the long-acting purpose and were approved for clinical use. They are semaglutide, albiglutide and dulaglutide. Similar to liraglutide, semaglutide is a modified GLP-1(7-36) binding with albumin. The plasma half-life of semaglutide is around 183 hours.[106] Both albiglutide and dulaglutide are protein fusion products that fuse 2 copies of modified GLP-1 with recombinant human albumin, or human immunoglobulin heavy chain, respectively.[107] The plasma half-life of them are around 5 days.

Table 1-3 Approved GLP-1 agonists categorized by peptide structure

Amino acid backbone	GLP-1 agonists	EMA approval	Structure feature	Plasma half-life
Exendin-4 backbone	Exenatide	2006	Synthetic exendin-4 with 50% homology to human GLP-1	2.4 hours
	Exenatide microspheres	2011	Exenatide encased in microspheres that slows the hydrolyzation and extends the release	controlled release
	Lixisenatide	2013	Synthetic exendin-4 modified from exenatide	3 hours
Human GLP-1(7-36) backbone	Liraglutide	2009	Acetylated GLP-1 with modification, bounded with albumin	13 hours
	Albiglutide	2014*	Dimeric GLP-1 that genetically fused to albumin	4.5 days
	Dulaglutide	2014	Dimeric GLP-1 that genetically fused to immunoglobulin heavy chain	5 days
	Semaglutide	2018	Acetylated GLP-1 with modification, bounded with albumin	7.6 days

** Albiglutide has been withdrawn from the market in 2018 for economic reason*

4.3.3 Cardiovascular benefit of GLP-1 agonists

GLP-1 agonists exert a versatile protective effect on multiple organs and tissues.[108] Although the mechanism is incompletely understood, GLP-1 agonists presented anti-fibrosis and anti-inflammation features.[109,110] The cardiovascular protection of GLP-1 agonists has been investigated in both preclinical and clinical studies.

4.3.3.1 The cardiovascular effects of GLP-1 agonists in diseased animals

Preclinical studies have demonstrated that both GLP-1 perfusion and GLP-1R agonists could improve cardiac functions in diseased animals. Intraperitoneal infusion of GLP-1 reduced cardiomyocyte apoptosis and protected the LV systolic function in a

rat model of spontaneous hypertension and heart failure.[111] In another rat model of chronic heart failure induced by ischemia, either GLP-1 or exenatide significantly improved the LVEF, and attenuated the LV dilatation.[112] Liraglutide restored the cardiac function in a mice model of obesity-associated cardiomyopathy.[113] To be specific, liraglutide (30 μg/kg i.p. bid) lead to the activation of AMP-activated protein kinase (AMPK) pathway. This activation may contribute to the improvement of the cardiac function and the reduction of the expression of heart failure biomarkers (*Nppa* and *Nppb*). In the rats with LV dysfunction induced by abdominal aortic banding, liraglutide (0.3 mg/kg s.c. bid) ameliorate cardiac fibrosis, improved the LV function through inhibiting the angiotensin II type 1 receptor.[114] Liraglutide improved the cardiac function and decreased the risk markers of heart failure in LV dysfunction mice exposed to angiotensin II or pressure overload. It was described that this effect was mediated by inhibition of the PI3K/Akt pathway and activation of AMPK axis.[115] Taken together, it has been well-proved that the GLP-1 agonists promote the cardiac function in diseased animals with multiple aetiology, however, the precise molecular mechanisms through which the GLP-1 improves the cardiac function remains largely unknown.

4.3.3.2 GLP-1 agonists significantly reduce cardiovascular risk

Several multicenter double-blind RCTs provided strong evidence that GLP-1 agonists, liraglutide and semaglutide, significantly reduced the cardiovascular risk, including the development of heart failure, in patients with type 2 diabetes.[116,117] One of the trails was the LEADER trial (liraglutide Effect and Action in Diabetes: Evaluation of cardiovascular outcomes Results).[116] This trial enrolled 9340 patients with long-standing type 2 diabetes and 81.3% of them had established cardiovascular conditions. The risks of both cardiovascular death and all-cause death were significantly lower in the liraglutide arm comparing to the placebo arm. The patients with liraglutide treatment had a significantly lower chance of cardiovascular events such as myocardial infarction and stroke. Moreover, the risk of the hospitalization due to heart failure was relatively lower in liraglutide arm comparing to the placebo arm (Hazard Ratio 0.87, *p* value = 0.14). A further subgroup analysis of the LEADER trial demonstrated a significantly lower risk of cardiovascular events in those patients with

heart failure who received liraglutide rather than the placebo.[118] Similarly, the SUSTAIN-6 trial (Evaluate Cardiovascular and Other Long-term Outcomes With Semaglutide in Subjects With Type 2 Diabetes) supported the cardiovascular benefits of semaglutide in diabetes patient.[117] The SUSTAIN-6 study enrolled 3297 patients with type 2 diabetes, 83.0% of them had established cardiovascular or nephrological conditions. The primary composite outcome of SUSTAIN-6 study is the rate of cardiovascular death, nonfatal myocardial infarction, or nonfatal stroke, which was the same as the LEADER study. The primary composite endpoint events were significantly less in the semaglutide arm comparing to the placebo controls. Although there was an RCT which investigated the cardiovascular effect of Lixisenatide in diabetes patients which yielded nonsignificant results,[119] the strong evidence from LEADER and SUSTAIN-6 (*Table 1-4*) implies that GLP-1 agonists modified from human GLP-1 structure have cardiovascular protective action which deserves further exploration. The precise mechanism of the cardiovascular protective action of liraglutide and semaglutide remains largely unknow and is being explored.[120]

Table 1-4 Cardiovascular effects of liraglutide and semaglutide in large-scale RCTs

Clinical trials	Treatment (median follow-up)	Primary composite outcome of the Treatment arm (Events/patients)	Primary composite outcome of the Placebo arm (Events/patients)	Hazard ratio, *p* value for superiority
LEADER [116]	Liraglutide (3.8 years)	608/4668 (13.0%)	694/4672 (14.9%)	0.87 *p* =0.01
SUSTAIN-6 [117]	Semaglutide (2 years)	108/1648 (6.6%)	146/1649 (8.9%)	0.74 *p* = 0.02

**The primary composite outcome comprises the first occurrence of death from cardiovascular causes, non-fatal myocardial infarction, and nonfatal stroke.*

4.3.3.3 Effects of GLP-1 agonists on patients with heart failure

Several clinical trials have been conducted to assess the capability of GLP-1 agonists on improving heart function. The beneficial effect of GLP-1 or its agonists on

cardiac function in patients with heart failure has not yet clearly demonstrated. There were a few small-scale clinical trials (7-20 patient enrolled) which performed intravenous delivery of GLP-1 in patients of chronic heart failure (CHF).[121-123] Whist the dosage and treatment duration were not consistent in these studies, improvement of LV ejection fraction (LVEF, 5-9% increase) was observed in general. One of the studies which delivered GLP-1 in a lower dose and shorter treatment duration only improved LVEF by 2%.[122] A meta-analysis indicated that the overall LVEF increase attributed to GLP-1 infusion was 4.4% (CI: 1.36–7.44), with no improvement in the plasma level of brain natriuretic peptide (BNP).[124]

Liraglutide has been reported to improve the cardiac function in diabetes patients with CHF.[125-127] Arturi *et al.* showed that liraglutide improved the LV ejection fraction by around 5% in patients with CHF.[125] Chen *et al.* evaluated the effect of liraglutide on cardiac function in myocardial infarction patients who underwent percutaneous coronary intervention. They reported that 7 days of liraglutide administration significantly improved the LVEF comparing to the placebo arm.[126,127] On the contrary, there are also several clinical trials reported no significant difference of the LV systolic function with liraglutide treatment.[128-131] One of the studies suggested that liraglutide reduced the LV diastolic pressure in heart failure (HF) patient, but there was no significant change in the cardiac output.[128] In a multicenter clinical trial with 241 enrollment of HF patients, no improvement of the LV function was observed in patient received liraglutide compared with the placebo control arm.[129] Margulies *et al.* completed a clinical trial of 271 HF patients, the results indicated that liraglutide led to neither better cardiovascular stability nor better cardiac function.[130] Kumarathurai *et al.* reported that liraglutide did not improve the LV function in exercising condition in patients with T2DM and stable coronary artery disease.[131]

4.3.4 The effects of GLP-1 agonists on PH

There have been preclinical studies that investigated the effect of GLP-1 agonists in animal models of PH. No studies to date have provided an explicit view of the effect of GLP-1 agonists on the dysregulated RV.

It has been demonstrated that liraglutide attenuated pulmonary vascular remodelling and RV systolic pressure in rat PH models induced by MCT, bleomycin, or chronic hypoxia.[132] Honda *et al* also showed that liraglutide attenuated hypoxia-induced PH in mice through ET(B) inhibition.[133] Wang *et al* have shown that liraglutide reduced RV hypertrophy and pulmonary vascular remodelling in the MCT-induced rat model of PH.[134] Their results suggested that liraglutide suppressed the hyper-proliferation of the PA smooth muscle cells (PASMCs) through downregulating ET-1 and enhancing eNOS/sGC/PKG pathway. Wu *et al* investigated the effect of liraglutide on apoptosis, autophagy, and mitochondrial stress in a cell model of PA remodelling (PDGF-treated PASMCs). In consistent with Wang *et al*., liraglutide was found to suppress the proliferation and migration of PDGF-treated PASMCs. Further, their results showed that liraglutide mitigated the ROS production, inhibited autophagy-related protein (Atg)-5, Atg-7 and Beclin-1, and suppressed the Drp1/NOX pathway.[135] In keeping with the studies above, the previous result from our group confirmed the attenuation of the PA remodelling through liraglutide treatment in MCT rats. The therapeutic effect may refer to the role of liraglutide in metabolic regulation through enhancing the AMPK signalling.[136]

These studies have focused on the GLP-1 treatment effect on the pulmonary vasculature rather than the RV phenotype in PH condition. Following the potential benefit of GLP-1 agonists on the heart, my PhD project explores the efficacy and molecular mechanism of liraglutide on RV function, especially if liraglutide could rescue RV failure in PH.

5. Evaluation of the RV performance using cardiac imaging

Structural and functional assessment of the RV could be hindered by its complex geometry. Clinical diagnose of RV failure requires both symptoms and objective measurements of the cardiac function.[16] Cardiac imaging technologies are important translational tools for assessing RV functional status in clinical and pre-clinical investigations.

5.1 Cardiac MRI

5.1.1 Volumetric measurements of the RV

Cardiac magnetic resonance imaging (MRI), which offers high-resolution imaging of the entire heart, has become a powerful and versatile non-invasive evaluation for the RV.[137,138] Cardiac MRI is the gold standard for quantitative measurement of RV anatomy and function.[139] Accurate and dynamic real-time volumetric variables of the heart, including the volumes of the myocardium and the heart chambers, can be obtained from cardiac cine MRI. These variables allow for further calculation of the functional parameters, *e.g.* stroke volume, ejection fraction and cardiac output. Volumetric measurements with cardiac cine MRI can be used to evaluate the risk and predict the mortality in patient with PH.[140] The measurements of cine MRI have been evidenced to have a strong clinical relevance closely correlated to the prognosis and survival of the patients with PH. It has also been used in preclinical studies for validating the disease models and evaluating therapeutic efficacity.[141] Increase in RV mass (RVM) might be a predictor of motility in patients with PAH, while there were inconsistent conclusions regarding the correlation of RVM with the outcome of PH. [7,142,143] Enlarged RV volume (RV end-diastolic volume, RVEDV) and reduced LV volume (LV end-diastolic volume, LVEDV) have been found correlated well with the prognosis of the patient with PH.[7] RV end-systolic volume (RVESV) could partly reflect the compliance and impedance of the PA, and it has recently been extensively suggested to have a predictive value of the survival in patients with PAH.[138,140,144]

Dynamic volumetric information obtained from the cardiac cine MRI enables accurate analysis of the cardiopulmonary function. Measurements which are reflective of the cardiopulmonary function can be calculated from the consecutive

volumetric measurements covering the cardiac cycle. For example, RV stroke volume (RVSV), RV ejection fraction (RVEF) and cardiac output (CO) can be calculated and analysed. RVEF is one of the sensitive parameters of RV dysfunction. The decrease of RVEF was observed before the clinical worsening in patients with PAH.[144] The RV adaptation, as defined by $E\mathrm{es}/E\mathrm{a}$, is of prognostic value. $E\mathrm{es}/E\mathrm{a}$ can be estimated using volumetric metrics from cardiac MRI (Estimated $E\mathrm{es}/E\mathrm{a}$ = RVSV/RVESV).[32,145] The approximation is highly correlative with the values obtained with simultaneous pressure and volume measurements.[146] As the heart catheterization to simultaneously measure the RV pressure and volume is not usually achievable both in the clinic and on the bench, cardiac MRI makes it much more practical to get this metric with little compromised accuracy.

5.1.2 MR phase-contrast imaging

MRI phase-contrast imaging is a technique that makes the velocity of blood or moving tissue quantifiable, which offers informative parameters of the cardiovascular haemodynamic. Phase-contrast imaging is actively used in the clinic for imaging the flow of vessels and heart valves. In terms of PH condition, it allows for mapping the velocity of the PA trunk and the PA vasculature, as well as the atrioventricular valves. Through phase-contrast imaging, haemodynamic parameters such as flow acceleration time, flow volume, and tricuspid velocity and regurgitation can be obtained.[147]

One of the most common clinical use of phase-contrast imaging in PH is to assess the flow of the arterial trunk. In patients with PH, there is a significant decrease in flow velocities in PA.[148] It has been noted that the pulmonary artery acceleration time (PAAT), the time interval from the beginning of the systole to the peak systolic flow, had a strong correlation with mPAP and PVR in patients with PAH.[148,149] The through-panel blood volumes during PAAT and the average mean velocity of the PA were also found to be correlated with mPAP and PVR.[150,151] Phase-contrast imaging quantifies the flow volume and provides an accurate assessment of $\mathrm{Q}p/\mathrm{Q}s$ (the ratio of pulmonary blood flow to systemic blood flow). This is of diagnostic value in PAH patients suspected to congenital heart disease.

An emerging phase-contrast imaging technique, four-dimensional (4D) phase-contrast imaging, can produce more detailed flow data and it allows for assessments of velocity, vorticity, and kinetic energy in any region of interest.[152]

5.1.3 Myocardium mapping

Cardiac MRI is able to reveal the pathological changes of the myocardium using gadolinium-enhanced imaging and T1 mapping, as well as the T1-dependent ECV mapping.

5.1.3.1 Gadolinium hyperenhancement

The gadolinium contrast agent changes the magnetic property of the regions where it accumulates, and cause hyperenhancement in the late-gadolinium enhancement (LGE) imaging. The hyperenhancement in LGE imaging is usually attributable to focal cardiac fibrosis.[153] A common pattern of LGE found in the heart of PH patients is the hyperenhancement around the RV insertion points.[154] This pattern of LGE at the insertion points is reflective of paradoxical interventricular septal motion.[155] LGE at the basal arterial insertion point correlated with reduced regional RV contractility in PH patients.[156] LGE was linked with the clinical worsening in patients with PH.[154] However, recent studies suggest that LGE found at the regions of the insertion points is irrelevant to the clinical outcome of patients with PH.[153,157]

5.1.3.2 T1 mapping and ECV mapping

T1 mapping is to map the T1 relaxation time of the myocardium to acquire information about the tissue composition. As myocardial collagen content increases T1 relaxation time, the contrast-free native T1 mapping is capable to identify fibrosis. Native T1 mapping may also help to detect oedema and increase of interstitial space (fibrosis); however, there may be a high variation which limited its applicability.[158] Contrast-enhanced T1 mapping, which refers to the T1 mapping performed after injection of the gadolinium contrast agent, is more sensitive to the pathological changes. Moreover, contrast-enhanced T1 enables calculation of the ECV map. ECV mapping affords better accuracy and minimizes variations between studies. Increase of ECV is mainly caused by cardiac fibrosis, while it can also result from myocardium disarray.[159] Unlike the LGE imaging, which only detects focal fibrosis, T1 mapping and ECV mapping are able to identify both the focal and diffuse fibrosis.

Native T1 is increased at the RV insertion points in patients with PH. The increase of the T1 of the insertion points correlates with LV structure degeneration.[160] The increased native T1 in the heart of PH patients reflected the abnormal motion of the septum.[161] Both native T1 and ECV mapping showed a similar pattern of enhancement at the insertion points and the septum in the heart of PH patients.[158] This increase correlates with the decline of RV function. The ECV enhancement at the insertion points is strongly associated with PA pressure increase as well.[158] Moreover, the pattern of enhancement is predictive of the prognosis of PH.[162]

5.2 Other imaging options

5.2.1 Echocardiography

Echocardiography is an easily-available and cost-effective option for non-invasive volumetric and functional evaluation of the RV in clinical practise. measurements of the RV volumetric and the RV function could also be easily obtained using echocardiography. Ventricular area dimensions, including cavity diameter/area and ventricular wall thickness, can be measured by echocardiography. RV systolic function could be reflected by measuring the tricuspid annular plane systolic excursion (TAPSE). TAPSE actually measures the excursion of a single point of tricuspid annulus, which indicates the longitudinal shortening of the RV cavity during systole.[163] Additional measures of RV systolic dysfunction includes the RV tissue Doppler peak velocity at the tricuspid annulus (S'RV) and RV fractional area change (RVFAC). RV diastolic dysfunction may be measured in a way similar to the measurement of LV diastolic function. The parameters include the diastolic Doppler velocities of the trans-tricuspid flow (E velocity, A velocity, and E/A) and the tricuspid annulus (E', A', E'/A').

5.2.2 Computed Tomography

Computed tomography (CT) is an appealing option for RV assessment with relatively less scanning time than cardiac MRI.[137] Cardiac CT with no electrocardiogram (ECG) gating acquires images showing the heart size and overall morphology. When ECG gating and proper contrast agent applied, CT is able to imaging the heart chambers without motion artefact, and it allows for ventricular assessment similar to cardiac MRI.[164] However, the temporal resolution (time period covering the cardiac cycle) is much lower than MRI and echocardiography, and is less

accurate.[165] Imaging the pulmonary vasculature and pulmonary parenchyma with thoracic CT is of diagnostic value in group 2 PH (PH due to lung diseases) and thromboembolic PH. The nephrotoxic contrast agent and the ionizing radiation are not avoidable in CT imaging.

5.2.3 Radionuclide imaging

Positron emission tomography (PET) imaging can be used to demonstrate glucose and fatty acid metabolism changes in the heart and the lung. One of the PET tracers, 18F-fludeoxyglucose (^{18}F-FDG), is a glucose analogue that can be absorbed by the cardiac myocytes and it remains in the myocyte. FDG uptake is increased in the RV of patients with PH. The uptake increase of FDG is an indicator of impaired cardiac function and increased PVR.[166-170] F-18-fluoro-6-thioheptadecanoic acid (FTHA) is a novel long-chain fatty acid analogue. Increased FTHA uptake was reported in the RV of patients with PAH, and was linked with RVEF degeneration.[171]

6. Experimental models of PH and/or RV dysfunction

Experimental models serve as helpful tools for comprehending the pathophysiological mechanisms and to investigate novel treatments of this complex disease.[172] Compare to clinical trials, animal studies take more advantages in regards to variable control and tissue availability. A variety of preclinical models of PH were developed to mimic the human disease. Although none of the currently available models fully replicates the human PH, they are highly relevant to the features of haemodynamic, histopathology and pathophysiology of clinical PH and the consequently RV dysfunction.[173]

PH can be induced in animals with the pathological insults alone, such as monocrotaline (MCT) or hypoxia, or the combination of multiple insults, such as the combination of SU5416 and hypoxia (SuHx).[174] Experimental afterload-induced RV dysfunction could also be achieved through surgical operations, such as pulmonary artery banding (PAB) in rodents and surgical systemic-to-pulmonary shunt in big animals.[175] PAB model has been used to investigate the load-induced RV dysfunction, which the RV pathology is independent of pulmonary vasculature pathology.[71] The following paragraphs briefly introduce the commonly-used animal models of PH and/or RV dysfunction.

6.1 MCT-induced PH in rats

Experimental PH induced by MCT has been introduced half a century ago and has been continuously contributing to the preclinical research of PH.[176] This model reproduces some of the common pathological features of human PH, including small pulmonary artery muscularization, infiltrate of inflammatory cells, proliferation pulmonary vascular cells and RV dysfunction and failure.[177] The bioactivation of MCT relies on its hepatic metabolism by cytochrome P-450, which is deficient in mice. Therefore, the rat is the most feasible specie for establishing this model. A single subcutaneous/ intraperitoneal injection of MCT is sufficient to induce PH. MCT can lead to pulmonary vascular injuries and perivascular inflammation, causing severe pulmonary vascular remodelling within 3 weeks. The severity of the experimental PH correlates with the dose of MCT injection.[174,178] With the typical dose of 60 mg/kg MCT, the vascular remodelling can be observed within one week, along with the

haemodynamic changes and RV hypertrophy in two weeks after administration.[174] RV decoupling happens after the second week.[38,178] MCT exerts a toxicological effect on the myocardium, as well as liver and kidney.[177] MCT-related proinflammatory responses and systemic procoagulant cause myocarditis and coronary arteriolar thickening, which limit the value of this model in RV-specific studies.[179]

6.2 Hypoxia-induced PH

Oxygen deprivation, through hypoxic exposure or hypobaric conditions, leads to pulmonary vascular remodelling in various types of animals. Typically, rats and mice are subjected to 3-week hypoxia exposure, which leads to an increase of PA pressure, as well as mild RV hypertrophy. However, unlike the pulmonary vascular lesions observed in PH patients, the pulmonary vascular remodelling induced by hypoxia is not robust. The most common vasculopathy is the increase of PA wall thickness and the muscularization of non-muscularized vessels.[172] Occlusive lesions are minimal in the pulmonary vasculature of hypoxia-induced PH. Moreover, RV decompensation and failure are not normally observed in animals with hypoxia. Therefore, the inadequacy of the replication of the PA lesions and the lack of RV decompensation in hypoxia-induced experimental PH make this model not favourable for the research of the RV behaviour in PH condition.

6.3 SuHx models of PH

The SuHx PH model is produced by the combination of SU-5416 (Su) injection and chronic hypoxia (Hx). SU-5416 is a vascular endothelial growth factor (VEGF) receptor blockade. This model was proposed in 2001, however, the initiating purpose was to attenuate the PH using SU-5416, as the expression of both VEGF and its receptor had been found upregulated in the PA lesions in PAH patients.[18] The exact mechanism of how the SU-5416 aggregates the PH phenotype remains uncertain. Possibly, the VEGF receptor blockade initially induces apoptosis of PA endothelial cells (PAEC). Under the hypoxic condition, the survived PAEC develops apoptosis resistance. The proliferation of the survived PAEC occludes the vascular lumen and causes PA lesions. The over-proliferation of the PASMC was also observed in the SuHx rats.[180]

The rats with the double hits of SU-5416 and hypoxia presents severe PH and occlusive PA lesion in 3 weeks.[180] Remarkably, both occlusive neointimal lesions and

plexiform lesions were found in the peripheral PA in SuHx rats, which shares similarity to the vasculopathy of human PAH.[181] RV failure is established in this model.[182,183] The hypertrophy of RV happens in the first week of the hypoxic period. Although returning the rats to normoxia may lead to a partial reversal of RV hypertrophy,[184] the vasculature remodelling and haemodynamic deterioration persists and continues to progress.[181,184] There is a variation of the severity of PH phenotype among different rat strains, or even between colonies of the same strain,[185] but signs of RV failure can be constantly observed among the animals. The pressure increase and the RV dysfunction was also profound in mice with SU5416 and hypoxia, while the pulmonary vascular lesions were less severe in mice.[186]

6.4 PAB models of RV dysfunction

Banding the pulmonary artery reproduce load-related RV dysfunction that is independent from the changes of the pulmonary vasculature.[187] The PAB model offer advantage for RV studies, as it allows the researchers to distinguish whether an intervention has a direct effect on the RV or the effect is secondary to its action on the pulmonary vasculature. PA banding can be performed in various experimental animals. Proficient surgical technique is needed to produce the model. During the surgery, the main PA of the animal is constrained through a suture, clip, or inflatable ring, leading to a rise in the RV pressure which eventually induce right ventricular dysfunction.[187,188] The extend of constriction determines the severity of RV dysfunction, which ranges from adaptive hypertrophy to RV decompensation.[188]

7. Summary

To summarize, PH is a devastating disease. RV performance is the key determinant of the disease prognosis. The medication to improve the RV function in PH condition is in urgent need. Metabolic modulators, GLP-1 agonists, are promising candidates. Robust evidence supported their cardiovascular benefits. However, the effect of GLP-1 agonists on the dysfunctional RV in PH condition was yet to be explored. Animal models of PH serves as fundamental tools for the preclinical investigation of potential drugs. Cardiac MR is the reference standard for evaluating the RV status, and its *in vivo* availability warrants the translational value of the research.

8. Hypothesis and objectives of this PhD project

8.1 Hypothesis

GLP-1 agonist, liraglutide, by modulating metabolic homeostasis, attenuates RV functional and structural remodelling in PH.

8.2 Objectives

The objectives of this project are:

- To characterize the RV behaviour in the experimental PH of MCT and SuHx rats using cardiac MRI;
- To examine the effect of liraglutide treatment on MCT and SuHx rat PH models;
- To investigate the direct impact of liraglutide on the remodelled RV using the PA banding mice model;
- To identify the underlying signalling pathways involved in RV remodelling and elucidate the molecular mechanisms of liraglutide.

Chapter 2 Materials and Methods

1. An outlook of the methodology

This chapter describes the methods used in this study. We made use of three diseased animal models, namely, *1*) PH induced by MCT in rats (MCT model), *2*) PH induced by the combination of a VEGF inhibitor (SU5416) and hypoxia (SuHx model), and *3*) RV dysfunction induced by pulmonary artery banding (PAB model). The progress of the RV degeneration, as well as the effect of liraglutide on the RV in PH rats, were studied comprehensively in a translational manner using the RV catheterization and the cutting-edge *in vivo* cardiac MRI platform. Effect of liraglutide on RV haemodynamic and function was evaluated using percutaneous puncture and *in vivo* echocardiography in mice with PAB. The RV pathological changes of fibrosis, hypertrophy, and microcirculation were inspected by Sirius Red staining, wheat germ agglutinin (WGA) fluorescent staining, and CD31 immunofluorescence, respectively. The potential mechanisms that accounted for the phenotypic features were screened by RNA sequencing and were then further validated by PCR and western blots.

2. Animal model setting-up

All the animal experiments were approved by the UK Home Office and were conducted under the Procedure Project Licence (PPL) in complying with the UK Home Office Animals (Scientific Procedures) Act 1986. I hold a Procedure Personal Licence (PIL) and I was qualified for all the procedures of animal work included in this thesis. All animal works were in accordance with the principles of the 3Rs - Replacement, Reduction and Refinement.

2.1 MCT-induced rat PH

MCT (Sigma-Aldrich 37024) was dissolved in hydrochloric acid (HCl, 1 M), and the pH was adjusted to 7.3 with sodium hydroxide (NaOH, 0.5 M). The final concentration of the MCT solution is 40mg/mL. Adult male Sprague-Dawley (SD) rats (Charles River, UK) of 5 weeks (body weight ranging from 220g to 250g) received a single subcutaneous injection of MCT solution with the dose of 60mg/kg. The animals were inspected on a daily basis. Bodyweight and health condition were recorded.

2.2 SuHx rat model of PH

The VEGF receptor inhibitor, SU-5416 (TOCRIS 3037), was dissolved in carboxyl methylcellulose sodium (CMC, CAS Number 9004-32-4, Sigma-Aldrich) solution. The dissolvent for SU-5416 was composed of 0.5% CMC, 0.4% polysorbate-80 (Tween-80, Sigma-Aldrich) and 0.9% benzyl alcohol (Sigma-Aldrich). To prepare 100mL dissolvent, mix 0.5g CMC, 400uL polysorbate-80 and 900uL benzyl alcohol into 98.7mL normal saline, and then put the container on a magnetic stirrer until the solution became clear. Dissolve the SU-5416 powder into the ready dissolvent to the final concentration of SU-5416 of 5mg/mL. The SU-5416 solution was made fresh and was injected subcutaneously at the dose of 20mg/kg to male SD rats of 5-week age (bodyweight around 200g to 250g). After the injection, these rats were subjected to hypoxic exposure for 4 weeks. After 4-week hypoxia exposure, the rats were taken out from the hypoxia chamber to normal breeding environment for a further 6 weeks until phenotyping (or 10 weeks for the last time point for cardiac MR scanning). The animals were inspected on a daily basis. Bodyweight and health condition were recorded.

2.3 PAB mice model of RV dysfunction

Animal work of the PAB mice was conducted at the University of Giessen by the collaborators. Mice (C57BL/6, weight 18-20g, from Charles River) were anaesthetized using continuous isoflurane inhalation (2.0 - 2.5% in oxygen). Then tracheal intubation and mechanical ventilation were performed. The left thorax was opened at the third intercostal space. The tissue was carefully pushed aside to expose the main PA. The main PA was bluntly dissected free from the ascending aorta, after which small titanium ligating clip was used to constrict the PA to a width of 0.3 mm in diameter. Then the chest was closed, and the animal was monitored during resuscitating from anaesthesia. Sham-operated controls underwent the same surgical procedure except for the PA banding. Carprofen (Rimadyl) was used for postoperative analgesia, which was mixed in drinking water and the intake was kept at 4mg/kg/day. Sham control mice went through the same surgery except for the placement of the ligating clip to the pulmonary artery.

3. Experimental design

3.1 Sample size estimation and randomization

Sample size calculation and power estimation were performed beforehand on the OpenEpi platform.[189] The significant level (α) and the statistic power (β) were set as 0.05 and 0.80 respectively. The outcome of interest, input for power calculation, is mPAP. According to our previous experience, the standard deviation (SD) of mPAP in healthy and diseased PH rodents was ~8.0 mmHg. Therefore, SD was set as 8.0 mmHg for power calculation. It was assumed that the mPAP is normally distributed with mean in both healthy and diseased rodent. The power calculation concluded that the sample size (N) of 5 per group is able to detect a difference that no less than 15 mmHg. Therefore at least 5 animals were assigned into each group. The sample size of each group was detailed in relevant sections.

The rats were randomized into different (scanning/treatment) groups on the first day they arrived at the facility. They were clearly tail-labelled and were arranged into the cages according to the randomization on the first day. For the longitudinal MR investigation of the PH rats (*Chapter 3*), the MRI data of the rats may from different batches of studies, while the study design (the timepoints of model establishment and scanning) were kept consistent.

3.2 Time points of MRI scanning for characterization of the PH models

In MCT rats, MRI scanning was performed at the day before MCT injection (baseline) (N= 18), and 2-weeks (N= 16) and 4-weeks (N= 12) after injection. In SuHx rats, MRI scanning was performed at 4-weeks (N= 8), 6-weeks (N= 8), 8-weeks (N= 5), and 10-weeks (N= 5) timepoints (*Figure 2-1*).

3.3 Experimental design of liraglutide administration and RV phenotyping

3.3.1 Dose conversion and preparation of liraglutide solution

Liraglutide (6 mg/mL, Victoza® of Novo Nordisk) is a clinically available drug. The dose given to the PH animals, *i.e.* the animal equivalent dose (AED), was converted from the highest human dose (3.0 mg/day) using the equation below.[190] Typical human bodyweight was considered as 60 kg. The Km is 6.2 for rats, and 12.3 for mice.

$$AED = Human\ dose\ (mg/kg) \times Km\ ratio$$

Based on the conversion, a pilot study has been performed to test the dose range of liraglutide on rats and mice. Optimal dosage was chosen based on the pilot data. Liraglutide was either diluted in normal saline before injecting to rats or injected directly to PAB mice. Liraglutide was injected at the dose of 0.4mg/kg for rats and 3.2mg/kg for mice on a daily basis, for a duration of two weeks (*Figure 2-1*).

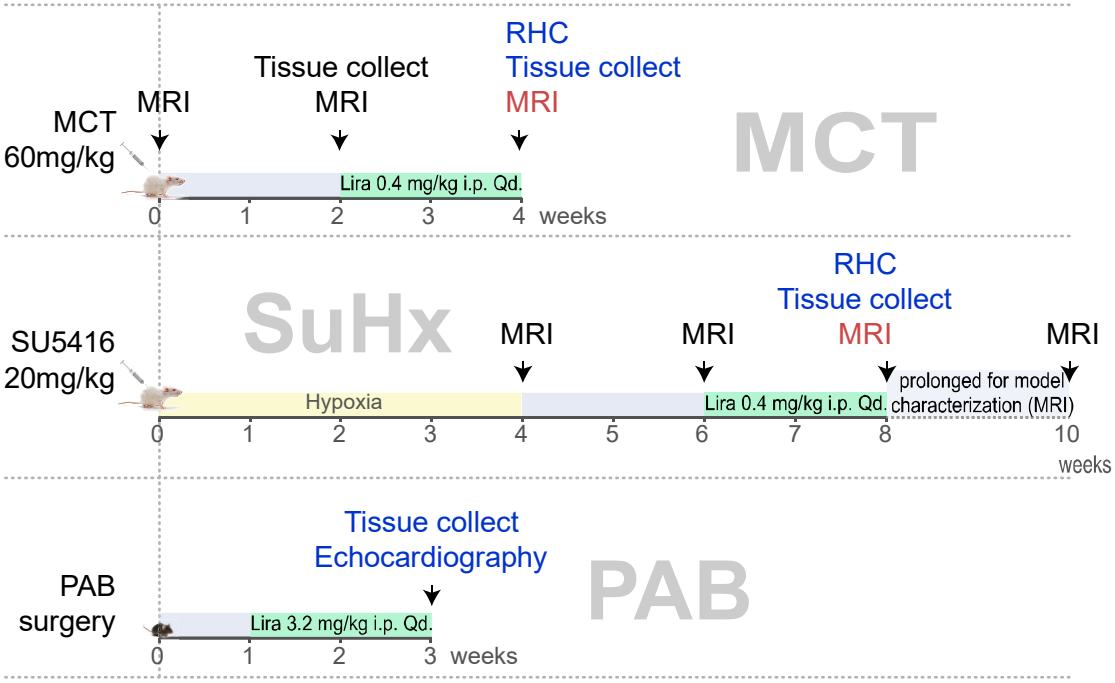

Figure 2-1 Illustration of the experimental design

3.3.2 Liraglutide administration protocol in MCT rats

Rats injected MCT were randomized into two groups. Two weeks (14 days) after MCT injection, liraglutide was given intraperitoneally on the dose of 0.4mg/kg/day for 2 weeks to the rats from the treatment group (MCT +Lira group). The other group of rats received the same volume of saline daily intraperitoneally as a placebo (MCT group). Cardiac MRI scanning was performed after the 2-week treatment. (*Figure 2-1*) Right heart catheterization (RHC) was performed at the next day of the MRI scanning to avoid anaesthetic stress. Detailed RHC methodology will be described in the following part. Tissue was collected immediately after RHC for biological investigation and histological analysis, as will be detailed in the RHC part.

3.3.3 Liraglutide administration protocol SuHx rats

Rats subjected to SuHx procedure were randomized into two groups. Liraglutide was given to the rats from the treatment group (SuHx +Lira group) on the first day of the 6th week at the dose of 0.4mg/kg/day for 2 weeks. The placebo group was given daily saline at the same volume (SuHx group). Cardiac MRI scanning was performed after the duration of 2-week treatment, *i.e.* at the end of the 8th week (*Figure 2-1*). RHC was performed at the next day of the MRI scanning to avoid anaesthetic stress. Tissue was collected immediately after RHC.

3.3.4 Liraglutide administration protocol PAB mice

Mice were randomized into the following three groups: sham-operated control mice (SHAM, n = 15), chronic pulmonary artery banding mice with the normal saline injection once per day (PAB, n = 13), and chronic PAB mice with liraglutide 3.2mg/kg *i.p.* once a day (PAB +Lira, n =11). Echocardiographic analysis and haemodynamic evaluation were performed at 21 days after surgery (by collaborators at Giessen). Tissue was collected immediately after the acquisition of the haemodynamic information.

4. Haemodynamic measurements

4.1 Right heart catheterization (RHC) in rats

RV catheterization has been performed to confirm the establishment of experimental PH in rats (*Figure 2-2*). Rats were anaesthetised using an injectable combination of Ketamine (75mg/kg *i.p.*) and Medetomidine (0.5mg/kg *i.p.*). Appropriate anaesthetic depth was confirmed by checking the loss of the pedal reflex. The anaesthetized rat was placed on its back on a heating mat. The neck area was sprayed with 70% ethanol. Then a small skin incision was made at the right side of the neck. The tissue was dissected carefully to expose and isolate the right jugular vein. A pre-curved heparin-rinsed catheter was inserted into the right jugular vein of the rats. After insertion, the catheter was pushed to go sequentially through the right atrial, the RV and the PA. The pressure information was continuously recorded (PowerLab, ADInstruments). The systemic systolic blood pressure (SBP) was obtained by inserting a catheter to the carotid artery of the rats. Analysis of the haemodynamic records was

performed with the PowerLab 5.0 software (ADInstruments). The raw hemodynamic data were analysed by two researchers independently. The researchers were blinded of the grouping information. The mean values of the analysis of the two researchers were adopted. If there is a significant discrepancy between them, the measurements were judged by a third researcher.

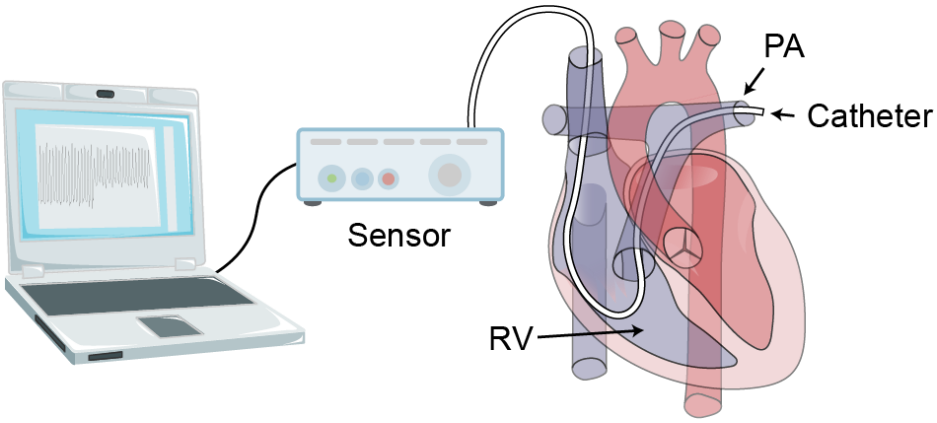

Figure 2-2 Schematic plot showing the settings of the *in vivo* RHC.

4.2 Percutaneous puncture for RV pressure measurement in PAB mice

The RV pressure of PAB mice was directly measured through a percutaneous puncture. The injectables of Ketamine (75mg/kg *i.p.*) and Medetomidine (0.5mg/kg *i.p.*) was used for anaesthesia. Once the loss of pedal reflex was confirmed, the mice were placed on a heating mat at a supine position with the chest area shaved and sprayed with 70% ethanol. Then a heparin-rinsed needle pierced into the RV from the third intercostal space of the right side. The pressure of RV was recorded for further analysis (PowerLab, ADInstruments). The analysis of the RV pressure tracers was performed in a blinded manner as similar to the analysis of RHC data of rats.

4.3 Tissue collection and preservation

After the acquisition of all the haemodynamic information, the animals were immediately sacrificed. The heart chambers and the pulmonary vasculature were flushed using 2 unit/mL heparin to remove excessive blood cells. The whole heart was cut off and the atriums were removed. The RV free wall was carefully dissected from the heart. The hearts were dissected and the weight ratio of RV over LV with septum was recorded. RV and lung tissues were divided into several pieces for multiple

biological investigations. For histological inspection, the left lung lobe and a piece of RV were saved in formalin. Samples for RNA works were stabilized in RNAlater solution (Invitrogen) overnight at 4°C and were frozen in -80°C on the next day. The rest of the tissue pieces were snap-frozen in liquid nitrogen and were moved into -80°C for preservation.

5. Cardiac MRI scanning and analysis

5.1 Overview of the workflow of the cardiac MRI

In this study, cardiac MRI was ideally suited to detect the early biventricular cardiac involvement in the proposed PH animal models because it allows: *1*) comprehensive assessment of ventricular morphology and cardiac performance (cine short-axis stack); *2*) depiction and quantification of PA haemodynamic (MR phase-contrast velocity encoding imaging); *3*) identification of global and regional changes in myocardial composition (LGE and T1 mapping acquisition) which can potentially outline early markers of tissue remodelling associated with RV systolic dysfunction.

Cardiac MRI was performed at the Biological Imaging Centre on a 9.4 T-BioSpec system (Bruker BioSpin GmbH, Ettlingen, Germany) using an 86-mm inner diameter volume transmit quadrature coil and a rat heart array receiver. The scanning procedure was standardized and was demonstrated in *Figure 2-3*.

The interpretation and analysis the MR images were performed independently by two experienced researchers who were blinded of the grouping information. The mean values of the analysis of the two researchers were adopted. If there is a significant discrepancy between the two researchers, the analysis was performed by a third researcher.

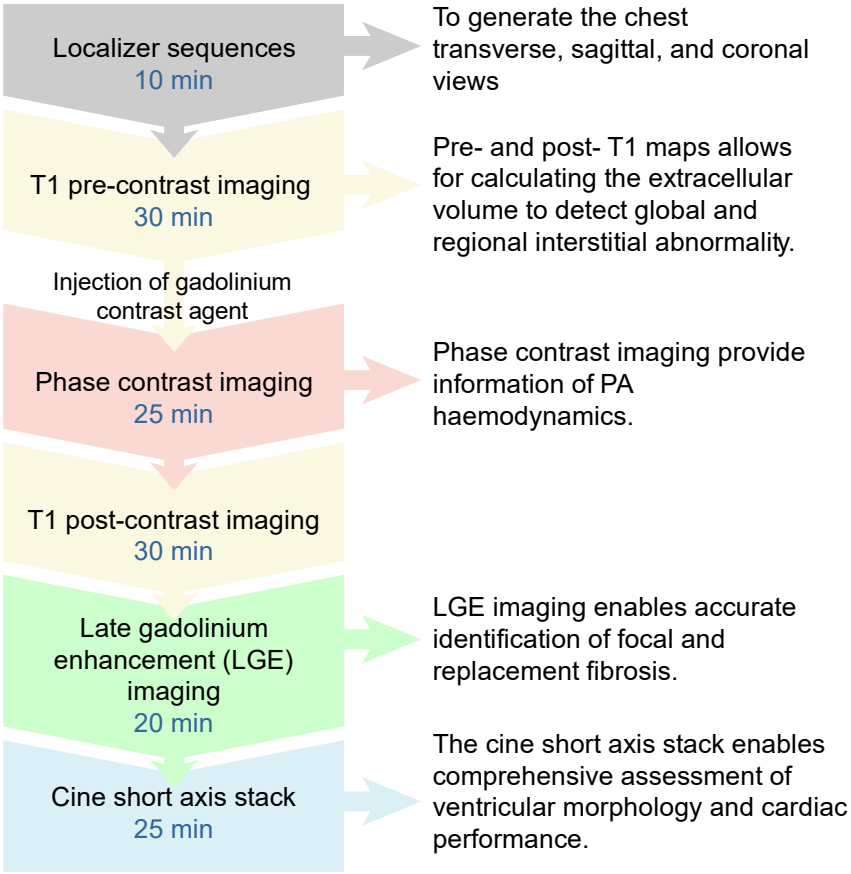

Figure 2-3 Sketch of established *in vivo* MR scanning practise

The rats were anaesthetized with continuous isoflurane inhalation and were placed on the rat cradle in a prone position. During the scanning, the electrocardiogram (ECG) was constantly monitored with three subcutaneous electrodes placed separately at both the proximal end of the forelimbs and the proximal end of the left hindlimb. The respiration was detected using a pressure sensor placed below the abdomen (SA Instruments, Stony Brook, NY). The body temperature was monitored by a rectal temperature probe. A circulating warm water heating mat was used to maintain the body temperature at 37 °C. To synchronize MRI acquisition with the cardiac cycle (RR interval) and the respiration, combined ECG and respiratory prospective triggering were applied, *i.e.* scans were double triggered by the R wave and the respiration.

Due to the anatomy and morphology of the heart, it is not accurate to use orthogonal transverse, sagittal and coronal views to acquire images of the heart for volumetric analysis. Standard cardiac imaging planes were used instead. They are

double oblique planes oriented to the heart chambers and valves. According to the American Heart Association's (AHA) statement of the cardiac standardized myocardial segmentation and nomenclature for tomographic imaging, the cardiac planes used for clinical MRI should be the short axis, vertical long axis, and horizontal long axis.[191] The three standard cardiac planes are starting to be widely adopted in animal cardiac MR as well. The definition of cardiac MR planning and acquisition in our study complies with this standard.

A freely available software (Segment V2.2 R6190, http://segment.heiberg.se) was used to analyse cine MR images, T1 mapping, and LGE images.[192] For the construction of the PA waveform, the phase-contrast images were analysed using a self-developed MATLAB-based programme (ArtFun). The image process and analysis were separately repeated by two experienced researchers.

5.2 Cine MRI for anatomical information and systolic function evaluation

5.2.1 Overview of the cine short-axis stack in cardiac MRI

The multi-slice cine cardiac MRI acquires a stack of slices covering the entire heart with 20 to 25 frames sampled through one cardiac cycle. Cine MR movies were reconstructed from the image stack. The cine MR movies were then used for volumetric and functional analysis. Acquisition of cine images of the heart is crucial for the measurement of myocardial mass, ventricular volumes and assessment of overall cardiac performance. Due to its particularly thin walls and the consequent partial volume effects, imaging the RV has proved to be challenging with other imaging modalities rather than MRI.

The planning of the scanning planes was adapted from the clinical cardiac MR practice,[193] and was kept consistent among all the scanning sequences. The LV long axis is the axis going through the apex and the centre of the mitral valve. The LV long axis is the reference for all cardiac imaging planes. The short-axis view of the heart is the perspective perpendicular to the LV long axis. The vertical long axis (VLA) view comprises vertical slices perpendicular to the short axis perspective. The horizontal long axis (HLA) view comprises horizontal slices perpendicular to the short axis

perspective. These three views are perpendicular to each other. A graphical representation of short axis, VLA and HLA are illustrated in *Figure 2-4*.

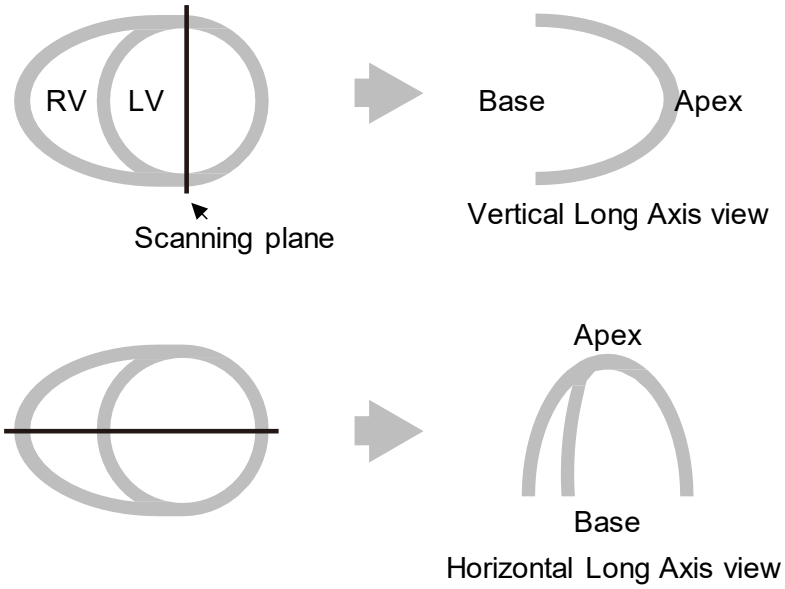

Figure 2-4 Cardiac plane definition for the *in vivo* cardiac MRI scanning (reproduced from the AHA statement[193])

5.2.2 Cine short axis stack acquisition

Multi-slice spoiled gradient echo (FLASH) sequence was performed to acquire standard short-axis cine stacks. The sequence was triggered by both respiratory sensor and ECG, which synchronises the scanning with the cardiac cycles and also reduces motion artefact. The scanning planes (slices) covered both ventricles from the base to the apex.

5.2.2.1 Detailed scanning procedures

Standardized scanning procedures are described step by step as following, with *Figure 2-5* demonstrating the steps.

1) First, run the three-plane localizer sequence covering the rat chest. This will provide the standard transverse, sagittal and coronal views.
2) VLA planning: Find the left ventricular (LV) apex and mitral valve (MV) in the localizer at end-diastole. For this, use the transverse view (*Figure 2-5 A*) and take the coronal slices as references. Since the LV apex and the MV are not in the same slice, look through all transversal slices and ensure that the planed slice crosses both the apex and the MV. The resulting image is the VLA (*Figure*

2-5 B).

3) HLA planning: Define a plane crossing the VLA vertically which captures the LV apex and the MV. The resulting image is the HLA (*Figure 2-5 C*)
4) Short axis stack: To obtain a series of adjacent short-axis slices covering both ventricles from the apex to the base of the heart, the following steps are required: Place the stack of the slices perpendicular to both long axis of the heart, represented by the VLA and HLA views. Make sure the number of cardiac frames covers a full cardiac cycle (one RR interval) This will enable to acquire the cine images required for assessing the global cardiac function (*Figure 2-5 D*).

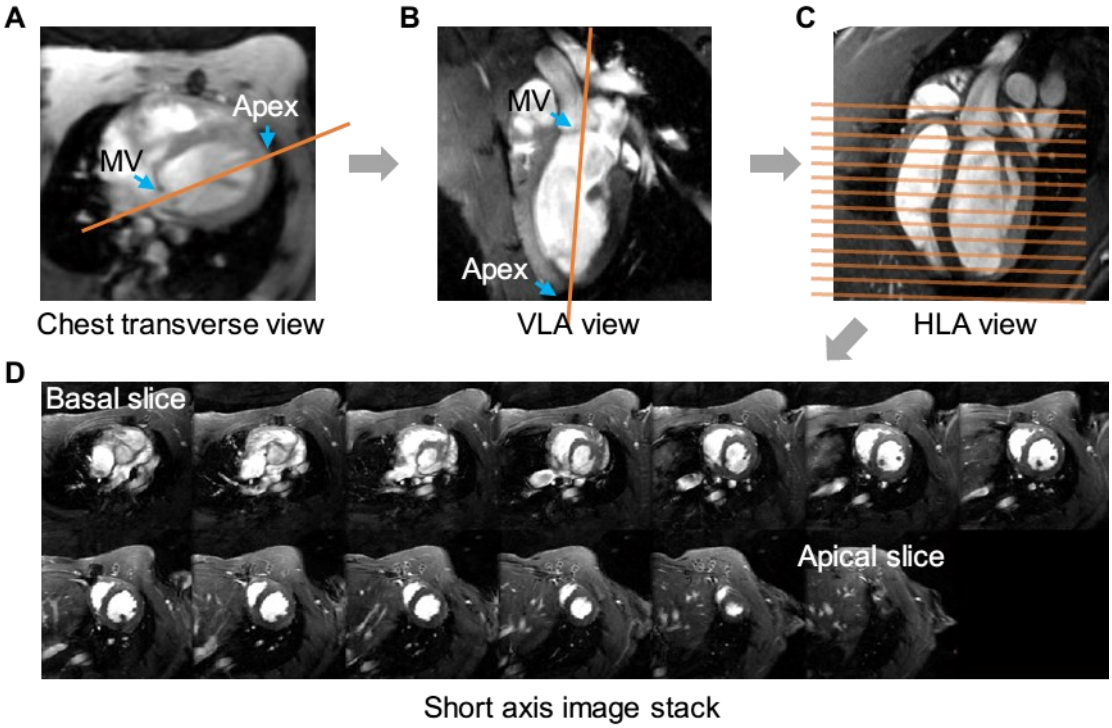

Figure 2-5 Process of cine image planning

A) The transverse view for VLA planning. B) The VLA view. C) The HLA view. D) The short-axis image stack. Lines in the images are the planned scanning planes. MV stands for the mitral valve.

5.2.2.2 Scanning parameters of short-axis cine imaging

The ECG and respiratory-triggered gradient-echo spoiled images (FLASH) cine sequence were performed. This established scanning sequence provide high spatial and temporal resolution, good tissue contrast and signal-to-noise ratio within a reasonable scaning time. The scanning parameters were: repetition time (TR) = 6.2ms, echo time (TE) =2.2ms, flip angle =18°. Total scan time was between 20 to 25 min.

5.2.3 Cine image analysis

End-systole and end-diastole were considered to be the smallest and the largest cavity area during a cardiac circle. End-diastole was defined as the first cine phase of the R-wave triggered acquisition. The endocardium and the epicardium of LV and RV at end-systole and end-diastole were manually delineated. The papillary muscle and trabeculations were excluded from the myocardium. The cardiac measurements were exported for further statistic process. The parameters of ventricular mass, volume, and cardiac output have been standardized with body surface area (BSA). BSA was calculated using Meeh's formula (BSA = $kW^{2/3}$, k=10).[194]

5.3 MR phase-contrast imaging for flow and velocity quantification

MR phase-contrast imaging technique allows for mapping the tissue velocity and has been mostly applied to measure the blood flow. Emerging applications of phase-contrast imaging include assessment of myocardial motion and vessel compliance.[195] Velocity can be mapped in two manners. One is mapping the velocity along a direction within an imaging plane (in-plane velocity). The other is mapping the velocity of a direction perpendicular to an imaging plane (through-plane velocity). This study uses MR phase-contrast imaging techniques to acquire the velocity of the PA flow. The tissue contrast of the MR phase-contrast imaging is inferior. For this reason, a high-contrast cine image with the same geometry was required as a reference for segmenting the PA in the MR phase-contrast image.

5.3.1 Phase-contrast images for the pulmonary artery flow

5.3.1.1 Detailed scanning procedures

1) Find the pulmonary arteries in the HLA and VLA views and make a scanning plane that cuts through the pulmonary arteries in both views. Use the standard coronal slices as references to make sure the plane goes through the main

pulmonary artery trunk.

2) The obtained image should contain the trunk of the pulmonary artery and the two main branch vessels. Define a plane located halfway between the valve and the pulmonary bifurcation which is perpendicular to the trunk of the PA. Pay attention to avoid the turbulent flow proximal to the valve.
3) The resulting image contains a cross-sectional cut of the main PA which will be used as the anatomical reference.
4) Load the phase-contrast protocol and copy the geometry and orientation from the anatomical reference image. Set the effective repetition time close to the RR interval and adjust the velocity encoding to avoid phase wraps in the phase image.

5.3.1.2 Scanning parameters of phase-contrast imaging

A phase-contrast pulse sequence was used with a velocity encoding along the slice direction (VENC of 140 cm/s). The sequence parameters were: TR = 6ms, TE = 2.6 ms, flip angle = 25°, slice thickness = 1.5 mm.

5.3.2 Phase-contrast images analysis

The lumen of the main PA was delineated semi-automatically on the magnitude images used for morphological reference and then the PA delineation was copied to the phase-contrast velocity images to plot the PA waveform of velocity and flow.

5.4 T1 mapping to detect the myocardial interstitial abnormality

Both the T1 mapping based extracellular volume (ECV) mapping and the LGE imaging need an injection of gadolinium contrast agent. The contrast agent is not permeable to the cell membrane and thus accumulates in the extracellular space. The contrast agent shortens T1 relaxation time (the longitudinal relaxation time of hydrogen nuclei proton after a magnetisation inversion) in a concentration-dependent manner.

T1 mapping is to fit the T1 relaxation time pixel-wise into a visualizable image. The Look-Locker pulse sequence is the most commonly used sequence to map the T1 relaxation times in the heart.[196] The impact of different pathologies on the T1 value varies from disease to disease. ECV maps can be reconstructed with the pre- and post-T1 maps and it have been increasingly used both in clinical and preclinical settings for

the identification and quantification of myocardial fibrosis.[159] ECV correlates well with fibrosis on histology and can sensitively detect the diffuse myocardial fibrosis.[197] LGE imaging and T1 mapping sequences have been recently developed and established in our scanning practice. They enabled the quantitative assessment of the distribution of cardiac fibrosis occurring in the RV, and to potentially link regional myocardium pathology with cardiac function deterioration *in vivo*.

5.4.1 T1 mapping for ECV calculation

5.4.1.1 T1 mapping procedures

Estimation of the ECV requires the acquisition of T1 maps, before and after the administration of gadolinium contrast agent (0.5 mmol/kg Gadovist).

The following steps have been performed:

1) Take the haematocrit of the animals for ECV calculation.
2) Plan the three short-axis views perpendicular to HLA and the VLA views at the level of the basal, the mid-cavity and the apical LV according to the AHA standardized myocardial segmentation.[193]
3) Run the T1 mapping sequence to acquire the pre-contrast T1 maps.
4) Repeat the T1 mapping 20 to 35 min after the intraperitoneal injection of contrast agent to obtain the post-contrast T1 maps.

5.4.1.2 Scanning parameters of T1 mapping

A gradient echo-based look-locker inversion recovery sequence was performed with 20 inversion times (TI) which followed a global inversion. All inversions were ECG triggered to allow images to be acquired at the same part of the cardiac cycle (end-diastole), with the TI points restricted to multiples of the R-R interval (RR ~ 160ms). Additional acquisition parameters were: inversion repetition time: 6s (to allow full relaxation between inversions), TR = 4.5ms, TE = 2.1ms, flip angle 7°, slice thickness 1.5mm.

5.4.2 T1 map construction and ECV calculation

The T1 inversion points acquired during respiratory motion (frames with an excessive artefact) were manually removed. T1 curve fitting was subsequently performed on a pixel-wise basis on the remaining measured inversion times using a non-linear least square three-parameter fit which accounted for Look-Locker

correction. T1 maps were constructed from the pixel-wise T1 curve fitting. Pre- and post-contrast T1 maps were used to construct the ECV maps.

To generate the ECV map, the ECV values of each pixel were calculated using the equation below. A predefined region of blood, as well as the haematocrit value, are needed as references.

$$\mathrm{ECV} = \frac{(1 - \mathrm{haematocrit})\left(\frac{1}{post\ contrast\ T1\ myo} - \frac{1}{pre\ contrust\ T1\ myo}\right)}{\frac{1}{post\ contrast\ T1\ blood} - \frac{1}{pre\ contrust\ T1\ blood}}$$

Representative pre- and post-contrast T1 maps along with the reconstructed ECV map of a healthy rat is shown in *Figure 2-6*.

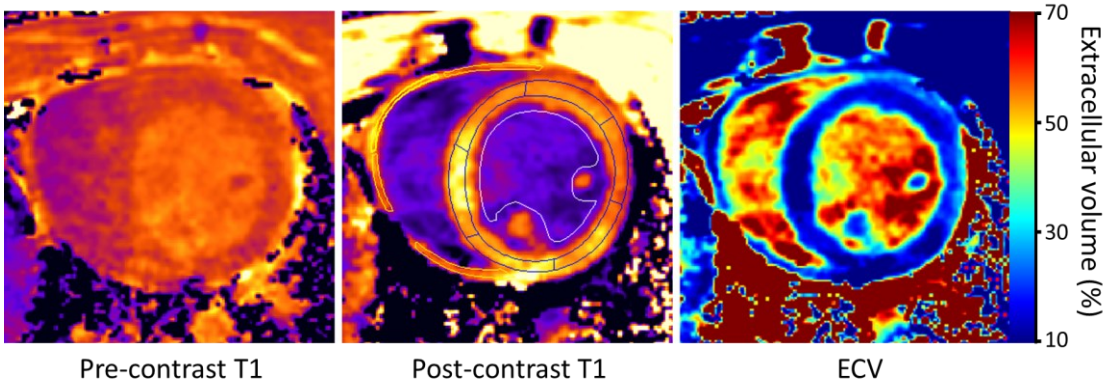

Figure 2-6 Representative pre- and post-contrast T1 maps and the constructed ECV map of a healthy rat from our scanning.

The delineations in the image of post-contrast T1 with the colours of yellow, blue and white represent the RV, LV and the sampling region of blood, separately.

5.4.3 Visualization and quantification of the segmental ECV

We have established a customized segmentation of both ventricles, using the AHA 16-segment model for LV and a self-defined 10-segment model of the RV. The segmental ECV value was mapped into a model of 26 segments (*Figure 2-7*). Each segment illustrates the average ECV values of the group of animals. Definition of the 26-segment model and the insertion points (IPs) are descripted here.

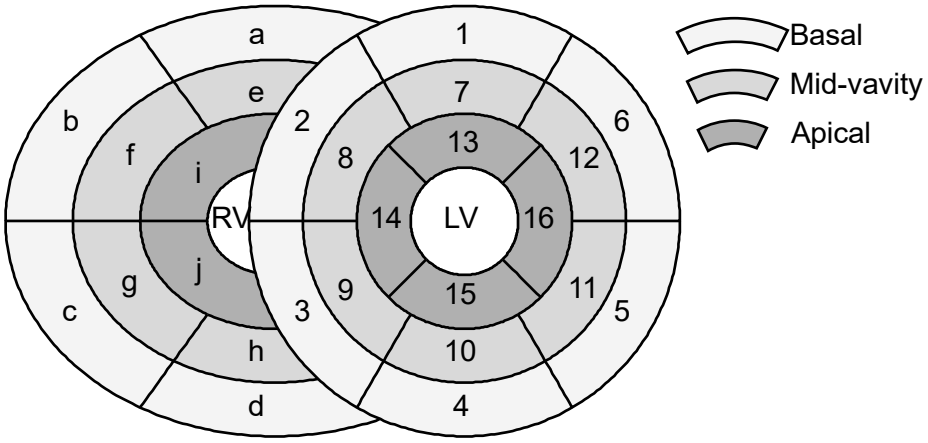

Figure 2-7 Polar plot describing the proposed segments of the heart

The customized 26-segment polar plot was developed from the AHA standard myocardial segment. This plot was used to visualize the ECV values of the heart. Illustration of the segments can be found in the following table.

Table 2-1 Illustration of the 26-segment polar plot

	Basal Segments	Mid-cavity Segments	Apical Segments
LV	1 - basal anterior	7 - mid anterior	13 - apical anterior
	2 - basal anteroseptal	8 - mid anteroseptal	14 - apical septal
	3 - basal inferoseptal	9 - mid inferoseptal	15 - apical inferior
	4 - basal inferior	10 - mid inferior	16 - apical lateral
	5 - basal inferolateral	11 - mid inferolateral	
	6 - basal anterolateral	12 - mid anterolateral	
RV	a - basal anterior	e - mid anterior	i - apical anterior
	b - basal anterolateral	f - mid anterolateral	j - apical inferior
	c - basal inferolateral	g - mid inferolateral	
	d - basal inferior	h - mid inferior	

For LV segmentation, the endocardium and the epicardium of LV were manually delineated in ECV maps. The LV was segmented into 16 regions of interest according to the AHA cardiac standardized myocardial segmentation. Specifically, the basal LV was divided into six segments of 60° each, the mid-cavity LV was also divided into six

60°parts, and the apical LV into 4 segments of 90° each. The nomenclature, complied with the AHA standard practise, is illustrated in the bullseye plot below (*Figure 2-7*).

For RV segmentation, first, the endocardium and the epicardium of RV were delineated in the ECV maps. The septum was excluded from RV and was regarded as part of the LV. The RV was segmented into 10 parts in total. Specifically, the basal and mid slices were divided into 4 equidistant regions, and the apical slice into 2 equal parts as shown in the bullseye plot below (*Figure 2-7*).

The insertion points (IPs) of the LV and the RV was defined as the middle point of the joint of RV myocardium and the LV epicardium. The anterior IPs were the endpoint of the anterior segment and the start point of the anteroseptal segment of mid-cavity and basal images. In the basal and mid-cavity slices, the anterolateral papillary muscles should fall into the anterolateral segment and the posteromedial papillary muscles into the inferior segment. The anterior IPs were the starting points for segmentation if: *1*) the papillary muscles could not be visualized in the short axis views, or *2*) the morphology and trabeculation of the LV have changed due to the disease progression of PH.

5.4.4 LGE imaging for myocardial tissue characterization

On an LGE image, the myocardium appears to be black (nulled) and extracellular regions with the accumulation of the contrast agent is bright. The bright region is 'enhanced' by the accumulation of the gadolinium contrast agent in the extracellular space. LGE imaging can identify focal and replacement fibrosis; while LGE imaging is not able to detect diffuse myocardial fibrosis.

5.4.4.1 LGE image acquisition

The LGE images were acquired using the geometry of the short axis stack at 20 to 35 minutes after contrast agent injection.

5.4.4.2 Scanning parameters of LGE imaging

A multi-slice IR-FLASH sequence with a single inversion time and flip angle of 90° was used. The other parameters were similar to the previously described T1 map look locker acquisition in order to preserve an effective nulling of healthy myocardium. TE = 1.39ms; slice thickness = 1mm. LGE scan takes 2.5min per slice.

5.4.5 LGE analysis

The endocardium and the epicardium of LV and RV were delineated manually. The LGE positive regions were automatically detected in Segment Using the build-in function for 'scar' analysis.

6. ^{18}F-FDG PET imaging

The *in vivo* ^{18}F-FDG PET imaging was performed by a senior group member (Dr. Ali Ashek), with a Siemens Inveon small-animal multimodal PET/CT scanner (Siemens Healthcare Molecular Imaging) as previously described.[198] Rats were initially treated with insulin (8 mU/g) and glucose (1 mg/g) to enhance myocardial ^{18}F-FDG uptake. Following morphological CT, ^{18}F-FDG PET scans were acquired in the list-mode format over 60 minutes (~35 MBq, <0.5ml). Imaging analysis was performed by Dr. Ali Ashek as well. Briefly, tissue time-activity curves (TACs) of the heart were calculated at the mid-cavity level. Decay corrected RV TACs were normalized to injected activity (kBq) and body weight for standardized uptake values (SUV). Kinetic analysis was performed.[199] The kinetic influx rate constant (Ki) was estimated from the linear regression slope of the Patlak plot 10 to 60 minutes after injection. Plasma and RV tissue samples were harvested, weighed and measured for radioactivity on a gamma counter. The amount of radioactivity was expressed as the percentage of injected dose per gram of tissue (%ID/g).

7. Echocardiography

Mice echocardiography was performed by collaborators at the University of Giessen. Mice were anaesthetized with continuous isoflurane inhalation and were placed on a heating mat in the supine position with ECG and body temperature monitored. After shaving the chest, pre-warmed ultrasound gel was applied. The platform of Vevo 2100 (VisualSonics) with a mouse cardiovascular ultrasound transducer (MS400) was used to acquire the echocardiogram.

8. Histology

Formalin-fixed tissue samples were embedded in paraffin in preparation of further histological experiments. The paraffin block was then trimmed and sectioned at the thickness of 5 µm. The sections were then used for further histological investigations. The histological experiments conducted in this study include: 1) staining of haematoxylin-eosin (HE) for the overall structure, and Sirius Red (SR) for detection of collagen fibres, and elastic van Gieson (EVG) for elastic fibres; 2) Fluorescent staining with fluorescein (FITC)-labelled wheat germ agglutinin (WGA) in order to visualize the cardiomyocytes; 3) Immunofluorescence of CD31 (CD31 antibody from Abcam, ab28364) to detect endothelial cells (capillaries). Photographing of the stained sections had been performed in a blinded manner and ten random fields were acquired for each section at 40× magnification for analysis. The histomorphology images were processed and analysed with ImageJ 1.52o for quantification.

9. Gene expression quantification using PCR

9.1 Reverse transcription of RNA into cDNA

In preparation for real-time PCR amplification, the first-strand cDNA was synthesised through reverse transcription PCR using the ImProm-II™ Reverse Transcription System (Promega). The total RNA samples served as the template for cDNA synthesis. The first step was RNA denaturation and primer hybridization. Total RNA (500ng) was mixed with Oligo $(dT)_{15}$ Primer (1µL) and DNase-free water were added to make the final volume of 5µL. The mix was then fixed into a PCR machine (Applied Biosystems) for a 5-minute pre-incubation and was then immediately chilled on ice. The second step was the reverse transcription PCR. The reaction mixture for reverse transcription was prepared by combining the following components in *Table 2-2*.

Table 2-2 The experimental reaction of the reverse transcription

Components	Volume(µL)
5× Reaction Buffer	4
$MgCl_2$ (25mM)	2.4

dNTP (10mM)	1
Ribonuclease Inhibitor	0.5
Reverse Transcriptase	1
Nuclease-Free Water	6.1
The primer/RNA mixture from the previous step	5
Final volume	20

The reaction mixture was then put into the PCR machine for the following incubation procedures as follows: 25°C for 5 minutes (annealing), 42°C for 60 minutes (extension) and a final step at 70°C for 15 minutes (heat-inactivation). A 10-fold dilution of the RT reaction for each sample was prepared for the further PCR reaction.

9.2 Real-time PCR and analysis

Real time PCR was performed with TaqMan Gene Expression Assays (ThermoFisher Scientific) to detect the expression of the target genes at the mRNA level. The assays are hydrolysis probes and they were commercially available. The cDNA samples were used to prepare the PCR reaction mix for the TaqMan gene expression assay. Here are the Assay IDs of the genes been tested in this study:

Ppfia1 (Mm01276516_m1, Rn01498298_m1); *Adamts9* (Mm00614433_m1, Rn01425216_m1); *Gdf15* (Mm00442228_m1, Rn00570083_m1); *Ankrd37* (Mm01200803_m1, Rn01767470_g1); *Phactr4* (Mm00614398_m1, Rn01515505_m1); *Nr4a3* (Mm00450071_g1, Rn01354012_m1); *Pdk4* (Mm01166879_m1, Rn00585577_m1); *Hbegf* (Mm00439306_m1, Rn00585577_m1); *Gapdh* (Mm99999915_g1, Rn01775763_g1).

The content of a single reaction (a single well on the 384-well plate) of the real-time PCR amplification is listed in Table **2-3**.

Table 2-3 The experimental reaction of real-time PCR amplification

Components	Volume(μL)
2× TaqMan® Gene Expression Master Mix	5
20× TaqMan® Gene Expression Assay	0.5
cDNA template	2
Nuclease-Free Water	2.5
Final volume	10

Each cDNA sample had triplicate wells. A negative reaction was loaded for each target gene. When the PCR plate was ready with all the reactions loaded, the plate was then put into the QuantStudio 12K Flex Real-Time PCR System (ThermoFisher Scientific) for real-time PCR amplification. After a 10-minute incubation at 95°C to activate the enzymes, the reaction was subjected to 40 thermal cycles of 15 seconds at 95°C (denaturation) and 1 minute at 60°C (annealing). The amplification curve was recorded. The adjusted cycle threshold values (Ct) of the target genes were normalized to the housekeeping gene GAPDH and relative expression was calculated as fold changes of the control group.

10. Western blots

10.1 Protein extraction and quantification

Protein was extracted from the tissue pieces preserved in -80°C. The tissue collection and preservation have been detailed in *Section 4.3*. Tissue pieces were homogenised in phosphate buffer (75mM K_2HPO_4, 25mM KH_2PO_4, 1mM EDTA, 1mM dithiothreitol) supplemented with phosphorylase and protease inhibitors (PhosSTOP™ and cOmplete™ from Sigma-Aldrich). The homogenate was centrifuged at 15,000 × g for 15 minutes. The supernatant is the extracted protein was carefully collected and aliquoted. The protein samples were quantified immediately after the extraction process using Bicinchoninic Acid (BCA) protein assay (Thermo Scientific). The aliquoted protein samples were saved in -80°C.

10.2 Electrophoresis

Electrophoresis was performed using a commercial standardized electrophoresis system (NuPAGE®, Invitrogen) following the user manual. To prepare the protein samples for electrophoresis, 20µg of extracted protein were well mixed with lithium dodecyl sulphate (LDS) sample buffer and reducing agent (NuPAGE®, Invitrogen). The mixture was then heated at 70°C for 10 minutes to denature the protein. Then the samples, together with one well of protein marker (BioRad), were loaded to a 4-12% Bis-Tris gel (NuPAGE®, Invitrogen). The loaded gel was then electrophoresed at the constant voltage of 200 volts for about 50 minutes.

10.3 Electro-transfer

After electrophoresis, the proteins in the gel was immediately transferred to a nitrocellulose membrane (GE Healthcare). The transfer buffer contained 20% of methanol and the buffer was made from the condensed solution (NuPAGE®, Invitrogen). The wet transfer was conducted. The transfer module was subjected to a constant voltage of 30 volts for 60 minutes. After the protein transfer, the membrane was stained with ponceau red dye to visualize the transferred proteins and to judge the transfer efficiency.

10.4 Immunoblotting

The membrane was blocked in 5% skimmed milk. Primary antibodies in 5% skimmed milk were added to the membrane. The protein of interest was probed with the antibody overnight at 4°C on a shaker. The primary antibodies used in this study were listed in Table. On the next day, the membrane was washed with tris-buffered saline (20 mM Tris, 150 mM NaCl, pH 7.6) with 1‰ Tween-20 (TBST) for 3 times (5 minutes each time). The corresponding horseradish peroxidase (HRP) conjugated the second antibody was then added to the membrane for incubation of 1.5 hours. The membrane was then washed for 3 times and it was ready for the imaging process. The primary antibodies used for immunoblotting are listed in *Table 2-4*.

Table 2-4 Primary antibodies used in this study

Target	Dilution	Host	Catalogue No.	Manufacturer
SERCA2	1:1000	Rabbit	ab3625	Abcam
p-PI3K	1:1000	Rabbit	4228	Cell Signaling Technology
PI3K	1:1000	Rabbit	4249	Cell Signaling Technology
p-AKT	1:1000	Rabbit	9271S	Cell Signaling Technology
AKT	1:1000	Rabbit	9272S	Cell Signaling Technology
p-AMPKα	1:1000	Rabbit	2535S	Cell Signaling Technology
AMPKα	1:1000	Rabbit	5832S	Cell Signaling Technology
p-mTOR	1:1000	Rabbit	5536S	Cell Signaling Technology
mTOR	1:1000	Rabbit	2983S	Cell Signaling Technology
GAPDH	1:5000	Rabbit	G9545	Sigma-Aldrich

10.5 Blots imaging and analysis

The chemiluminescence of the protein bolts was generated by adding ECL substrate (Invitrogen Novex ECL kit) to the membrane. Then, the chemiluminescence

of the protein bolts was detected and imaged using an imaging system (ChemiDoc MP Imaging System, BioRad). The lanes and blots were analysed using the Image Lab Software (BioRad).

11. RNA sequencing and analysis

11.1 Background knowledge

RNA sequencing (RNAseq) is a next-generation sequencing (NGS) technology which allows for the comprehensive analysis of the transcriptome at single-nucleotide resolution. The most common usage of RNAseq is the analysis of differential gene expression. More than this, RNAseq also serves as an indispensable tool for all the other transcriptome-wide studies, including micro RNAs, non-coding RNAs *etc*. With the development of NGS technology, RNAseq has become versatile in many parts of RNA biology analysis, including single-cell transcriptome, translation, and RNA structure.[200]

RNAseq experiments follow a similar workflow. The typical workflow of RNAseq comprises RNA isolation and purification, library preparation, library sequencing, and the analysis processes. The RNAseq procedures in this study are demonstrated in *Figure 2-8*, and the procedures are detailed in the following sections.

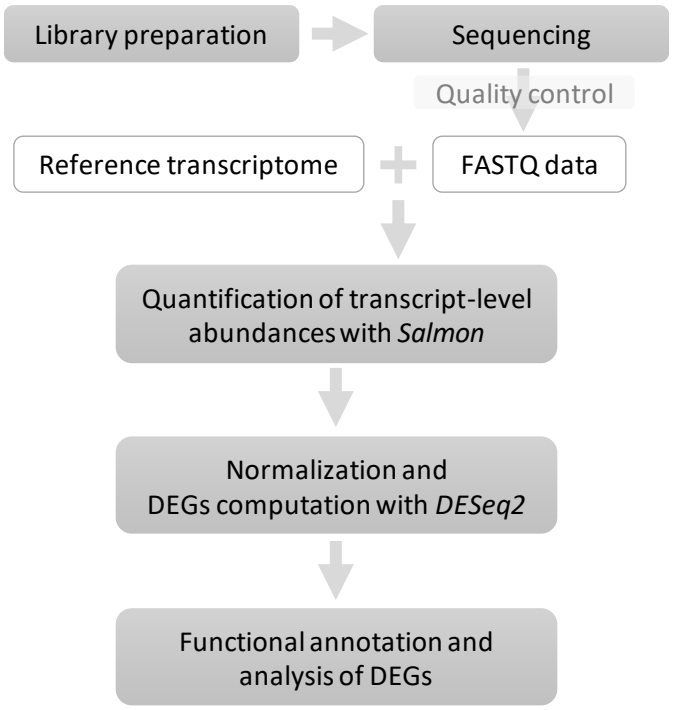

Figure 2-8 Workflow of the bioinformatic analysis of RNAseq data

11.2 Total RNA isolation and purification

To start with, total RNA needs to be isolated and purified to build the library for sequencing. Total RNA was isolated from frozen RV tissues of the experimental models using the RNeasy Mini Kit (Qiagen). The tissues (no more than 30mg) were homogenized in 500µL Buffer RLT (containing 0.01% ß-mercaptoethanol). The homogenate was then mixed with 1 volume of 70% ethanol and was transferred to RNeasy Mini spin column and centrifuged. After this step, the on-column DNase digestion was performed following the manufacture instruction. Following the DNase digesting steps, the column was washed with 700µL Buffer RW1 for once and 500 µL Buffer RPE for twice sequentially. Then the spin column was transferred to RNA collection tubes, and the RNA was eluted in 30µL RNase-free water. RNA concentration and quality were estimated using a NanoDrop Spectrophotometer.

The absorbance at 260nm (A260), 280nm (A280) and 230(A230) were used to assess the quality of the RNA samples. The peak of the absorption spectrum of nucleotides is at A260. The RNA quality is accepted when both the A260/A280 ratio was around 2.0 and the A260/A280 ratio was higher than the A260/A280 ratio.

11.3 Library preparation and sequencing

The total RNA was submitted to Imperial Genomics Facility for library preparation and sequencing. The sequencing library was constructed from the total RNA using the TruSeq RNA Sample Preparation Kit (Illumina) following the product manual. Then the library was subjected to Illumina HiSeq 4000 platform and was sequenced with the read depth of 25 million reads per sample. The raw sequencing data were archived in FASTQ files. The FASTQ files, along with the quality control reports, were returned to us for analysis.

11.4 Sequencing analysis

The analysis steps include: (1) mapping the sequencing reads to the genome; (2) quantification of the reads/abundance; (3) normalization of the expression matrix; (4) computing the differential expressing genes (DEGs); (5) functional analysis of the DEGs.

Sequencing data (FASTQ files) were subjected to Salmon (version 0.14.1) for reads mapping and counting.[201] The transcriptome index used for reads mapping was built with the mice genome, transcriptome and annotation files (GRCm38.p6). DEGs between groups were computed using the built-in Wald statistic of the DESeq2 R package (version 1.24.0).[202] Benjamini-Hochberg procedure was applied to control the false discovery rate (FDR) and to offer the *p* values with adjustment. The adjusted *p* value < 0.01 and the fold change > 2 were set as the criteria of DEGs. The annotation of the DEGs and the pathway enrichment were performed using clusterProfiler R package (version 3.12.0).[203]

12. Statistics

Statistical analysis was performed using either R (version 3.6.3) or GraphPad Prism 7 (GraphPad Software, San Diego, California). All values are presented as mean (SD) unless otherwise stated. One-way analysis of variance (ANOVA) was used for multi-group analysis. Turkey *post hoc* test was performed between the specific two groups if there was a statistically significant one-way ANOVA result. Two-tailed unpaired student's *t* tests were performed to determine the difference of two datasets. Linear regression was performed to define the correlation between two

variables. Significant differences were reached when p <0.05. The false discovery rate (FDR) in multiple statistical analysis was controlled by Benjamini–Hochberg procedure. RNA sequencing data were processed with the R packages as mentioned above, and the statistics were concluded using the built-in algorithms. The significant code of the p values in all the figures in this thesis: *** stands for $p < 0.001$ (*e.g.* $p = 0.00068$); ** stands for $p < 0.01$; * stands for $p < 0.05$; *ns* stands for no significance.

Chapter 3

Longitudinal Investigations of PH Experimental Models

1. Highlights

Given that the function of the RV determines the prognostic of PH, a better characterization of the RV behaviour in PH condition will advance the knowledge of RV adapting mechanism and promote the development of RV-directed therapeutic strategies.[204] Currently there is limited knowledge of cardiac imaging in reflecting RV performance and pathology. In the research setting, experimental animal models are essential tools designed to explore the underlying pathophysiological mechanisms of diseases. Better characterization of PH experimental models serves the purpose to investigate the coupling mechanisms of the cardiopulmonary unit. The comprehensive description of the RV behaviour will also offer references in preclinical evaluation of the efficacy of potential drugs.

Works presented in this chapter offered rigorous metrics to characterize the RV remodelling and cardiopulmonary status in two widely used experimental PH models, the MCT and SuHx PH rats. I assessed the RV morphology, physiology and function using the gold standard translational tool in the two PH models. I aimed to identify the specific imaging biomarkers, including the early signs of deleterious RV remodelling, as well as the molecular signatures of RV decoupling. This chapter sets up standard key techniques for accessing the RV remodelling in the preclinical setting, which will benefit the PH research community.

2. Results

2.1 Haemodynamic assessment of the rodent PH models

MCT and SuHx rats presented with increased mPAP, but no significant changes in SBP. *Figure 3-1* presents the haemodynamic data in rats of 4-week MCT and 8-week SuHx. Representative pressure curves of the RV and PA are presented in *Figure 3-1 A*. Compared to healthy controls, MCT and SuHx rats had a significantly increased mean PAP (mPAP; MCT 38.0 ±9.41 mmHg, SuHx 51.5 ±6.78 mmHg vs. 17.5 ±3.66 mmHg in controls; *Figure 3-1 B*). MCT and SuHx rats had a significantly increased RV systolic pressure (RVSP; MCT 65.2 ±22.3 mmHg, SuHx 105.0 ±20.5 mmHg vs. 28.3 ±5.42 mmHg in controls; *Figure 3-1 C*). There is no significant difference in the system systolic blood pressure (sSBP) among the three groups (*Figure 3-1 D*). The weight ratio of RV over LV

with the septum, as an indicator of RV hypertrophy, was also increased significantly in MCT and SuHx PH rats (MCT 0.552 ±0.110, SuHx 0.749 ±0.074 vs. 0.248 ±0.019 in controls; *Figure 3-1 E*). The mPAP and RVSP, as well as the weight ratio of RV over LV plus septum, were relatively higher in 8-weeks SuHx comparing to the 4-week MCT rats.

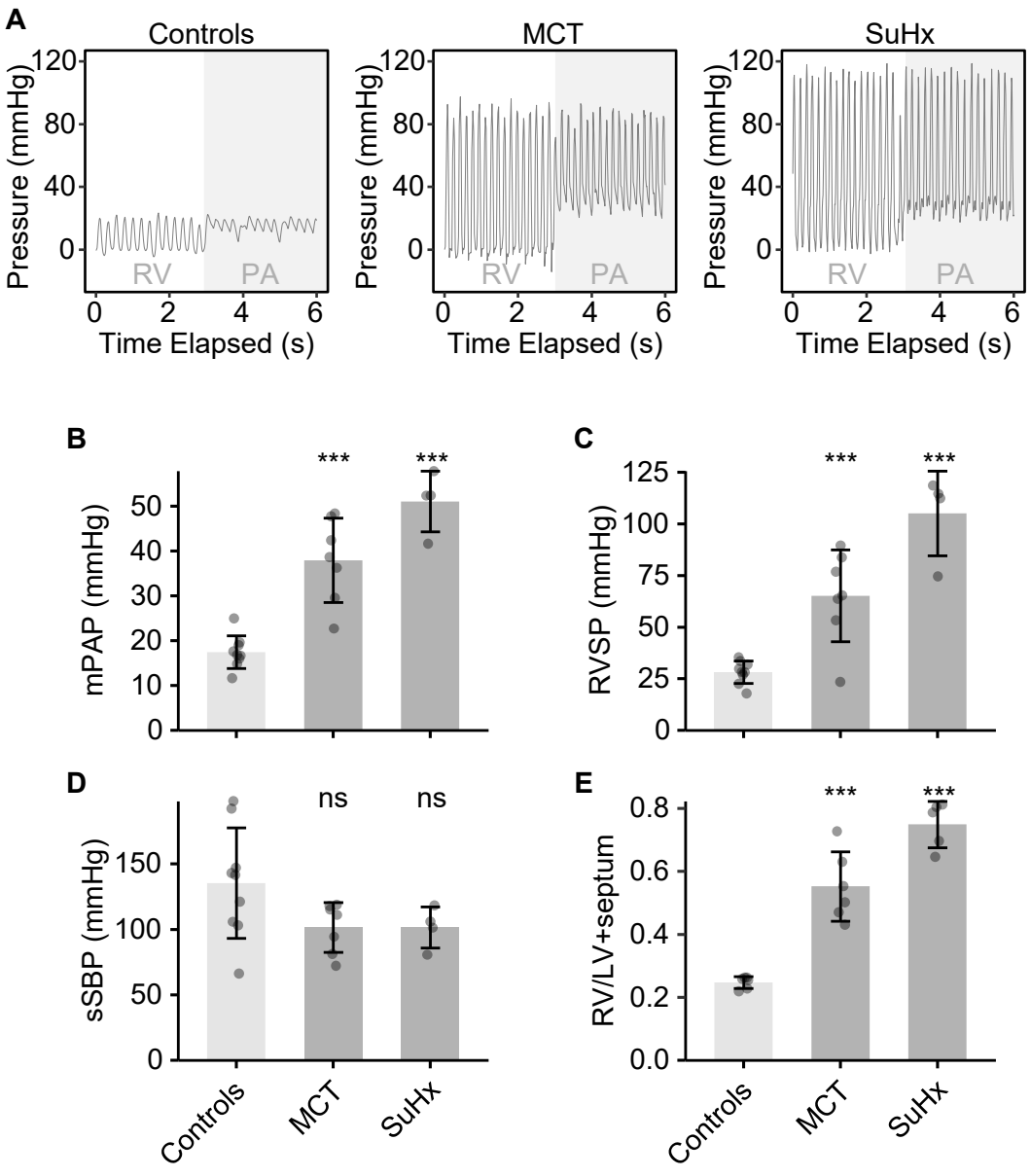

Figure 3-1 Haemodynamic assessment of the rodent PH models.

(A) Representative pressure trace of the RV and PA as indicated; (B) Compare of the mean PAP (mPAP); (C) Compare of the RV systolic pressure (RVSP); (D) Compare of the system systolic blood pressure (sSBP); (E) The

weight ratio of RV over LV with the septum. Sample size N = 4 ~ 9. Asterisks significant code (*) stands for the *p* values versus the control groups.

2.2 Characterization of RV structure and function in experimental PH in a longitudinal manner

2.2.1 Preview of the cine measurements of the cardiac MRI

Short axis cine stacks covering the entire heart were acquired for volumetric analysis in the PH rats of MCT and SuHx longitudinally (at baseline, 2- and 4-week timepoints of MCT, and 6-, 8- and 10-week timepoints of SuHx). *Figure 3-2* shows the representative short-axis MR images of the heart at the papillary muscle level (mid-cavity). A short-axis cine image of healthy rat hearts is presented in *Figure 3-2 A.* In MCT rats (*Figure 3-2 B*), a slight dilation of the RV cavity, as well as a small shift of the interventricular septum toward the LV, can be noticed at the end of the second week. At the end timepoint (4 weeks), prominent RV dilatation and hypertrophy was observed. The interventricular septum was flattened totally, and shifted towards the LV, making the RV cavity a D shape. In SuHx rats (*Figure 3-2 C*), remarkable RV dilatation and RV wall hypertrophy, as well as septum flattening, were observed at 4-week timepoint after the hypoxia exposure and these persisted thereafter at 8- and 10-week timepoint. The detailed cine parameters at different time point were listed in *Table 3-1* (for MCT rats) and *Table 3-2* (for SuHx rats) separately.

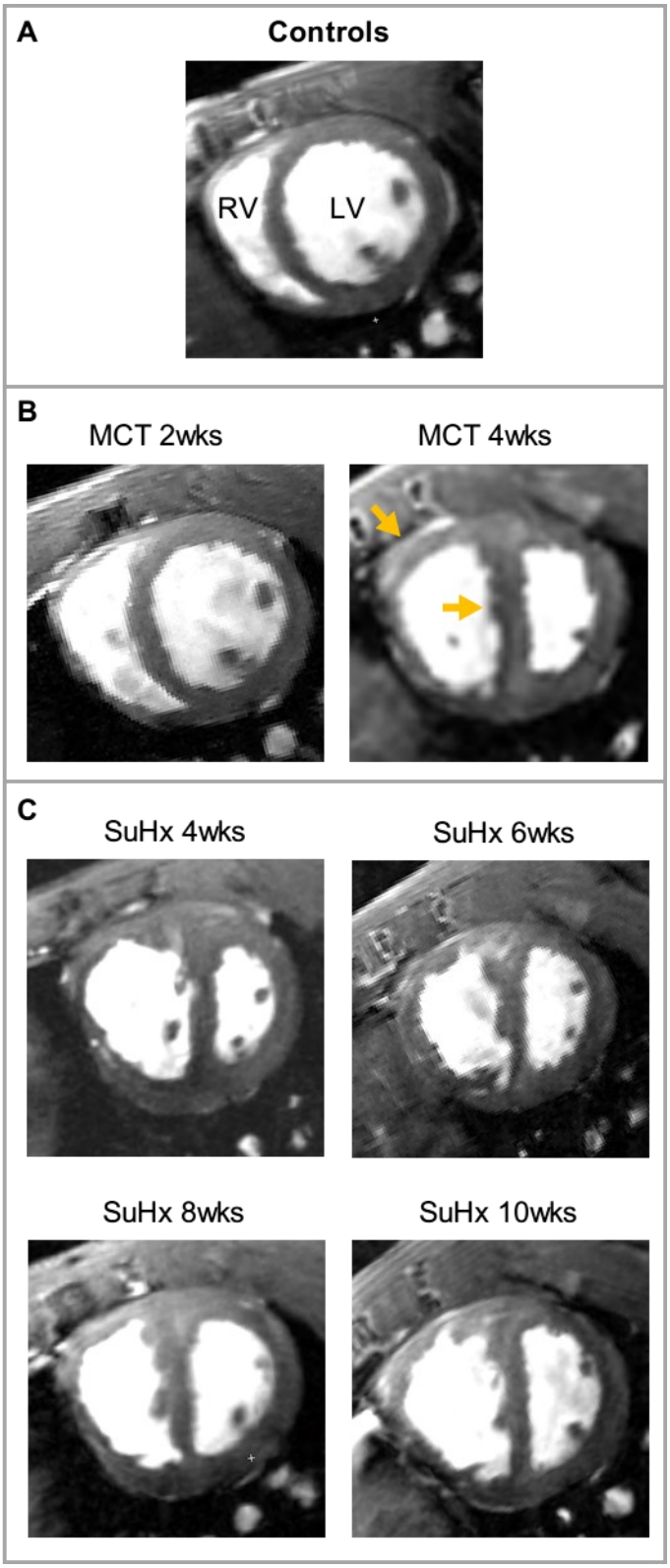

Figure 3-2 Representative short-axis MR images of PH rats

Short axis view of the heart at papillary muscle level (mid-cavity) of (A) healthy control rats, (B) MCT rats, and (C) SuHx rats. The yellow arrows point to examples of the cardiac hypertrophy and septum flattening.

The key measurements of the heart morphology and function in PH rats were plotted longitudinally in *Figure 3-3*. In MCT rats, the RV function was maintained, and the RV was less dilated and hypertrophied at the early stage (2 weeks). At the 4-week timepoint, both the RV function and structure had a significant degeneration. (*Figure 3-3 A*). At the end stage of MCT rats, the LV cavity was squeezed by the left shift of the septum, which lead to a decreased cardiac function of LV as can be indicated by the LVCI (*Figure 3-3 C*). In SuHx rats, RV dilatation and hypertrophy were observed after 4-week hypoxia exposure. RV function parameters also had a remarkable decrease at this timepoint. These RV parameters were then maintained for further 4 weeks in the normoxia (*Figure 3-3 B*). In terms of LV, the dilated RV flattened the interventricular septum and decreased LV cavity. The LV hypertrophy was severer in SuHx rats in comparison to MCT rats, which may help to maintain the LVEF. The LV cavity (LVEDV) was increased as possibly a compensating response to the septum flattening (*Figure 3-3 C*). The dilating RV gradually diminished the LV cavity increase, which may impair the LV function.

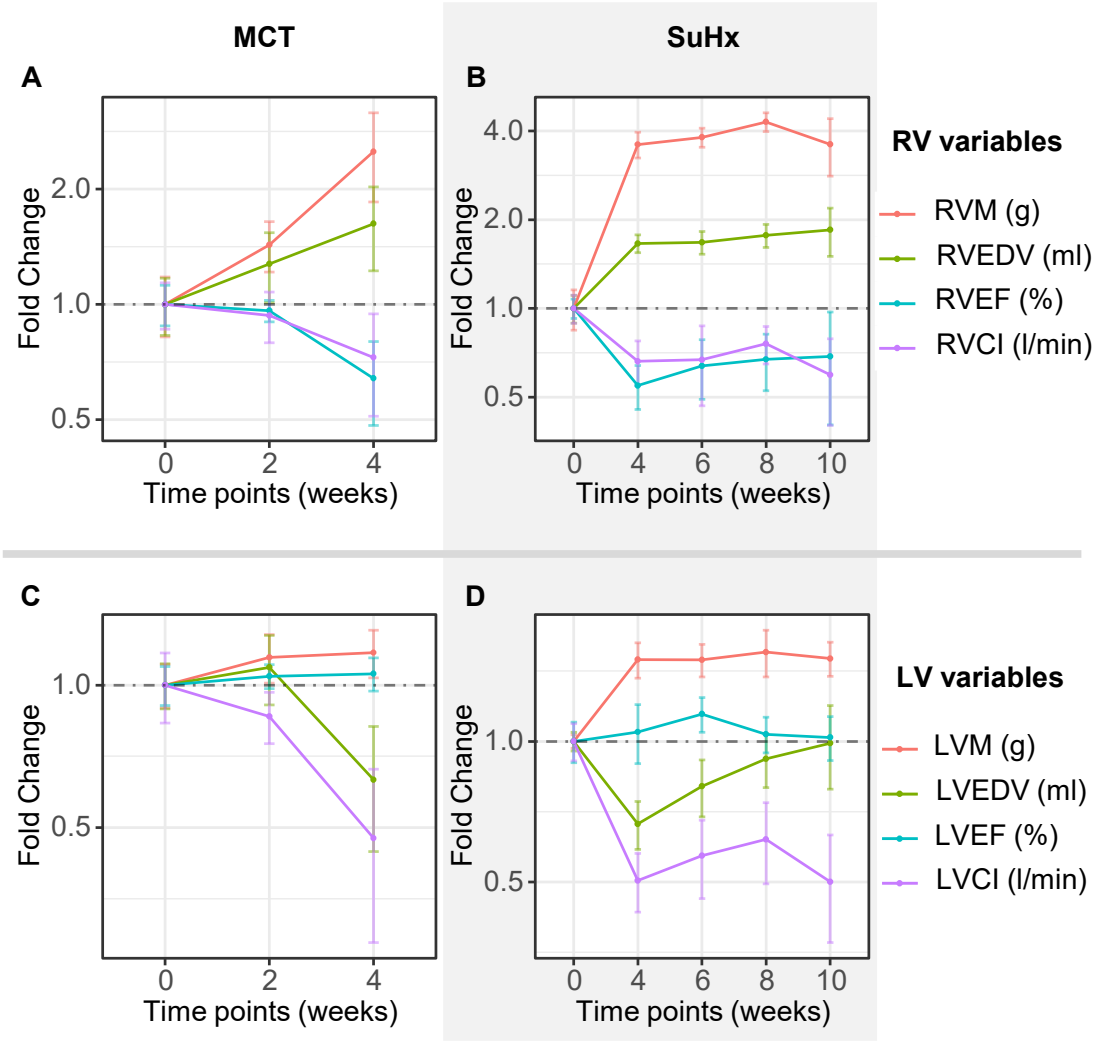

Figure 3-3 Overview of the key cine measurements in PH rats.

RV functional and structural parameters of (A) MCT and (B) SuHx rats; LV functional and structural parameters of (C) MCT and (D) SuHx rats; Sample size: N = 21, 16 and 12 for MCT rats at baseline, 2 and 4 weeks respectively, N = 9, 8, 8, 5, and 5 for SuHx rats at baseline, 4, 6, 8, and 10 weeks respectively. The *p* values are listed in *Table 3-1* and *Table 3-2*.

2.2.2 Description of RV hypertrophy and dilatation

To detail the changes of RV hypertrophy, the key parameters of the ventricular mass index (VMI) and RV end-diastolic volume (RVEDV) were presented (*Figure 3-4*). VMI, the indicator of RV hypertrophy, was calculated as the MRI-measured RV mass divide LV mass (septum included). RVEDV was used as a parameter of RV dilatation.

In MCT rats, an initial increase in VMI was observed at 2 weeks, meanwhile, the RVEDV did not show a significant change at this stage. This implied that RV hypertrophy, as an adaptive response to the load, occurred before RV dilatation. In 4-week MCT, excessive RV hypertrophy and dilatation were recorded. (*Figure 3-4 A, C*) In SuHx rats, the significant increase of VMI and RVEDV were observed after 4 weeks of hypoxic exposure. The parameters remained at similar levels thereafter at 6, 8 and 10 weeks timepoints. (*Figure 3-4 B, D*)

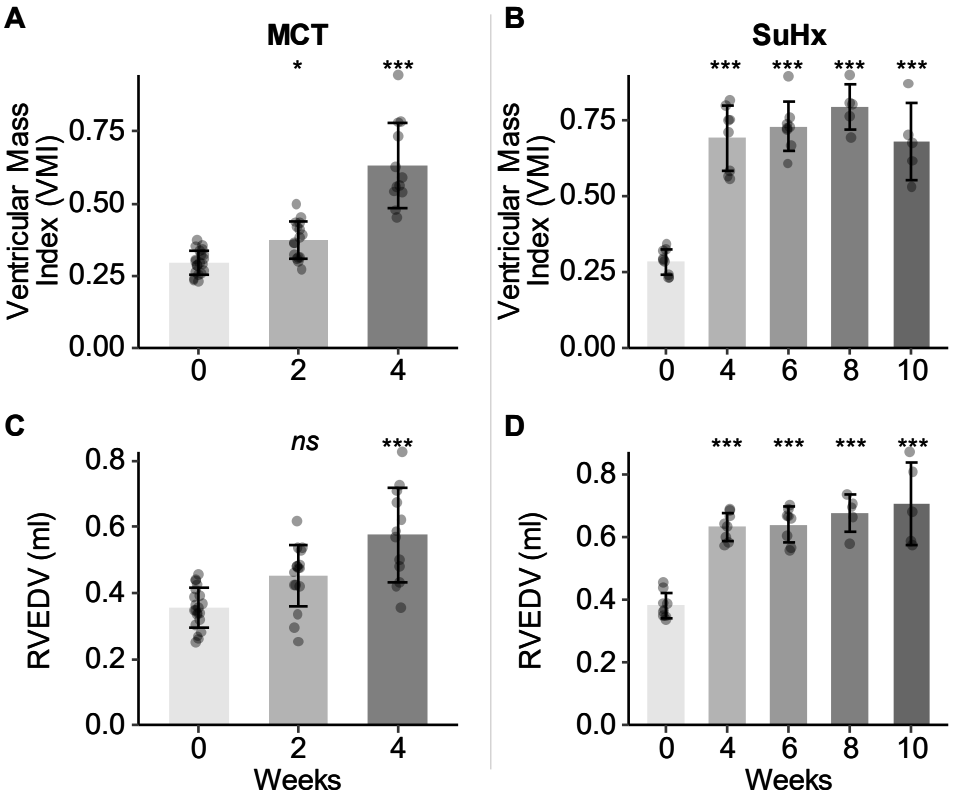

Figure 3-4 The progression of the RV structural degeneration in PH rats

(A) VMI in MCT rats; (B) VMI in SuHx rats; (C) RVEDV in MCT rats; (D) RVEDV in SuHx rats. VMI: ventricular mass index (RV mass/LV mass); RVEDV: RV end-diastolic volume. Sample size: N =15~21 for MCT study; N = 5~9 for

SuHx study. Asterisks significant code (*) stands for the *p* values versus the control groups.

2.2.3 Description of the functioning state of the cardiopulmonary unit

Figure 3-5 demonstrates the longitudinal changes of the functioning state of the cardiopulmonary unit in the two PH models. As described in *Chapter 1*, $E\mathrm{es}/E\mathrm{a}$ serves as an important measurement for evaluating the coupling state of the cardiopulmonary unit. Here MRI volumetric parameters were used to estimate $E\mathrm{es}/E\mathrm{a}$. RVEF is a widely used parameter to assess the RV function. In 2-week MCT rats, the cardiopulmonary unit remains coupled and the RV function preserved, as there were no significant changes of $E\mathrm{es}/E\mathrm{a}$ and RVEF at this stage. Function deterioration of RV was observed in 4-week MCT rats, as both the parameters decreased significantly at this timepoint (*Figure 3-5 A,C*). In SuHx rats, RV functional impairment happened at a relatively early stage of SuHx model setting. There was a steady decrease of both $E\mathrm{es}/E\mathrm{a}$ and RVEF at 4 weeks when the SuHx rats were moved back to normoxia condition. This functional decrease was not reversed by returning the rats to normoxic environment, as the values of $E\mathrm{es}/E\mathrm{a}$ and RVEF stayed at the 4-weeks level from week 4 to the final week 10. However, it could be noted that the variation of the values of $E\mathrm{es}/E\mathrm{a}$ and RVEF had an increase after returning the rats to normoxia condition (*Figure 3-5 B, D*).

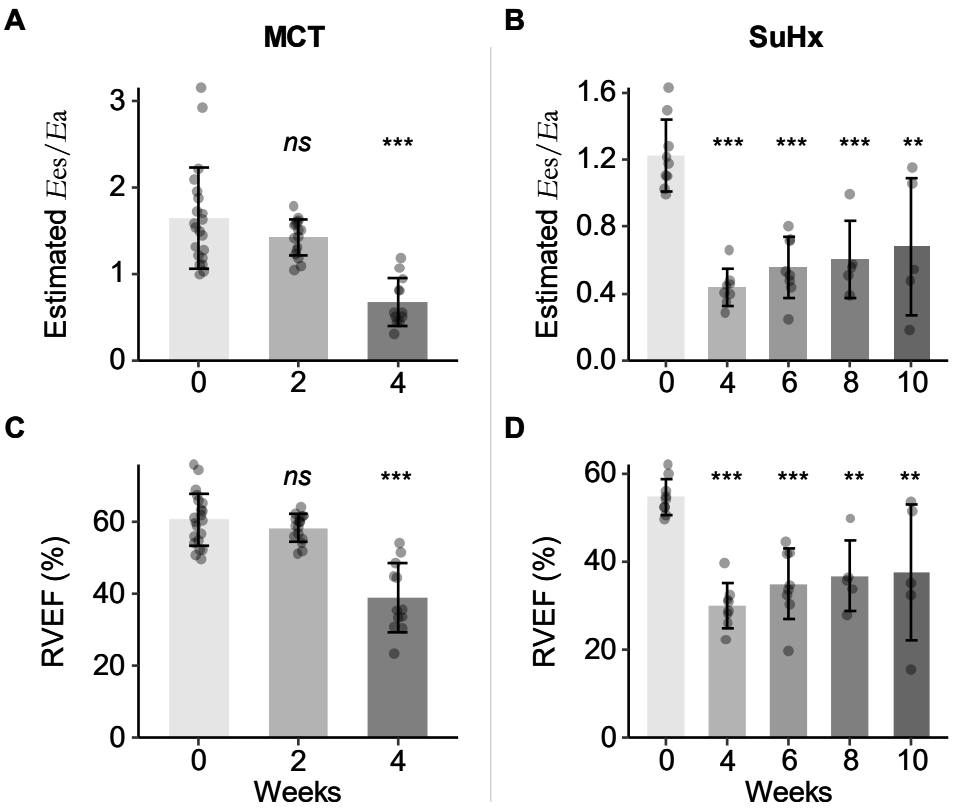

Figure 3-5 The downward course of RV coupling in PH rats

(A) MRI-estimated Ees/Ea in MCT rats; (B) MRI-estimated Ees/Ea in SuHx rats; (C) RVEF in MCT rats; (D) RVEF in SuHx rats. Ees/Ea was estimated by RVSV/RVESV. RVEF: RV ejection fraction. Sample size: N =15~21 for MCT study; N = 5~9 for SuHx study. Asterisks significant code (*) stands for the *p* values versus the baseline (0 week) groups.

Table 3-1 Cine measurements of MCT rats

Measurements	0 week (N=21)		2 weeks (N=16)			4 weeks (N=12)		
	Mean	SD	Mean	SD	*p* value	Mean	SD	*p* value
Weight (g)	230.0	34.6	293.6	40.5	<0.0001	298.4	45.6	0.0001
HR (bpm)	371	46	332	25	0.0068	308	29	0.0001
VMI	0.30	0.04	0.37	0.06	0.0246	0.63	0.15	<0.0001
Ees/Ea*	1.65	0.58	1.42	0.22	0.2685	0.68	0.28	<0.0001
RVM (g)	0.17	0.03	0.25	0.04	0.0024	0.43	0.11	<0.0001
RVMI (g/m^2)	4.60	0.74	5.60	0.89	0.0637	9.65	2.24	<0.0001
RVEDV (ml)	0.35	0.06	0.45	0.09	0.0103	0.58	0.14	<0.0001
RVEDVI (ml/m^2)	9.49	1.59	10.22	1.88	0.5141	12.85	2.67	0.0001
RVESVI (ml/m^2)	3.79	1.18	4.29	1.09	0.5625	7.87	2.21	<0.0001
RVSV (ml)	0.21	0.03	0.26	0.05	0.0143	0.22	0.07	0.8626
RVSVI (ml/m^2)	5.70	0.80	5.93	0.91	0.7864	4.98	1.52	0.1536
RVEF (%)	60.72	7.34	58.45	3.82	0.6004	38.93	9.60	<0.0001
RVCO (l/min)	0.08	0.01	0.09	0.02	0.2480	0.07	0.02	0.2230
RVCI (l/min)	2.10	0.29	1.96	0.30	0.4578	1.53	0.46	0.0001
LVM (g)	0.58	0.06	0.66	0.08	0.0028	0.68	0.08	0.0011
LVMI (g/m^2)	15.52	1.08	15.08	1.17	0.4645	15.28	1.14	0.8182
LVEDV (ml)	0.48	0.05	0.52	0.09	0.1987	0.30	0.09	<0.0001
LVEDVI (ml/m^2)	12.76	1.34	11.73	1.32	0.0960	6.73	1.79	<0.0001
LVESVI (ml/m^2)	5.00	0.98	4.29	0.76	0.0294	2.34	0.44	<0.0001
LVSV (ml)	0.29	0.04	0.33	0.06	0.0798	0.20	0.07	0.0001
LVSVI (ml/m^2)	7.76	0.97	7.45	0.80	0.6447	4.40	1.45	<0.0001
LVEF (%)	60.96	5.74	63.63	3.73	0.2547	64.40	5.16	0.1522
LVCO (l/min)	0.11	0.02	0.11	0.02	0.9263	0.06	0.03	<0.0001
LVCI (l/min)	2.88	0.49	2.47	0.31	0.0253	1.37	0.54	<0.0001

* MRI estimated Ees/Ea; # The *p* values here are from Tukey *post hoc* tests comparing against 0-week controls.

Table 3-2 Cine measurements of SuHx rats

Measurements	0 week (N=9)		4 weeks (N=8)			6 weeks (N=8)			8 weeks (N=8)			10 weeks (N=5)		
	Mean	SD	Mean	SD	*p* value	Mean	SD	*p* value	Mean	SD	*p* value	Mean	SD	*p* value
Weight (g)	213.3	17.1	288.4	17.7	<0.0001	344.3	22.3	<0.0001	384.6	29.0	<0.0001	439.0	35.6	<0.0001
HR (bpm)	351	26	312	23	0.0344	298	26	0.0021	335	13	0.7967	282	40	0.0005
VMI	0.28	0.04	0.69	0.11	<0.0001	0.73	0.08	<0.0001	0.79	0.08	<0.0001	0.68	0.13	<0.0001
Ees/Ea*	1.23	0.21	0.43	0.11	<0.0001	0.56	0.18	<0.0001	0.60	0.23	0.0003	0.68	0.41	0.0016
RVM (g)	0.16	0.02	0.57	0.06	<0.0001	0.60	0.04	<0.0001	0.68	0.05	<0.0001	0.57	0.13	<0.0001
RVMI (g/m^2)	4.47	0.80	13.11	1.29	<0.0001	12.33	0.98	<0.0001	12.93	1.17	<0.0001	9.90	2.01	<0.0001
RVEDV (ml)	0.38	0.04	0.63	0.04	<0.0001	0.64	0.06	<0.0001	0.68	0.06	<0.0001	0.71	0.13	<0.0001
RVEDVI (ml/m^2)	10.74	1.31	14.56	1.01	<0.0001	13.03	0.81	0.0149	12.81	1.13	0.0794	12.28	2.57	0.2898
RVESVI (ml/m^2)	4.86	0.77	10.23	1.33	<0.0001	8.48	1.18	0.0009	8.16	1.62	0.0099	7.91	3.35	0.0200
RVSV (ml)	0.21	0.03	0.19	0.03	0.8940	0.22	0.06	0.9676	0.25	0.03	0.6462	0.25	0.08	0.4649
RVSVI (ml/m^2)	5.88	0.83	4.33	0.53	0.0141	4.55	1.11	0.0457	4.65	0.64	0.1494	4.38	1.42	0.0501
RVEF (%)	54.73	4.09	29.97	5.10	<0.0001	34.92	7.99	0.0002	36.77	8.02	0.0037	37.60	15.56	0.0059
RVCO (l/min)	0.07	0.01	0.06	0.01	0.3675	0.07	0.02	0.9457	0.08	0.01	0.8422	0.07	0.02	0.9985
RVCI (l/min)	2.05	0.22	1.36	0.23	0.0006	1.38	0.42	0.0008	1.56	0.23	0.0513	1.22	0.40	0.0003

Measurements	0 week (N=9)		4 weeks (N=8)			6 weeks (N=8)			8 weeks (N=8)			10 weeks (N=5)		
	Mean	SD	Mean	SD	*p* value	Mean	SD	*p* value	Mean	SD	*p* value	Mean	SD	*p* value
LVM (g)	0.56	0.02	0.83	0.07	<0.0001	0.83	0.07	<0.0001	0.87	0.10	<0.0001	0.84	0.07	<0.0001
LVMI (g/m^2)	15.65	0.76	19.12	1.70	0.0001	16.96	1.18	0.2584	16.35	1.39	0.8712	14.56	1.45	0.5640
LVEDV (ml)	0.48	0.02	0.32	0.04	<0.0001	0.38	0.05	0.0073	0.44	0.06	0.6752	0.47	0.10	0.9999
LVEDVI (ml/m^2)	13.39	0.92	7.26	0.73	<0.0001	7.78	1.07	<0.0001	8.28	1.07	<0.0001	8.23	1.85	<0.0001
LVESVI (ml/m^2)	5.59	0.98	2.86	0.83	<0.0001	2.57	0.53	<0.0001	3.24	0.36	0.0001	3.37	0.98	0.0002
LVSV (ml)	0.28	0.03	0.19	0.03	0.0013	0.26	0.05	0.7909	0.27	0.06	0.9867	0.28	0.05	1.0000
LVSVI (ml/m^2)	7.80	0.74	4.41	0.53	<0.0001	5.21	0.87	<0.0001	5.04	0.98	<0.0001	4.86	1.03	<0.0001
LVEF (%)	58.40	5.79	61.19	8.86	0.9079	66.81	5.73	0.0950	60.49	5.30	0.9794	59.56	6.41	0.9979
LVCO (l/min)	0.10	0.01	0.06	0.01	0.0001	0.08	0.02	0.0356	0.09	0.02	0.8336	0.08	0.02	0.1575
LVCI (l/min)	2.73	0.25	1.38	0.20	<0.0001	1.56	0.30	<0.0001	1.69	0.33	<0.0001	1.37	0.35	<0.0001

* MRI estimated Ees/Ea; # The *p* values here are from Tukey *post hoc* tests comparing against 0-week controls.

2.3 PA flow pattern from the MR phase-contrast images

2.3.1 Changes in the parameters of the PA flow curves

Shortening of pulmonary artery acceleration time (PAAT), which indicated the increase of PA pressure, was observed in both MCT and SuHx rats. In MCT rats, PAAT had a decrease at 2 weeks after MCT injection and it decreased progressively (*Figure 3-6 A,B*). In SuHx rats, shortening of PAAT was observed after 4-week hypoxia and then the PAAT was maintained thereafter (*Figure 3-6 C,D*). The abnormal mid-systolic velocity deceleration (dicrotic notch on the PA velocity curve), which is attributable to PA regurgitation and stiffness, was consistently observed (pointed by the arrow in *Figure 3-6 A,C*) on the PA curves of established experimental PH (of both models).

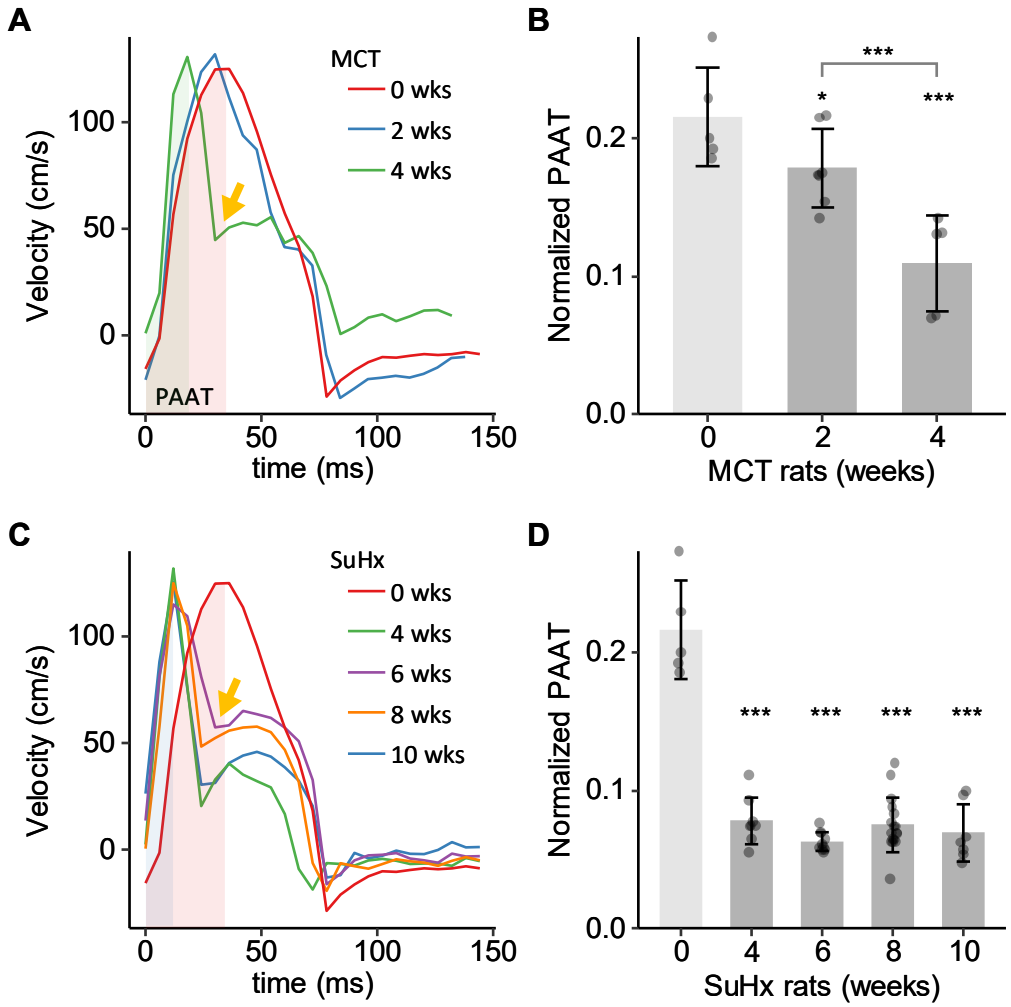

Figure 3-6 PA haemodynamic of the two PH rat models

(A) Representative curves and (B) normalized PAAT of the MCT rats; (C) Representative curves and (D) normalized PAAT of the SuHx rats. Arrow

indicates the dicrotic notch. Sample size: N = 5, 7, 5 for MCT rats at baseline, 2 and 4 weeks respectively, N = 5, 8, 10, 17, 7 for SuHx rats at baseline, 4, 6, 8, and 10 weeks respectively. Asterisks significant code (*) stands for the *p* values versus the baseline (0 week) group or the *p* values as indicated in the figure.

2.3.2 PAAT shortening correlates with RVH and RV dilatation

As the shortening of PAAT implies the damage of PA haemodynamic, it is useful to explore the correlation of the PAAT value to the RV performance. Linear regression was performed to determine if the PAAT is correlated with the RV structural and/or functional changes in both MCT and SuHx models.

Results of the linear regression analysis between RV cine measurements and the PAAT value are presented in *Table 3-3*, and the correlation plots are in *Figure 3-7*. A strong correlation between the RV hypertrophy (VMI) and PAAT value was found in both MCT and SuHx rats. PAAT value was also correlated with RV dilatation (RVEDV), but the correlation was found much weaker in MCT rats. The shortening of PAAT indicated decreased coupling and reduced function of RV in SuHx rats, while this correlation is not detectable in MCT rats.

Table 3-3 Correlation of the RV Cine measurements and the PAAT value

Cine measurements	Models	R^2	*p* value	FDR adjusted *p* value
VMI	MCT	0.62	1.1×10^{-4}	2.2×10^{-4}
	SuHx	0.62	1.4×10^{-7}	1.1×10^{-6}
RVEDV (ml)	MCT	0.19	4.4×10^{-2}	5.9×10^{-2}
	SuHx	0.52	4.1×10^{-6}	1.7×10^{-5}
Estimated Ees/Ea	MCT	0.08	0.14	0.15
	SuHx	0.47	1.7×10^{-5}	4.6×10^{-5}
RVEF (%)	MCT	0.10	0.12	0.13
	SuHx	0.38	1.9×10^{-4}	3.0×10^{-4}

* The FDR of the multiple analyses was corrected using Benjamini-Hochberg method.

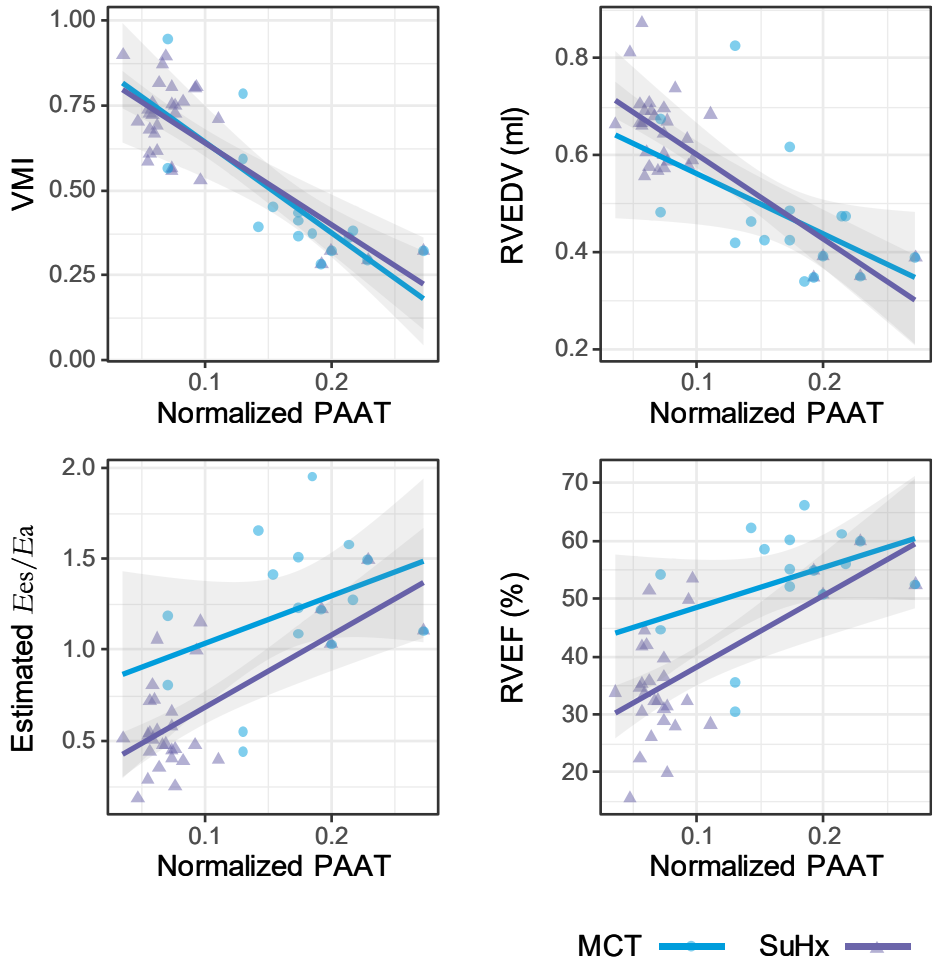

Figure 3-7 Correlation between PAAT and RV cine measurements

The linear regression plots plotting the RV cine measurements against PAAT values. Number of rats included into the correlation analysis: total number was 47, number of MCT rats was 17, number of SuHx rats was 30.

2.4 Myocardium characterization of the RV in experimental PH

2.4.1 LGE patterns of the overloaded RV in PH condition

The LGE sequence was performed to reveal the cardiac fibrosis in the heart of PH rats. Representative LGE images are presented in *Figure 3-8*. Collectively, in PH rats, LGE areas can be frequently observed at the insertion points (IPs) and the inter-ventricular septum (IVS). The enhancement can also be observed at the RV free wall in PH rats, though the artefacts may hinder the interpretation at the regions of the RV wall. Overall, the LGE pattern of the predominant enhancement at the regions of IPs

and IVS was observed. The enhancement was co-validated by the ECV maps, which offered quantifiable results of the pathological changes of the enhanced regions.

2.4.2 ECV mapping demonstrate altered extracellular matrix at the RV insertion points

T1 mapping sequences were performed to characterize the myocardium abnormalities of the RV. Extracellular volume (ECV) maps were reconstructed with the T1 maps. Regional average ECV changes were visualized using the 26-seg polar plot (*Figure 3-8*; The 26-seg polar plot was described in *Chapter 2*). Both MCT and SuHx model showed a progressive increase of the ECV values especially at the regions of the IPs, the IVS and the RV free wall. LGE was observed at the insertion points of the heart in both models. Mechanical stress was proved to lead to either myocardium fibrosis or myocardial disarray, especially at the insertion points. In patients with PH, the presence of LGE at the insertion points was highly correlated to the severity of RV afterload and RV systolic function.[205] Here the patterns of ECV and LGE maps in the PH rats were similar to the PH patients.

The ECV values of the insertion points (IPs) were plotted in *Figure 3-9*. In MCT rats, the ECV values of the IPs were not changed at the 2-week timepoint. At the late stage of 4 weeks, IP-ECV values of the basal and mid-cavity levels were significantly increased. In SuHx rats, an increase of ECV was observed at the basal IPs at 6-week timepoint. At the later time points, ECV increase was found at most of the IPs. This implied that pathological changes may start at the basal level where the mechanical stress accumulate.

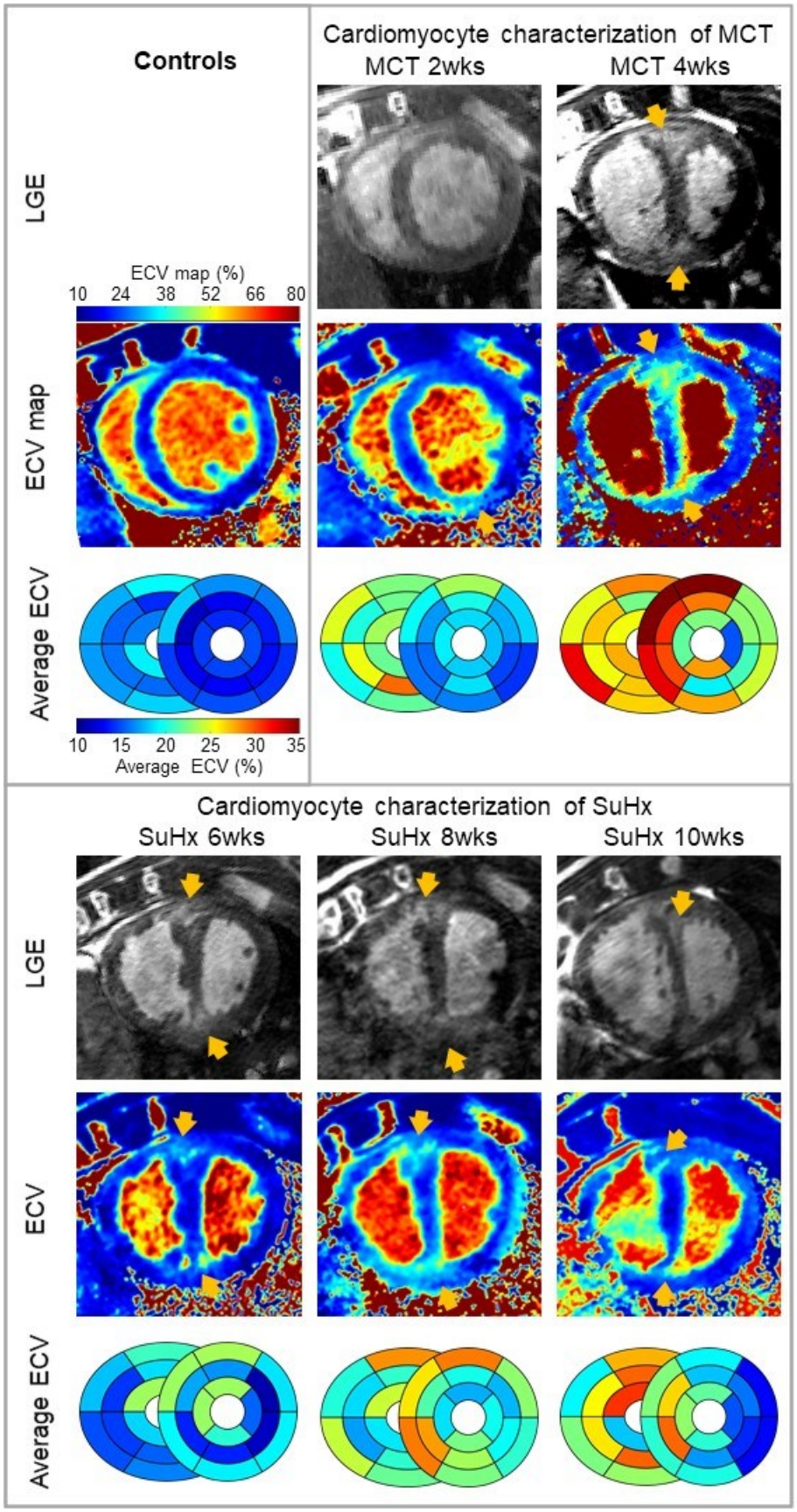

Figure 3-8 Representative images of myocardium characterization and regional ECV visualization

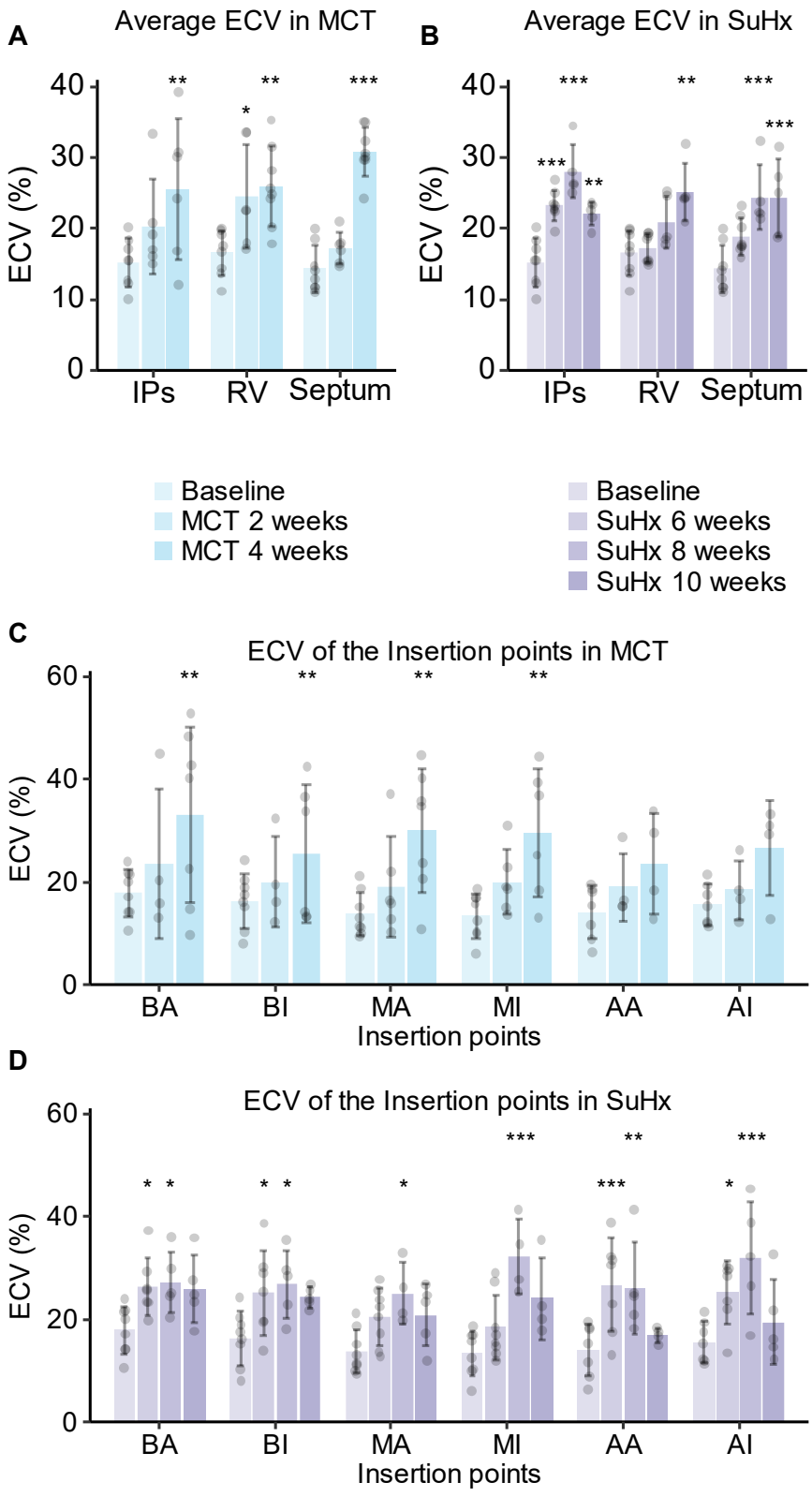

Figure 3-9 Quantification of the ECV in the IPs, RV free wall, and intraventricular septum in PH rats at different timepoints

(A) Average ECV in the indicated regions of the heart in MCT rats; (B) Average ECV in the indicated regions of heart in SuHx rats; (C) ECV of the

individual IPs in MCT rats; (D) ECV of the individual IPs in SuHx rats. Insertion points: basal anterior (BA), basal inferior (BI), mid-cavity anterior (MA), mid-cavity inferior (MI), apical anterior (AA), apical inferior (AI). Sample size: N for each timepoint of MCT rats (0, 2, and 4 weeks) ranges from 6 to 10. N for each timepoint of SuHx rats (0, 6, 8, and 10 weeks) ranges from 5 to 8. Asterisks significant code (*) stands for the *p* values *versus* the baseline (0 week) group.

2.4.3 Increased ECV of the IPs indicate the worsening of RV performance

Given that the ECV was increased in the IPs in PH rats, the correlation between the ECV increase and the RV structure and performance was analysed. Linear regression was performed to determine whether the ECV of IPs correlates with the MR metrics reflective of RV function and structure. The analysis revealed a strong correlation between the ECV value of IPs and the key RV volumetric parameters (*Table 3-4, Figure 3-10*). The increase of the ECV at IPs was an effective indicator of the RV hypertrophy and dilatation (VMI, RVEDV), as well as the deterioration of the RV function (Ees/Ea, RVEF). The IPs at the basal level is under higher mechanistic pressure when the RV is overloaded. The higher mechanistic pressure could possibly be reflected by the relatively closer correlation (higher R^2) between the ECV of IPs at basal and the key parameters of RV volumetric measurements.

Table 3-4 Linear regression of the RV Cine parameters and the ECV of IPs

Cine measurements	Model	Basal IPs		Mid IPs		Apical IPs	
		R^2	adjusted *p* value	R^2	adjusted *p* value	R^2	adjusted *p* value
VMI	MCT	0.60	9.9×10^{-4}	0.40	6.2×10^{-3}	0.32	2.3×10^{-2}
	SuHx	0.46	7.7×10^{-4}	0.28	6.2×10^{-3}	0.31	1.1×10^{-2}
RVEDV (ml)	MCT	0.62	8.2×10^{-4}	0.61	6.0×10^{-4}	0.56	1.0×10^{-2}
	SuHx	0.41	8.2×10^{-4}	0.22	1.6×10^{-2}	0.14	4.7×10^{-2}
Ees/Ea	MCT	0.40	8.6×10^{-3}	0.50	2.6×10^{-3}	0.32	3.3×10^{-2}
	SuHx	0.43	8.0×10^{-4}	0.16	3.4×10^{-2}	0.24	1.8×10^{-2}
RVEF (%)	MCT	0.50	3.0×10^{-3}	0.61	6.0×10^{-4}	0.43	1.8×10^{-2}
	SuHx	0.37	1.2×10^{-3}	0.10	7.1×10^{-2}	0.15	4.3×10^{-2}

* The adjusted *p* values listed in the table are adjusted for multiple analyses using the Benjamini-Hochberg method.

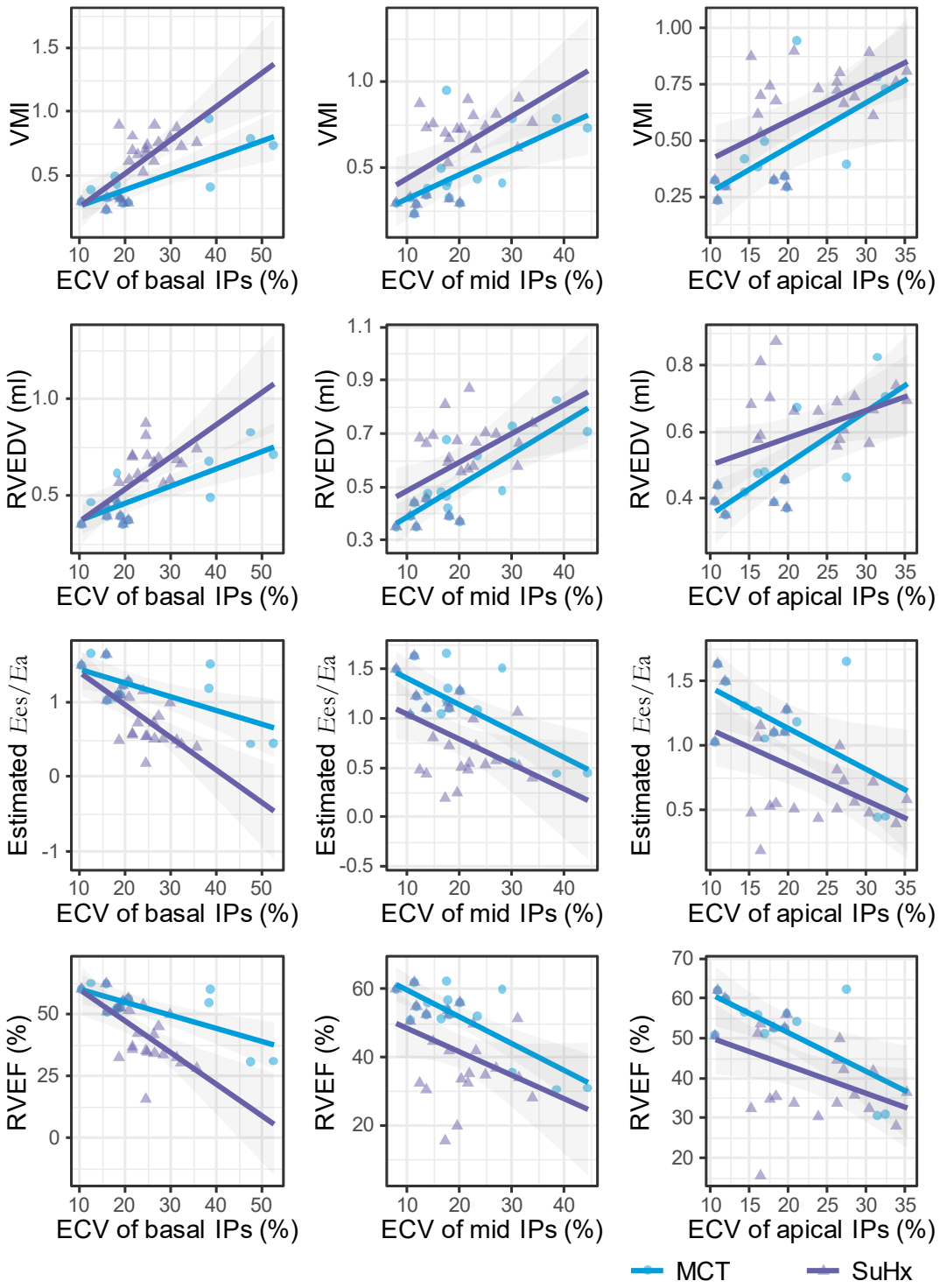

Figure 3-10 Correlation between the ECV of IPs and the key volumetric measurements.

The three columns of the plots represent the IPs of three levels, *i.e.* the basal, mid-cavity, and the apical level respectively. The four rows of the plots represent the volumetric MR parameters to be correlated with. Number of rats

included into the correlation analysis: total number was 63, number of MCT rats was 32, number of SuHx rats was 31.

2.5 Comprehensive insight of fibrosis, hypertrophy and microcirculation of the IPs in the heart of the PH rats

2.5.1 Fibrosis co-localized with increased ECV at the IPs

To determine the pathological changes that were accountable for the ECV increase at the IPs, histological investigations were performed to reveal the pathological changes in the area of the IPs (*Figure 3-11*). Representative images of Sirius Red staining showed both the typical overall distribution of the fibrosis in the heart and the fibrosis within the IPs (the magnified field) in healthy and diseased rats (*Figure 3-11* Sirius Red panels). Sirius Red stain accumulated at the areas of the IPs, as well as the septum and the RV free wall. The stain was dominantly been observed at the IPs where the ECV increased prominently as discussed above. The quantification of the fibrosis of IPs is presented in *Figure 3-12 A*. Mild increase of the fibrosis staining appeared at the IPs of 2-week MCT rats while the change is not significant. Excessive fibrotic degeneration in the IPs was observed in 4-week MCT and 8-week SuHx rats.

2.5.2 Description of RV cardiomyocyte hypertrophy and microcirculation

Cardiomyocyte diameter served as a parameter of cardiomyocyte hypertrophy and it was measured from the WGA immunofluorescent sections. The capillary density was determined with the CD31 immunofluorescent sections, as a reflection of the perfusion state of the microcirculation. The images used for analysis were taken from the IPs regions (*Figure 3-11* WGA and CD31 panels). Remarkable cardiomyocyte hypertrophy and reduction of capillary density were observed at the insertion points in both MCT and SuHx rats comparing to the healthy controls (*Figure 3-12 B,C*). Cardiomyocyte hypertrophy was observed in MCT rats of both 2 and 4 weeks, while there was no significant difference of the degree of cardiomyocyte hypertrophy between the 2-week and 4-week MCT rats (*Figure 3-12 B*). Reduction of the capillary density was observed in the 2-week MCT rats, and exacerbated significantly at the 4-week timepoint (*Figure 3-12 C*).

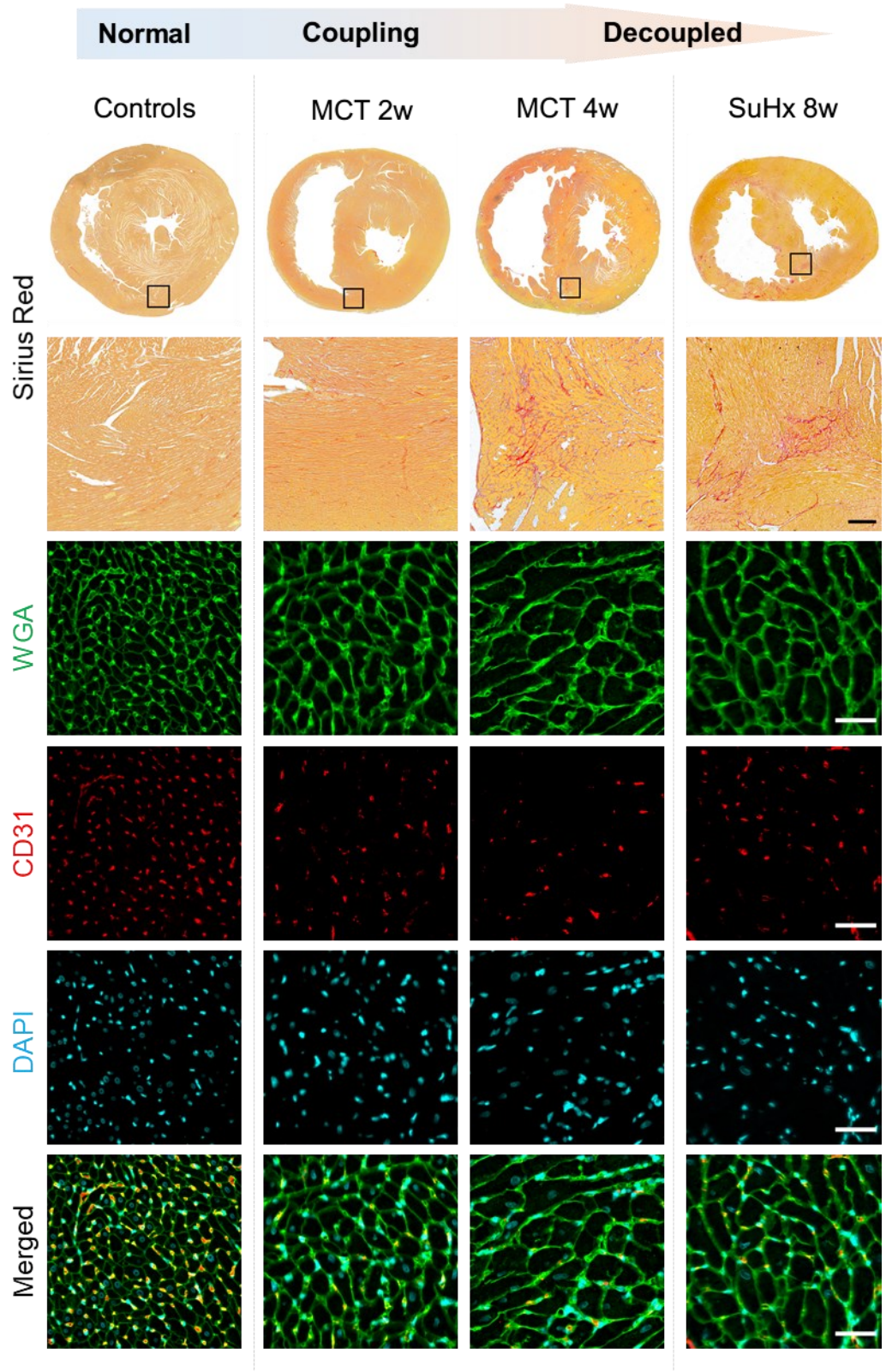

Figure 3-11 Pathological investigations of the IPs

Magnified histology micrographs show an example of the accumulation of ventricular fibrosis at the RV insertion points (Picrosirius red stained sections, scale bar 200 µm). Increased cardiomyocyte size was noted in 2- and 4-week

MCT, as well as 8-week SuHx rats (WGA-stained sections, scale bar 100 μm). Reduced capillary density was observed in 2- and 4-week MCT, as well as 8-week SuHx rats (CD31-stained sections, scale bar 100 μm).

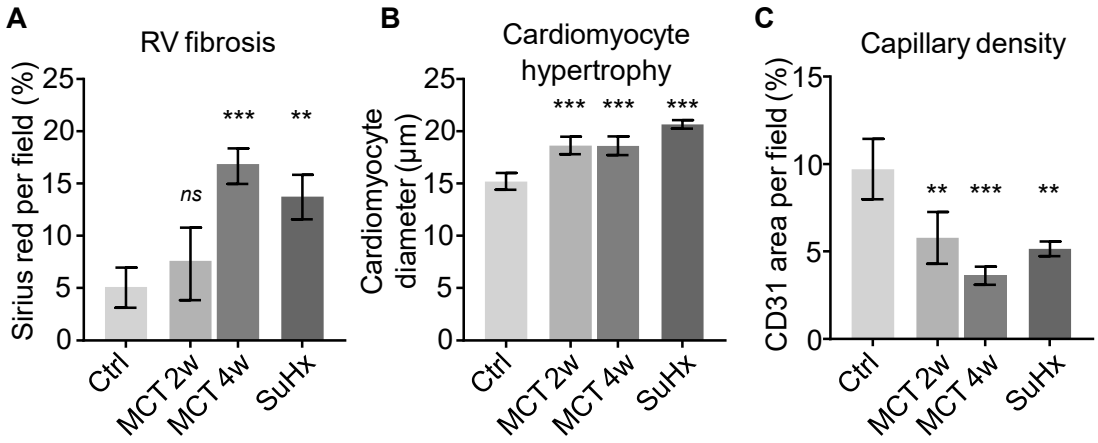

Figure 3-12 Quantification of the pathological observations of IPs in PH rats.

(A) RV fibrosis of the IPs quantified from the Sirius Red staining sections; (B) Cardiomyocyte hypertrophy of the IPs as calculated by measuring the cardiomyocyte diameter using the WGA immunofluorescence sections; (C) Quantification of the perfusion of the microcirculation with the CD31 immunostaining. Sample size: N = 4 for each group. Asterisks significant code (*) stands for the *p* values versus the healthy control (Ctrl) group.

2.6 Molecular signatures reflecting the RV failure

Western blots were performed to characterise the molecular crosstalk between the key signalling. AMPK is a critical metabolic regulator which facilitates energy production and utilization. AMPK also involves in cardiac hypertrophic pathology through its downstream molecule mTOR. SERCA2 is known to promote metabolic functioning through regulating mitochondrial calcium dynamics. The phosphorylation of AMPK (the ratio of phosphate AMPK over total AMPK) was down-regulated in both MCT and SuHx rats compared to healthy controls (*Figure 3-13*). This change was accompanied by enhanced phosphorylation of mTOR (the ratio of phosphate mTOR

over total mTOR). The expression of SERCA2 was significantly decreased in the MCT and SuHx rats, suggesting altered calcium dynamics in the RV pathogenesis.

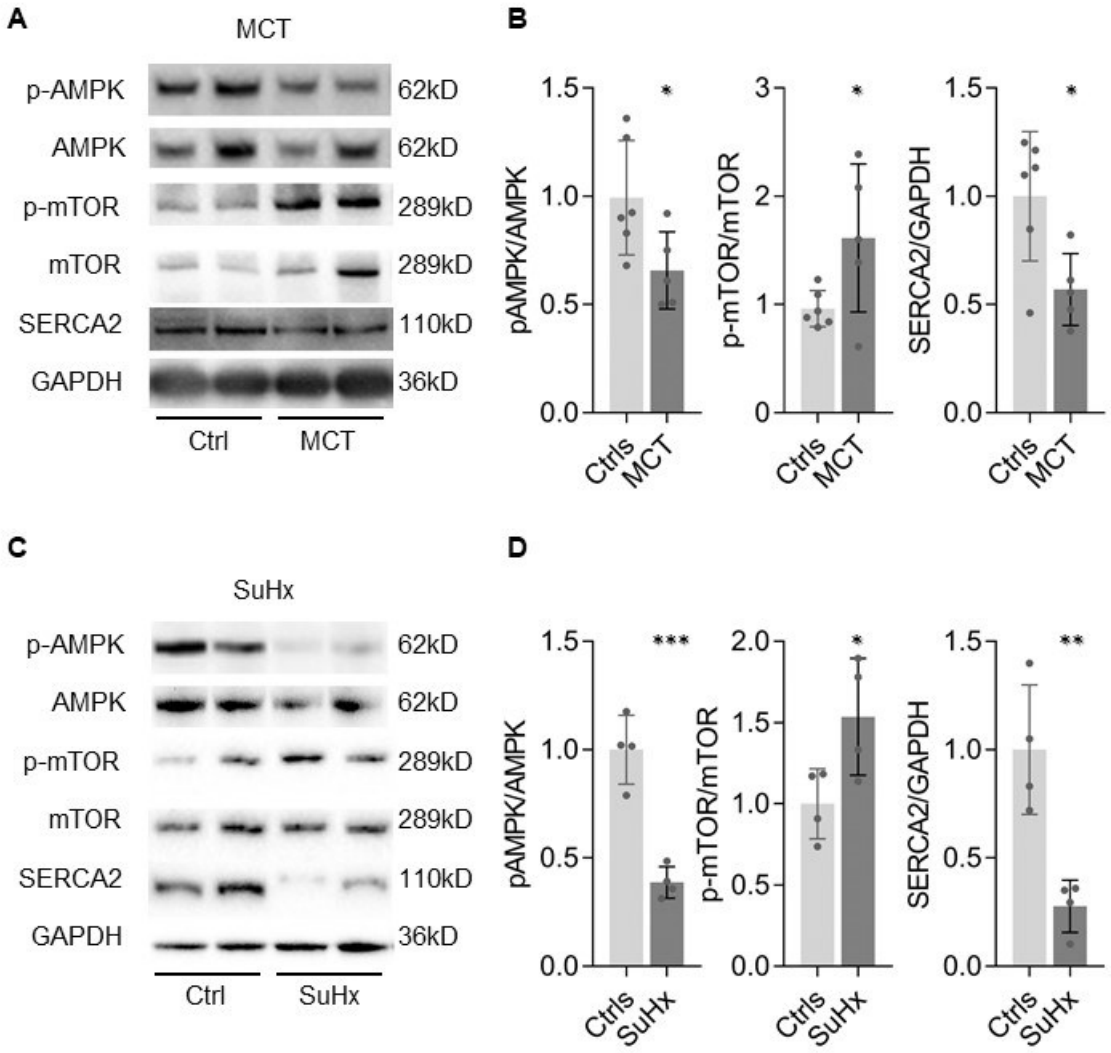

Figure 3-13 Expression of key molecules in cardiomyocyte metabolism and mitochondrial functioning.

Representative western blots of the RV tissue from (A) MCT and (C) SuHx rats and the quantification of the blots (C, D). Key molecules shown here are AMPKα and mTOR and their phosphates as indications of cellular metabolic status, and SERCA2 as an indication of calcium dynamics. Sample size: N = 4~5 for each group. Asterisks significant code (*) stands for the *p* values versus the healthy control (Ctrl) group.

3. Summary of the results in this chapter

In this chapter, I characterised the RV remodelling in aspects of structure, function, haemodynamic, and pathology, along the PH development course in the MCT and SuHx PH rat models. I explored and established the cardiac MRI as a key technique in full details in these rodent models.

- Haemodynamic measurements of the mPAP showed the well-established PH phenotype in MCT and SuHx models as previously described.
- RV structural and functional status were documented using cardiac MRI in both models longitudinally along the PH developing course. The cardiac MR parameters revealed that RV hypertrophy was the initiating change which progressed from the early phase to the decompensated stage. The hypertrophic change is more distinct in SuHx rats comparing to the MCT rats. In terms of RV function, at the early stage of MCT rats, the RV remained coupled to the pressure increase. RV decoupling was observed in 4-week MCT rats. In SuHx rats, RV decoupling presented after 4 weeks hypoxia exposure and persisted after returning in normoxia condition.
- PAAT shortening was observed in both MCT and SuHx rats, more distinctive in MCT rats at the early phase. The decline of PAAT correlated with the RV structure/functional parameters, suggesting the interplay between the RV and the progressive pulmonary vascular remodelling.
- Predominant increases of ECV, at the regions of the insertion points and the RV and the septum, were observed at the late stage in both MCT and SuHx rats. The ECV at the insertion points had a strong correlation with RV function and structure.
- Accompany the MRI observations, pathological assessment of the RV tissues revealed increased fibrosis and hypertrophy, as well as decreased capillary perfusion at the insertion points in the PH rats at the decompensated stage.
- AMPK signaling, the energy sensor/coordinator, was dysfunctional in the failing RV. The downregulation of SERCA2 supported the disruption of the calcium dynamic in the failing RV.

4. Discussion of the results in this chapter

RV function is the single most important prognostic determinant of survival in various forms of PH. Preclinical experimental studies employing animal models that mimic the overloaded RV in PH condition are essential for our understanding of the RV behaviour.[204]

PH models such as MCT and SuHx were established and well-adopted in PH studies. These two models serve as fundamental tools for preclinical pharmacological and therapeutic studies. Limited studies to date have described the dysfunctional RV in these two models.[184] Here I have established cardiac MRI as a non-invasive tool for assessing the RV function longitudinally along the PH development course in both MCT and SuHx PH rat models, defining the MR parameters for RV coupling. Detailed ECV mapping was performed, for the first time, in these models and revealed the fibrotic pattern of the heart in PH rodents. A 26-segment plot was created for visualization of the ECV data. The regional ECV values, especially at the insertion points, were closely correlated with RV volumetric changes. Validation of the ECV changes with the pathological examinations of fibrosis established the ECV indices for experimental PH models in the future.

4.1 Phenotypic description of the RV decoupling process

In both MCT and SuHx models, the RV hypertrophy occurs at the early stage and serves as a prelude of the subsequent RV dysfunction in both models. In MCT rats, RV dilatation was observed at 4-week timepoint. In parallel, the cardiac index dropped significantly at this timepoint. This is also the timepoint when the decoupling was observed, consistent with the previous description of RV hypertrophy, dilatation and dysfunction in MCT rats.[174] In the SuHx model, the injection of SU5416 with 4 weeks hypoxia exposure had significant impacts on the RV mass, volume and function, as well as RV uncoupling. These changes persisted after the returning to normoxia for 4 weeks. This *in vivo* MRI study provided some insight into the longitudinal progression of SuHx model, as there were controversial points regarding the cardiac dysregulation and possible reversal of the RV phenotype on re-normoxic condition in this model.[184,206] Compared to the MCT rats, the functional MR parameters of SuHx model suggest a much more severe cardiac deterioration in regard to hypertrophy, dilatation,

cardiac function and PA-RV coupling, in line with previous comments from a systemic review of Sztuka *et al*.[174]

4.2 Quantification of interaction between the PA haemodynamic and the RV

PAAT is highly correlated with the PVR in PH patients.[149] Preclinical studies have also linked the PAAT shortening with the increased PA pressure.[207] In our study, both MCT and SuHx rats showed a significant shortened PAAT, reflecting the increased PVR and PA pressure in these two PH models.[207] In MCT rats, the PAAT shortening happened in 2 weeks at the early phase and worsened by week 4, featuring the progressive course of pulmonary remodelling in MCT rats. In SuHx rats, the PAAT decreased significantly at week 4 (the end of hypoxia exposure), and remained after returning to normoxia, suggesting the irreversible pulmonary pathology in this model.[184] The pattern of the dicrotic notch in the arterial waveform is associated with PA pressure.[207] Deep dicrotic notches have been observed in the PA waveform of the PH rats, which is reflective of the dysfunctional PA haemodynamic. One limitation of our PA phase-contrast imaging is that the scanning plane of the cross-section of the PA may be difficult to be defined precisely in some cases, which causes the variation of the pattern of dicrotic notches and limits the qualifying analysis of the notches.

It was reported that PAAT shortening was associated with increased PVR and PA pressure in patients with PH.[149] In the presented study, a correlation has been found between the PAAT and the RV structural/functional parameters. Noticeably, a stronger correlation was detected in SuHx rats in comparison to MCT rats. The shortening of PAAT indicated RV dilatation and hypertrophy, as well as a decline of RV coupling and functioning, revealing the potential interplay between the PA haemodynamic and the RV behaviour in PH rats.

4.3 Longitudinal myocardium characterization

Using the T1 mapping and ECV assessment, regional interstitial abnormalities of the myocardium have been detected with high sensitivity in this study. This method enables us to associate the functional changes and the consequent tissue remodelling with the underlying pathology. My results presented the ECV of the entire heart in PH rats at different disease stage. Overall, a progressive increase in ECV was

demonstrated in both models. Specifically, increased ECV at the insertion points and the RV free wall were observed at the early stage of SuHx and MCT rats respectively. At the late stage, an overall increase of the ECV at the regions of insertion points, RV free wall, and the septum was recorded. This implied that the insertion points and the RV free wall are subjected to higher susceptibility of pathological damage. This ECV pattern is similar to the MRI findings at the insertion points in PH patients.[157] Interestingly, our results suggest that changes of the ECV at the regions of insertion points and RV wall may occur before the RV decoupling. The pattern of regional ECV changes provides useful information of the regions that are susceptible to increased RV load. Mechanical stress can lead to myocardium fibrosis or myocardial disarray.[208,209] The interventricular septum has been recognised to be more affected by mechanical stress caused by elevated RV pressure.[49,210] Regions with increased ECV at the early phase are under higher stress, in particular, the increase of the ECV at the insertion points reflects that these regions are under higher mechanical stress during the PH development in the MCT and SuHx rats.

The ECV increase at insertion points correlates well with the functional and structural remodelling of RV in PH rats. In PH patients, the presence of LGE at the RV insertion point of the interventricular septum is highly related with increased RV dilatation, decreased RV function and elevated mPAP.[209] The LGE in the insertion point has also been linked to the clinical worsening.[154,211] My data provided quantified coefficients of the ECV value and the RV status in PH condition. The results associated increased ECV with profound structural and functional degeneration. ECV mapping may be used for pharmacological assessment of drugs on RV function longitudinally in the preclinical setting.

4.4 Pathological inspection of the insertion points

The ECV increase at the insertion points features the pattern of ECV mapping in the failing RV. The pathological changes of these regions were of interest for a better interpretation of the pattern of ECV enhancement. The pathological assessments demonstrated a progressive increase of fibrosis, myocardium hypertrophy, as well as microcirculation ischemia at the insertion points in both MCT and SuHx rats. It has been suggested that the decompensated RV showed a higher degree of fibrotic

degeneration.[47] A recent review has highlighted the vital role of fibrosis in the process of RV decompensation.[51] Similarly, our data showed that fibrosis is a key component of the pathology in the decoupled RV. Distinct fibrosis was observed in the rodent PH at the late stage rather than at the early stage MCT rats, suggesting the distinctive increase of fibrosis may serve as a strong indicator of the transition from RV coupling to RV decompensation.

RV hypertrophy is the main source of the increase of RV contractility for adapting to the pressure increase. RV hypertrophy itself could not reflect the RV coupling status as it occurs both at the early and the late stage in overloaded RV. However, the cardiomyocyte hypertrophy increases the stiffness and promotes oxygen consumption, which eventually impairs the heart function and leads to decompensation.[46] Here, the observation of cardiomyocyte hypertrophy at the insertion points throughout the PH development course in MCT and SuHx rats affirms the findings with the cardiac MRI. At the early phase, adaptive RV hypertrophy is featured by concentric hypertrophy with minimal RV dilatation. The later on developed maladaptive RV hypertrophy is commonly accompanied by the occurrence of dilatation and cardiac fibrosis.[47] My results showed that RV dilation and fibrosis were dominating at the late stage, along with the excessive RV hypertrophy, indicating RV decompensation.

Several studies in PH animals have demonstrated that the capillary rarefaction in the RV myocardium could be an index of RV decoupling.[48] I found the impairment of the capillary density in both PH rats. The capillary rarefaction at the insertion points was much severer in 4-week MCT rats comparing to the 2-week MCT and SuHx rats. This finding implied a progressive feature of the capillary impairment in the transition of RV coupling states. In PH rats, reduced RV capillary density served as a key marker of the transition from RV adaptive remodelling to maladaptive remodelling.[212] A direct correlation was found between the RV ischemia and RV decompensating characters such as RV dilation and pressure increase.[213] The decrease of myocardial capillaries is a hallmark that comes together with the pathological cardiac hypertrophy.[214] Decreased myocardial capillary density reduces oxygen availability, which makes it more difficult to meet the increasing energy demand upon the hypertrophic condition, accelerating the decoupling process.[215] In this study, a decrease of capillary density

was observed at the early phase at the IPs in PH rats. A significantly decreased capillary density was noted at the late stage. The capillary rarefaction is recognized to drive the transit from coupling state to decoupling and RV failure.

4.5 The molecular basis of the RV decoupling

AMPK serves as an energy sensor/regulator coordinating cellular metabolism with specific energy demands. The deficiency of AMPK was well described in the failing heart.[216] AMPK activation benefits cardiac function and was intensively proposed as a therapeutic target.[217] My data showed that AMPK phosphorylation decreased in the RV, and this deactivation may account for the enhancement of mTOR. AMPK's downstream molecule mTOR plays a fundamental role in promoting protein synthesis which is essential for hypertrophic growth of cardiomyocytes.[218] It has been demonstrated that mTOR signalling was upregulated during cardiomyocyte hypertrophy.[218] The results supported the deactivation of the AMPK and its downstream mTOR in the RV decoupling pathophysiology.

SERCA2 has been extensively studied as this molecule plays versatile roles in several key signalling pathways that involved in modulating cardiomyocyte function, such as the calcium dynamic and mitochondrial function.[219] In my study, SERCA2 was upregulated in the RV myocardium. This result supports that SERCA2 may be involved in the adaptive process of the RV myocardium, and the function loss of SERCA2 may disrupt the adapting mechanism. Increasing SERCA2 is a potential treatment option for PA remodelling.[220] SERCA2 has been found to increase calcium concentration and thus increase cardiac contractility.[221] Toya *et al.* have reported that function loss of SERCA2 was a key component to LV impairment in patients with non-ischemic cardiomyopathy.[222] However, there is another study that reported increased SERCA2 in the RV of SuHx rats.[223] The variance might come from the difference of the experimental purpose and design, such as different timepoints and disease models. SERCA2 might be increasing at the early phase in order to compensate for the pressure increase through increasing the contractility. However, this regulatory process might be exhausted at the late stage where decompensation happens.

Chapter 4 Liraglutide Reverses PH and RV Failure in Experimental PH

1. Highlights

GLP-1 agonist liraglutide is an approved anti-diabetic medication. The cardioprotective effect of liraglutide has been demonstrated. Large clinical trials have shown liraglutide can significantly reduce the risk of cardiovascular events, including the development of heart failure, in patients with type 2 diabetes.[116] Moreover, patients with existing cardiovascular conditions can also benefit from liraglutide, as it reduces the risk of cardiovascular events such as heart failure.[118] There were inconsistent clinical data on liraglutide in improving the cardiac function of patients with heart failure.[125,127,128] However, preclinical investigations have extensively shown the capability of liraglutide on improving the cardiac function in the rodents with deteriorated heart function.[114,224] Previous research from our group has shown that liraglutide decreased the mPAP, and reduced the muscularization and inflammation of pulmonary vasculature, in MCT rats.[136] Similar to our laboratory findings, several studies also reported that liraglutide was able to attenuate the pulmonary arterial remodelling in PH animal models induced by MCT, hypoxia, or bleomycin.[132-135] The effect of liraglutide on the RV performance, which is the key determinant of PH patient survival, remains unexplored either in clinical or preclinical scenarios.

I presented the results of the pharmacological evaluation of the effect of liraglutide in rodent MCT and SuHx PH models in this chapter. This is a comprehensive evaluation of the cardiopulmonary status in terms of haemodynamic, structure, function and pathology. These results demonstrated that liraglutide restores the cardiopulmonary coupling, improves RV function, and attenuates the maladaptive pathological changes. This is the first study that investigated the effect of liraglutide on the RV in PH. The cardiopulmonary benefit of liraglutide offers promise to the treatment of the failing RV in PH.

2. Results

2.1 Expression of GLP-1 receptor in the lung and RV in PH models

GLP-1 agonists act as ligands of the GLP-1 receptor, and GLP-1 receptor (GLP1-R) has been localized to human heart including the RV.[101] Immunoblotting was performed to examine the expression of GLP1-R in the RV of both MCT and SuHx rats

(*Figure 4-1 A, C*). There was increased expression of GLP-1R in the RV homogenate of MCT rats, compared to the healthy controls (p = 0.045). A significant increase of GLP-1R expression was observed in the RV of SuHx rats compared to the healthy control rats. The results indicated that GLP-1R was upregulated in the overloaded RV in PH rats. (*Figure 4-1 B, D*).

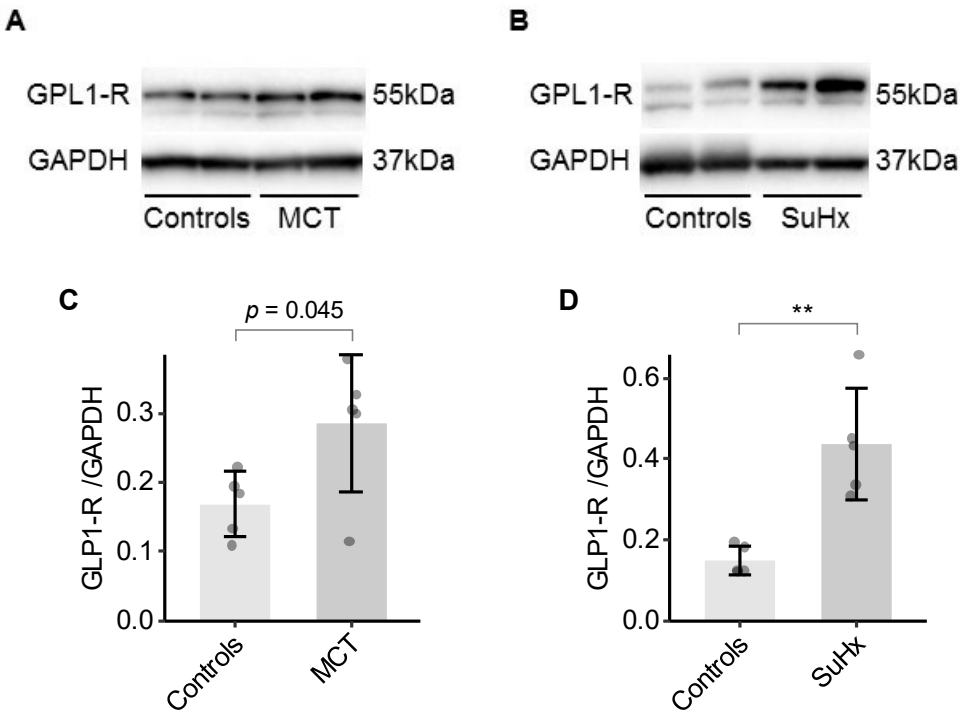

Figure 4-1 GLP-1R expression in the RV of the PH rats.

(A) Representative immunoblots of GLP-1R in the RV homogenate of the MCT rats; (B) Representative immunoblots of GLP-1R in the RV homogenate of the SuHx rats; (C) Quantification of the GLP-1R in the MCT rats; (D) Quantification of the GLP-1R in the SuHx rats. Sample size: N = 5 for each group.

2.2 Haemodynamic phenotyping of liraglutide in PH models

2.2.1 Liraglutide decreased PA pressure in MCT rats

To investigate the effect of liraglutide in PH models, the PH rats were injected with liraglutide intraperitoneal for a duration of 2 weeks at the dose of 0.4 mg/kg daily. In MCT rats, the injection started at the start of the second week until the end of the fourth week (experimental design detailed in *Section 3.3*). Haemodynamic parameters

of the RV and the PA were obtained through right heart catheterization. *Figure 4-2 A* presents a serial of representative pressure curves of the RV and the PA in the groups of healthy control rats, and MCT rats with and without liraglutide treatment respectively. In *Figure 4-2 A*, a remarkable decrease in the pressure of the RV and the PA can be observed in MCT rats with liraglutide treatment (MCT + Lira). Liraglutide decreased the mPAP significantly in MCT rats (*Figure 4-2 B*). RV hypertrophy (weight ratio of RV/LV +septum) was reduced by liraglutide in MCT rats as well (*Figure 4-2 D*). The systemic systolic blood pressure was not different among the three groups.

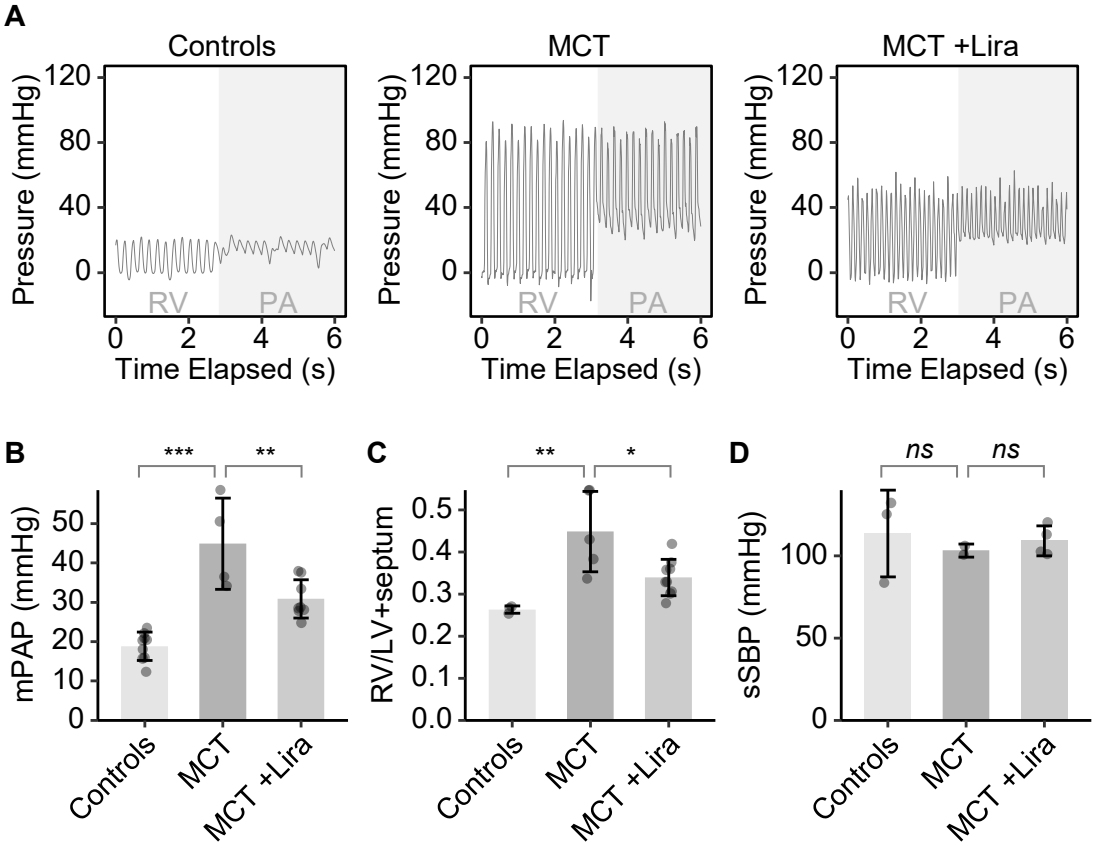

Figure 4-2 Haemodynamic phenotyping of liraglutide in MCT rats

(A) Representative pressure curves of the RV and PA in the healthy control rats, and MCT rats with and without liraglutide treatment; (B) Quantification of the mPAP in MCT rats; (C) Quantification of the Fulton index (weight ratio of RV over LV with septum) in MCT rats; (D) Quantification of the systemic systolic blood pressure in MCT rats. Sample size: N = 4 ~ 9 for each group.

2.2.2 Liraglutide decreased PA pressure in SuHx rats

Liraglutide (0.4 mg/kg i.p. Qd.) was given to SuHx rats at the start of the 6th week for 2 weeks (experimental design detailed in *Chapter 2 Section 3.3*). Representative pressure curves of the RV and the PA recorded from the right heart catheterization are presented in *Figure 4-3 A*. Liraglutide attenuated mPAP (*Figure 4-3 B*) and RV hypertrophy (*Figure 4-3 C*) in SuHx PH rats. The systemic systolic blood pressure stayed unaltered (*Figure 4-3 D*).

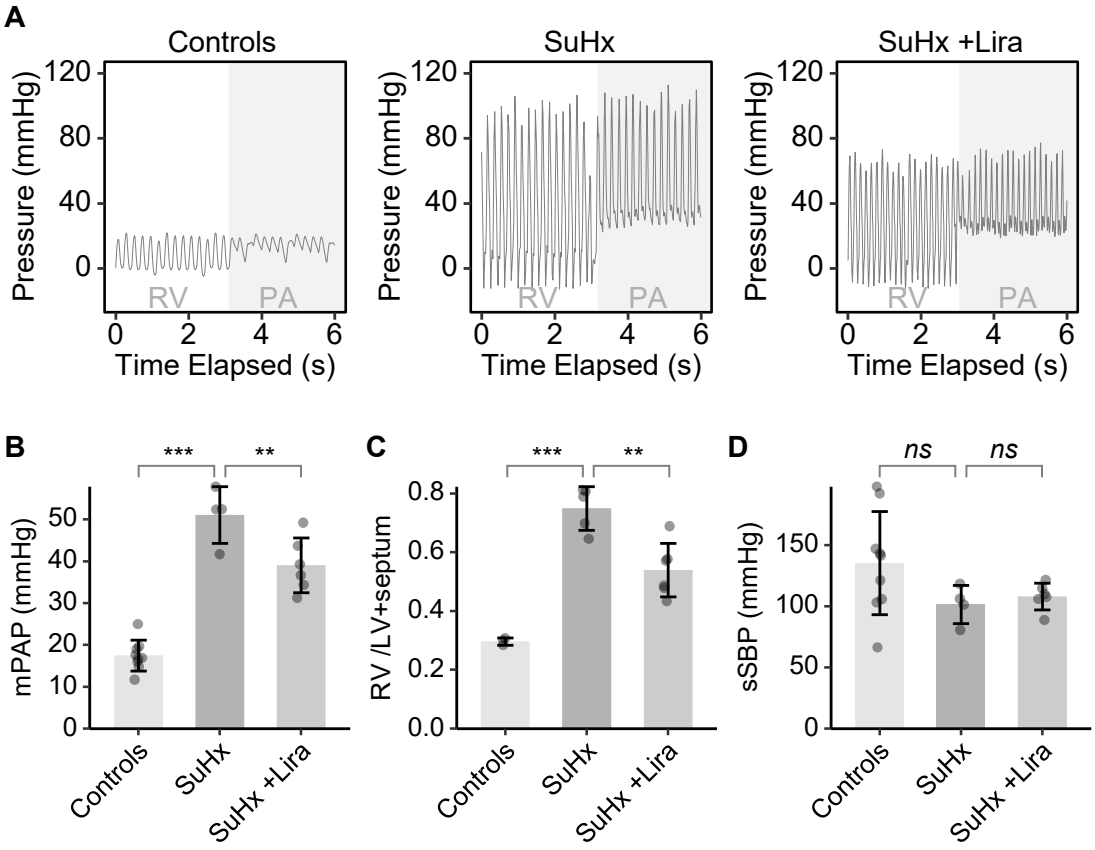

Figure 4-3 Haemodynamic phenotyping of liraglutide in SuHx rats

(A) Representative pressure curves of the RV and PA in the healthy control rats, and SuHx rats with and without liraglutide treatment; (B) Quantification of the mPAP in SuHx rats; (C) Quantification of the Fulton index (weight ration of RV over LV with septum) in SuHx rats; (D) Quantification of the systemic systolic blood pressure in SuHx rats. Sample size: N = 4~9 for each group.

2.3 Functional and structural evaluation of the cardiopulmonary unit in PH animals using cardiac MRI

2.3.1 Liraglutide did not change the heart rate on PH rats

Table 4-1 presented the comparison of the body weight and heart rate between the PH rats with placebo and liraglutide. The heart rate was not impacted by liraglutide treatment in PH rats. Liraglutide could decrease the body weight in SuHx rats.

Table 4-1 Impact of liraglutide on bodyweight and heart rate

Measurement	4-week MCT with placebo (n=12)	4-week MCT with Lira (n=12)	*p* value	8-week SuHx with placebo (n=5)	8-week SuHx with Lira (n=6)	*p* value
Weight (g)	298 ±46	305 ±27	0.67	385 ±29	328 ±33	0.01
HR (bpm)	334 ±38	308 ±29	0.07	335 ±13	326 ±35	0.57

* Variables in this table are presented as mean ±(SD). The *p* values are concluded from student *t* test.

2.3.2 Liraglutide reversed the RV structural remodelling in PH

Liraglutide treatment was able to reverse the RV structural remodelling in both the experimental PH models of MCT and SuHx. In MCT rats with liraglutide treatment, the parameters of the RV hypertrophy and dilatation, *e.g.* ventricular mass index (VMI, the ratio of the MRI-derived mass of RV over LV and septum, *Figure 4-4 A*), and the RV end-diastolic volume (RVEDV, *Figure 4-4 C*), were nearly restored to its baseline. Similarly, the remarkable attenuation of the RV hypertrophy (VMI) and dilatation (RVEDV) was also observed in SuHx rats with liraglutide treatment (*Figure 4-4 B,D*).

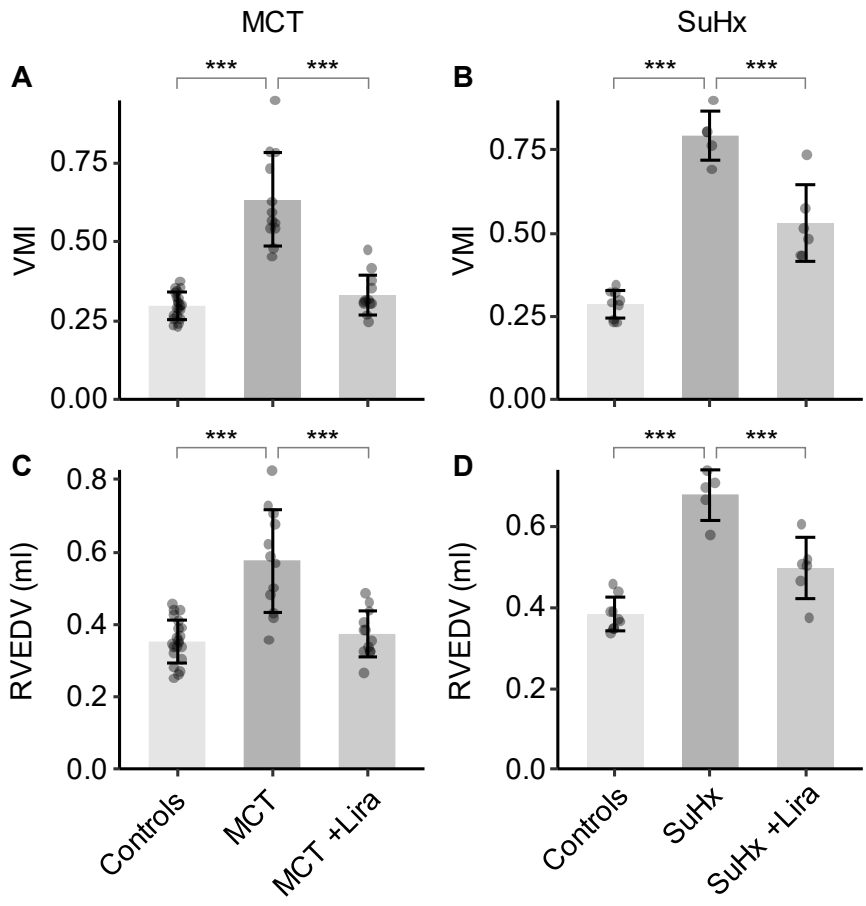

Figure 4-4 Cardiac MR parameters showing that liraglutide reduced the RV hypertrophy and dilation in PH rats

VMI (ventricular mass index) as an index of RV hypertrophy in (A) MCT rats and (B) SuHx rats with and without liraglutide treatment; RVEDV (RV end-diastolic volume) as an index of RV dilatation in (C) MCT rats and (D)SuHx rats with and without liraglutide treatment. Sample size: N = 12~21 for each group in MCT study; N = 5~9 for each group in SuHx study.

2.3.3 Liraglutide restored cardiopulmonary performance in PH

In terms of the functioning of the cardiopulmonary unit, cardiac MR measurements of estimated Ees/Ea and RV ejection fraction (RVEF) are presented here as the key indications of the cardiopulmonary performance. Liraglutide treatment improved the RV performance in both experimental PH models significantly. Both estimated Ees/Ea and RVEF had significant improvement by liraglutide administration in PH rats of MCT (*Figure 4-5 A,C*) and SuHx (*Figure 4-5 B,D*).

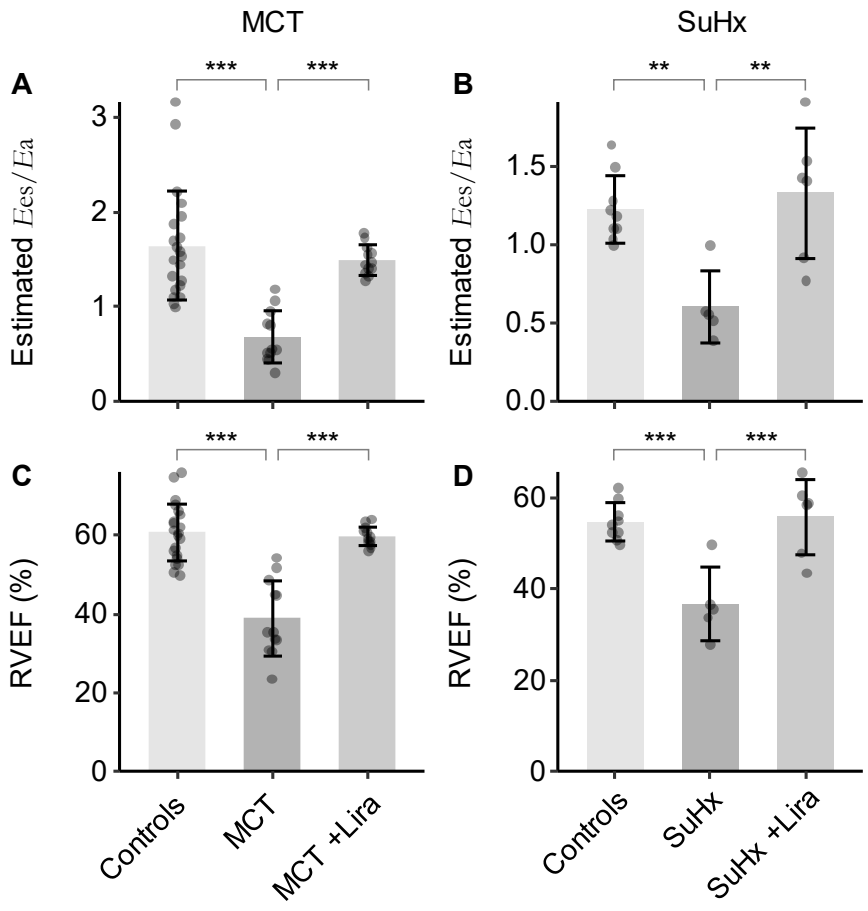

Figure 4-5 MR parameters showing that liraglutide improved RV function and attenuated structural degeneration in MCT and SuHx PH models.

Ees/Ea indicating the coupling state in (A) MCT, and (B) SuHx model. RVEF describing the RV systolic function in (C) MCT, and (D) SuHx model. The sample size of MCT experiment: 21 for the control group, 12 for the MCT group, and 12 for the group of MCT with liraglutide treatment. The sample size of SuHx experiment: 9 for the control group, 5 for SuHx group, and 6 for the group of SuHx with liraglutide treatment. Sample size: N = 12~21 for each group in MCT study; N = 5~9 for each group in SuHx study.

2.3.4 Reversal of the RV structural and functional degeneration by liraglutide treatment

SuHx rats (N number of 6) were scanned right before they received the liraglutide injection, and right after the 2-week liraglutide treatment. *Figure 4-6* presents the short axis cardiac MR images (at the papillary muscle level) showing the

reversal of the RV degeneration by liraglutide administration. Remarkable attenuation of the RV hypertrophy and dilatation could be observed in the post-treatment image stacks of the heart comparing to their pre-treatment counterparts. The septum was less flattened and the LV was less squeezed following the 2-week treatment as well.

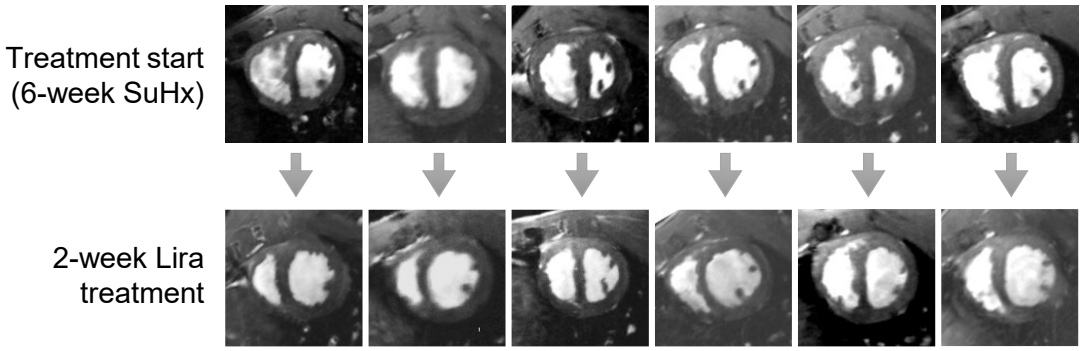

Figure 4-6 Short axis images of the heart of SuHx rats before and after the liraglutide treatment

The first row is the heart image before the start of liraglutide treatment. The second row is the corresponding heart image of the same rats after 2-week liraglutide treatment.

Quantification of the cine MR stacks was conducted and was plotted in *Figure 4-7*. The results supported that 2-week administration of liraglutide successfully attenuated/ partially reversed the established RV hypertrophy (*Figure 4-7 A*) and dilatation (*Figure 4-7 B*) in 6-week SuHx rats. The therapeutic efficacy was also remarkable in terms of RV performance. Liraglutide treatment significantly improved the cardiopulmonary coupling (estimated Ees/Ea, *Figure 4-7 C*) and improve RV function (RVEF, *Figure 4-7 D*).

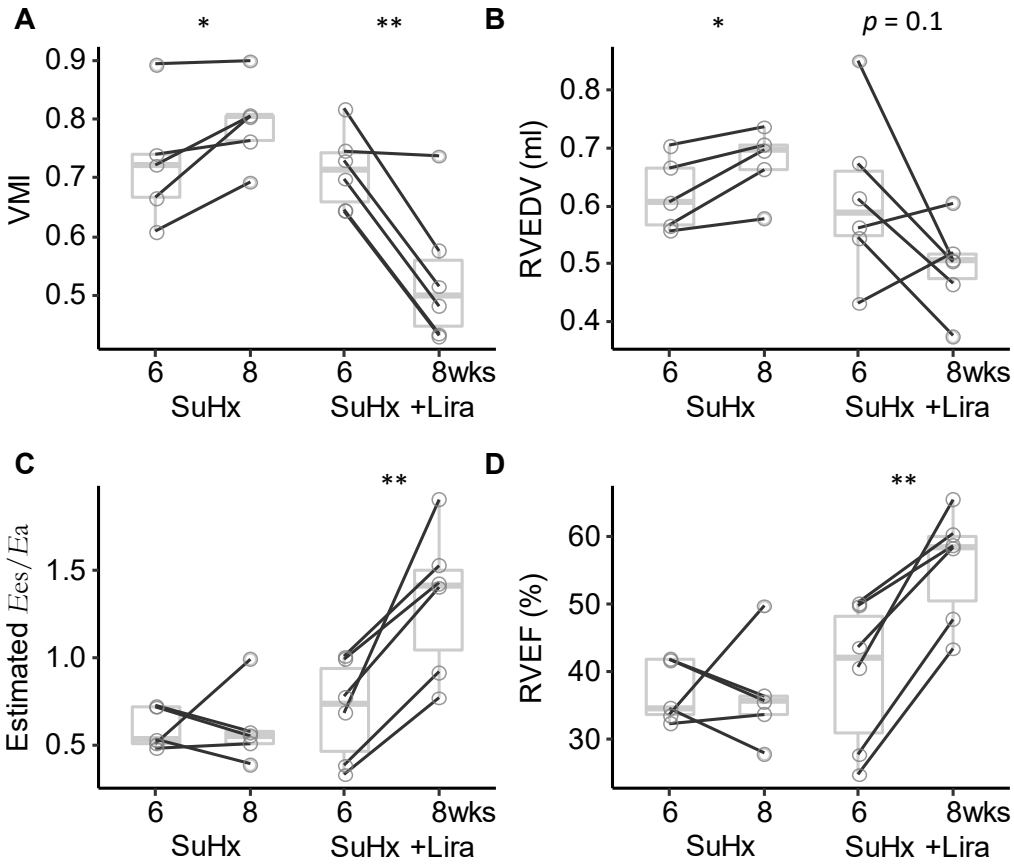

Figure 4-7 Comparison of the RV volumetric changes of the SuHx rats before and after liraglutide treatment

(A) VMI as a measurement of the RV hypertrophy; (B) RVEDV as an indicator of RV dilatation; (C) Estimated Ees/Ea to reflect the RV coupling state; (D) RVEF to evaluate the RV function. The significant code (*) indicates the statistical significance of paired t tests between 6wks and 8wks. Sample size: N = 5~6 for each pair.

2.4 Liraglutide decreased the RV glucose uptake in MCT rats

^{18}F-FDG PET imaging was performed by a senior researcher (Dr. Ali Ashek) in order to examine the changes in glucose metabolism in the RV in MCT rats with liraglutide treatment. The representative ^{18}F-FDG PET images and the quantification of the ^{18}F-FDG uptake were presented in *Figure 4-8*. Significantly increased RV ^{18}F-FDG accumulation was found at 2- and 4-weeks MCT rats. ^{18}FDG standardized uptake values were 2-fold and 3-fold increased at 2-, and 4-weeks respectively. MCT rats with

liraglutide treatment had significant lower ^{18}F-FDG standardized uptake values (*Figure 4-8 A*). Subsequent measurement of RV ^{18}F-FDG uptake by gamma counting (*Figure 4-8 B*) and kinetic analysis (*Figure 4-8 C*) confirmed that liraglutide reduced the enhancement of glucose uptake in the RV of MCT rats. These observations indicated that liraglutide reduced the glucose uptake in the overloaded RV and suppressed the metabolic shift in the RV of MCT rats.

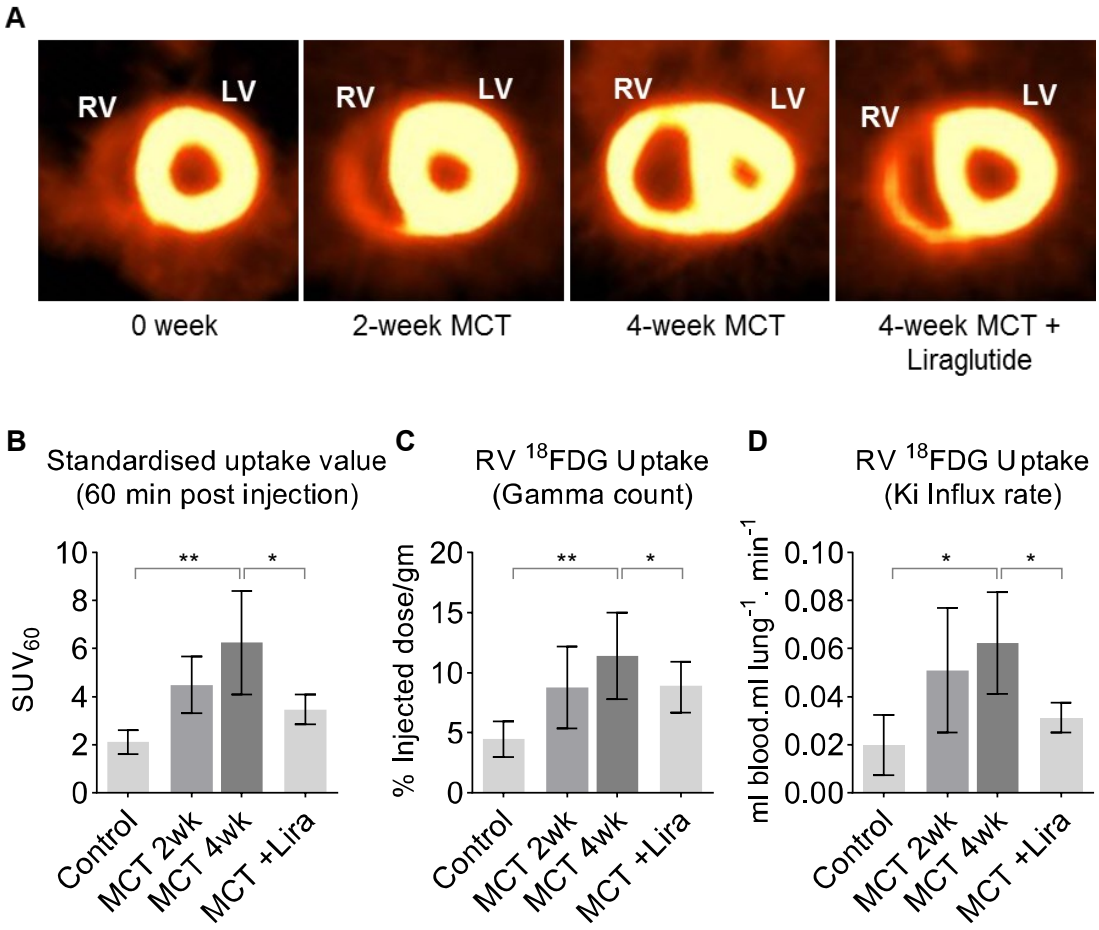

Figure 4-8 ^{18}F-FDG PET of the heart in MCT rats with liraglutide treatment

(A) Representative ^{18}F-FDG PET images of the heart of healthy control rats, 2- and 4-week MCT rats, and MCT rats with liraglutide treatment. (B) Standardised uptake value of ^{18}F-FDG. (C) RV ^{18}F-FDG uptake measured by Gamma count. (D) RV ^{18}F-FDG uptake measured through kinetic analysis. Sample size: N = 5~7 for each group.

2.5 The pathological improvement in PH with liraglutide treatment

2.5.1 Liraglutide prevented the fibrotic deterioration in the RV in PH

2.5.1.1 Visualization of the myocardium characterizing MR maps of the PH rats with liraglutide treatment

MR T1 mapping and LGE imaging were performed to reveal the pathological changes in PH rats with liraglutide treatment. *Figure 4-9 A* and *B* shows the representative images of cine MR, LGE and ECV maps in PH rats with and without liraglutide treatment. Accumulation of LGE and increase of ECV, as the reflection of fibrotic changes, were observed in the RV insertion points, as well as the RV and septum in PH rats (in both MCT and SuHx groups). Liraglutide restored the LGE and ECV maps in PH rats, which suggested that liraglutide could attenuate the fibrotic changes in the heart of the PH rats. *Figure 4-9 C* and *D* visualized the segmental ECV changes. From the segmental model of ECV visualization, a remarkable attenuation of the fibrosis in the segments around the insertion, septum and RV free wall can be observed.

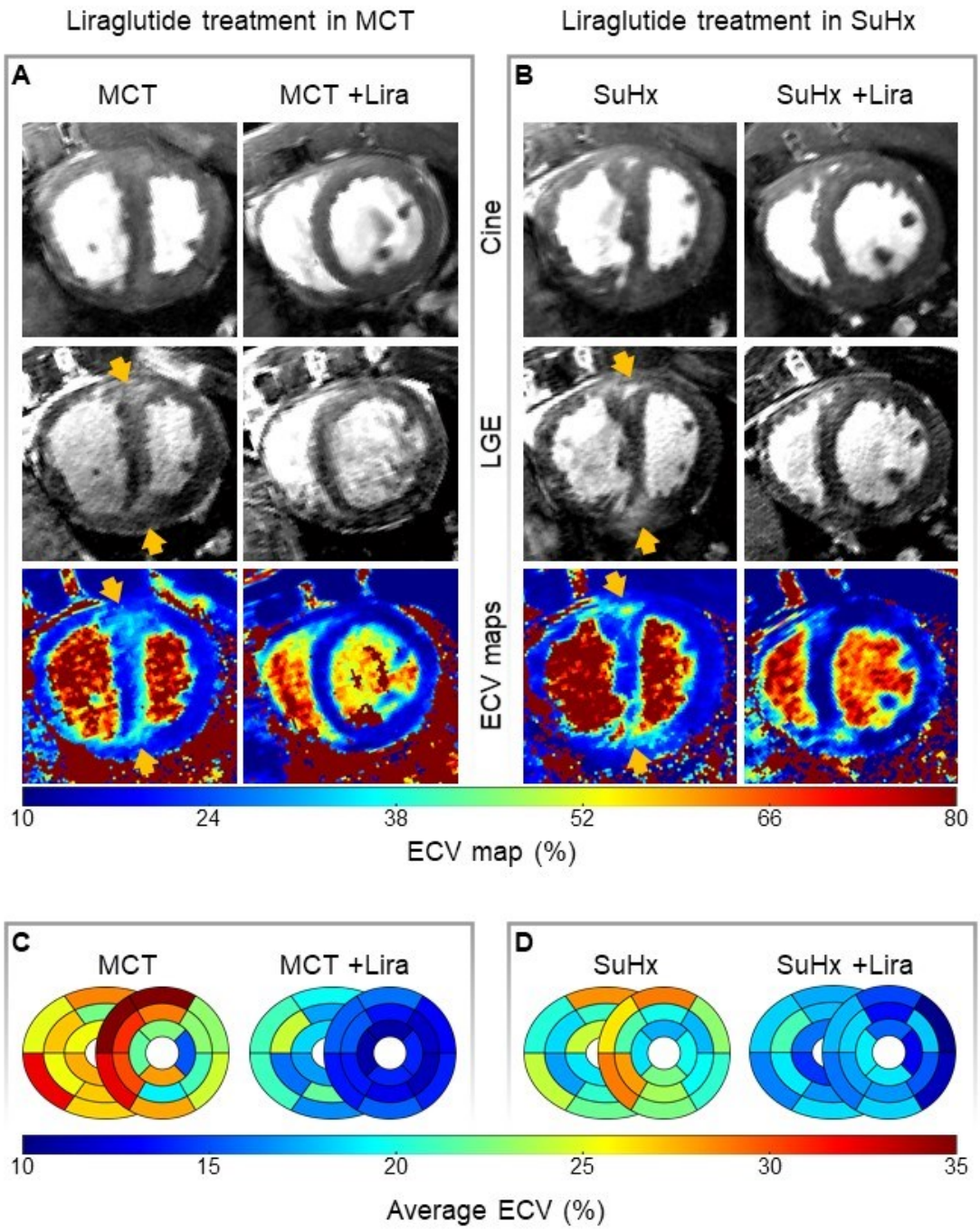

Figure 4-9 Liraglutide decrease LGE and ECV in experimental PH

Representative images of cine MR, LGE and ECV maps of (A) MCT rats and (B) SuHx rats with and without liraglutide treatment; Visualization of the segmental average ECV values of (C) MCT rats and (D) SuHx rats with and without liraglutide treatment using the 26-segment polar plot. Sample size: N = 8~10 for each group in MCT study; N = 5 for each group in SuHx study.

2.5.1.2 Comparison of the ECV values between PH rats with and without liraglutide treatment

Quantification of the regional ECV provided evidence that liraglutide attenuated the fibrosis significantly at the IPs and the septum in both PH models (*Figure 4-10*). In MCT rats, the fibrosis in the RV free wall was decreased by liraglutide as well. In SuHx rats, the increase of ECV at the RV free wall is moderate, and the ECV-reducing effect of liraglutide did not reach significance.

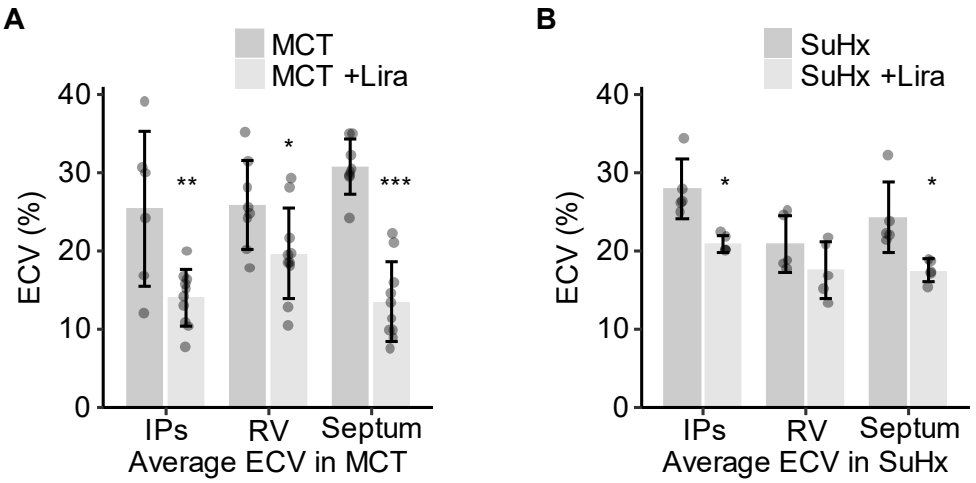

Figure 4-10 Liraglutide attenuated the fibrotic process in the heart of PH rats

This figure compares the average ECV values at the insertion points (IPs), RV free wall, and septum in the heart of (A) MCT, and (B) SuHx rats. Sample size: N = 8~10 for each group in MCT study; N = 5 for each group in SuHx study.

2.5.2 The effect of liraglutide on hypertrophy and capillary density at the insertion point in the heart of PH rats

As ECV mapping showed liraglutide decreased the excessive fibrosis at the IPs of PH rats, pathological experiments were performed to confirm the related cardiomyocyte hypertrophy and capillary density change. In MCT rats, fluorescence staining of cardiomyocyte membrane (WGA) and the capillary endothelial cells (CD31) was conducted. The representative image of the groups is presented in *Figure 4-11 A*. The quantification bar plot (*Figure 4-11 B, C*) showed that there was decreased cardiomyocyte diameter, as well as increased CD31 fluorescence, at the IPs in MCT rats with liraglutide treatment, comparing to those without liraglutide treatment. This

result supported that liraglutide decreased the cardiomyocyte hypertrophy and improved the microcirculation perfusion at the IPs in PH rats.

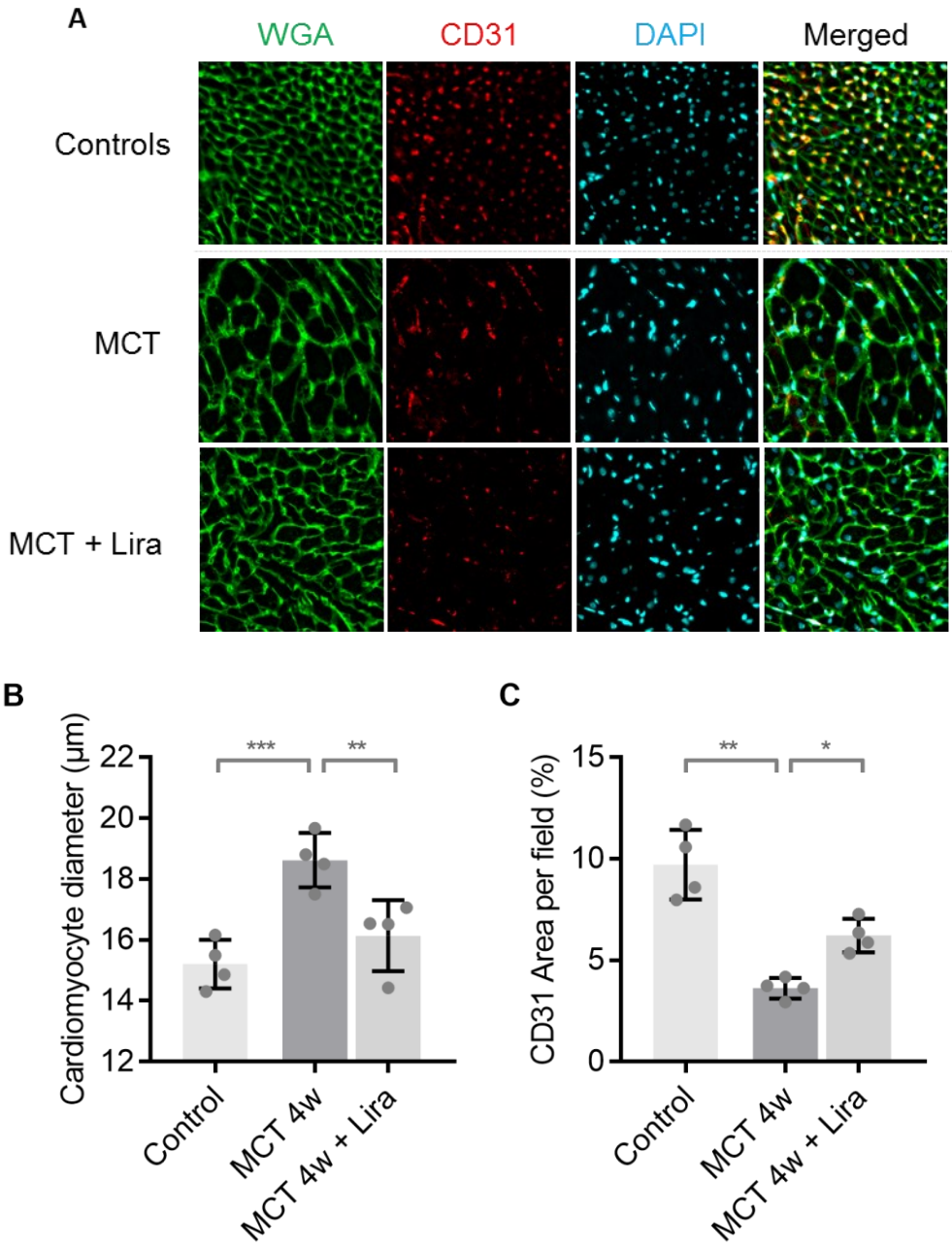

Figure 4-11 Liraglutide attenuated the pathological degeneration at the IPs of the heart in PH rats

(A) Representative fluorescence images of WGA and CD31 at the IPs of the heart in MCT rats; (B) Quantification of the cardiomyocyte diameter (from WGA fluorescence) at the IPs; (C) Quantification of the capillary density (from CD31 quantification) at the IPs. Sample size: N = 4 for each group.

2.6 Liraglutide improved RV performance and ameliorated the structural changes of the RV in PAB mice

The RV-protective effect of liraglutide was validated in PAB mice in collaboration with the PH group at the University of Giessen (Germany). The PAB mice model of RV dysfunction was introduced to distinguish the impact of liraglutide on the RV function independent from the pulmonary vasculature, *i.e.* the RV-specific effect. Liraglutide (3.2 mg/kg *i.p.* Qd.) or placebo were given to the PAB mice (7 days after the surgery, details in *Section 3.3.4* of *Chapter 2*). To assess the RV performance at the endpoint (21 days), the mice were subject to echocardiography and then RV catheterization for RV phenotyping. Group abbreviations in the figures: *Sham*: sham-operated mice; *PAB +placebo*: PAB mice with an equal volume of saline injection as placebo; *PAB +Lira*: PAB mice with liraglutide.

2.6.1 Liraglutide reduced the RV pressure and hypertrophy

Liraglutide treatment reduced the increased RV systolic pressure (RVSP) in PAB mice (52.51 ± 5.47 mmHg in PAB + Lira *vs.* 57.98 ± 7.57 mmHg in PAB, $p = 0.062$, *Figure 4-12 A*). Importantly, the Fulton Index (weight ratio of RV over LV plus septum) showed a significant decrease in PAB mice with liraglutide treatment (*Figure 4-12 B*). Liraglutide had no impact on systolic system blood pressure (SBP) (*Figure 4-12 C*). These results suggested that liraglutide has a direct effect in preventing RV hypertrophy.

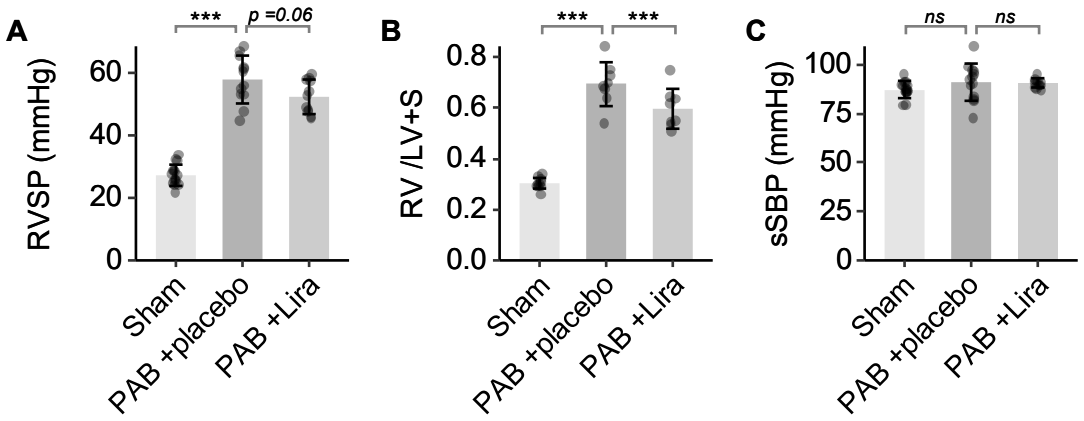

Figure 4-12 Liraglutide reduced the RV pressure load

(A) RVSP measured through percutaneous puncture; (B) Fulton index (RV/LV +septum) record from RV dissection; (C) Direct measurement of the systolic systemic blood pressure (sSBP). Sample size: Sham: N = 15; PAB +placebo: N = 13; PAB +Lira: N = 11.

2.6.2 Liraglutide attenuated functional and the structural degradation in PAB mice

PAB mice showed reduced RV systolic function, as indicated by the echocardiography parameters including tricuspid annular plane systolic excursion (TAPSE) and pulsed tissue Doppler-derived RV annular systolic excursion velocity (S'RV). These parameters were improved in PAB mice with liraglutide treatment, indicating the beneficial effects of liraglutide treatment on the RV function in PAB mice (*Figure 4-13 A, B*). Liraglutide reduced the excessive dilation of the RV in PAB mice (*Figure 4-13 C*). Liraglutide had no significant impact on the RV wall thickness in PAB mice (*Figure 4-13 D*).

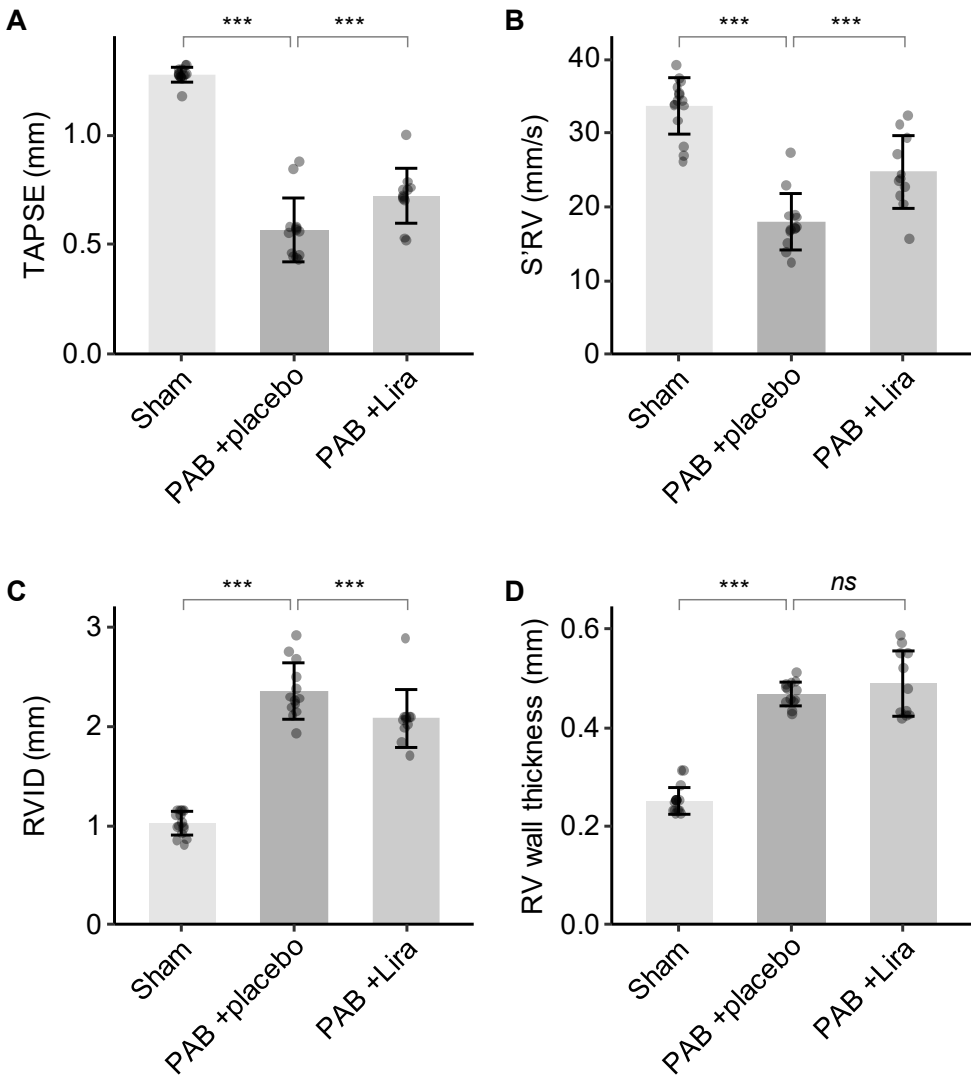

Figure 4-13 RV functional and structural changes in PAB mice with liraglutide

(A) TAPSE, (B) S'RV, (C) RV internal diameter (RVID) and (D) RV wall thickness (RVWT) measured using echocardiography. Sample size: Sham: N = 15; PAB +placebo: N = 13; PAB +Lira: N = 11.

3. Summary of the results in this chapter

I presented the results of liraglutide on RV remodelling in MCT and SuHx rat PH models, as well as in PAB mice, a model of RV pressure loading without PAH. RV haemodynamics, function, structure and pathology were investigated, providing evidence supporting an overall beneficial effect of liraglutide on rescuing the failing RV. Key results were listed as following.

- Increased GLP-1 receptor expression was found in the remodelled RV of MCT and SuHx rats.
- Liraglutide treatment reduced increased PAP in MCT and SuHx rats.
- Liraglutide reduced RV hypertrophy and dilatation (VMI and RVEDV), and improved RV performance (RVEF and Ees/Ea) in MCT and SuHx rats.
- MRI ECV indices indicated that liraglutide treatment decreased fibrosis in IPs and IVS region in MCT and SuHx rats.
- Pathological examination showed the effects of liraglutide in attenuating the cardiomyocyte hypertrophy, and capillary rarefaction in MCT rats.
- Liraglutide decreased the RV pressure, reduced the RV hypertrophy, and improved the RV function in PAB mice.

4. Discussion of the results in this chapter

This is the first report investigating the effect of a GLP-1 agonist on the RV remodelling in PH. Increased expression of GLP-1 receptor was demonstrated in the RV in SuHx rats. Further to the effects of liraglutide in reducing the increased pulmonary arterial pressure induced by MCT and SuHx, I demonstrated that liraglutide treatment attenuated the RV structural and functional remodelling using cardiac MRI indexes as key indicators. Moreover, liraglutide reduced cardiac fibrosis and cardiomyocyte hypertrophy, as well as the increased capillary density at the insertion regions in MCT and SuHx rats. My data provided strong evidence to support the main hypothesis of this project that metabolic modulator liraglutide resolves RV remodelling and improves RV function in PH.

4.1 Liraglutide improved RV haemodynamic in PH condition

Abundant expression of GLP-1 receptor has been identified in human RV.[101] I found increased expression of GLP-1 in the decompensated RV of SuHx rats, which implies that the receptor may be involved in the RV pathophysiology in response to RV overload. Activation of GLP-1R by GLP-1 infusion improves cardiac performance.[111,112] Therefore, the upregulation of the GLP-1 receptor in overloaded RV could serve as adaptive feedback attempting to strengthen the RV function.

Several studies claimed that liraglutide was able to attenuate pulmonary vascular remodelling in rodent PH induced by MCT, hypoxia, or bleomycin.[132-134] Liraglutide alleviated the arterial muscularization and the perivascular inflammatory infiltration in PH rats.[132] It also reduced RV fibrosis and cardiomyocyte hypertrophy in PH condition.[132] Moreover, studies have consistently demonstrated that liraglutide decreased the load of the RV in these rodent PH models.[132-134] Here in my study, decreased pressure in the PA and RV were observed in the PH rodents treated with liraglutide.

The Fulton index (weight ratio of RV over LV plus septum) showed a decrease in PH rats with liraglutide treatment. This was suggestive of the anti-hypertrophic effect of liraglutide on overloaded RV, which was co-validated by the *in vivo* cardiac MR. The systemic blood pressure stayed unaltered among groups, which indicated that the

pressure-reducing effect of liraglutide was not achieved through lowing the systemic pressure or the cardiac function.

Overall, the haemodynamic results provided evidence that liraglutide reliefs the dysfunction of the overloaded RV in PH condition. The observations are in keeping with the conclusions of other publications.

4.2 Liraglutide attenuated RV hypertrophy and dilatation in PH

RV structure change is closely linked to both RV functional statue and patient prognosis.[138,143] Here in my study, the profound RV hypertrophy (VMI) and dilatation (RVEDV, RVID) in PH rats were relieved by liraglutide administration. In line with the imaging measurements, the pathological inspection showed a decrease of the cardiomyocyte diameter in PH rats with liraglutide treatment (will be discussed in *section 4.5*). This anti-hypertrophic effect of liraglutide on RV is similar to its effect on the LV as reported in other published studies.[224,225] It has shown that liraglutide reduced cardiac hypertrophy and dilation in rat exposed to angiotensin II infusion or thoracic aorta coarctation.[224] More relevantly, there was a study reported that liraglutide restored the imbalanced renin-angiotensin system in rats with type 1 diabetes and thus decrease the RV weight.[225] Therefore, liraglutide is able to inhibit the excessive hypertrophic mechanism in the heart.

RV dilatation is a sign of the RV decoupling and it is linked to patient survival.[32] Liraglutide effectively attenuated the RV dilatation in PH rats, as well as in PAB mice. The attenuation of RV dilatation may be attributed to the decrease of PVR and/or the enhancement of RV adaptive mechanisms. There were published data claiming the vaso-protective properties of liraglutide over the pulmonary vasculature, leading to a potential reduction of the RV filling from liraglutide treatment. [105,124,125] This could be a factor contributing to the attenuation of RV dilatation. Nonetheless, it is noteworthy that a significant improvement of RV performance was recorded in PH rats with liraglutide treatment. The RV structure change is closely linked to the RV coupling status, and attenuation of RV dilatation could be reflective of the improved RV performance.

4.3 Liraglutide restored the cardiopulmonary function in PH

One of the main findings in this study was that liraglutide improved the RV performance in PH rodents. The RV function and the coupling status of the cardiopulmonary unit were evaluated in multiple rodent models using precise imaging technologies such as MRI and echocardiography. Significant improvement of the RV function (RVEF) and the cardiopulmonary coupling (Ees/Ea) was observed in liraglutide-treated PH rats. Further, this therapeutic effect of liraglutide on RV function (TAPSE, S'RV) has been demonstrated in PAB mice, supporting the direct therapeutic effect of liraglutide on the RV. The result is indicative that the treatment effect of liraglutide on the RV was independent from its effect on the pulmonary vasculature.

Existing publications have extensively demonstrated the effect of GLP-1 on the failing heart. For example, in a rat model of the chronic heart failure induced by coronary binding, subcutaneously administration of GLP-1 or its agonists significantly improved cardiac performance, as demonstrated by improved left ventricular (LV) ejection fraction and reduced LV diastolic and systolic volumes.[112] The GLP-1 agonist liraglutide has also been reported to improve the cardiac function in rodents with heart failure.[114] This PhD study is the first one that validated the cardiac protective effect of liraglutide on the right side of the heart. Published studies demonstrated the therapeutic role of liraglutide on pulmonary vasculature.[132-134] In line with these studies, our results indicated that liraglutide improved the cardiopulmonary coupling in PH rats. Our previous study has also shown that liraglutide attenuated the pulmonary vascular remodelling and restored the metabolic profile of the lung in PH rats.[136] Taken together the results here focusing on the RV, it is sufficient to conclude that liraglutide exerts overall benefit over the cardiopulmonary unit in PH condition. The improvement of cardiopulmonary performance is associated with a reduction of cardiac fibrotic degeneration, as well as improved perfusion of cardiac microcirculation, as will be discussed as follows.

4.4 Liraglutide restored the metabolic efficiency of the dysfunctional RV

In the healthy heart, the predominant source of energy supply is made up by fatty acid oxidation (FAO, 60% to 90%) rather than glucose metabolism (10% to 40%).[226,227] In a diseased state such as RV overload, increased glucose uptake can be

observed in the RV myocardium, which is suggestive of the metabolic disorder in the cardiac pathogenesis.[228,229] Metabolic disorder of RV cardiomyocytes involves different mechanisms such as uncoupled glycolysis, dysregulated fatty acid oxidation, and impaired mitochondrial function.[226,227,230,231] Increased ^{18}F-FDG uptake in the RV of MCT was observed in our study, which suggests dysfunctional glucose metabolism in the RV in MCT rats. The increase of glucose uptake may be an adaptive mechanism, through which the RV cardiomyocyte remains coupling with the increased energy demand.[226,232] This mechanism is ending up with increased anaerobic glycolysis instead of glucose oxidative phosphorylation, due to the impairment of mitochondrial function.[233] In PAH patients, increased RV ^{18}F-FDG uptake is indicative of the decrease of RVEF and the increase of pulmonary vascular resistance.[228] ^{18}F-FDG uptake Increase in the RV of PAH patients was predictable of the poor clinical outcomes (exercise capacity, cardiac function and survival).[229,234] In my PhD study, the increased glucose uptake coincided with the functional degeneration of the RV in MCT rats. The dysfunctional glucose metabolism in the overloaded RV was reversed by liraglutide treatment, indicating that liraglutide could enhance the efficiency of glucose utilization and restore the metabolic status in RV cardiomyocytes.

4.5 Liraglutide alleviated the pathological deterioration of the decoupling RV

Increased cardiac fibrosis, as accurately quantified from the MR ECV mapping, was found in the decompensated RV of PH rats, specifically at both the RV wall and the interventricular parts. The remarkable fibrotic change in PH rats was attenuated by liraglutide. Pathological inspection of cardiomyocyte size and capillary density showed profound RV hypertrophy and microcirculation rarefaction at the heart IPs in PH rats, which could also be significantly alleviated by liraglutide administration.

RV fibrosis facilitates RV decoupling through increasing cardiac stiffness or causing electromechanical dyssynchrony.[50] Presence of RV fibrosis has been closely linked to RV function deterioration.[49] Cardiac fibrosis is a consequent of the accumulation of extracellular content (*e.g.* collagens) in the myocardial interstitium.[50] There were cell experiments demonstrated that liraglutide inhibited the proliferation, invasion, and migration in the cardiac fibroblasts exposed to high glucose

concentration.[235] Animal experiments have also proved the anti-fibrotic feature of GLP-1 agonists. For example, liraglutide attenuated the renal fibrosis in mice with unilateral ureteral obstruction.[109] Very few *in vivo* studies have investigated GLP-1 and its agonist regarding their effect on the cardiac fibrosis of the overloaded RV. There was a study showed that liraglutide attenuated the fibrosis in the RV in PH rats induced by MCT.[132] Overwhelmingly, the knowledge of the cardiac effect of GLP-1 and its agonists came from studies of the LV. In rats with diabetic cardiomyopathy, liraglutide treatment decreased cardiac fibrosis and improved heart function.[236] Liraglutide significantly reduced the deposition of collagen content in the heart of mice with heart failure caused by myocardial infarction, and thus improved cardiac function.[237] In this PhD project, the fibrotic change of the entire heart was inspected using *in vivo* MR ECV mapping. Liraglutide suppressed the enhancement of ECV in the heart of the PH rats, especially at the interventricular parts (where mechanism stress accumulated). Similar to the existing publications, this is suggestive of an anti-fibrotic effect of liraglutide on the decoupling heart in PH condition. Although it has not yet been fully understood, the pathogenetic mechanisms of cardiac fibrosis vary among different aetiologies. Pressure overload could be a trigger of the fibrotic genesis. This could partially explain the accumulation of the fibrosis at the interventricular part because this region is where the mechanic stress accumulated. Myofibroblasts are the key modulator of cardiac fibrosis; however, multiple cell types, including inflammatory cells, cardiomyocytes, and vascular endothelial cells, may also be involved in the fibrotic change.[50] GLP-1 receptors are widely distributed in multiple cell types,[101,238] which makes GLP-1 and its agonists potentially act on various cells. Therefore the cardioprotective effect of liraglutide could result from a combination of pleiotropic effects on different cell types.[239]

The anti-hypertrophic effect of liraglutide on cardiomyocytes was extensively reported. Cell studies showed that the GLP-1 agonist Exendin-4 attenuated the phenylephrine-induced hypertrophy in primary neonatal rat cardiomyocyte.[240] A recently published study demonstrated that liraglutide attenuated the cardiomyocyte hypertrophy in neonatal rat cardiomyocytes and human cardiomyocyte cell line (AC16).[115] This study also presented *in vitro* evidence that liraglutide decreased the cardiomyocyte size in the mice subjected to thoracic aorta coarctation and

angiotensin II perfusion. This anti-hypertrophic effect of liraglutide was attributed to the inhibition of the PI3K/Akt1 pathway and the activation of AMPK.[115] The anti-hypertrophic effect of liraglutide could also result from inhibiting the angiotensin II type 1 receptor.[114] More relevantly, regarding the RV cardiomyocytes, there was a publication reported that liraglutide decreased the RV cardiomyocyte hypertrophy (quantified as RV cardiomyocytes cross-section area) in MCT rats.[132] The data presented here in this PhD project showed that liraglutide attenuated the cardiomyocyte hypertrophy at the RV insertion points in the heart of PH rats. This result is in keeping with the conclusions of the existing publications which investigated the anti-hypertrophic effect on the left side of the heart.

RV ischemia was found in the RV of PH and it contributes to the process of RV decompensation.[213] GLP-1 could improve cardiac microcirculation perfusion as GLP-1 serves a potent vasodilator of coronary arteries.[241,242] GLP-1 agonist liraglutide has also shown significant vasodilating capability in a rat model of metabolic syndrome.[243] As have discussed in previous sections, RV rarefaction serves a marker of the decompensated RV. Ameliorating the RV rarefaction in PH condition could halt the transition from RV coupling to decoupling. However, there is yet no study investigated whether liraglutide could increase the capillary density and ameliorate the RV rarefaction in the overloaded RV. In this regard, using immunofluorescence to mark the microvessels, we were able to demonstrate that liraglutide significantly increased the capillary density in the RV at the insertion points in PH rats. Of significance, it can be therefore concluded that liraglutide could significantly improve the microcirculation perfusion through not only vasodilating but also restoring the capillary density, preventing the RV from ischemia and the consequent functional deterioration.

4.6 Liraglutide improves the RV directly

In MCT and SuHx rats, the increase of the RV load may be secondary to the changes of the pulmonary vasculature. The afterload of the RV in both MCT and SuHx rats is not fixed. For this reason, the MCT and SuHx models are less informative to distinguish whether the functional change of RV is directly attributed to an intervention or it is an indirect consequence of the pulmonary vascular changes.[187,188]

In PAB mice, the afterload of the RV is fixed, which makes the RV dysfunction independent from the changes of the pulmonary vasculature. Using this model, we presented trustable results that showed liraglutide directly reduced the myocardium hypertrophy (RVID) and improved the cardiac function (TAPSE, S'RV) in the overloaded RV. The study of liraglutide in PAB mice offered evidence supporting that the RV-beneficial effect of liraglutide is not fully associated with its therapeutic effect on the pulmonary vasculature.

Taken together, the beneficial effect of liraglutide on the RV was validated in three rodent models. The pathological basis of this effect has been discussed as well. Next, RNA sequencing was performed to figure out the molecular basis underlying the phenotypic change.

Chapter 5 Molecular Signatures of the Overloaded RV with Liraglutide Treatment

1. Highlights

It is important to understand the potential underlying molecular mechanisms of GLP-1 agonist involved in RV remodelling in PH. Previous studies have shown that GLP-1 and its agonists impact cardiac pathology such as hypertrophy and fibrosis via multiple signalling regulations.[114,224,244] Liraglutide is implemented in an intricate network of the metabolic regulations. It is known to be able to deactivate the renin-angiotensin axis, which leads to the attenuation of cardiac hypertrophy and fibrosis in a rodent model of heart failure.[114,244] Signalling pathways such as the PI3K-Akt and AMPK pathways have also been reported to contribute to the liraglutide-related attenuation of cardiac remodelling. These molecular findings are mostly based on the studies of LV, knowledge on the molecular regulation of liraglutide on the failing RV is limited.

Employing the high-throughput RNA sequencing, I investigated the molecular changes caused by liraglutide in the overloaded RV of PAB mice and SuHx rats. The results profiled the liraglutide-related differential gene expression. The significantly impacted pathways were revealed at the transcriptional level, and the regulations of these pathways were validated at the protein level. I have focused on deciphering the intricate molecular regulations underlying the RV decoupling and the effect of liraglutide on the RV.

2. Results

2.1 RNAseq analysis revealed the transcriptome signature of the overloaded RV with liraglutide treatment in PAB mice

As an initiation to explore the molecular basis of the therapeutic effect of liraglutide on the RV, RNAseq was performed firstly with the RV samples collected from the PAB mice. This helps to reduce the variables in studying the RV, because the RV behaviour in this model is irrelevant to the pressure changes of the PA. Sequentially, RNAseq was also performed with the RV samples of SuHx rats, to co-validate the changes of both the gene expression and the pathway signalling.

2.1.1 The overview of the RNAseq data of PAB mice

There were 12 RV samples in the RNAseq dataset of PAB mice, which consisted of three different conditions:

1) Sham-operated controls (Sham), N=4;

2) PAB with placebo control (PAB + Placebo), N=3;

3) PAB with liraglutide treatment (PAB + Lira), N=5.

Prior to the identification of the differentially expressed genes (DEGs), a global overview of the data was made. Principal component analysis (PCA) were performed to assess the intra- and inter-group variability and similarity of the RNAseq data. Intragroup variability represents the biological differences within the group. Intergroup variability is the variability between groups. The first 2 principal components (PCs) were plotted (*Figure 5-1*). PC1 and PC2 describe 64% and 12% of the variability respectively, among the RV samples of PAB mice, *i.e.* the majority of the variance within the dataset was described by the first two PCs. The intergroup variability was greater than intragroup variability. The intragroup similarity was observed as the points from the same group were generally clustered together.

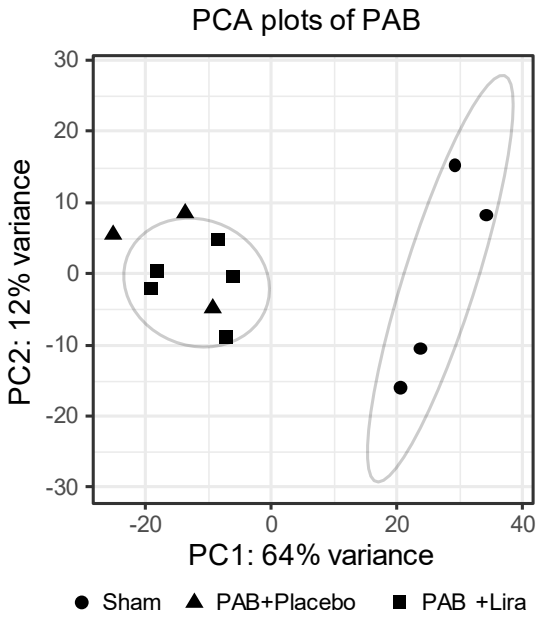

Figure 5-1 PCA plot of the RNAseq data of PAB mice

PCA plot displaying all 12 samples along PC1 and PC2, which respectively describe 64% and 12% of the variability within the expression dataset of PAB mice.

2.1.2 Identification of the DEGs attributed to liraglutide treatment

2.1.2.1 Venn diagrams demonstrating the numbers of DEGs

Genes with the cut-off adjusted *p* value < 0.05 were considered as DEGs. The PAB dataset was comprised of three separated conditions. Therefore, two pairwise comparisons of the gene transcription were made: *1)* PAB + placebo *vs.* Sham; and *2)* PAB + Lira *vs.* PAB + placebo.

The overlapped DEGs of the two comparisons were pulled out. These overlapped DEGs were considered as the co-regulated genes (by both PAB surgery and liraglutide treatment). Specifically, 5570 DEGs (2868 up-regulated and 2702 down-regulated) were identified in the comparison of PAB + placebo group *versus* Sham group. There were 452 DEGs (209 up-regulated and 243 down-regulated) identified in the comparison of PAB + Lira group *versus* PAB + placebo group. The number of overlapped (co-regulated) DEGs is 362. *Figure 5-2* demonstrates the numbers of the DEGs identified in PAB mice.

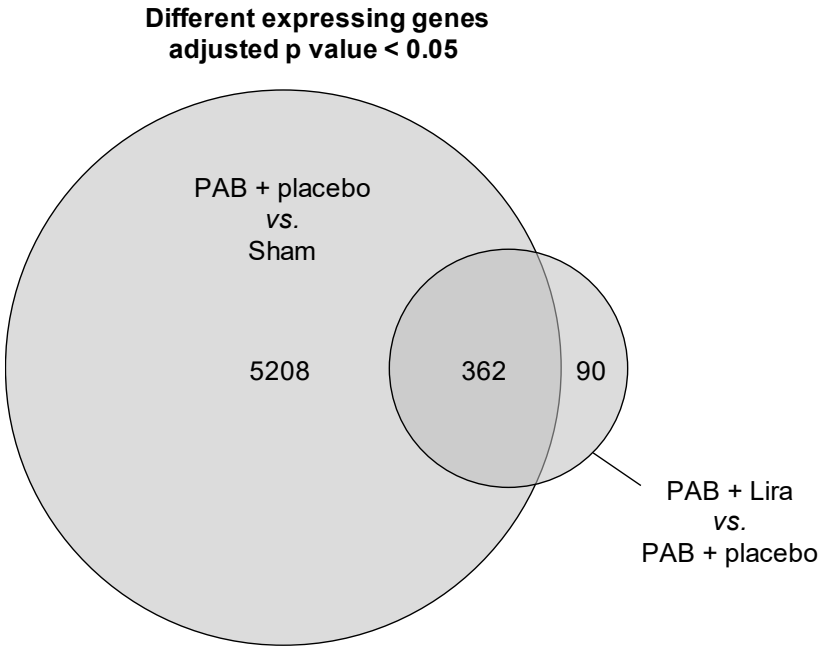

Figure 5-2 Venn graph demonstrates the number of DEGs in each comparison and the relations of the DEG sets in RNAseq analysis of PAB mice

2.1.2.2 Heatmap visualizing the expressing pattern of the samples

A heatmap with unsupervised clustering (of both samples and genes) was generated using the 452 DEGs from the PAB mice with liraglutide versus placebo

(*Figure 5-3*). Samples from the same group clustered together and showed the intragroup similarity of the gene-expressing pattern. The heatmap suggested that the expression pattern of the PAB mice with liraglutide treatment shared similarity with the sham-operated controls.

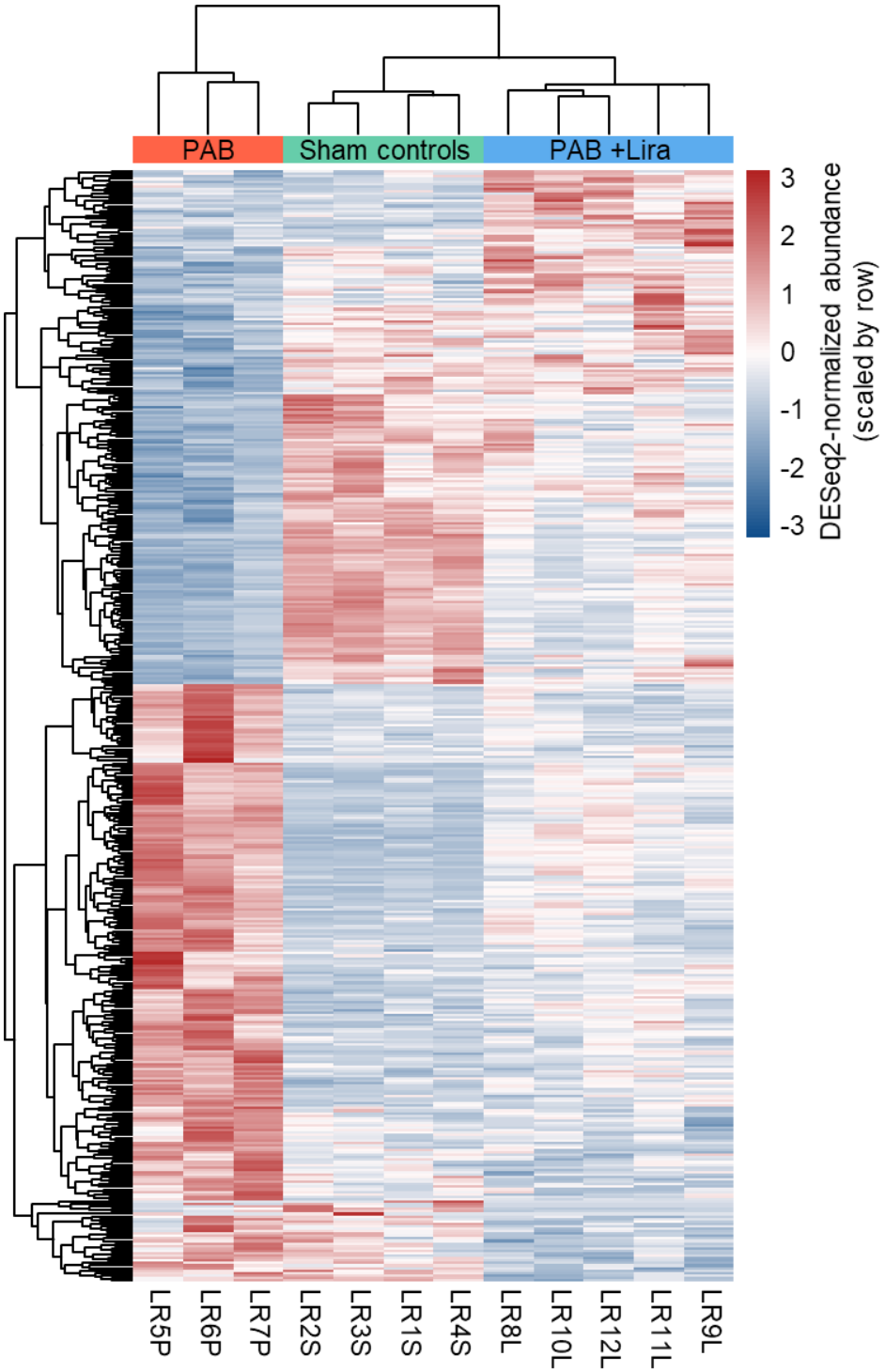

Figure 5-3 Gene expressing heatmap generated from the DEGs of PAB + Lira vs. PAB + placebo

2.1.2.3 Volcano plots

The gene expression of PAB dataset was demonstrated in volcano plots in *Figure 5-4*. The volcano plots, which plots the fold change against the adjusted *p* values of all the genes, demonstrated the gene expression of the comparisons of PAB + placebo *vs.* Sham (*Figure 5-4 A*), and PAB + Lira *vs.* PAB + placebo (*Figure 5-4 B*).

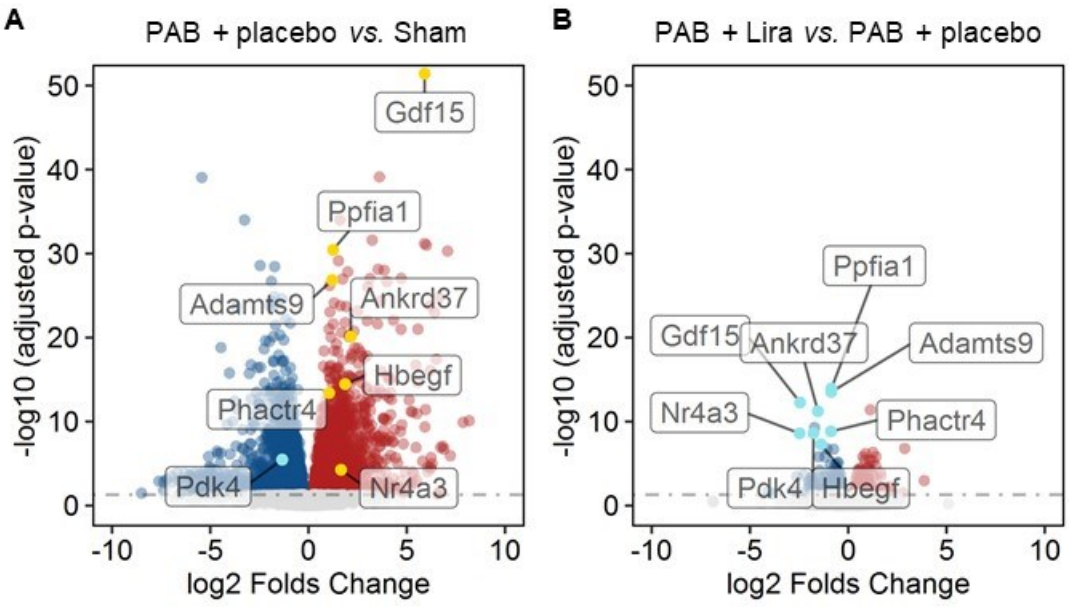

Figure 5-4 Volcano plots illustrating the gene expression of PAB mice.

(A) Gene expression in the comparison of PAB + placebo *vs.* Sham; (B) Gene expression in the comparison of PAB + Lira *vs.* PAB + placebo. Points in red refer to the upregulated genes, and blue refers to the downregulated genes. Points highlighted in yellow and cyan are the top 25 DEGs of the overlapping DEGs.

The top 25 genes in the overlapping part of the two comparisons (number of 362 in Venn plot *Figure 5-2*) are highlighted in the Volcano plots (*Figure 5-4*) and listed in *Table 5-1*. *Table 5-1* is ranked by adjusted *p* values of PAB + Lira *vs.* PAB + placebo. Significantly, some of the overlapping (co-regulated) DEGs were been found clinically relevant. I reviewed the bio-function and the clinical relevance of these genes and selected eight of them for further validation in other PH rodent models using PCR. The eight selected DEGs are highlighted in the volcano plots in *Figure 5-4*. The boxplots of the normalized expression of these eight DEGs are present in *Figure 5-5*. Brief descriptions of the bio-function of these eight DEGs are presented in *Table 5-2*.

Table 5-1 The top 25 DEGs ranked by adjusted *p* values (PAB dataset)

Rank	DEGs	PAB *vs.* Sham		Liraglutide *vs.* Placebo	
		log_2 Fold Change	FDR corrected *p* values	log_2 Fold Change	FDR corrected *p* values
1	*Ppfia1 **	1.25	3.6E-31	-0.86	1.1E-14
2	*Adamts9 **	1.21	1.4E-27	-0.86	3.0E-14
3	*Gdf15 **	5.91	3.8E-52	-2.45	5.3E-13
4	*Fam78a*	-0.93	6.2E-09	1.12	4.0E-12
5	*Ankrd37 **	2.15	7.5E-21	-1.54	5.8E-12
6	*Abra*	1.94	2.3E-13	-1.72	5.3E-10
7	*Phactr4 **	1.05	4.0E-14	-0.88	1.5E-09
8	*Pdk4 **	-1.34	3.4E-06	-1.77	2.4E-09
9	*Nr4a3 **	1.65	5.4E-05	-2.47	2.5E-09
10	*Hbegf **	1.86	3.4E-15	-1.39	5.0E-08
11	*Grhl2*	-4.02	1.7E-16	2.87	1.6E-07
12	*Arid5a*	1.86	1.7E-22	-1.08	1.7E-07
13	*Tinagl1*	0.94	2.1E-12	-0.75	2.0E-07
14	*Gal3st3*	-2.47	2.7E-29	1.26	4.5E-07
15	*Irx4*	-0.65	1.3E-04	0.88	6.2E-07
16	*Otud1*	1.50	2.3E-11	-1.18	1.5E-06
17	*Phyhip*	-0.69	1.8E-06	0.74	1.5E-06
18	*Ankrd34a*	-1.22	1.2E-05	1.41	1.5E-06
19	*Kcnj5*	-1.38	1.1E-10	1.10	3.6E-06
20	*A530016L24Rik*	-1.89	9.2E-15	1.25	4.9E-06
21	*Picalm*	1.07	6.1E-27	-0.51	7.5E-06
22	*Hspa12b*	0.29	2.2E-02	-0.58	8.1E-06
23	*Synpo2l*	2.00	1.5E-28	-0.91	1.4E-05
24	*Xirp1*	0.71	2.6E-07	-0.66	1.4E-05
25	*Gpr22*	-2.23	2.6E-15	1.39	1.8E-05

* selected for further qPCR validation (*Section 2.1.3*).

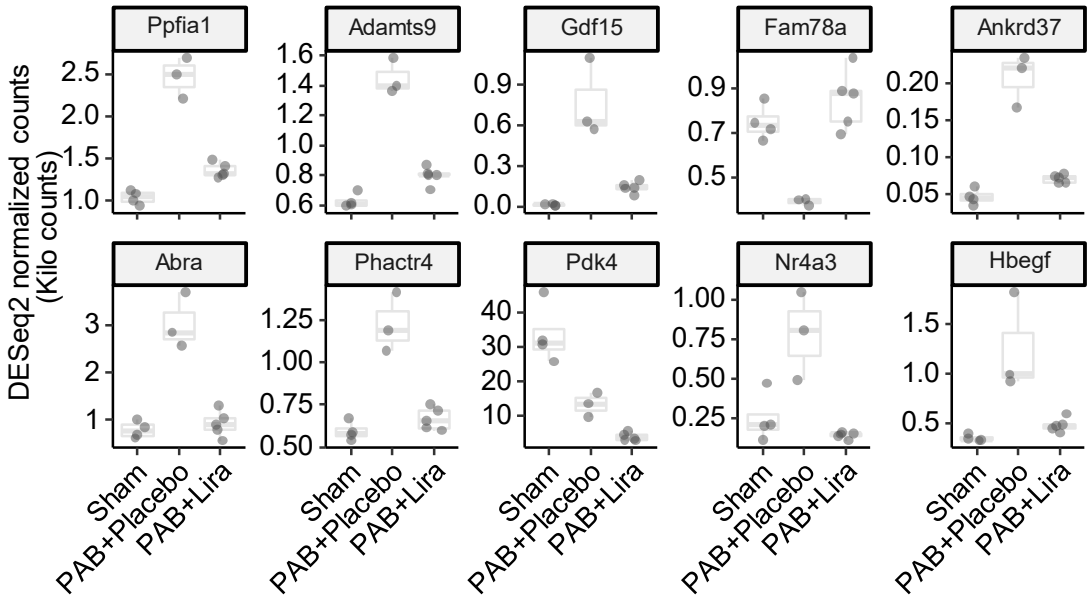

Figure 5-5 Boxplots of the expression of top co-regulated DEGs in PAB dataset

Table 5-2 Summary of the biofunction of the highlighted co-regulated DEGs in PAB mice

DEGs	Gene description	Bio-function	Relevance to the heart and/or the lung	Ref
Gdf15	Growth differentiation factor 15	GDF15 is a member of the TGF-β cytokine superfamily. It binds to the TGF-β receptors and thus activates SMAD transcription factors. GDF15 is a biomarker for diabetes and cardiovascular diseases.	Increased expression of *GDF15* was associated with cardiac hypertrophy and dilatation in the overloaded heart in rodents. Circulating level of GDF15 predicts the prognosis in patients with chronic LV failure. GDF-15 is increased in the lungs of patients with PH and serves as a prognostic marker.	*245-249*
Ppfia1	Liprin-Alpha1	PPFIA1 regulates focal adhesion signalling. This protein is implemented in cell migration, integrin expression, cell-matrix interactions, and tumour invasion.	PPFIA1 facilitate fibronectin fibrillogenesis and vascular morphogenesis through interacts with α5β1 integrin. Gene variation of *PPFIA1* is associated with the risk of acute lung injury (ALI) in major trauma	*250,251*
Hbegf	Heparin binding EGF like growth factor	HBEGF is a member of the EGF family, produced by monocytes and macrophages. It is an epidermal growth factor with heparin affinity.	HBEGF plays a role in heart development and function. Increased HBEGF is observed around lung microvessels in PH.	*252-255*
Phactr4	Phosphatase and actin regulator 4	PHACTR4 is a member of the PHACTR family. PHACTR4 binds to actin and protein phosphatase 1 (PP1). It regulates neural tube and optic fissure closure. It suppresses hepatocellular carcinoma through inhibiting IL-6/STAT3 pathway.	PHACTR1 facilitate atherosclerotic development. No publications have stated the function of PHACTR4 in the lung and heart diseases.	*256-258*

DEGs	Gene description	Bio-function	Relevance to the heart and/or the lung	Ref
Ankrd37	Ankyrin repeat domain protein 37	ANKRD37 is an effector of HIF1α. It involves in hypoxia-induced autophagy, angiogenesis, and glucose metabolism reprogramming in cancer cells.	No publications have stated the function of ANKRD37 in the lung and heart diseases.	*259,260*
Adamts9	ADAM metallopeptidase with thrombospondin type 1 motif 9	ADAMTS9 is a member of ADAMTS family. Members of the ADAMTS family have play roles in the organ development, proteoglycan cleavage, and the inhibition of angiogenesis.	ADAMTS9 haploinsufficiency leads to cardiac and aortic anomalies.	*261-266*
Pdk4	Pyruvate dehydrogenase kinase 4	PDK4 is a member of the PDK protein kinase family. PDK4 inhibits (phosphorylates) the pyruvate dehydrogenase complex. It plays a role in the regulation of glucose and fatty acid metabolism and homeostasis. PDK4 involved in the metabolic dysregulation in tumour pathology. It serves as an anti-tumour target.	Increased PDK4 expression correlates with the increase of fatty acid oxidation in heart. PDK4 is a vital manipulator of myocardial glucose oxidation rate. Upregulating PDK4 impairs RV function in PH rats. Increased PDK4 in lung pericytes is associated with reduced endothelial-pericyte interactions and reduce of capillary vessels in pulmonary arterial hypertension.	*267-271*
Nr4a3	Nuclear receptor subfamily 4 group a member 3	NR4A3 is a transcription factor of NR4A family. The bio-function of NR4A3 is intricate and pleiotropic. It involves in immune function and cell. development. It plays an important role in cell survival and proliferation. It regulates insulin sensitivity and improves glucose tolerance.	NR4A3 interacts with PARP1 and induces cardiac hypertrophy. NR4A3 suppressing inflammatory responses via JAK2-STAT3/NF-κB pathway in acute myocardial infarction. NR4A nuclear receptors regulate cardiac remodelling and heart failure in multiple mechanisms. NR4A3 promotes proliferation of PASMC via cyclin D1.	*272-277*

2.1.3 RV gene expression validated by quantitative PCR

Eight of the selected co-regulated DEGs identified by RNAseq in PAB mice were validated through quantitative real-time PCR (qPCR) in the RV of all the three rodent models (PAB mice, MCT and SuHx rats). To be specific, the 8 top genes subjected to qPCR validation were: *Ppfia1, Adamts9, Gdf15, Ankrd37, Phactr4, Pdk4, Nr4a3, Hbegf*. Trends of the gene expression changes in the RV of the models were in keeping with the RNAseq data. The qPCR results were plotted in *Figure 5-6*.

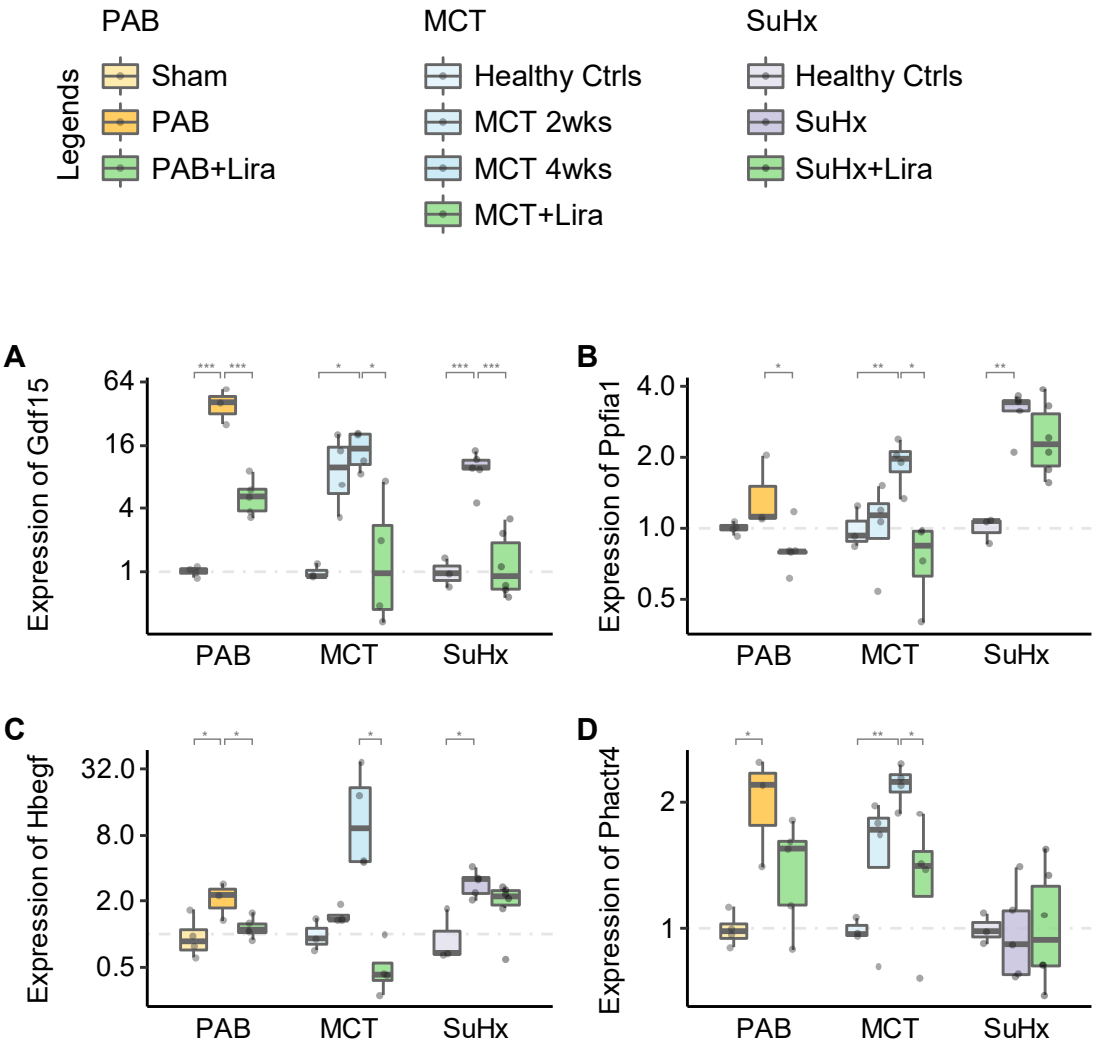

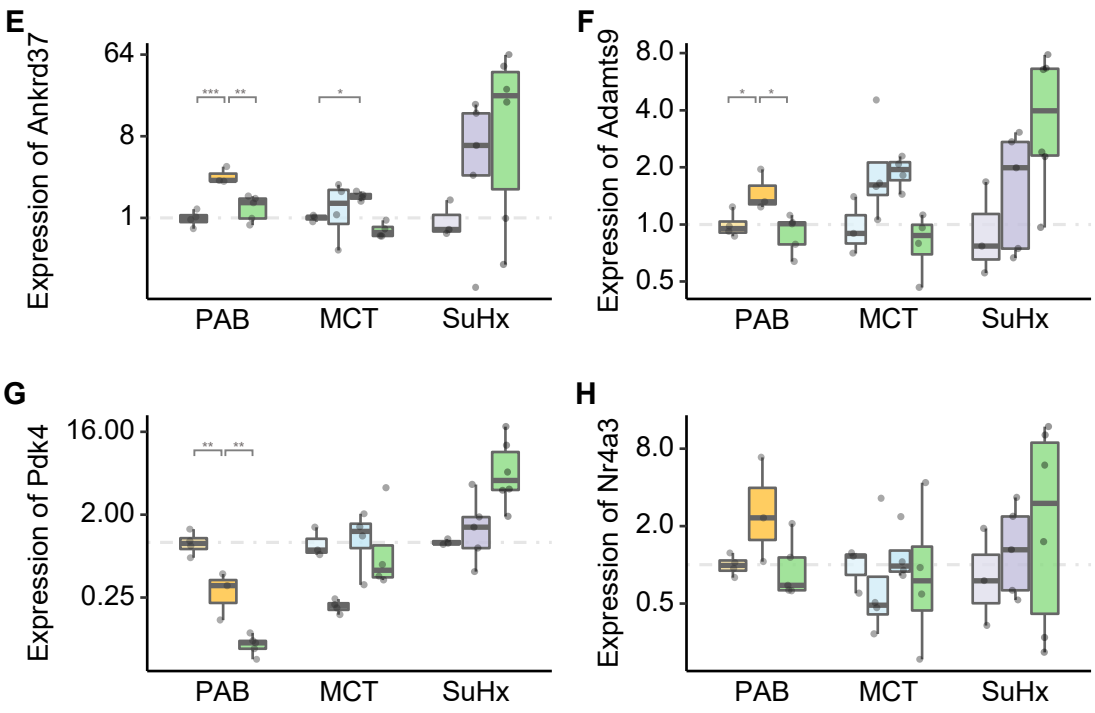

Figure 5-6 qPCR Validation of the co-regulated DEGs identified by RNAseq

The boxplots in this figure presents the relative expression ($2^{\Delta\Delta Ct}$) of the target genes in the RV of three diseased models. The genes presented are: (A) *Gdf15*; (B) *Ppfia1*; (C) *Hbegf*; (D) *Phactr4*; (E) *Ankrd37*; (F) *Adamts9*; (G) *Pdk4*; (H) *Nr4a3*. Sample size: N = 3~ 5 for each group.

2.1.4 Pathway enrichment of the DEGs

To understand the molecular mechanisms underlying the overloaded RV and the therapeutic effects of liraglutide, DEGs were subjected to the over-representation analysis (ORA) with the gene sets of KEGG (Kyoto Encyclopaedia of Genes and Genomes) pathway database. The pathway changes of the RV in PAB mice with and without liraglutide treatment were visualized (*Figure 5-7*). Among the 457 DEGs (PAB +Lira *versus* PAB), 186 were annotated in the KEGG gene sets and were matched into the KEGG maps. Among the 5570 DEGs (PAB *versus* Sham), 2344 were annotated in KEGG genes sets and were matched into the KEGG maps. The PI3K-Akt pathway and the AMPK pathway (highlighted in red) are significantly enriched in both sets of the DEGs.

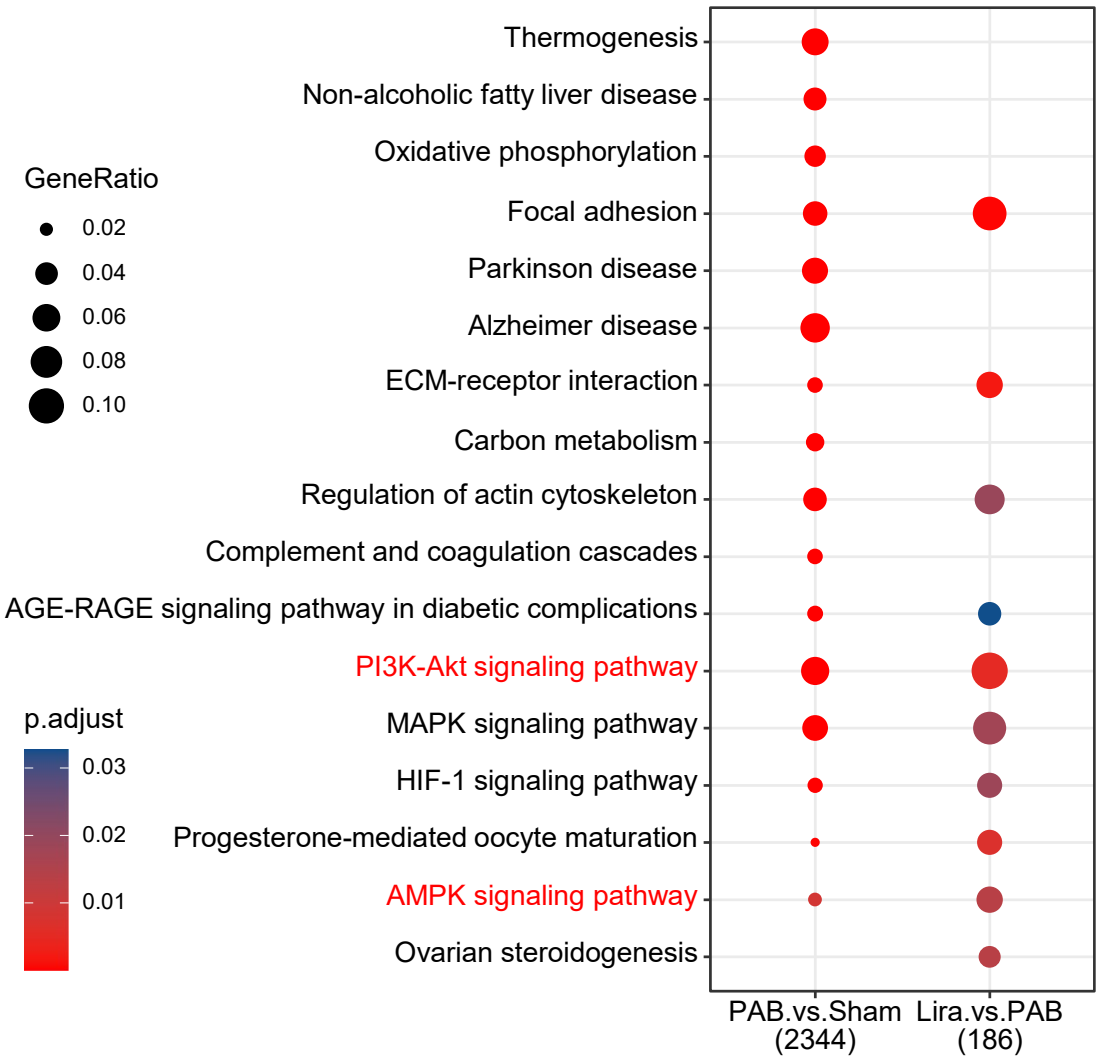

Figure 5-7 Pathway enrichment of the DEGs in PAB mice

2.1.5 Liraglutide improved the metabolic status of the overloaded RV

In order to understand the metabolic regulation of the overloaded RV with liraglutide treatment, the RNAseq data were subjected to Gene Set Enrichment Analysis (GSEA) for revealing the changes of the oxidative phosphorylation module (The Molecular Signatures Database; Systematic name of the Gene Set: M19540). The analysis showed that the oxidative phosphorylation in the RV was significantly downregulated in PAB mice comparing to the sham-operated mice (normalized enrichment score: -1.98, *p* value: 0.0021, adjusted *p* value: 0.0114). Liraglutide was able to improve the oxidative phosphorylation in the overloaded RV in PAB mice (normalized enrichment score: 1.68, *p* value: 0.0019, adjusted *p* value: 0.0953). (*Figure 5-8*).

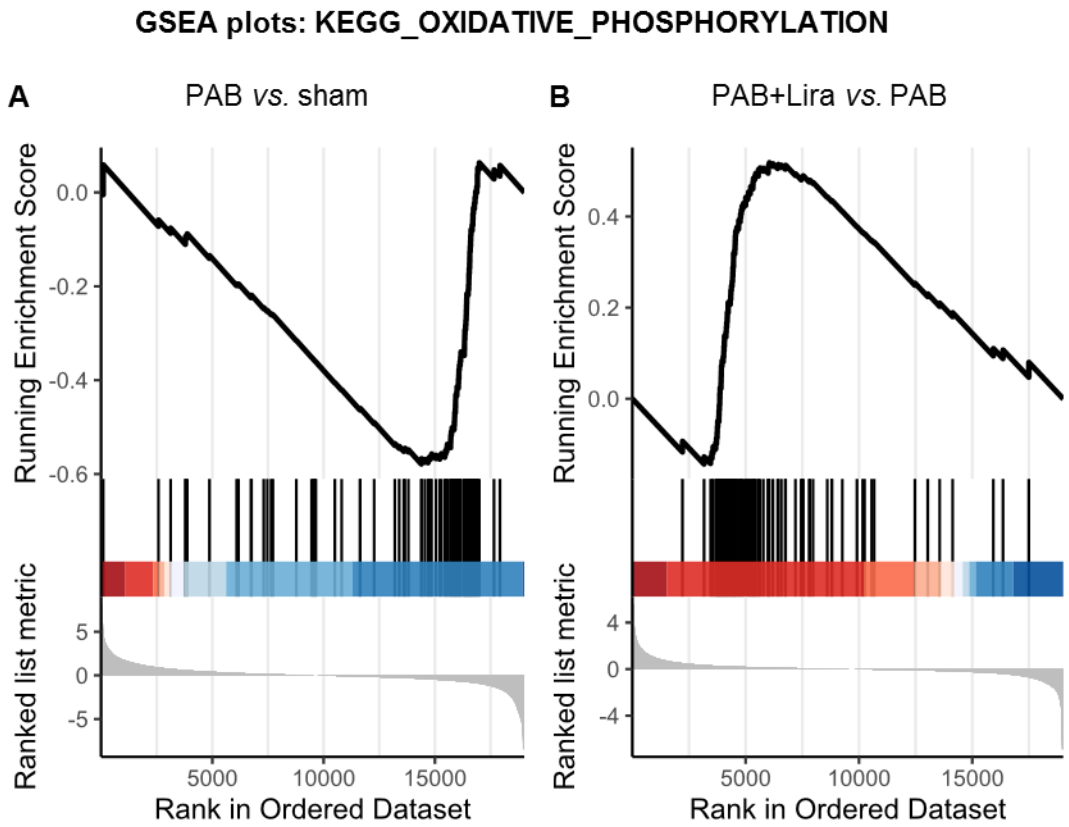

Figure 5-8 Liraglutide improved the oxidative phosphorylation of the overloaded RV

GSEA of the oxidative phosphorylation gene set of: (A) PAB mice *versus* sham-operated mice, and (B) PAB mice with liraglutide *versus* PAB mice with placebo.

2.2 RNAseq analysis of the RV in SuHx rats co-validated the regulation of the pathways

2.2.1 The overview of the RNAseq data of SuHx rats

The transcriptional regulation of liraglutide in overloaded RV was also investigated with the RV tissues of SuHx rats, through RNAseq. There were 9 RV samples in the RNAseq dataset of SuHx rats, which was comprised of three conditions:

1) Healthy controls (Ctrls), N=3;

2) SuHx with placebo control (SuHx + placebo), N=3;

3) SuHx with liraglutide treatment (SuHx + Lira), N=3.

PCA was performed for an overview of the variance among the samples of the SuHx dataset. PC1 and PC2 describe 31% and 17% of the variability among the RV samples of SuHx rats (*Figure 5-9*). Intragroup similarity was observed as the points from the same group were generally clustered together. The data was then processed to DEG identification.

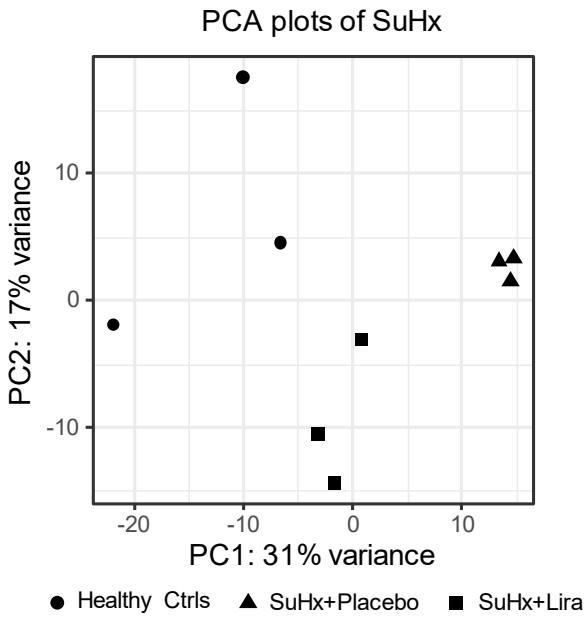

Figure 5-9 PCA plot of the RNAseq data of SuHx rats

PCA plot displaying all 9 samples along PC1 and PC2, which respectively describe 31% and 17% of the variability within the expression SuHx dataset.

2.2.2 Identification of the DEGs attributed to liraglutide treatment in the RV of SuHx rats

2.2.2.1 Venn diagrams demonstrating the numbers of DEGs

In SuHx rats, 955 DEGs (568 up-regulated and 387 down-regulated) were identified in the comparison of SuHx + placebo group *versus* healthy controls. There were 528 DEGs (238 up-regulated and 290 down-regulated) identified in the comparison of SuHx + Lira group *versus* SuHx + placebo group. There were 305 overlapping (co-regulated) DEGs between the two DEG sets. The numbers of DEGs was demonstrated with a Venn diagram in *Figure 5-10 A*.

According to the gene names, there were 15 genes identified in both overlapping (co-regulated) sections of SuHx and PAB datasets (*Figure 5-10 C*). The 15 genes were listed in *Table 5-3*. Their bio-functions are described in *Table 5-4*.

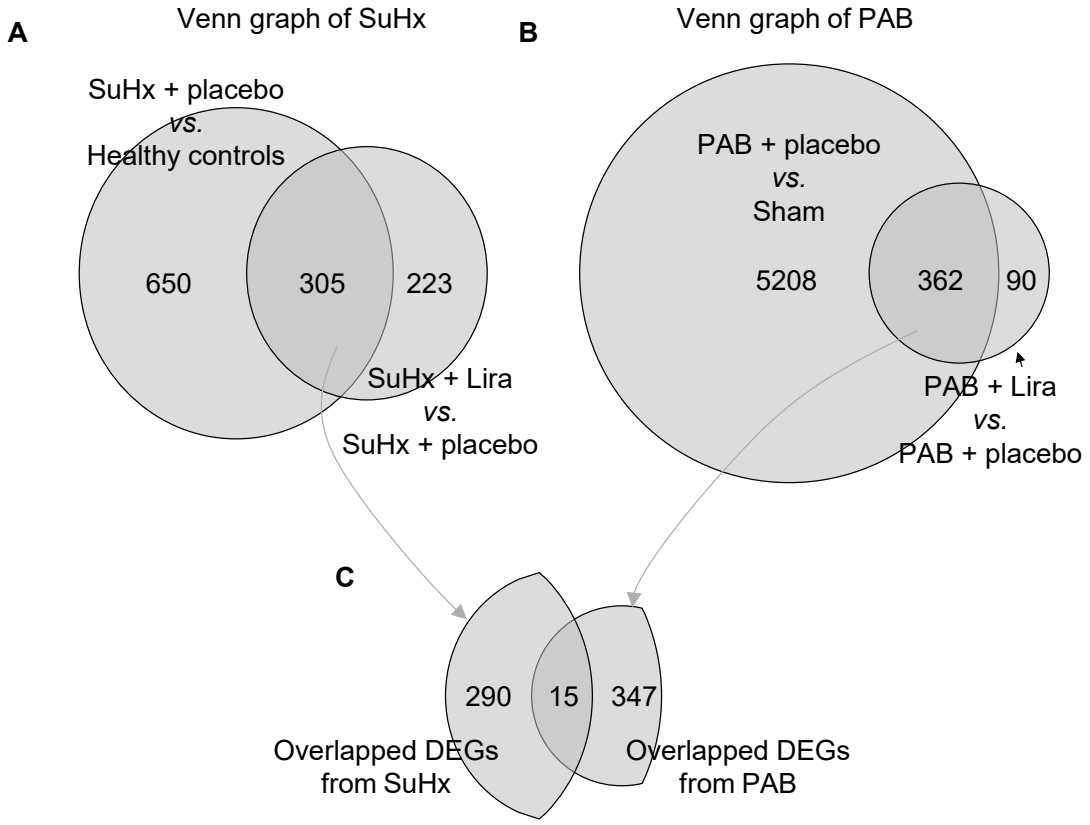

Figure 5-10 Venn graph demonstrates the numbers and the relations of DEGs sets in SuHx and PAB RNAseq datasets

Table 5-3 The 15 DEGs been identified in both models

Rank	DEGs	SuHx +Lira *vs.* SuHx		PAB +Lira *vs.* PAB	
		log_2 Fold Change	FDR corrected *p* values	log_2 Fold Change	FDR corrected *p* values
1	*Selenbp1*	1.36	8.3E-16	0.57	4.1E-03
2	*Xirp2*	-2.14	6.0E-11	-0.80	2.1E-02
3	*Plod2*	-1.25	1.6E-06	-0.74	1.0E-02
4	*Hdac11*	1.42	3.9E-04	0.44	4.2E-03

5	*Zadh2*	0.72	6.8E-04	0.31	2.2E-02
6	*Synpo2l*	-1.71	1.1E-03	-0.91	1.4E-05
7	*Egln3*	-1.06	1.1E-03	-0.48	4.2E-02
8	*Enah*	-0.86	4.7E-03	-0.72	3.3E-04
9	*Lamb3*	-1.26	6.9E-03	0.73	2.2E-02
10	*Lrrfip1*	-0.55	1.0E-02	-0.32	8.2E-03
11	*Dst*	-0.46	2.0E-02	-0.44	2.4E-03
12	*Map2k6*	1.02	2.4E-02	1.00	2.5E-02
13	*Itga9*	-1.15	2.8E-02	-0.66	7.2E-04
14	*Rcan1*	-0.84	2.8E-02	-0.62	8.4E-03
15	*Ky*	0.78	4.7E-02	0.99	2.0E-02

Table 5-4 Brief descriptions of the 15 DEGs identified in both PAB and SuHx

DEGs	Gene description	Bio-function	Ref
Selenbp1	Selenium binding protein 1	In cancer biology, downregulation of this protein is reflective of increased cell proliferation and decreased differentiation. Selenium is a trace element involved in redox signalling. Elevated serum *SELENBP1* concentration is predictive of higher cardiovascular stress and risk.	*278,279*
Xirp2	Xin actin binding repeat containing 2	Expression of *Xirp2* is mostly localized in cardiac and skeletal muscle. XIRP2 protects actin filaments from depolymerization.	*280,281*
Plod2	Lysyl hydroxylases 2	PLOD2 implements in the formation of stabilized collagen cross-links. PLOD2 is upregulated in tumours and it is linked to a poor prognosis. PLOD2 interacts with TGFβ1, involving in fibrotic pathologies.	*282-284*
Hdac11	Histone deacetylase 11	Histone deacetylases (HDAC) modulate the epigenetic mechanisms in PH pathology. Increased activity of HDAC was noted in PH.	*285,286*

DEGs	Gene description	Bio-function	Ref
		HDAC inhibitors showed therapeutic potential in PH.	
Zadh2	Prostaglandin reductase-3	Prostaglandin reductase-3 represses PPARγ activity and inhibits adipogenesis.	*287*
Synpo2l	*Synaptopodin 2-like protein*	This is an actin-binding protein. Gene variants of *SYNPO2L* was identified as a risk factor of heart failure. The bio-function of this gene remains largely unknown.	*288*
Egln3	Egl-9 family hypoxia inducible factor 3	This molecule is also known as prolyl hydroxylase domain-containing protein 3 (PDH3). This is a prolyl hydroxylase. HIF1 is one of its target proteins.	*289*
Enah	ENAH actin regulator	This an actin regulatory protein which modulates cell motility and adhesion. ENAH was increased in tumours, and the increased expression correlates with poor prognosis.	*290,291*
Lamb3	Laminin subunit beta-3	Laminin mediates cell differentiation, migration, and adhesion. LAMB3 regulates the PI3K/Akt signalling pathway and play a role in invasive and metastatic behaviours in cancer biology.	*292*
Lrrfip1	Leucine-rich repeat flightless-interacting protein-1	This protein is a key regulator of gene transcription. It plays a role in thrombus formation.	*293-295*
Dst	Dystonin	This is a member of spectraplakin family. It is a cytoskeletal-linker protein. Mutations in *DST* cause hereditary sensory and autonomic neuropathy.	*296,297*

DEGs	Gene description	Bio-function	Ref
Map2k6	Dual specificity mitogen-activated protein kinase kinase 6	MAP2K6 is a critical upstream regulator of MAPK. This protein kinase acts as an essential component of the MAP kinase signal transduction pathway. MAP2K6 mediated MAPK activation down-regulates SERCA2 and prolongs the cardiac contractile calcium transient in cardiomyocytes. Activation of MAPK pathway contributes to the hypertrophic and fibrotic changes in the overloaded RV. Inhibiting the MAPK pathway improved the cardiac function of the overloaded RV.	*298-300*
Itga9	Integrin subunit alpha 9	ITGA9 is a subunit of α9β1 heterodimer. The α9β1 heterodimer is distributed epithelial cells, neutrophils, hepatocytes, muscle and endothelial cells.	*301*
Rcan1	Regulator of calcineurin 1	RCAN1 inhibits calcineurin, thus inhibits the activation of NFAT. Abnormal regulation of RCAN1 was associated with cardiac valve development.	*302-304*
Ky	Kyphoscoliosis peptidase	This is a protease required for normal muscle growth. Deficiency of kyphoscoliosis peptidase cause myopathy.	*305,306*

2.2.2.2 Heatmap visualizing the expressing pattern of the samples

A heatmap of the DEGs of the comparison of SuHx+ Lira *vs.* SuHx +placebo was presented in *Figure 5-11*. Samples from the same group clustered together, showing intragroup similarity. It can be observed that the gene expressing pattern of the SuHx rats with liraglutide treatment is similar to the pattern of the healthy controls

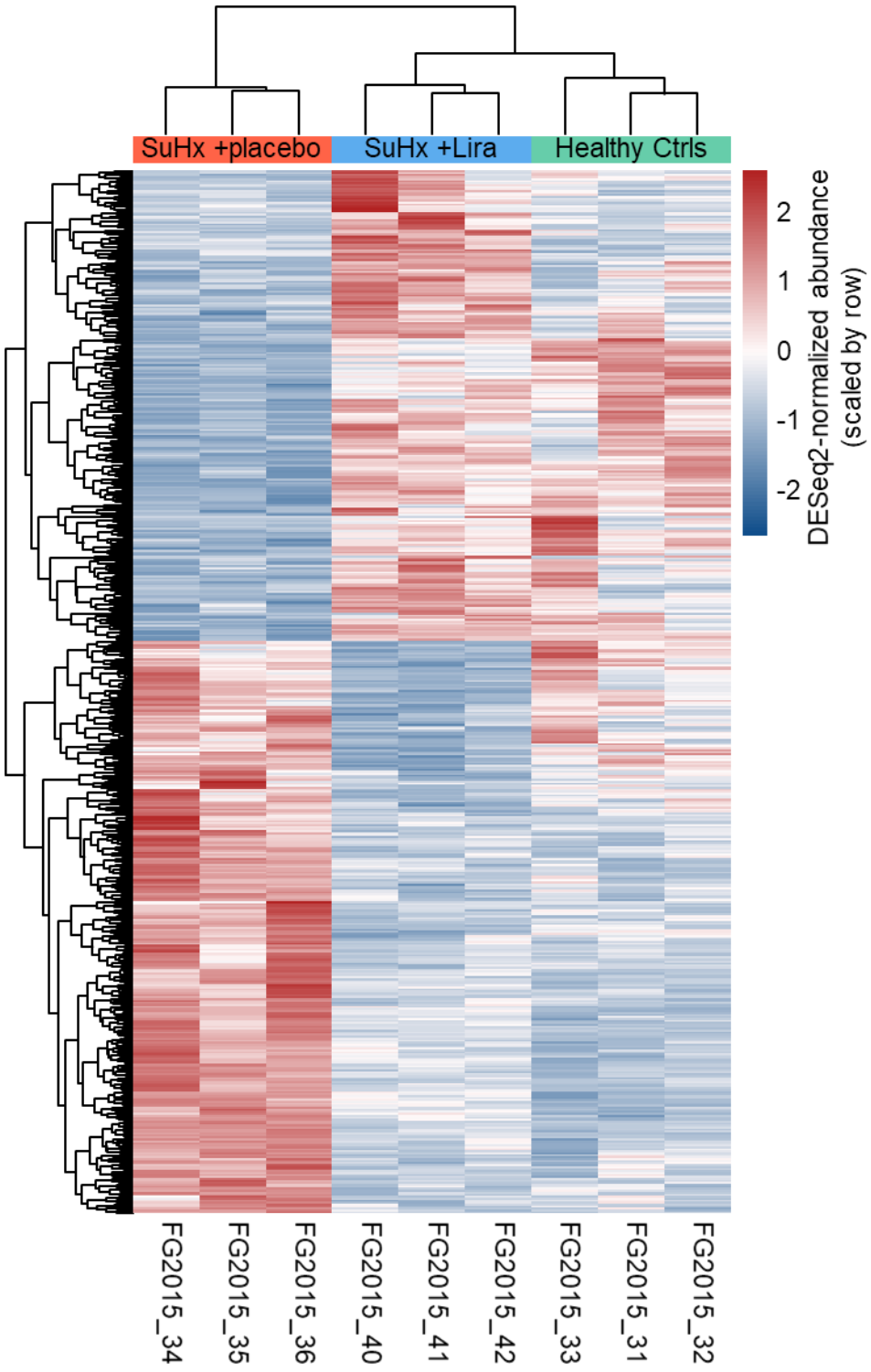

Figure 5-11 Gene expressing heatmap generated from the DEGs of SuHx+ Lira vs. SuHx + placebo

2.2.2.3 Volcano plots

The gene expression of SuHx dataset was illustrated in volcano plots (*Figure 5-12*). The volcano plot of *Figure 5-12 A* demonstrates the gene expression of SuHx + placebo *vs.* healthy controls. *Figure 5-12 B* demonstrates SuHx + Lira *vs.* SuHx + placebo. The 15 DEGs identified in both the overlapped section of SuHx and PAB were highlighted in the plots (*Figure 5-12*).

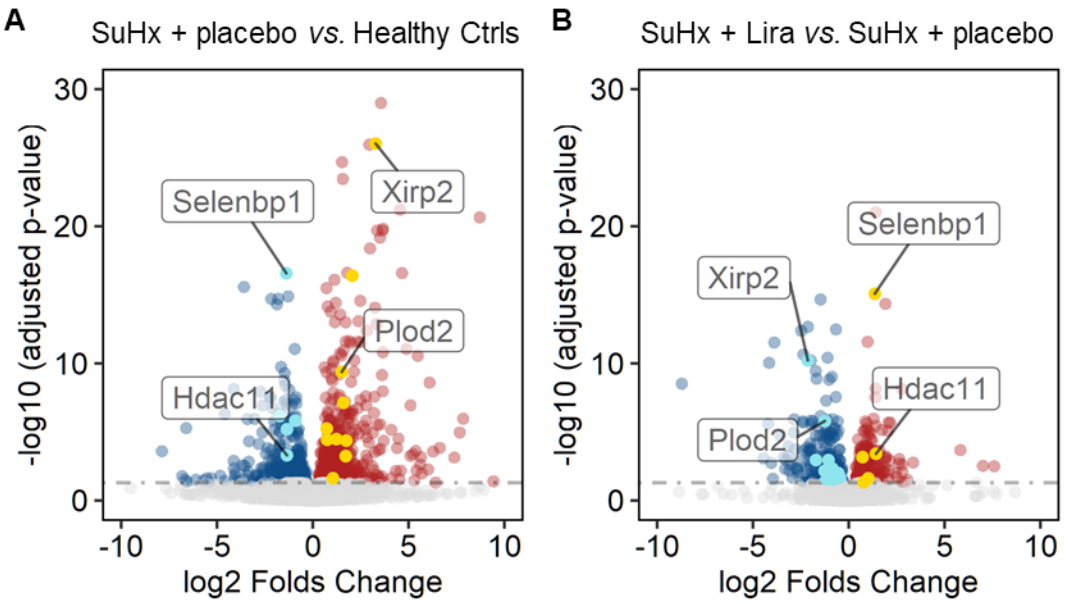

Figure 5-12 Volcano plots illustrating the gene expression of SuHx rats.

(A) Gene expression in the comparison of SuHx + placebo *vs.* healthy controls; (B) Gene expression in the comparison of SuHx + Lira *vs.* SuHx + placebo. Points in red refer to the upregulated genes; points in blue refer to the downregulated genes. Points highlighted in yellow and cyan are the 15 DEGs (with the top 4 been labelled) that were identified in both overlapped section of SuHx and PAB (listed in *Table 5-3*).

2.2.3 Pathway enrichment of the DEGs

In SuHx rats, among the 955 DEGs (SuHx +placebo *versus* Healthy controls), 417 were matched into the KEGG maps. Among the 528 DEGs (SuHx +Lira *versus* SuHx +placebo), 245 were matched into the KEGG maps. *Figure 5-13* Shows the top pathway terms in each comparison. The top 10 enriched pathway terms of each comparison, as well as the overlapped terms, are shown. It can be observed that the P13K-Akt

pathway (highlighted in red in *Figure 5-13*) was regulated by liraglutide treatment in the RV of SuHx rats.

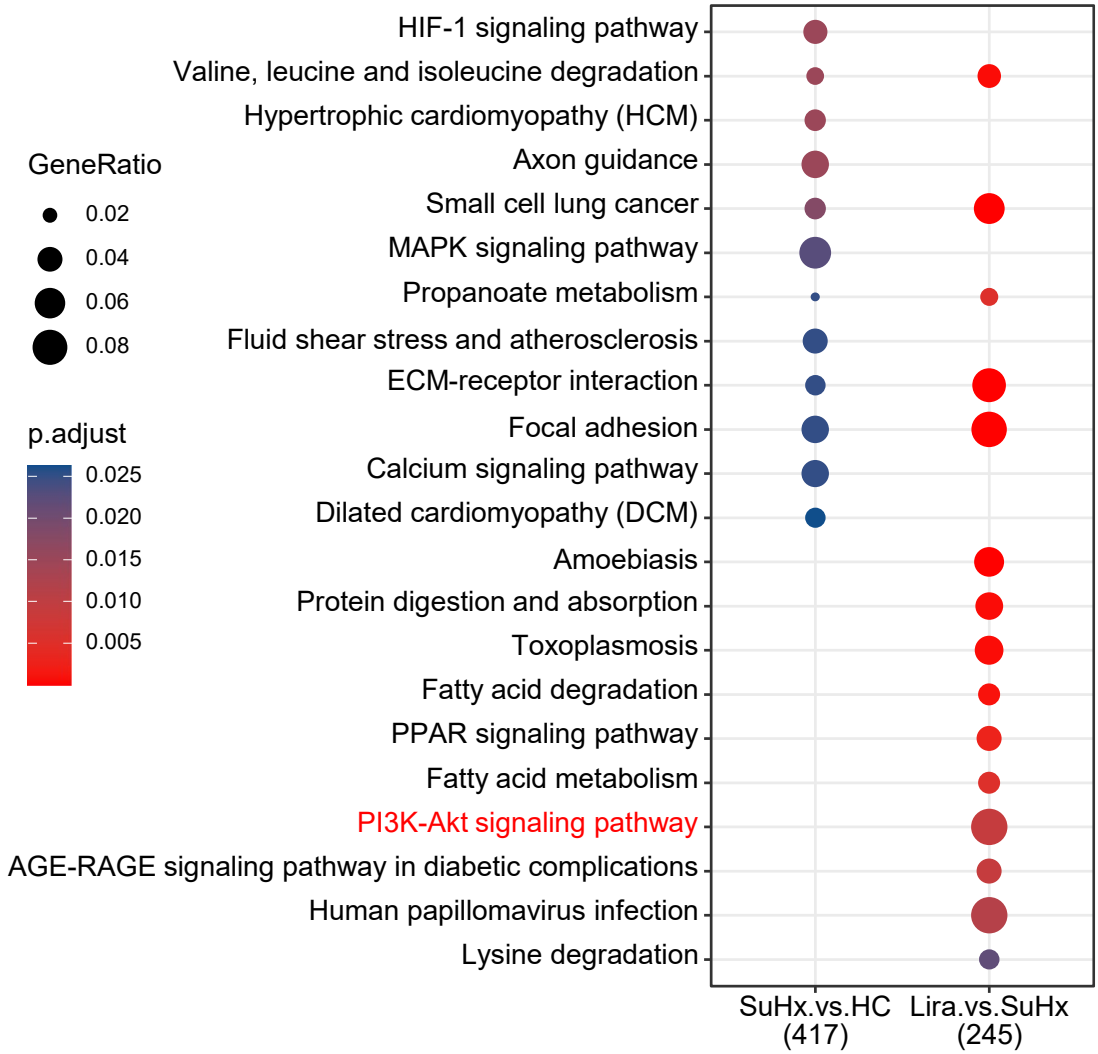

Figure 5-13 Pathway enrichment of the DEGs in SuHx rats

2.3 Immunoblotting of the key molecules in PI3K-Akt and AMPK pathways

The pathway analysis revealed several key pathways that may implement in the RV coupling mechanisms. As a validation in protein level, we checked the key molecules in two of the significant pathways with the RV tissue in PH rats: the PI3K-Akt pathway and the AMPK pathway. These two pathways have been previously reported to be regulated by GLP-1 agonists in cardiomyocyte. The key molecules in these two pathways were examined by immunoblotting and the representative blots

were presented in *Figure 5-14 A,C*. Quantification of the density of the blots was presented in *Figure 5-14 B,D*. The results show that liraglutide suppressed the activation of PI3K-Akt and enhanced the AMPK pathway in both MCT and SuHx rats.

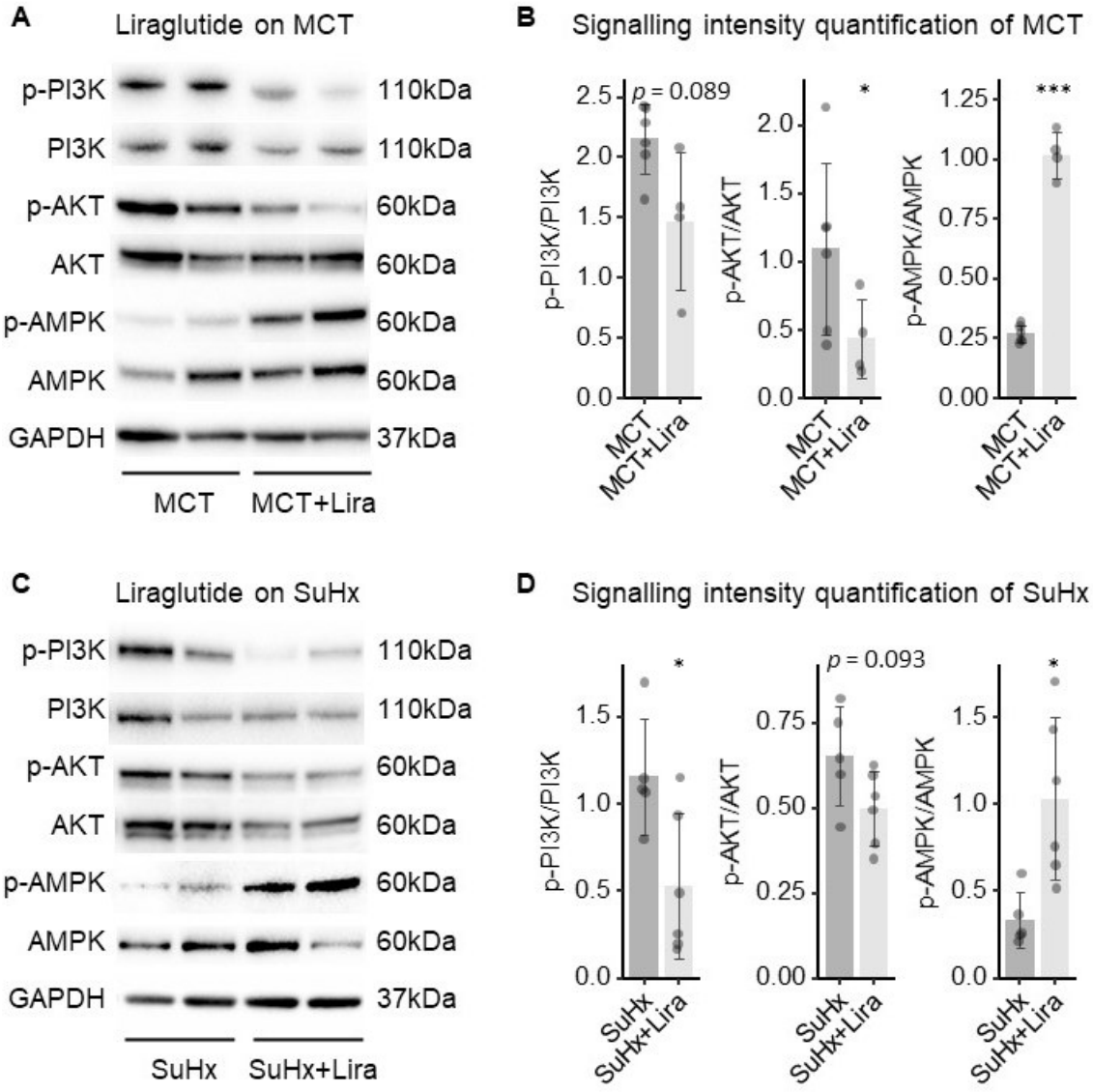

Figure 5-14 Liraglutide regulated the key molecules in PI3K-Akt and AMPK pathways in the overloaded RV

Representative immunoblots of the phosphate and the total PI3K, AKT, and AMPK in the RV of (A) MCT, and (C) SuHx rats. Quantification and analysis of the blots density of the immunoblots of (B) MCT, and (D) SuHx rats. Sample size: N =4~6 in MCT study; N =5~6 in SuHx study.

3. Summary of the results in this chapter

To summarise, this section explored the signalling involved in the RV dysfunction and the underlying mechanism explains for the therapeutic effects of liraglutide. The main points of findings are listed below.

- Differential expressing genes were identified through RNAseq, which revealed the transcriptional changes of the overloaded RV, as well as the transcriptional changes attributed to liraglutide administration, in both PAB and SuHx rodents.
- The most significant pathways were concluded and co-validated from the RNAseq data in two models. The observation of the disturbed pathways provided an overview of the intricate signalling mechanism.
- The changes of some of the top genes were validated through qPCR in the RV of multiple rodent models.
- Among the pathways concluded from RNAseq, the regulation of the key molecules in two of them were validated in protein level in the RV of PH rats. This validation indicated that liraglutide led to the suppression of the PI3K-Akt pathway and activation of the AMPK pathway in the overloaded RV in PH condition.

4. Discussion of the results in this chapter

The phenotyping data presented in this study indicated that the GLP-1 agonist, liraglutide, improved RV function and attenuated maladaptive RV remodelling in multiple rodent models. Changes in gene expression may play an important role in the RV pathophysiology. Therefore, RNAseq was performed in order to figure out the possible transcriptional changes. Through a comprehensive analysis of the RNAseq data, the genes associated with the therapeutic efficacy of liraglutide were identified. The related biological pathways were inferred for further research.

4.1 Identification and validation of individual DEGs

The RNAseq analysis screened out the DEGs of the diseased RV, and the DEGs regulated by liraglutide treatment. The common part (overlap) of these two sets of DEGs (the co-regulated genes) were considered more important, because the expression of genes was impacted by both the diseased status and the liraglutide administration. The numbers of the coregulated regulated DEGs were 305 in SuHx set and 362 in PAB set. Among the coregulated regulated DEGs of PAB and SuHx rats, there were overlaps of 15 DEGs: *Selenbp1*, *Xirp2*, *Plod2*, *Hdac11*, *Zadh2*, *Synpo2l*, *Egln3*, *Enah*, *Lamb3*, *Lrrfip1*, *Dst*, *Map2k6*, *Itga9*, *Rcan1*, and *Ky* (*Table 5-3*). The biological role of these genes in RV, as well as the interplay with GLP1 signalling are mostly uncertain. The descriptions of these DEGs are listed in *Table 5-4*. These 15 DEGs implements in a variety of biological processes. Our RNAseq analysis provides useful information on the gene expression profile of these DEGs in the overloaded RV in experimental animals. The precise mechanisms of the regulation of the DEGs with liraglutide treatment are yet to be determined.

We preferred to select the DEGs in PAB model for further validation in other PH models, because the RV dysfunction in PAB mice is independent from the PVR changes of the lung. Eight of the top DEGs in PAB model were selected for further qPCR validation. The biological function of these genes was listed in *Table 5-2*. Among the 8 genes, *Gdf15* and *Pdk4* have been studied in the RV in PH condition. GDF15 is a stress-responsive cytokine serving as a biomarker of cardiac degeneration. PDK4 activation drives the metabolic shift towards the inefficient anaerobic glycolysis mode.

RNAseq identified the *Gdf15* gene in the RV of PAB mice, which had a remarkable elevation of expression and liraglutide administration significantly reduced the expression. This change was validated by qPCR in the RV of MCT and SuHx rats as well. *Gdf15* encodes the cytokine GDF15 (growth differentiation factor 15) of the transforming growth factor-β (TGF- β) superfamily. *GDF15* expression increases hugely in multiple pathological conditions such as inflammation, tissue hypoxia, or increased oxidative stress.[307,308] Increased plasma GDF15 levels were noted in cardiopulmonary conditions such as acute coronary syndrome and acute pulmonary embolism.[309,310] Circulation GDF15 level serves as an effective predictor of the prognosis of the patients with heart failure. [246,311] In the heart of mice, elevated GDF15 expression was induced by transverse aortic banding and coronary artery ligation.[307] Similarly, we observed a significant increase of *Gdf15* expression in the overloaded RV of the diseased animals of PAB, MCT, and SuHx rodents. More relevantly, in IPAH patients, the plasma GDF15 level is elevated and it is closely related to the risk of death.[312] Studies showed that the elevation of plasma GDF15 is associated with the increase of mean RV pressure and PCWP.[312] Our data is in keeping with these observations. Validated in multiple rodent models, the increase of *Gdf15* expression coincided with the pressure increase of RV and PA in PH condition. Liraglutide treatment decreased the increased *Gdf15* expression in the overloaded RV. This is suggestive that liraglutide relieved the stress of the RV.

Among these 15 genes, published studies also addressed the role of *Pdk4* in RV pathogenesis. In the overloaded RV, PDK-mediated inhibition of pyruvate dehydrogenase (PDH) contributed to the glycolytic shift from oxidative phosphorylation to anaerobic glycolysis.[65] Upregulation of PDK4 impairs RV function and facilitates RV hypertrophy in PH rodents.[65,271] My data shows that liraglutide decreased the expression of *Pdk4* in PAB mice. This implies that liraglutide could potentially restore glucose metabolism to oxidative phosphorylation by targeting PDK4 in the RV.

The roles of other identified top DEGs that refers to liraglutide regulation remains largely unknown (DEGs listed in *Table 5-1*, *Table 5-2*). My RNAseq study presented a profile of the gene expression of these DEGs for further investigations.

4.2 The regulation of oxidative phosphorylation in the overloaded RV

The majority part of the cardiomyocyte energy supply comes from fatty acid oxidation (FAO), rather than glucose metabolism in the healthy heart.[313] In PH condition, a profound increase of RV glucose uptake was observed in PH patients,[166,314] as well as in the experimental PH rodents.[315] The increased glucose uptake is an adaptive response to the load increase, by which the cardiomyocytes attempt to meet the increased energy demand. The glycolysis process converts glucose to pyruvate. If the pyruvate is not going into mitochondrial Krebs' cycle for oxidative phosphorylation, anaerobic glycolysis happens and only 2 units of ATP are generated (instead of 32 units ATP during oxidative phosphorylation).[212] In the overloaded RV, impaired mitochondrial function is associated with the excessive hypertrophy and reduced RV contractility.[316-318] Potus *et al.* performed an RNAseq analysis with the RV tissue of MCT rats.[319] Their results indicated that mitochondrial biogenesis is the most impacted pathway in the RV of MCT rats. The changes in the transcriptomic pattern were highly attributed to mitochondrial dysfunction.[319] Here in my study, GSEA of the RNAseq data showed suppressed oxidative phosphorylation in the RV of PAB mice. Liraglutide enhanced the activity of the module of oxidative phosphorylation in transcriptional level. This is suggestive that liraglutide is able to increase glucose oxidation and improve the metabolic efficiency in the overloaded RV.

4.3 Identification and validation of the changes in the pathways

The PI3K/Akt pathway is one of the primary pathways that contribute to physiological cardiac hypertrophy.[320] McMullen *et al.* showed that the upregulation of insulin-like growth factor 1 receptor (IGF-1R) induces physiological cardiac hypertrophy and myocardial infarction through activating PI3K.[321] Mice with deficient PI3K were protected from isoproterenol-induced cardiac hypertrophy and heart failure.[322] Akt is a well-characterized downstream molecule of PI3K. Activation of Akt has been closely linked to cardiac hypertrophy.[323,324] Increased Akt phosphorylation was observed in the failing hearts in patients.[323] Pharmacological inactivation of the Akt blocked the hypertrophic response in cardiomyocytes.[323] PI3K/Akt signalling pathway has also been associated with cardiac fibrosis.[325,326]

Although the biological signalling that regulated by liraglutide is not completely clear, previous studies have shown that liraglutide regulates cardiac cytoprotective pathways, such as the regulations of SIRT1/Parkin, PPARα, JNK, mTOR, PI3K-Akt, and AMPKα.[224,235,327-331] Here, my results showed that there is a significant suppress of the activation of the PI3K-Akt signalling in the RV of PH rats. GLP-1 agonist Exendin prevented the heart from ischemic damage through attenuating the phosphorylation of PI3K-Akt pathway.[332] Li *et al.* reported that liraglutide prevented cardiac hypertrophy induced by pressure overload through inhibiting the PI3K-Akt pathway and promoting the AMPK pathway.[224] In their publication, profound cardiac hypertrophy was induced by angiotensin II or thoracic aorta coarctation in mice. Liraglutide suppressed the hypertrophic change and improved the cardiac function in both models. In cardiomyocytes treated with angiotensin II, the PI3K-Akt pathway was significantly activated and AMPK was suppressed. Liraglutide inhibited the PI3K-Akt pathway and activated AMPK in a dose-dependent manner.[224] In my results, the anti-hypertrophic effect of liraglutide was also observed in the RV of multiple rodent models with RV load increase. My results are indicative that the anti-hypertrophic effect of liraglutide on the RV could be linked to the regulation of PI3K-Akt and AMPK pathways as well.

AMPK plays an important role in regulating energy metabolism in the heart.[333] Activation of AMPK promotes energy production and inhibits apoptosis in cardiomyocytes.[334-337] AMPK is phosphorylated upon the increase of the cellular AMP/ATP ratio, leading to the activation of downstream signalling cascade which improves mitochondrial function and energy supply.[338] Once activated, AMPK increase glucose uptake by facilitating GLUT4 translocation from the cytosol to the cell membrane.[339,340] AMPK activation also increases fatty acids uptake and oxidation, by promoting the translocation of fatty acid transporters CD36.[341] AMPK regulates mitochondrial biogenesis in multiple ways. For example, AMPK phosphorylates PPARγ coactivator-1α (PGC-1α), a strong activator of mitochondrial function, promoting energy production.[342] More than its metabolic-regulating role, AMPK has been reported to be involved in various pathogenetic processes in cardiac remodelling. AMPK activators, such as metformin or resveratrol, prevents cardiac hypertrophy.[343,344] AMPK prevents myocardial ischemia by suppressing apoptosis and

cardiac oxidative stress.[345] My results identified decreased activity of AMPK in the RV of PH rats (*Figure 3-13*). In addition, liraglutide enhanced the activation of AMPK, which is reflective of a restoration of the metabolic states in the RV of PH rats.

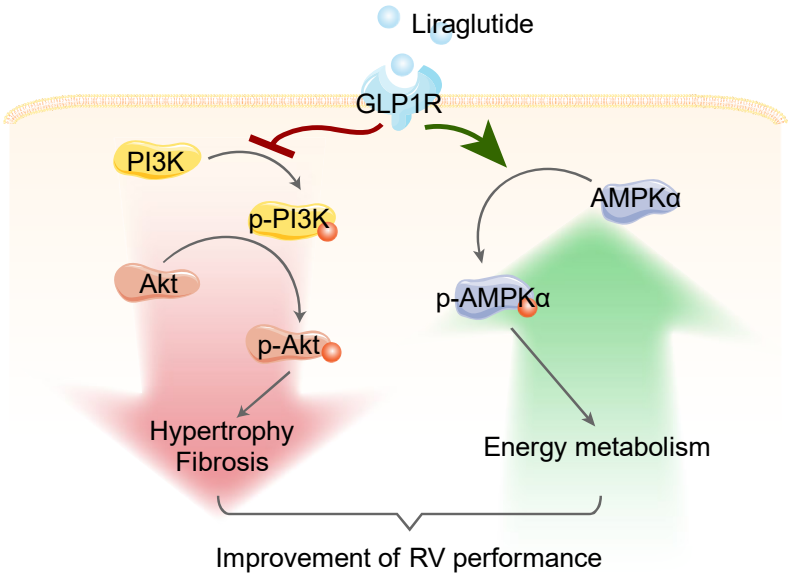

Figure 5-15 Illustration of the molecular changes caused by liraglutide treatment in the overloaded RV

A sketch is presented in *Figure 5-15* to summarise the signalling mechanism of the liraglutide's beneficial effect on the overloaded RV. Taken together, my data provide useful information on the gene expression in the potentially-involved signalling modules. Two significant signallings were validated in protein level. The results suggest that the RV-protecting effects of liraglutide are attributable to the suppression of PI3K-Akt and AMPK pathways.

Chapter 6 Conclusions

1. Significance of this PhD study

1.1 Comprehensive characterization of the experimental PH models

It has been increasingly recognized that the RV plays a crucial role in determining symptomatic status and clinical outcomes in multiple diseases.[43,226] A recent research statement addressed the knowledge gaps and the future direction of the researches focusing the RV.[204] This statement identified three major topics of current knowledge gaps and described these topics in details. Briefly, the three major topics been addressed are: 1) developing the methodology to assess RV function in both preclinical research setting and clinical scenarios; 2) optimizing the analysis of advanced RV parameters; and 3) deciphering the pathogenic and molecular mechanisms of RV function and failure.

Corresponding to the first two major topics, my study affords depth in characterizing the RV in the preclinical research setting. Employing the 9.4T MRI scanner, I detailed the volumetric changes of the RV in the two commonly-used PH rat models longitudinally. The characterizations, as well as the established methodology, provide rigour for the following pharmacological study and optimized the framework for accessing the RV in aspects of morphology, function, and coupling status in PH preclinical studies. In addition, the PA haemodynamics was assessed using MR phase-contrast imaging. Shortening of PAAT was associated with the progression of RV decoupling and it could serve as an indicator of the cardiopulmonary functional status. Moreover, MRI T1 modality and ECV mapping offered a non-invasive evaluation of the RV pathology. The cardiac fibrosis patterns in different stages of PH were presented and the correlation between the ECV and RV performance were revealed, which indicates that the increase in ECV is reflective of the decrease of RV coupling. These MRI measurements provided defined RV phenotypes of the rodent PH models, especially the characterisation of RV coupling status along the course of PH development.

I also investigated the pathologic features of the RV in PH models, including cardiac fibrosis, cardiomyocyte hypertrophy, and microvascular rarefaction. The results are conclusive that the decoupled RV is featured by excessive cardiac fibrosis and insufficient myocardium perfusion at the IPs. Cardiac fibrosis happens at the

decoupled phase of the overloaded RV. The fibrotic changes at the IPs in the overloaded RV corresponded well with the ECV findings from cardiac MRI, which was supportive that the increase of ECV accurately reflects cardiac fibrosis. Cardiomyocyte hypertrophy happens at the early stage of RV decoupling. The occurrence of cardiomyocyte hypertrophy can serve as an indicator of early adaption. The reduction of capillary density can be observed at the early stage as well, but the decrease of capillary density dominates at the end stage, which features RV decoupling. These pathological observations contribute to better recognition of the RV coupling statues in PH conditions.

The results are of translational value. Cardiac MRI is the reference method for RV function assessment.[139] The MRI methodology in my study is established in accordance with the standard MRI practise,[191] which made the MRI imaging practise highly reproducible in both preclinical and clinical settings. The MRI results in my study promote cardiac MRI modalities as an essential tool for a comprehensive evaluation of the RV. It is of great value to popularize the established cardiac scanning practise with the 9.4T MRI scanner in our facility, which will add value to other cardiac research projects.

Well-established animal models and optimized RV evaluation methods are essential for gaining new knowledge of the RV pathophysiology and developing RV-specific medications. In this study, the longitudinal characterization of the RV remodelling of the experimental PH models formed the methodology for the pharmacological investigation of liraglutide on the overloaded RV.

1.2 Preclinical evaluation of the GLP-1 agonist liraglutide in PH in a translational manner

Current treatments for PAH are still limited vasodilators that modulate the endothelin, prostacyclin, and nitric oxide pathways. Treatments that target/resolve the pulmonary and RV remodelling in PH are needed. Metabolic dysregulation has been identified as a crucial component in PH pathogenesis,[346] *e.g.* glucose metabolism is altered in both the remodelled pulmonary vessels and the RV.[346] The major aberration of glucose metabolism is the shift from oxidative phosphorylation to anaerobic glycolysis (*glycolytic shift*).[68,69]

GLP-1 agonist liraglutide is an anti-diabetic drug. Liraglutide has shown to promote energy metabolism, such as improving the mitochondrial function.[347,348] It has also shown versatile protective effects on the cardiovascular system. Published studies indicate that liraglutide was able to improve cardiac function in heart failure rodents, and it reduced the risk of heart failure in T2DM patients.

Previous results from our group showed that liraglutide attenuated PA remodelling in MCT rats.[136] Published studies also claimed that liraglutide suppressed the vasculopathy in the pulmonary vasculature in multiple PH models (include rodent PH induced by MCT, bleomycin, or hypoxia).[132-134] These preclinical observations were supportive of the therapeutic role of liraglutide on the pulmonary vasculature. Here my PhD study provided rigorous preclinical evidence which strongly supports that liraglutide reduces the RV dysfunction in PH condition through restoring the glucose metabolism and promoting the mitochondrial function. Combining my results with our previous study and the existing publications, liraglutide is efficient to attenuating the remodelling of both the lung and the RV in PH condition.

One of the key conclusions of the results is that liraglutide attenuates RV structural changes and improves RV function in PH. The therapeutic effect of liraglutide was confirmed in three rodent models, using the well-established cardiac imaging modalities. The data from PAB mice differentiated the specific effect of liraglutide on RV. Cardiac performance of PH rats was recorded at pre- and post-treatment timepoint, showing that liraglutide reversed the established RV impairment. The volumetric changes of the heart were measured precisely using gold-standard

cardiac MRI in PH rats, which provided trustable results supporting the therapeutic effect of liraglutide on the overloaded RV.

Moreover, the metabolic mechanisms attributing to liraglutide's therapeutic effect were revealed. RV ^{18}F-FDG PET offered direct evidence showing liraglutide regulates the glucose metabolism in the RV of MCT rats. In addition, the in-depth RNAseq analysis of the oxidative phosphorylation pathways supported that liraglutide improved oxidative phosphorylation. Conclusively, liraglutide restores the metabolic efficiency in the RV myocardium in PH condition.

Liraglutide reduces cardiac fibrosis and hypertrophy, and improves myocardium perfusion in the overloaded RV. The pathologic effect of liraglutide in the overloaded RV was examined using MRI ECV mapping and fluorescence labelling. There was an overall decrease of ECV in the interventricular parts and the RV free wall in PH rats with liraglutide treatment, suggesting decreased cardiac fibrosis with liraglutide treatment. Pathological inspection with fluorescence showed decreased cardiomyocyte hypertrophy and improved microcirculation at the IPs of MCT rats.

Liraglutide is a licensed drug in clinical practice. It is an attractive option to develop medications by repurposing drugs that are currently used in clinic for other medical conditions, which accelerates the drug developing and reduces the costs.[349]

The pharmacological study of liraglutide was designed and conducted in a translational manner. The methodology (RHC and MRI) was adopted in coordination with the evaluations used in clinical practice, which enables easier bench-to-bedside translation of the research results.

My results lead to the conclusion that liraglutide is a promising therapeutic option resolving both RV and pulmonary remodelling in PH. The therapeutic effect of liraglutide is related to the modulation of energy metabolism.

1.3 Depth in the molecular mechanisms underlying the therapeutic effect of liraglutide

Deciphering the molecular mechanisms underlying RV pathophysiology is one of the major research topics of the RV in PH.[204] My RNAseq analysis offered insights into the transcriptome changes in the overloaded RV. Moreover, the transcriptome changes attributed to liraglutide treatment were revealed. Analysis of the transcriptome changes led to the findings of significant gene expression changes, as well as the regulation of pathway modules, which accounted for the treatment effect of liraglutide on the overloaded RV.

The expressing changes of individual genes that are responsible for liraglutide treatment were discussed. *Gdf15* is a stress-responsive cytokine that has been linked to the severity and prognosis of PH. Liraglutide treatment reduced the expression of *Gdf15* in the overloaded RV, which implies reduced stress of the RV by liraglutide. *Pdk4* encodes PDK4 which inhibits pyruvate dehydrogenase, leading to decreased pyruvate dehydrogenation and suppressed mitochondrial oxidation. Liraglutide reduced the expression of *Pdk4*, which is suggestive that liraglutide could promote mitochondrial oxidation through this mechanism.

Gene module analysis revealed that liraglutide promotes oxidative phosphorylation in transcriptional level. This is conclusive that liraglutide enhances the energy metabolism efficiency in the RV myocardium. Regulating the energy metabolism could be a vital mechanism accounting for liraglutide's cardioprotective effect. This result is in coordination with the RV ^{18}F-FDG PET results. Collectively, it is convincing that liraglutide is able to restore the energy metabolism in the overloaded RV.

The RNAseq analysis of the overloaded RV provided a profile of the intricate molecular changes impacted by liraglutide and pointed out possible directions for mechanism studies of liraglutide in RV pathology. In particular, my data highlighted the involvement of the PI3K-Akt and AMPK pathways. The possible mechanisms implemented in the two pathways are labelled in *Figure 6-1*. Taken together the phenotyping results of the cardiac MRI, the RV ^{18}F-FDG PET, and the pathological inspection, my results indicated that liraglutide suppresses cardiomyocyte

hypertrophy and enhance energy metabolism through deactivating the PI3K-Akt signalling and upregulating the AMPK signalling.

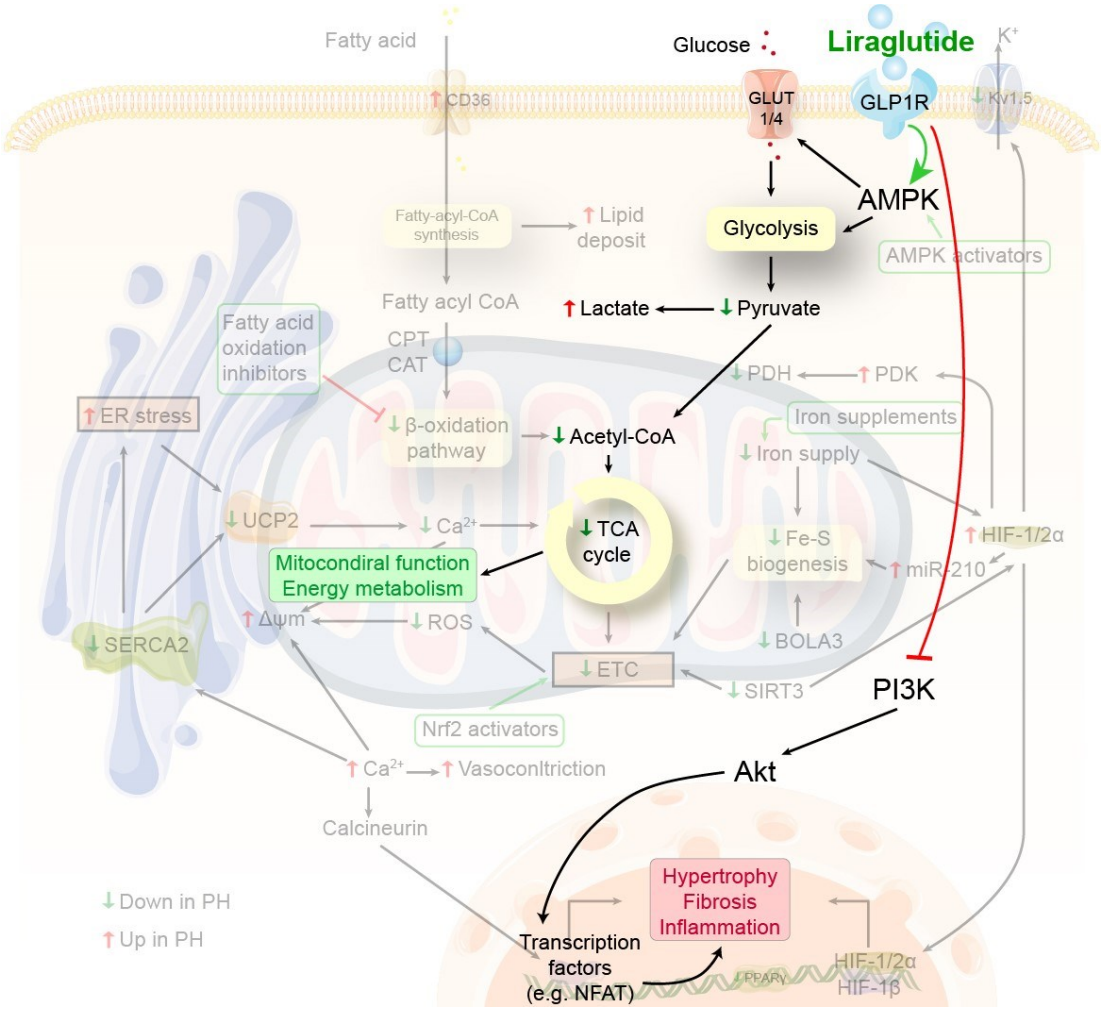

Figure 6-1 Possible mechanisms of liraglutide in the metabolic network

2. Conclusion

In this PhD thesis, I have demonstrated that GLP-1 agonist liraglutide rescues RV remodelling in PH rodent models. Liraglutide promotes the metabolic efficiency and directly improves RV performance. AMPK and PI3K-Akt are potential major molecular signalling pathways involved. This study supports the hypothesis that liraglutide is an emerging PH treatment that benefits the RV function.

3. Limitations of this PhD study

There are limitations of this study need to be noted.

- This PhD study is limited as a preclinical investigation of the effect of liraglutide on the RV in rodent PH models. My data supports the clinical investigation in the future.
- Cardiac MRI was not performed in PAB mice. The PAB experiments were conducted in collaboration with Giessen group in Germany.
- RV ^{18}F-FDG PET imaging was only performed in the MCT rats. Interpretation of the data can be impeded as the pathogenesis of MCT model is more related to inflammation.
- RV tissue from PH patients were not available for validation of the DEGs screened out by RNAseq.
- The molecular pathway analysis was limited to the AMPK and PI3K-Akt pathway.

4. Future plans

- It could be interesting to investigate the effect of liraglutide in other PH *in vivo* models, such as rodent PH caused by HFpEF (Heart failure with preserved ejection fraction).[88,350] Metabolic syndrome is a major risk factor of HFpEF. Liraglutide could modulate the energy metabolism that implemented in HFpEF and therefore could be a possible option for preclinical research.
- Efforts are needed to propose a clinical trial of liraglutide in PH patients. In this regard, collaborations with hospitals/registry centres are required to make solid progress.
- Future publications: There will be two papers deriving from this PhD study. One of them refers to the characterization of the PH rodent models (the main results are from *Chapter 3* in this thesis). The other is the preclinical evaluation of liraglutide in PH (*Chapter 3* and *4*). The two papers have been drafted and the drafts are currently being improved.

References

1. Hatano S*, et al.* Primary pulmonary hypertension: report on a WHO meeting, Geneva, 15-17 October 1973. 1975.
2. Hoeper MM*, et al.* Definitions and diagnosis of pulmonary hypertension. *J Am Coll Cardiol*. 2013;62:D42-50.
3. Lau EM*, et al.* Resting pulmonary artery pressure of 21–24 mmHg predicts abnormal exercise haemodynamics. *European Respiratory Journal*. 2016;47:1436-1444.
4. Assad TR*, et al.* Prognostic Effect and Longitudinal Hemodynamic Assessment of Borderline Pulmonary Hypertension. *JAMA Cardiol*. 2017;2:1361-1368.
5. Kovacs G*, et al.* Pulmonary arterial pressure during rest and exercise in healthy subjects: a systematic review. *European Respiratory Journal*. 2009;34:888-894.
6. Simonneau G*, et al.* Haemodynamic definitions and updated clinical classification of pulmonary hypertension. *Eur Respir J*. 2019;53.
7. van Wolferen SA*, et al.* Prognostic value of right ventricular mass, volume, and function in idiopathic pulmonary arterial hypertension. *European heart journal*. 2007;28:1250-1257.
8. Stacher E*, et al.* Modern age pathology of pulmonary arterial hypertension. *Am J Respir Crit Care Med*. 2012;186:261-72.
9. Humbert M*, et al.* Pulmonary arterial hypertension in France: results from a national registry. *American journal of respiratory and critical care medicine*. 2006;173:1023-1030.
10. Ling Y*, et al.* Changing demographics, epidemiology, and survival of incident pulmonary arterial hypertension: results from the pulmonary hypertension registry of the United Kingdom and Ireland. *American journal of respiratory and critical care medicine*. 2012;186:790-796.
11. McGoon MD*, et al.* Design of the REVEAL registry for US patients with pulmonary arterial hypertension. *Mayo Clinic Proceedings*. 2008;83:923-931.
12. Badesch DB*, et al.* Pulmonary arterial hypertension: baseline characteristics from the REVEAL Registry. *Chest*. 2010;137:376-387.
13. Mair K*, et al.* Pulmonary arterial hypertension: basis of sex differences in incidence and treatment response. *British journal of pharmacology*. 2014;171:567-579.
14. D'Alonzo GE*, et al.* Survival in patients with primary pulmonary hypertension: results from a national prospective registry. *Annals of internal medicine*. 1991;115:343-349.
15. Benza RL*, et al.* An evaluation of long-term survival from time of diagnosis in pulmonary arterial hypertension from the REVEAL Registry. *Chest*. 2012;142:448-456.
16. Vonk Noordegraaf A*, et al.* Pathophysiology of the right ventricle and of the

pulmonary circulation in pulmonary hypertension: an update. *Eur Respir J*. 2019;53.

17. Stacher E*, et al.* Modern age pathology of pulmonary arterial hypertension. *American journal of respiratory and critical care medicine*. 2012;186:261-272.
18. Tuder RM*, et al.* Expression of angiogenesis‐related molecules in plexiform lesions in severe pulmonary hypertension: evidence for a process of disordered angiogenesis. *The Journal of Pathology: A Journal of the Pathological Society of Great Britain and Ireland*. 2001;195:367-374.
19. Stenmark KR*, et al.* Hypoxia-induced pulmonary vascular remodeling: cellular and molecular mechanisms. *Circulation research*. 2006;99:675-691.
20. Zhang W*, et al.* LOX-1 mediated phenotypic switching of pulmonary arterial smooth muscle cells contributes to hypoxic pulmonary hypertension. *European journal of pharmacology*. 2018;818:84-95.
21. Owens GK*, et al.* Molecular regulation of vascular smooth muscle cell differentiation in development and disease. *Physiological reviews*. 2004;84:767-801.
22. Chazova I*, et al.* Pulmonary artery adventitial changes and venous involvement in primary pulmonary hypertension. *The American journal of pathology*. 1995;146:389.
23. Newman JH*, et al.* High-altitude pulmonary hypertension in cattle (brisket disease): candidate genes and gene expression profiling of peripheral blood mononuclear cells. *Pulmonary circulation*. 2011;1:462-469.
24. Stenmark KR*, et al.* Role of the adventitia in pulmonary vascular remodeling. *Physiology (Bethesda)*. 2006;21:134-45.
25. Stenmark KR*, et al.* Metabolic reprogramming and inflammation act in concert to control vascular remodeling in hypoxic pulmonary hypertension. *Journal of Applied Physiology*. 2015;119:1164-1172.
26. Tuder RM*, et al.* Exuberant endothelial cell growth and elements of inflammation are present in plexiform lesions of pulmonary hypertension. *The American journal of pathology*. 1994;144:275.
27. Mitani Y*, et al.* Mast cell chymase in pulmonary hypertension. *Thorax*. 1999;54:88-90.
28. Perros F*, et al.* Dendritic cell recruitment in lesions of human and experimental pulmonary hypertension. *European Respiratory Journal*. 2007;29:462-468.
29. Humbert M*, et al.* Increased interleukin-1 and interleukin-6 serum concentrations in severe primary pulmonary hypertension. *American journal of respiratory and critical care medicine*. 1995;151:1628-1631.
30. Price LC*, et al.* Inflammation in pulmonary arterial hypertension. *Chest*. 2012;141:210-221.
31. Joppa P*, et al.* Systemic inflammation in patients with COPD and pulmonary hypertension. *Chest*. 2006;130:326-333.

32. Vonk Noordegraaf A*, et al.* The Relationship Between the Right Ventricle and its Load in Pulmonary Hypertension. *J Am Coll Cardiol*. 2017;69:236-243.

33. Suga H*, et al.* Load independence of the instantaneous pressure-volume ratio of the canine left ventricle and effects of epinephrine and heart rate on the ratio. *Circulation research*. 1973;32:314-322.

34. Brimioulle S*, et al.* Single-beat estimation of right ventricular end-systolic pressure-volume relationship. *American Journal of Physiology-Heart and Circulatory Physiology*. 2003;284:H1625-H1630.

35. Spruijt OA*, et al.* The effects of exercise on right ventricular contractility and right ventricular-arterial coupling in pulmonary hypertension. *Am J Respir Crit Care Med*. 2015;191:1050-7.

36. Sunagawa K*, et al.* Optimal arterial resistance for the maximal stroke work studied in isolated canine left ventricle. *Circulation Research*. 1985;56:586-595.

37. Vanderpool RR*, et al.* RV-pulmonary arterial coupling predicts outcome in patients referred for pulmonary hypertension. *Heart*. 2015;101:37-43.

38. Alaa M*, et al.* Right ventricular end-diastolic stiffness heralds right ventricular failure in monocrotaline-induced pulmonary hypertension. *American Journal of Physiology-Heart and Circulatory Physiology*. 2016;311:H1004-H1013.

39. Hsu S. Coupling Right Ventricular–Pulmonary Arterial Research to the Pulmonary Hypertension Patient Bedside. 2019.

40. Brewis MJ*, et al.* Imaging right ventricular function to predict outcome in pulmonary arterial hypertension. *International journal of cardiology*. 2016;218:206-211.

41. Hsu S*, et al.* Right Ventricular Functional Reserve in Pulmonary Arterial Hypertension. *Circulation*. 2016;133:2413-22.

42. Tuder RM*, et al.* Development and pathology of pulmonary hypertension. *J Am Coll Cardiol*. 2009;54:S3-9.

43. Vonk-Noordegraaf A*, et al.* Right heart adaptation to pulmonary arterial hypertension: physiology and pathobiology. *J Am Coll Cardiol*. 2013;62:D22-33.

44. Sydykov A*, et al.* Inflammatory Mediators Drive Adverse Right Ventricular Remodeling and Dysfunction and Serve as Potential Biomarkers. *Frontiers in Physiology*. 2018;9:609.

45. Asosingh K and Erzurum S. Mechanisms of right heart disease in pulmonary hypertension (2017 Grover Conference Series). *Pulm Circ*. 2018;8:2045893217753121.

46. Wong YY*, et al.* Right ventricular failure in idiopathic pulmonary arterial hypertension is associated with inefficient myocardial oxygen utilization. *Circulation: Heart Failure*. 2011;4:700-706.

47. Ryan JJ*, et al.* Right ventricular adaptation and failure in pulmonary arterial hypertension. *Can J Cardiol*. 2015;31:391-406.

48. Noly P-E*, et al.* The importance of capillary density–stroke work mismatch for right

ventricular adaptation to chronic pressure overload. *The Journal of thoracic and cardiovascular surgery*. 2017;154:2070-2079.

49. McCann GP*, et al.* Extent of MRI delayed enhancement of myocardial mass is related to right ventricular dysfunction in pulmonary artery hypertension. *American Journal of Roentgenology*. 2007;188:349-355.
50. Kong P*, et al.* The pathogenesis of cardiac fibrosis. *Cellular and molecular life sciences*. 2014;71:549-574.
51. Andersen S*, et al.* Right Ventricular Fibrosis: A Pathophysiological Factor in Pulmonary Hypertension? *Circulation*. 2019;139:269-285.
52. Tonelli AR*, et al.* Pulmonary vasodilator testing and use of calcium channel blockers in pulmonary arterial hypertension. *Respiratory medicine*. 2010;104:481-496.
53. Del Pozo R*, et al.* The prostacyclin pathway in pulmonary arterial hypertension: a clinical review. *Expert review of respiratory medicine*. 2017;11:491-503.
54. Rubin LJ. Endothelin receptor antagonists for the treatment of pulmonary artery hypertension. *Life sciences*. 2012;91:517-521.
55. Lammi M*, et al.* SAT0463 Initial Therapy with an Endothelin Receptor Antagonist (ERA) is Associated with Worse Outcomes in Patients with Systemic Sclerosis and Pulmonary Arterial Hypertension: Observations from the Pulmonary Hypertension Assessment and Recognition of Outcomes in Scleroderma Cohort (Pharos). 2015.
56. Koller B*, et al.* Pilot study of endothelin receptor blockade in heart failure with diastolic dysfunction and pulmonary hypertension (BADDHY-Trial). *Heart, Lung and Circulation*. 2017;26:433-441.
57. Arora TK*, et al.* Pulmonary hypertension: Molecular aspects of current therapeutic intervention and future direction. *J Cell Physiol*. 2018;233:3794-3804.
58. Humbert M and Ghofrani HA. The molecular targets of approved treatments for pulmonary arterial hypertension. *Thorax*. 2016;71:73-83.
59. Guazzi M*, et al.* Pulmonary hypertension in heart failure with preserved ejection fraction: a target of phosphodiesterase-5 inhibition in a 1-year study. *Circulation*. 2011;124:CIRCULATIONAHA. 110.983866.
60. Redfield MM*, et al.* Effect of phosphodiesterase-5 inhibition on exercise capacity and clinical status in heart failure with preserved ejection fraction: a randomized clinical trial. *Jama*. 2013;309:1268-1277.
61. van de Veerdonk MC*, et al.* Progressive right ventricular dysfunction in patients with pulmonary arterial hypertension responding to therapy. *Journal of the American College of Cardiology*. 2011;58:2511-2519.
62. Hoeper MM*, et al.* A global view of pulmonary hypertension. *Lancet Respir Med*. 2016;4:306-22.
63. Harvey LD and Chan SY. Emerging Metabolic Therapies in Pulmonary Arterial Hypertension. *J Clin Med*. 2017;6.

64. Zamanian RT*, et al.* Insulin resistance in pulmonary arterial hypertension. *European respiratory journal*. 2009;33:318-324.

65. Piao L*, et al.* The inhibition of pyruvate dehydrogenase kinase improves impaired cardiac function and electrical remodeling in two models of right ventricular hypertrophy: resuscitating the hibernating right ventricle. *Journal of molecular medicine*. 2010;88:47-60.

66. Goncharov DA*, et al.* Mammalian target of rapamycin complex 2 (mTORC2) coordinates pulmonary artery smooth muscle cell metabolism, proliferation, and survival in pulmonary arterial hypertension. *Circulation*. 2014;129:864-874.

67. Chen C-N*, et al.* Pathobiology of Pulmonary Hypertension *Reference Module in Biomedical Sciences*: Elsevier; 2020.

68. Paulin R and Michelakis ED. The metabolic theory of pulmonary arterial hypertension. *Circ Res*. 2014;115:148-64.

69. Ahmadi A*, et al.* FDG PET imaging for identifying pulmonary hypertension and right heart failure. *Current cardiology reports*. 2015;17:555.

70. Liberti MV and Locasale JW. The Warburg effect: how does it benefit cancer cells? *Trends in biochemical sciences*. 2016;41:211-218.

71. Gomez-Arroyo J*, et al.* Metabolic gene remodeling and mitochondrial dysfunction in failing right ventricular hypertrophy due to pulmonary arterial hypertension. *Circulation: Heart Failure*. 2012:CIRCHEARTFAILURE. 111.966127.

72. Fessel JP*, et al.* Metabolomic analysis of bone morphogenetic protein receptor type 2 mutations in human pulmonary endothelium reveals widespread metabolic reprogramming. *Pulmonary circulation*. 2012;2:201-213.

73. Fijalkowska I*, et al.* Hypoxia inducible-factor1α regulates the metabolic shift of pulmonary hypertensive endothelial cells. *The American journal of pathology*. 2010;176:1130-1138.

74. Shimoda LA and Semenza GL. HIF and the lung: role of hypoxia-inducible factors in pulmonary development and disease. *American journal of respiratory and critical care medicine*. 2011;183:152-156.

75. Bonnet S*, et al.* An abnormal mitochondrial–hypoxia inducible factor-1α–Kv channel pathway disrupts oxygen sensing and triggers pulmonary arterial hypertension in fawn hooded rats: similarities to human pulmonary arterial hypertension. *Circulation*. 2006;113:2630-2641.

76. Kim J-w*, et al.* HIF-1-mediated expression of pyruvate dehydrogenase kinase: a metabolic switch required for cellular adaptation to hypoxia. *Cell Metab*. 2006;3:177-185.

77. McMurtry MS*, et al.* Dichloroacetate prevents and reverses pulmonary hypertension by inducing pulmonary artery smooth muscle cell apoptosis. *Circulation research*. 2004;95:830-840.

78. Stacpoole PW*, et al.* Efficacy of Dichloroacetate as a Lactate-Lowering Drug. *The Journal of Clinical Pharmacology*. 2003;43:683-691.

79. Michelakis E*, et al.* Metabolic modulation of glioblastoma with dichloroacetate. *Science translational medicine*. 2010;2:31ra34-31ra34.

80. Marsboom G*, et al.* Lung 18F-fluorodeoxyglucose positron emission tomography for diagnosis and monitoring of pulmonary arterial hypertension. *American journal of respiratory and critical care medicine*. 2012;185:670-679.

81. Zhao L*, et al.* Heterogeneity in lung (18)FDG uptake in pulmonary arterial hypertension: potential of dynamic (18)FDG positron emission tomography with kinetic analysis as a bridging biomarker for pulmonary vascular remodeling targeted treatments. *Circulation*. 2013;128:1214-24.

82. Michelakis ED*, et al.* Inhibition of pyruvate dehydrogenase kinase improves pulmonary arterial hypertension in genetically susceptible patients. *Sci Transl Med*. 2017;9.

83. Noordali H*, et al.* Cardiac metabolism—A promising therapeutic target for heart failure. *Pharmacology & therapeutics*. 2017;182:95-114.

84. Fang Y-H*, et al.* Therapeutic inhibition of fatty acid oxidation in right ventricular hypertrophy: exploiting Randle's cycle. *Journal of molecular medicine*. 2012;90:31-43.

85. Khan SS*, et al.* Effects of ranolazine on exercise capacity, right ventricular indices, and hemodynamic characteristics in pulmonary arterial hypertension: a pilot study. *Pulmonary circulation*. 2015;5:547-556.

86. Han Y*, et al.* Ranolazine and Right Ventricular Function in Patients with Pulmonary Hypertension *D108 GOOD VIBRATIONS: NOVEL TREATMENT APPROACHES IN PULMONARY HYPERTENSION*: American Thoracic Society; 2018: A7583-A7583.

87. Moral‐Sanz J*, et al.* AMP‐activated protein kinase inhibits Kv1. 5 channel currents of pulmonary arterial myocytes in response to hypoxia and inhibition of mitochondrial oxidative phosphorylation. *The Journal of physiology*. 2016;594:4901-4915.

88. Lai Y-C*, et al.* SIRT3–AMP-Activated Protein Kinase Activation by Nitrite and Metformin Improves Hyperglycemia and Normalizes Pulmonary Hypertension Associated With Heart Failure With Preserved Ejection FractionCLINICAL PERSPECTIVE. *Circulation*. 2016;133:717-731.

89. Agard C*, et al.* Protective role of the antidiabetic drug metformin against chronic experimental pulmonary hypertension. *British journal of pharmacology*. 2009;158:1285-1294.

90. Lill R. Function and biogenesis of iron–sulphur proteins. *Nature*. 2009;460:831.

91. Rhodes CJ*, et al.* Iron deficiency in pulmonary arterial hypertension: a potential therapeutic target. *European Respiratory Journal*. 2011;38:1453-1460.

92. Cotroneo E*, et al.* Iron Homeostasis and Pulmonary HypertensionNovelty and Significance: Iron Deficiency Leads to Pulmonary Vascular Remodeling in the Rat. *Circulation research*. 2015;116:1680-1690.

93. Frise MC*, et al.* Clinical iron deficiency disturbs normal human responses to

hypoxia. *The Journal of clinical investigation*. 2016;126:2139-2150.

94. Ruiter G*, et al.* Intravenous iron therapy in patients with idiopathic pulmonary arterial hypertension and iron deficiency. *Pulmonary circulation*. 2015;5:466-472.
95. Chan SY and Loscalzo J. MicroRNA-210: a unique and pleiotropic hypoxamir. *Cell cycle*. 2010;9:1072-1083.
96. White K*, et al.* Genetic and hypoxic alterations of the microRNA‐210‐ISCU1/2 axis promote iron–sulfur deficiency and pulmonary hypertension. *EMBO molecular medicine*. 2015;7:695-713.
97. Marsboom G*, et al.* Dynamin-related protein 1–mediated mitochondrial mitotic fission permits hyperproliferation of vascular smooth muscle cells and offers a novel therapeutic target in pulmonary hypertensionnovelty and significance. *Circulation research*. 2012;110:1484-1497.
98. Chen K-H*, et al.* Epigenetic Dysregulation of the Drp1 Binding Partners MiD49 and MiD51 Increases Mitotic Mitochondrial Fission and Promotes Pulmonary Arterial Hypertension: Mechanistic and Therapeutic Implications. *Circulation*. 2018:CIRCULATIONAHA. 117.031258.
99. Dinkova-Kostova AT and Abramov AY. The emerging role of Nrf2 in mitochondrial function. *Free Radical Biology and Medicine*. 2015;88:179-188.
100. Eba S*, et al.* The Nuclear Factor Erythroid 2–Related Factor 2 Activator Oltipraz Attenuates Chronic Hypoxia–Induced Cardiopulmonary Alterations in Mice. *American journal of respiratory cell and molecular biology*. 2013;49:324-333.
101. Baggio LL*, et al.* GLP-1 Receptor Expression Within the Human Heart. *Endocrinology*. 2018;159:1570-1584.
102. Kim M*, et al.* GLP-1 receptor activation and Epac2 link atrial natriuretic peptide secretion to control of blood pressure. *Nature medicine*. 2013;19:567.
103. Muscogiuri G*, et al.* Glucagon-like peptide-1 and the central/peripheral nervous system: crosstalk in diabetes. *Trends in Endocrinology & Metabolism*. 2017;28:88-103.
104. Siraj MA*, et al.* Cardioprotective GLP-1 metabolite prevents ischemic cardiac injury by inhibiting mitochondrial trifunctional protein-α. *Journal of Clinical Investigation*. 2020;130:10.1172/JCI99934.
105. Nauck M. Incretin therapies: highlighting common features and differences in the modes of action of glucagon‐like peptide‐1 receptor agonists and dipeptidyl peptidase‐4 inhibitors. *Diabetes, Obesity and Metabolism*. 2016;18:203-216.
106. Christou GA*, et al.* Semaglutide as a promising antiobesity drug. *Obesity Reviews*. 2019;20:805-815.
107. Aroda VR. A review of GLP‐1 receptor agonists: evolution and advancement, through the lens of randomised controlled trials. *Diabetes, Obesity and Metabolism*. 2018;20:22-33.
108. Wang C*, et al.* GLP-1 receptor agonist ameliorates obesity-induced chronic kidney injury via restoring renal metabolism homeostasis. *PloS one*. 2018;13:e0193473.

109. Li Y-K*, et al.* The glucagon-like peptide-1 (GLP-1) analog liraglutide attenuates renal fibrosis. *Pharmacological research*. 2018;131:102-111.

110. Barreto-Vianna AR*, et al.* Beneficial effects of liraglutide (GLP1 analog) in the hippocampal inflammation. *Metabolic brain disease*. 2017;32:1735-1745.

111. Poornima I*, et al.* Chronic glucagon-like peptide-1 infusion sustains left ventricular systolic function and prolongs survival in the spontaneously hypertensive, heart failure–prone rat. *Circulation: Heart Failure*. 2008;1:153-160.

112. Liu Q*, et al.* Glucagon-like peptide-1 and the exenatide analogue AC3174 improve cardiac function, cardiac remodeling, and survival in rats with chronic heart failure. *Cardiovascular diabetology*. 2010;9:76.

113. Noyan-Ashraf MH*, et al.* A glucagon-like peptide-1 analog reverses the molecular pathology and cardiac dysfunction of a mouse model of obesity. *Circulation*. 2013;127:74-85.

114. Zheng R-H*, et al.* Liraglutide attenuates cardiac remodeling and improves heart function after abdominal aortic constriction through blocking angiotensin II type 1 receptor in rats. *Drug design, development and therapy*. 2019;13:2745.

115. Wang F*, et al.* Glp-1 analog, liraglutide protects against Angiotensin II and pressure overload induced cardiac hypertrophy via PI3K/Akt1 and AMPKa signaling. *Frontiers in pharmacology*. 2019;10:537.

116. Marso SP*, et al.* Liraglutide and Cardiovascular Outcomes in Type 2 Diabetes. *N Engl J Med*. 2016;375:311-22.

117. Marso SP*, et al.* Semaglutide and cardiovascular outcomes in patients with type 2 diabetes. *N Engl J Med*. 2016;375:1834-1844.

118. Marso SP*, et al.* Effects of Liraglutide on Cardiovascular Outcomes in Patients With Diabetes With or Without Heart Failure. *J Am Coll Cardiol*. 2020;75:1128-1141.

119. Pfeffer MA*, et al.* Lixisenatide in patients with type 2 diabetes and acute coronary syndrome. *New England Journal of Medicine*. 2015;373:2247-2257.

120. Verges B and Charbonnel B. After the LEADER trial and SUSTAIN-6, how do we explain the cardiovascular benefits of some GLP-1 receptor agonists? *Diabetes & metabolism*. 2017;43:2S3-2S12.

121. Nielsen R*, et al.* Metabolic effects of short-term GLP-1 treatment in insulin resistant heart failure patients. *Experimental and clinical endocrinology & diabetes*. 2012;120:266-272.

122. Halbirk M*, et al.* Cardiovascular and metabolic effects of 48-h glucagon-like peptide-1 infusion in compensated chronic patients with heart failure. *American Journal of Physiology-Heart and Circulatory Physiology*. 2010;298:H1096-H1102.

123. Nikolaidis LA*, et al.* Effects of glucagon-like peptide-1 in patients with acute myocardial infarction and left ventricular dysfunction after successful reperfusion. *Circulation*. 2004;109:962-965.

124. Munaf M*, et al.* A meta-analysis of the therapeutic effects of glucagon-like peptide-1 agonist in heart failure. *International journal of peptides*.

2012;2012:249827.

125. Arturi F*, et al.* Liraglutide improves cardiac function in patients with type 2 diabetes and chronic heart failure. *Endocrine*. 2017;57:464-473.

126. Chen W-R*, et al.* Effects of liraglutide on left ventricular function in patients with non-ST-segment elevation myocardial infarction. *Endocrine*. 2016;52:516-526.

127. Chen WR*, et al.* Effects of liraglutide on left ventricular function in patients with ST-segment elevation myocardial infarction undergoing primary percutaneous coronary intervention. *American heart journal*. 2015;170:845-854.

128. Bizino MB*, et al.* Effect of liraglutide on cardiac function in patients with type 2 diabetes mellitus: randomized placebo-controlled trial. *Cardiovascular diabetology*. 2019;18:55.

129. Jorsal A*, et al.* Effect of liraglutide, a glucagon-like peptide-1 analogue, on left ventricular function in stable chronic heart failure patients with and without diabetes (LIVE)-a multicentre, double-blind, randomised, placebo-controlled trial. *European journal of heart failure*. 2017;19:69-77.

130. Margulies KB*, et al.* Effects of Liraglutide on Clinical Stability Among Patients With Advanced Heart Failure and Reduced Ejection Fraction: A Randomized Clinical Trial. *JAMA*. 2016;316:500-8.

131. Kumarathurai P*, et al.* Effects of the glucagon-like peptide-1 receptor agonist liraglutide on systolic function in patients with coronary artery disease and type 2 diabetes: a randomized double-blind placebo-controlled crossover study. *Cardiovascular diabetology*. 2016;15:105.

132. Wang J*, et al.* Glucagon-like peptide-1 (GLP-1) mediates the protective effects of dipeptidyl peptidase IV inhibition on pulmonary hypertension. *Journal of biomedical science*. 2019;26:6.

133. Honda J*, et al.* The glucagon-like peptide-1 receptor agonist liraglutide improves hypoxia-induced pulmonary hypertension in mice partly via normalization of reduced ET(B) receptor expression. *Physiol Res*. 2018;67:S175-S184.

134. Lee MY*, et al.* Liraglutide prevents and reverses monocrotaline-induced pulmonary arterial hypertension by suppressing ET-1 and enhancing eNOS/sGC/PKG pathways. *Sci Rep*. 2016;6:31788.

135. Wu Y-C*, et al.* Glucagon-Like Peptide-1 Receptor Agonist Attenuates Autophagy to Ameliorate Pulmonary Arterial Hypertension through Drp1/NOX- and Atg-5/Atg-7/Beclin-1/LC3β Pathways. *International Journal of Molecular Sciences*. 2019;20.

136. Wang L. FDG-PET imaging of pulmonary vascular remodelling in PAH. 2016.

137. Konstam MA*, et al.* Evaluation and Management of Right-Sided Heart Failure: A Scientific Statement From the American Heart Association. *Circulation*. 2018;137:e578-e622.

138. Swift AJ*, et al.* Magnetic Resonance Imaging in the Prognostic Evaluation of Patients with Pulmonary Arterial Hypertension. *Am J Respir Crit Care Med*. 2017;196:228-239.

139. Kilner PJ*, et al.* Recommendations for cardiovascular magnetic resonance in adults with congenital heart disease from the respective working groups of the European Society of Cardiology. *European heart journal*. 2010;31:794-805.

140. Lewis RA*, et al.* Identification of Cardiac Magnetic Resonance Imaging Thresholds for Risk Stratification in Pulmonary Arterial Hypertension. *American Journal of Respiratory and Critical Care Medicine*. 2020;201:458-468.

141. Lewis AJ*, et al.* Non-Invasive Immuno-Metabolic Cardiac Inflammation Imaging Using Hyperpolarized Magnetic Resonance. *Circ Res*. 2018;122:1084-1093.

142. Saba T*, et al.* Ventricular mass index using magnetic resonance imaging accurately estimates pulmonary artery pressure. *European Respiratory Journal*. 2002;20:1519-1524.

143. Simpson CE*, et al.* Ventricular mass as a prognostic imaging biomarker in incident pulmonary arterial hypertension. *Eur Respir J*. 2019;53.

144. van de Veerdonk MC*, et al.* Signs of right ventricular deterioration in clinically stable patients with pulmonary arterial hypertension. *Chest*. 2015;147:1063-1071.

145. Pinsky MR. The right ventricle: interaction with the pulmonary circulation. *Critical Care*. 2016;20:266.

146. Truong U*, et al.* Non-invasive determination by cardiovascular magnetic resonance of right ventricular-vascular coupling in children and adolescents with pulmonary hypertension. *Journal of Cardiovascular Magnetic Resonance*. 2015;17:81.

147. Reiter U*, et al.* MR phase-contrast imaging in pulmonary hypertension. *The British journal of radiology*. 2016;89:20150995.

148. Sanz J*, et al.* Pulmonary arterial hypertension: noninvasive detection with phase-contrast MR imaging. *Radiology*. 2007;243:70-79.

149. Tossavainen E*, et al.* Pulmonary artery acceleration time in identifying pulmonary hypertension patients with raised pulmonary vascular resistance. *Eur Heart J Cardiovasc Imaging*. 2013;14:890-7.

150. Sanz J*, et al.* Evaluation of pulmonary artery stiffness in pulmonary hypertension with cardiac magnetic resonance. *JACC: Cardiovascular Imaging*. 2009;2:286-295.

151. Quail MA*, et al.* Noninvasive pulmonary artery wave intensity analysis in pulmonary hypertension. *American Journal of Physiology-Heart and Circulatory Physiology*. 2015;308:H1603-H1611.

152. Reiter G*, et al.* Blood flow vortices along the main pulmonary artery measured with MR imaging for diagnosis of pulmonary hypertension. *Radiology*. 2015;275:71-79.

153. Swift AJ RS, Capener D, Elliot C, Condliffe R, Wild JM, Kiely DG. LGE patterns in pulmonary hypertension do not impact overall mortality. *JACC Cardiovasc Imaging*. 2014:1209-17.

154. Freed BH*, et al.* Late gadolinium enhancement cardiovascular magnetic resonance predicts clinical worsening in patients with pulmonary hypertension. *Journal of*

Cardiovascular Magnetic Resonance. 2012;14:11.

155. Sato T*, et al.* Paradoxical interventricular septal motion as a major determinant of late gadolinium enhancement in ventricular insertion points in pulmonary hypertension. *PLoS One*. 2013;8.
156. Shehata ML*, et al.* Myocardial delayed enhancement in pulmonary hypertension: pulmonary hemodynamics, right ventricular function, and remodeling. *American Journal of Roentgenology*. 2011;196:87-94.
157. Grigoratos C*, et al.* Clinical importance of late gadolinium enhancement at right ventricular insertion points in otherwise normal hearts. *The International Journal of Cardiovascular Imaging*. 2020;36:913-920.
158. Roller FC*, et al.* Native T1 mapping and extracellular volume fraction measurement for assessment of right ventricular insertion point and septal fibrosis in chronic thromboembolic pulmonary hypertension. *European radiology*. 2017;27:1980-1991.
159. Haaf P*, et al.* Cardiac T1 Mapping and Extracellular Volume (ECV) in clinical practice: a comprehensive review. *J Cardiovasc Magn Reson*. 2016;18:89.
160. Reiter U*, et al.* Native myocardial T1 mapping in pulmonary hypertension: correlations with cardiac function and hemodynamics. *Eur Radiol*. 2017;27:157-166.
161. Saunders LC*, et al.* Diagnostic and prognostic significance of cardiovascular magnetic resonance native myocardial T1 mapping in patients with pulmonary hypertension. *Journal of Cardiovascular Magnetic Resonance*. 2018;20:78.
162. Habert P*, et al.* Quantification of right ventricular extracellular volume in pulmonary hypertension using cardiac magnetic resonance imaging. *Diagnostic and Interventional Imaging*. 2020.
163. Ghio S*, et al.* Prognostic relevance of the echocardiographic assessment of right ventricular function in patients with idiopathic pulmonary arterial hypertension. *International journal of cardiology*. 2010;140:272-278.
164. Gopalan D. Right heart on multidetector CT. *The British journal of radiology*. 2011;84:S306-S323.
165. Sugeng L*, et al.* Multimodality comparison of quantitative volumetric analysis of the right ventricle. *JACC: Cardiovascular Imaging*. 2010;3:10-18.
166. Fang W*, et al.* Comparison of 18F-FDG uptake by right ventricular myocardium in idiopathic pulmonary arterial hypertension and pulmonary arterial hypertension associated with congenital heart disease. *Pulmonary circulation*. 2012;2:365-372.
167. Kluge R*, et al.* Different mechanisms for changes in glucose uptake of the right and left ventricular myocardium in pulmonary hypertension. *Journal of Nuclear Medicine*. 2005;46:25-31.
168. Wang L*, et al.* Evaluation of right ventricular volume and ejection fraction by gated 18F-FDG PET in patients with pulmonary hypertension: Comparison with cardiac MRI and CT. *Journal of Nuclear Cardiology*. 2013;20:242-252.

169. Zhao L*, et al.* Heterogeneity in lung 18FDG uptake in pulmonary arterial hypertension: potential of dynamic 18FDG positron emission tomography with kinetic analysis as a bridging biomarker for pulmonary vascular remodeling targeted treatments. *Circulation*. 2013;128:1214-1224.

170. Wang L*, et al.* Right ventricular dyssynchrony in pulmonary hypertension: Phase analysis using FDG-PET imaging. *Journal of Nuclear Cardiology*. 2017;24:69-78.

171. Ohira H*, et al.* Myocardial fatty acid and glucose metabolism in patients with pulmonary arterial hypertension. *Journal of Nuclear Medicine*. 2014;55:130-130.

172. Stenmark KR*, et al.* Animal models of pulmonary arterial hypertension: the hope for etiological discovery and pharmacological cure. *Am J Physiol Lung Cell Mol Physiol*. 2009;297:L1013-32.

173. Colvin KL and Yeager ME. Animal Models of Pulmonary Hypertension: Matching Disease Mechanisms to Etiology of the Human Disease. *J Pulm Respir Med*. 2014;4.

174. Sztuka K and Jasinska-Stroschein M. Animal models of pulmonary arterial hypertension: A systematic review and meta-analysis of data from 6126 animals. *Pharmacol Res*. 2017;125:201-214.

175. Liu X*, et al.* Secretory clusterin is upregulated in rats with pulmonary arterial hypertension induced by systemic-to-pulmonary shunts and exerts important roles in pulmonary artery smooth muscle cells. *Acta Physiologica*. 2015;213:505-518.

176. Kay JM. Crotalaria (Monocrotaline) Pulmonary Hypertension: The Fiftieth Anniversary. *Chest*. 2017;152:1117-1119.

177. Gomez-Arroyo JG*, et al.* The monocrotaline model of pulmonary hypertension in perspective. *American Journal of Physiology-Lung Cellular and Molecular Physiology*. 2012;302:L363-L369.

178. Hessel MH*, et al.* Characterization of right ventricular function after monocrotaline-induced pulmonary hypertension in the intact rat. *Am J Physiol Heart Circ Physiol*. 2006;291:H2424-30.

179. Akhavein F*, et al.* Decreased left ventricular function, myocarditis, and coronary arteriolar medial thickening following monocrotaline administration in adult rats. *Journal of applied physiology (Bethesda, Md : 1985)*. 2007;103:287-95.

180. Taraseviciene-Stewart L*, et al.* Inhibition of the VEGF receptor 2 combined with chronic hypoxia causes cell death-dependent pulmonary endothelial cell proliferation and severe pulmonary hypertension. *The FASEB Journal*. 2001;15:427-438.

181. Abe K*, et al.* Formation of plexiform lesions in experimental severe pulmonary arterial hypertension. *Circulation*. 2010;121:2747-54.

182. Bogaard HJ*, et al.* Chronic pulmonary artery pressure elevation is insufficient to explain right heart failure. *Circulation*. 2009;120:1951-60.

183. Bogaard HJ*, et al.* Adrenergic receptor blockade reverses right heart remodeling and dysfunction in pulmonary hypertensive rats. *Am J Respir Crit Care Med*.

2010;182:652-60.

184. de Raaf MA*, et al.* SuHx rat model: partly reversible pulmonary hypertension and progressive intima obstruction. *Eur Respir J*. 2014;44:160-8.

185. Jiang B*, et al.* Marked strain-specific differences in the SU5416 rat model of severe pulmonary arterial hypertension. *American journal of respiratory cell and molecular biology*. 2016;54:461-468.

186. Vitali SH*, et al.* The Sugen 5416/hypoxia mouse model of pulmonary hypertension revisited: long-term follow-up. *Pulmonary circulation*. 2014;4:619-629.

187. Hirata M*, et al.* Novel model of pulmonary artery banding leading to right heart failure in rats. *BioMed research international*. 2015;2015:753210.

188. Andersen S*, et al.* A Pulmonary Trunk Banding Model of Pressure Overload Induced Right Ventricular Hypertrophy and Failure. *J Vis Exp*. 2018.

189. Dean A*, et al.* OpenEpi: open source epidemiologic statistics for public health, version. 2014.

190. Nair AB and Jacob S. A simple practice guide for dose conversion between animals and human. *J Basic Clin Pharm*. 2016;7:27-31.

191. Schulz-Menger J*, et al.* Standardized image interpretation and post processing in cardiovascular magnetic resonance: Society for Cardiovascular Magnetic Resonance (SCMR) board of trustees task force on standardized post processing. *J Cardiovasc Magn Reson*. 2013;15:35.

192. Heiberg E*, et al.* Design and validation of Segment-freely available software for cardiovascular image analysis. *BMC medical imaging*. 2010;10:1.

193. Cerqueira MD*, et al.* Standardized myocardial segmentation and nomenclature for tomographic imaging of the heart: a statement for healthcare professionals from the Cardiac Imaging Committee of the Council on Clinical Cardiology of the American Heart Association. *Journal of the American Society of Echocardiography*. 2002;15:463-467.

194. Gouma E*, et al.* A simple procedure for estimation of total body surface area and determination of a new value of Meeh's constant in rats. *Lab Anim*. 2012;46:40-5.

195. Nayak KS*, et al.* Cardiovascular magnetic resonance phase contrast imaging. *J Cardiovasc Magn Reson*. 2015;17:71.

196. Taylor AJ*, et al.* T1 Mapping: Basic Techniques and Clinical Applications. *JACC Cardiovasc Imaging*. 2016;9:67-81.

197. Kammerlander AA*, et al.* T1 mapping by CMR imaging: from histological validation to clinical implication. *JACC: Cardiovascular Imaging*. 2016;9:14-23.

198. Ashek A*, et al.* 3′-deoxy-3′-[18F] fluorothymidine positron emission tomography depicts heterogeneous proliferation pathology in idiopathic pulmonary arterial hypertension patient lung: a potential biomarker for pulmonary arterial hypertension. *Circulation: Cardiovascular Imaging*. 2018;11:e007402.

199. Cheebsumon P*, et al.* Measuring response to therapy using FDG PET: semi-quantitative and full kinetic analysis. *European journal of nuclear medicine and molecular imaging*. 2011;38:832-842.

200. Stark R*, et al.* RNA sequencing: the teenage years. *Nat Rev Genet*. 2019;20:631-656.

201. Patro R*, et al.* Salmon provides fast and bias-aware quantification of transcript expression. *Nature methods*. 2017;14:417.

202. Love MI*, et al.* Moderated estimation of fold change and dispersion for RNA-seq data with DESeq2. *Genome biology*. 2014;15:550.

203. Yu G*, et al.* clusterProfiler: an R package for comparing biological themes among gene clusters. *Omics: a journal of integrative biology*. 2012;16:284-287.

204. Lahm T*, et al.* Assessment of Right Ventricular Function in the Research Setting: Knowledge Gaps and Pathways Forward. An Official American Thoracic Society Research Statement. *Am J Respir Crit Care Med*. 2018;198:e15-e43.

205. Nielsen EA*, et al.* Regional septal hinge‐point injury contributes to adverse biventricular interactions in pulmonary hypertension. *Physiological reports*. 2017;5:e13332.

206. Toba M*, et al.* Temporal hemodynamic and histological progression in Sugen5416/hypoxia/normoxia-exposed pulmonary arterial hypertensive rats. *Am J Physiol Heart Circ Physiol*. 2014;306:H243-50.

207. Urboniene D*, et al.* Validation of high-resolution echocardiography and magnetic resonance imaging vs. high-fidelity catheterization in experimental pulmonary hypertension. *Am J Physiol Lung Cell Mol Physiol*. 2010;299:L401-12.

208. Van Den Borne SW*, et al.* Myocardial remodeling after infarction: the role of myofibroblasts. *Nature Reviews Cardiology*. 2010;7:30.

209. Bradlow WM*, et al.* Understanding late gadolinium enhancement in pulmonary hypertension. *Circulation: Cardiovascular Imaging*. 2010;3:501-503.

210. Nelson GS*, et al.* Compression of interventricular septum during right ventricular pressure loading. *American Journal of Physiology-Heart and Circulatory Physiology*. 2001;280:H2639-H2648.

211. Freed BH*, et al.* The role of late gadolinium enhancement of the right ventricular insertion point predicts survival in patients with pulmonary hypertension. *Journal of Cardiovascular Magnetic Resonance*. 2011;13.

212. Sutendra G*, et al.* A metabolic remodeling in right ventricular hypertrophy is associated with decreased angiogenesis and a transition from a compensated to a decompensated state in pulmonary hypertension. *Journal of molecular medicine*. 2013;91:1315-1327.

213. Gómez A*, et al.* Right ventricular ischemia in patients with primary pulmonary hypertension. *Journal of the American College of Cardiology*. 2001;38:1137-1142.

214. Gavin JB*, et al.* Microvascular involvement in cardiac pathology. *Journal of molecular and cellular cardiology*. 1998;30:2531-2540.

215. De Boer RA*, et al.* The imbalance between oxygen demand and supply as a potential mechanism in the pathophysiology of heart failure: the role of microvascular growth and abnormalities. *Microcirculation*. 2003;10:113-126.

216. Liao Y*, et al.* Exacerbation of heart failure in adiponectin-deficient mice due to impaired regulation of AMPK and glucose metabolism. *Cardiovascular research*. 2005;67:705-713.

217. Gélinas R*, et al.* AMPK activation counteracts cardiac hypertrophy by reducing O-GlcNAcylation. *Nature communications*. 2018;9:1-17.

218. Xu L and Brink M. mTOR, cardiomyocytes and inflammation in cardiac hypertrophy. *Biochimica et Biophysica Acta (BBA)-Molecular Cell Research*. 2016;1863:1894-1903.

219. Marchi S*, et al.* Mitochondrial and endoplasmic reticulum calcium homeostasis and cell death. *Cell Calcium*. 2018;69:62-72.

220. Hadri L*, et al.* Therapeutic efficacy of AAV1.SERCA2a in monocrotaline-induced pulmonary arterial hypertension. *Circulation*. 2013;128:512-23.

221. Williams AL*, et al.* HIF-1 regulation of miR-29c impairs SERCA2 expression and cardiac contractility. *American Journal of Physiology-Heart and Circulatory Physiology*. 2019;316:H554-H565.

222. Toya T*, et al.* Impact of oxidative posttranslational modifications of SERCA2 on heart failure exacerbation in young patients with non-ischemic cardiomyopathy: A pilot study. *IJC Heart & Vasculature*. 2020;26:100437.

223. Zungu-Edmondson M*, et al.* Modulators of right ventricular apoptosis and contractility in a rat model of pulmonary hypertension. *Cardiovasc Res*. 2016;110:30-9.

224. Li R*, et al.* The Glp-1 Analog Liraglutide Protects Against Angiotensin II and Pressure Overload-Induced Cardiac Hypertrophy via PI3K/Akt1 and AMPKa Signaling. *Front Pharmacol*. 2019;10:537.

225. Romani-Perez M*, et al.* Activation of the GLP-1 Receptor by Liraglutide Increases ACE2 Expression, Reversing Right Ventricle Hypertrophy, and Improving the Production of SP-A and SP-B in the Lungs of Type 1 Diabetes Rats. *Endocrinology*. 2015;156:3559-69.

226. Sanz J*, et al.* Anatomy, Function, and Dysfunction of the Right Ventricle: JACC State-of-the-Art Review. *J Am Coll Cardiol*. 2019;73:1463-1482.

227. Ryan JJ and Archer SL. Emerging concepts in the molecular basis of pulmonary arterial hypertension: part I: metabolic plasticity and mitochondrial dynamics in the pulmonary circulation and right ventricle in pulmonary arterial hypertension. *Circulation*. 2015;131:1691-702.

228. Yang T*, et al.* The ratio of (18)F-FDG activity uptake between the right and left ventricle in patients with pulmonary hypertension correlates with the right ventricular function. *Clin Nucl Med*. 2014;39:426-30.

229. Fang W*, et al.* Comparison of 18F-FDG uptake by right ventricular myocardium in

idiopathic pulmonary arterial hypertension and pulmonary arterial hypertension associated with congenital heart disease. *Pulm Circ*. 2012;2:365-72.

230. Kluge R*, et al.* Different mechanisms for changes in glucose uptake of the right and left ventricular myocardium in pulmonary hypertension. *J Nucl Med*. 2005;46:25-31.

231. Koop AMC*, et al.* Metabolic Remodeling in the Pressure-Loaded Right Ventricle: Shifts in Glucose and Fatty Acid Metabolism—A Systematic Review and Meta-Analysis. *Journal of the American Heart Association*. 2019;8:e012086.

232. Suliman HB and Nozik-Grayck E. Mitochondrial dysfunction: metabolic drivers of pulmonary hypertension. *Antioxidants & redox signaling*. 2019;31:843-857.

233. Kutsche HS*, et al.* Alterations in Glucose Metabolism During the Transition to Heart Failure: The Contribution of UCP-2. *Cells*. 2020;9:552.

234. Mielniczuk LM*, et al.* Relation between right ventricular function and increased right ventricular [18F] fluorodeoxyglucose accumulation in patients with heart failure. *Circulation: Cardiovascular Imaging*. 2011;4:59-66.

235. Zhao T*, et al.* Liraglutide protects high-glucose-stimulated fibroblasts by activating the CD36-JNK-AP1 pathway to downregulate P4HA1. *Biomed Pharmacother*. 2019;118:109224.

236. Zhao T*, et al.* Liraglutide alleviates cardiac fibrosis through inhibiting P4hα-1 expression in STZ-induced diabetic cardiomyopathy. *Acta biochimica et biophysica Sinica*. 2019;51:293-300.

237. Huang D*, et al.* Liraglutide improves myocardial fibrosis after myocardial infarction through inhibition of CTGF by activating cAMP in mice. *Eur Rev Med Pharmacol Sci*. 2018;22:4648-4656.

238. Love KM*, et al.* GLP-1 and Insulin Regulation of Skeletal and Cardiac Muscle Microvascular Perfusion in Type 2 Diabetes. *J Diabetes*. 2020;12:488-498.

239. Helmstädter J*, et al.* Endothelial GLP-1 (Glucagon-Like Peptide-1) Receptor Mediates Cardiovascular Protection by Liraglutide In Mice With Experimental Arterial Hypertension. *Arteriosclerosis, thrombosis, and vascular biology*. 2020;40:145-158.

240. Zhou Y*, et al.* Exendin-4 attenuates cardiac hypertrophy via AMPK/mTOR signaling pathway activation. *Biochemical and biophysical research communications*. 2015;468:394-399.

241. Clarke SJ*, et al.* GLP-1 Is a Coronary Artery Vasodilator in Humans. *Journal of the American Heart Association*. 2018;7:e010321.

242. Dokken BB*, et al.* Glucagon-like peptide-1 (GLP-1) attenuates post-resuscitation myocardial microcirculatory dysfunction. *Resuscitation*. 2010;81:755-760.

243. Sukumaran V*, et al.* Liraglutide treatment improves the coronary microcirculation in insulin resistant Zucker obese rats on a high salt diet. *Cardiovascular Diabetology*. 2020;19:1-16.

244. Zhang L-H*, et al.* Preservation of glucagon-like peptide-1 level attenuates

angiotensin II-induced tissue fibrosis by altering AT 1/AT 2 receptor expression and angiotensin-converting enzyme 2 activity in rat heart. *Cardiovascular drugs and therapy*. 2015;29:243-255.

245. Xu J*, et al.* GDF15/MIC-1 functions as a protective and antihypertrophic factor released from the myocardium in association with SMAD protein activation. *Circulation research*. 2006;98:342-350.

246. Kempf T*, et al.* Prognostic utility of growth differentiation factor-15 in patients with chronic heart failure. *Journal of the American College of Cardiology*. 2007;50:1054-1060.

247. Nickel N*, et al.* GDF-15 is abundantly expressed in plexiform lesions in patients with pulmonary arterial hypertension and affects proliferation and apoptosis of pulmonary endothelial cells. *Respiratory research*. 2011;12:62.

248. Emmerson PJ*, et al.* The metabolic effects of GDF15 are mediated by the orphan receptor GFRAL. *Nature medicine*. 2017;23:1215.

249. Adela R and Banerjee SK. GDF-15 as a target and biomarker for diabetes and cardiovascular diseases: a translational prospective. *Journal of diabetes research*. 2015;2015.

250. Mana G*, et al.* PPFIA1 drives active α5β1 integrin recycling and controls fibronectin fibrillogenesis and vascular morphogenesis. *Nature communications*. 2016;7:1-20.

251. Christie JD*, et al.* Genome wide association identifies PPFIA1 as a candidate gene for acute lung injury risk following major trauma. *PLoS One*. 2012;7:e28268.

252. Iwamoto R*, et al.* HB-EGF function in cardiac valve development requires interaction with heparan sulfate proteoglycans. *Development*. 2010;137:2205-14.

253. Iwamoto R and Mekada E. ErbB and HB-EGF signaling in heart development and function. *Cell structure and function*. 2006;31:1-14.

254. Iwamoto R*, et al.* Heparin-binding EGF-like growth factor and ErbB signaling is essential for heart function. *Proceedings of the National Academy of Sciences*. 2003;100:3221-3226.

255. Powell P*, et al.* Eosinophils expressing heparin-binding EGF-like growth factor mRNA localize around lung microvessels in pulmonary hypertension. *The American journal of pathology*. 1993;143:784.

256. Kim T-H*, et al.* Phactr4 regulates neural tube and optic fissure closure by controlling PP1-, Rb-, and E2F1-regulated cell-cycle progression. *Developmental cell*. 2007;13:87-102.

257. Cao F*, et al.* PHACTR4 regulates proliferation, migration and invasion of human hepatocellular carcinoma by inhibiting IL-6/Stat3 pathway. *Eur Rev Med Pharmacol Sci*. 2016;20:3392-3399.

258. Jarray R*, et al.* Disruption of phactr-1 pathway triggers pro-inflammatory and pro-atherogenic factors: new insights in atherosclerosis development. *Biochimie*. 2015;118:151-161.

259. Deng M*, et al.* HIF-1a regulates hypoxia-induced autophagy via translocation of ANKRD37 in colon cancer. *Experimental Cell Research*. 2020:112175.

260. Peng C*, et al.* Hypoxia Induced ANKRD37 Promotes Angiogenesis and Reprograms Glucose Metabolism in Hepatocellular Carcinoma Following Liver Transplantation. *Transplantation*. 2018;102:S683.

261. Stanton H*, et al.* Proteoglycan degradation by the ADAMTS family of proteinases. *Biochimica et Biophysica Acta (BBA)-Molecular Basis of Disease*. 2011;1812:1616-1629.

262. Binder MJ*, et al.* The extracellular matrix in cancer progression: role of hyalectan proteoglycans and ADAMTS enzymes. *Cancer letters*. 2017;385:55-64.

263. Dubail J*, et al.* ADAMTS-2 functions as anti-angiogenic and anti-tumoral molecule independently of its catalytic activity. *Cellular and molecular life sciences*. 2010;67:4213-4232.

264. Hsu YP*, et al.* Anti-angiogenic properties of ADAMTS-4 in vitro. *International journal of experimental pathology*. 2012;93:70-77.

265. Jungers KA*, et al.* Adamts9 is widely expressed during mouse embryo development. *Gene Expression Patterns*. 2005;5:609-617.

266. Kern CB*, et al.* Reduced versican cleavage due to Adamts9 haploinsufficiency is associated with cardiac and aortic anomalies. *Matrix biology*. 2010;29:304-316.

267. Guda MR*, et al.* Targeting PDK4 inhibits breast cancer metabolism. *American journal of cancer research*. 2018;8:1725.

268. Pettersen IKN*, et al.* Upregulated PDK4 expression is a sensitive marker of increased fatty acid oxidation. *Mitochondrion*. 2019;49:97-110.

269. Liu LX*, et al.* PDK4 inhibits cardiac pyruvate oxidation in late pregnancy. *Circulation research*. 2017;121:1370-1378.

270. Gopal K*, et al.* FoxO1 regulates myocardial glucose oxidation rates via transcriptional control of pyruvate dehydrogenase kinase 4 expression. *American Journal of Physiology-Heart and Circulatory Physiology*. 2017;313:H479-H490.

271. Piao L*, et al.* FOXO1-mediated upregulation of pyruvate dehydrogenase kinase-4 (PDK4) decreases glucose oxidation and impairs right ventricular function in pulmonary hypertension: therapeutic benefits of dichloroacetate. *Journal of molecular medicine*. 2013;91:333-346.

272. Cheng LEC*, et al.* Functional redundancy of the Nur77 and Nor-1 orphan steroid receptors in T-cell apoptosis. *The EMBO journal*. 1997;16:1865-1875.

273. Nomiyama T*, et al.* The NR4A orphan nuclear receptor NOR1 is induced by platelet-derived growth factor and mediates vascular smooth muscle cell proliferation. *Journal of Biological Chemistry*. 2006;281:33467-33476.

274. Qing H*, et al.* Deficiency of the NR4A orphan nuclear receptor NOR1 in hematopoietic stem cells accelerates atherosclerosis. *Stem Cells*. 2014;32:2419-2429.

275. Jiang Y*, et al.* The protective role of NR4A3 in acute myocardial infarction by suppressing inflammatory responses via JAK2-STAT3/NF-κB pathway. *Biochemical and biophysical research communications*. 2019;517:697-702.

276. Medzikovic L*, et al.* NR4A nuclear receptors in cardiac remodeling and neurohormonal regulation. *Trends in Cardiovascular Medicine*. 2019;29:429-437.

277. Liu YY*, et al.* Resveratrol prevented experimental pulmonary vascular remodeling via miR-638 regulating NR4A3/cyclin D1 pathway. *Microvasc Res*. 2020;130:103988.

278. Kühn EC*, et al.* Circulating levels of selenium-binding protein 1 (SELENBP1) are associated with risk for major adverse cardiac events and death. *Journal of Trace Elements in Medicine and Biology*. 2019;52:247-253.

279. Kühn-Heid ECD*, et al.* Selenium-Binding Protein 1 Indicates Myocardial Stress and Risk for Adverse Outcome in Cardiac Surgery. *Nutrients*. 2019;11.

280. Pacholsky D*, et al.* Xin repeats define a novel actin-binding motif. *Journal of cell science*. 2004;117:5257-5268.

281. Huang H-T*, et al.* Myomaxin is a novel transcriptional target of MEF2A that encodes a Xin-related α-actinin-interacting protein. *Journal of Biological Chemistry*. 2006;281:39370-39379.

282. Du H*, et al.* PLOD2 in cancer research. *Biomedicine & Pharmacotherapy*. 2017;90:670-676.

283. Witsch TJ*, et al.* Deregulation of the lysyl hydroxylase matrix cross-linking system in experimental and clinical bronchopulmonary dysplasia. *Am J Physiol Lung Cell Mol Physiol*. 2014;306:L246-59.

284. Gjaltema RA*, et al.* Procollagen lysyl hydroxylase 2 expression is regulated by an alternative downstream transforming growth factor β-1 activation mechanism. *Journal of Biological Chemistry*. 2015;290:28465-28476.

285. Lemon DD*, et al.* Cardiac HDAC6 catalytic activity is induced in response to chronic hypertension. *Journal of molecular and cellular cardiology*. 2011;51:41-50.

286. Zhao L*, et al.* Histone deacetylation inhibition in pulmonary hypertension: therapeutic potential of valproic acid and suberoylanilide hydroxamic acid. *Circulation*. 2012;126:455-467.

287. Yu Y-H*, et al.* Prostaglandin reductase-3 negatively modulates adipogenesis through regulation of PPARγ activity. *Journal of lipid research*. 2013;54:2391-2399.

288. Shah S*, et al.* Genome-wide association and Mendelian randomisation analysis provide insights into the pathogenesis of heart failure. *Nature communications*. 2020;11:1-12.

289. Chen N*, et al.* The oxygen sensor PHD3 limits glycolysis under hypoxia via direct binding to pyruvate kinase. *Cell Res*. 2011;21:983-6.

290. Chen D*, et al.* Enah overexpression is correlated with poor survival and aggressive phenotype in gastric cancer. *Cell Death Dis*. 2018;9:998.

291. Wang D-D*, et al.* The significance of ENAH in carcinogenesis and prognosis in

gastric cancer. *Oncotarget*. 2017;8:72466.

292. Zhang H*, et al.* LAMB3 mediates apoptotic, proliferative, invasive, and metastatic behaviors in pancreatic cancer by regulating the PI3K/Akt signaling pathway. *Cell Death Dis*. 2019;10:230.

293. Yin X*, et al.* LRRFIP1 expression triggers platelet agglutination by enhancing αIIbβ3 expression. *Experimental and Therapeutic Medicine*. 2019;18:269-277.

294. Goodall AH*, et al.* Transcription profiling in human platelets reveals LRRFIP1 as a novel protein regulating platelet function. *Blood*. 2010;116:4646-4656.

295. Suriano AR*, et al.* GCF2/LRRFIP1 represses tumor necrosis factor alpha expression. *Molecular and cellular biology*. 2005;25:9073-9081.

296. Fortugno P*, et al.* Recessive mutations in the neuronal isoforms of DST, encoding dystonin, lead to abnormal actin cytoskeleton organization and HSAN type VI. *Human Mutation*. 2019;40:106-114.

297. Lynch-Godrei A*, et al.* Dystonin-A3 upregulation is responsible for maintenance of tubulin acetylation in a less severe dystonia musculorum mouse model for hereditary sensory and autonomic neuropathy type VI. *Hum Mol Genet*. 2018;27:3598-3611.

298. Liu J*, et al.* F-box only protein 31 (FBXO31) negatively regulates p38 mitogen-activated protein kinase (MAPK) signaling by mediating lysine 48-linked ubiquitination and degradation of mitogen-activated protein kinase kinase 6 (MKK6). *Journal of Biological Chemistry*. 2014;289:21508-21518.

299. Andrews C*, et al.* The MKK6-p38 MAPK pathway prolongs the cardiac contractile calcium transient, downregulates SERCA2, and activates NF-AT. *Cardiovasc Res*. 2003;59:46-56.

300. Kojonazarov B*, et al.* p38 MAPK Inhibition Improves Heart Function in Pressure-Loaded Right Ventricular Hypertrophy. *Am J Respir Cell Mol Biol*. 2017;57:603-614.

301. Palmer EL*, et al.* Sequence and tissue distribution of the integrin alpha 9 subunit, a novel partner of beta 1 that is widely distributed in epithelia and muscle. *J Cell Biol*. 1993;123:1289-97.

302. Wu Y and Song W. Regulation of RCAN1 translation and its role in oxidative stress-induced apoptosis. *Faseb j*. 2013;27:208-21.

303. Davies KJ*, et al.* Renaming the DSCR1/Adapt78 gene family as RCAN: regulators of calcineurin. *Faseb j*. 2007;21:3023-8.

304. Chan B*, et al.* Identification of a peptide fragment of DSCR1 that competitively inhibits calcineurin activity in vitro and in vivo. *Proc Natl Acad Sci U S A*. 2005;102:13075-80.

305. Ebrahimzadeh-Vesal R*, et al.* Identification of a novel nonsense mutation in kyphoscoliosis peptidase gene in an Iranian patient with myofibrillar myopathy. *Genes Dis*. 2018;5:331-334.

306. Straussberg R*, et al.* Kyphoscoliosis peptidase (KY) mutation causes a novel congenital myopathy with core targetoid defects. *Acta Neuropathol*.

2016;132:475-8.

307. Kempf T*, et al.* The transforming growth factor-β superfamily member growth-differentiation factor-15 protects the heart from ischemia/reperfusion injury. *Circulation research*. 2006;98:351-360.

308. Schlittenhardt D*, et al.* Involvement of growth differentiation factor-15/macrophage inhibitory cytokine-1 (GDF-15/MIC-1) in oxLDL-induced apoptosis of human macrophages in vitro and in arteriosclerotic lesions. *Cell and tissue research*. 2004;318:325-333.

309. Wollert KC*, et al.* Prognostic Value of Growth-Differentiation Factor-15 in Patients With Non–ST-Elevation Acute Coronary Syndrome. *Circulation*. 2007;115:962-971.

310. Lankeit M*, et al.* Growth differentiation factor-15 for prognostic assessment of patients with acute pulmonary embolism. *American journal of respiratory and critical care medicine*. 2008;177:1018-1025.

311. George M*, et al.* GDF 15-a novel biomarker in the offing for heart failure. *Current cardiology reviews*. 2016;12:37-46.

312. Nickel N*, et al.* Growth differentiation factor-15 in idiopathic pulmonary arterial hypertension. *American journal of respiratory and critical care medicine*. 2008;178:534-541.

313. Ryan JJ and Archer SL. The right ventricle in pulmonary arterial hypertension: disorders of metabolism, angiogenesis and adrenergic signaling in right ventricular failure. *Circ Res*. 2014;115:176-88.

314. Oikawa M*, et al.* Increased [18F] fluorodeoxyglucose accumulation in right ventricular free wall in patients with pulmonary hypertension and the effect of epoprostenol. *Journal of the American College of Cardiology*. 2005;45:1849-1855.

315. Sharma S*, et al.* Dynamic changes of gene expression in hypoxia-induced right ventricular hypertrophy. *American Journal of Physiology-Heart and Circulatory Physiology*. 2004;286:H1185-H1192.

316. Karamanlidis G*, et al.* Impaired mitochondrial biogenesis precedes heart failure in right ventricular hypertrophy in congenital heart disease. *Circulation: Heart Failure*. 2011;4:707-713.

317. Montaigne D*, et al.* Myocardial contractile dysfunction is associated with impaired mitochondrial function and dynamics in type 2 diabetic but not in obese patients. *Circulation*. 2014;130:554-564.

318. Power AS*, et al.* Mitochondrial function remains impaired in the hypertrophied right ventricle of pulmonary hypertensive rats following short duration metoprolol treatment. *PloS one*. 2019;14:e0214740.

319. Potus F*, et al.* Transcriptomic Signature of Right Ventricular Failure in Experimental Pulmonary Arterial Hypertension: Deep Sequencing Demonstrates Mitochondrial, Fibrotic, Inflammatory and Angiogenic Abnormalities. *Int J Mol Sci*. 2018;19.

320. Aoyagi T and Matsui T. Phosphoinositide-3 kinase signaling in cardiac hypertrophy

and heart failure. *Current pharmaceutical design*. 2011;17:1818-1824.

321. McMullen JR*, et al.* The insulin-like growth factor 1 receptor induces physiological heart growth via the phosphoinositide 3-kinase (p110α) pathway. *Journal of Biological Chemistry*. 2004;279:4782-4793.

322. Oudit GY*, et al.* Phosphoinositide 3-kinase γ–deficient mice are protected from isoproterenol-induced heart failure. *Circulation*. 2003;108:2147-2152.

323. Sundaresan NR*, et al.* The sirtuin SIRT6 blocks IGF-Akt signaling and development of cardiac hypertrophy by targeting c-Jun. *Nature medicine*. 2012;18:1643-1650.

324. Shiojima I*, et al.* Disruption of coordinated cardiac hypertrophy and angiogenesis contributes to the transition to heart failure. *The Journal of clinical investigation*. 2005;115:2108-2118.

325. Phosri S*, et al.* Stimulation of adenosine A2B receptor inhibits endothelin-1-induced cardiac fibroblast proliferation and α-smooth muscle actin synthesis through the cAMP/Epac/PI3K/Akt-signaling pathway. *Frontiers in pharmacology*. 2017;8:428.

326. Yang W*, et al.* BMI1 promotes cardiac fibrosis in ischemia-induced heart failure via the PTEN-PI3K/Akt-mTOR signaling pathway. *Am J Physiol Heart Circ Physiol*. 2019;316:H61-H69.

327. Noyan-Ashraf MH*, et al.* GLP-1R agonist liraglutide activates cytoprotective pathways and improves outcomes after experimental myocardial infarction in mice. *Diabetes*. 2009;58:975-983.

328. Abbas NA and Kabil SL. Liraglutide ameliorates cardiotoxicity induced by doxorubicin in rats through the Akt/GSK-3β signaling pathway. *Naunyn-Schmiedeberg's archives of pharmacology*. 2017;390:1145-1153.

329. Zhang Q*, et al.* Liraglutide protects cardiac function in diabetic rats through the PPARα pathway. *Biosci Rep*. 2018;38.

330. Qiao H*, et al.* Liraglutide repairs the infarcted heart: The role of the SIRT1/Parkin/mitophagy pathway. *Mol Med Rep*. 2018;17:3722-3734.

331. Zhang Y*, et al.* Liraglutide relieves myocardial damage by promoting autophagy via AMPK-mTOR signaling pathway in zucker diabetic fatty rat. *Mol Cell Endocrinol*. 2017;448:98-107.

332. Basalay MV*, et al.* Glucagon-like peptide-1 (GLP-1) mediates cardioprotection by remote ischaemic conditioning. *Cardiovascular research*. 2016;112:669-676.

333. Qi D and Young LH. AMPK: energy sensor and survival mechanism in the ischemic heart. *Trends Endocrinol Metab*. 2015;26:422-9.

334. Sung MM*, et al.* AMPK deficiency in cardiac muscle results in dilated cardiomyopathy in the absence of changes in energy metabolism. *Cardiovascular research*. 2015;107:235-245.

335. He C*, et al.* Dissociation of Bcl-2–Beclin1 complex by activated AMPK enhances cardiac autophagy and protects against cardiomyocyte apoptosis in diabetes. *Diabetes*. 2013;62:1270-1281.

336. Adrian L*, et al.* AMPK Prevents Palmitic Acid-Induced Apoptosis and Lipid Accumulation in Cardiomyocytes. *Lipids*. 2017;52:737-750.

337. Gélinas R*, et al.* AMPK activation counteracts cardiac hypertrophy by reducing O-GlcNAcylation. *Nat Commun*. 2018;9:374.

338. Herzig S and Shaw RJ. AMPK: guardian of metabolism and mitochondrial homeostasis. *Nat Rev Mol Cell Biol*. 2018;19:121-135.

339. Eberli FR*, et al.* Protective effect of increased glycolytic substrate against systolic and diastolic dysfunction and increased coronary resistance from prolonged global underperfusion and reperfusion in isolated rabbit hearts perfused with erythrocyte suspensions. *Circ Res*. 1991;68:466-81.

340. Kramer HF*, et al.* Distinct signals regulate AS160 phosphorylation in response to insulin, AICAR, and contraction in mouse skeletal muscle. *Diabetes*. 2006;55:2067-76.

341. Choi YJ*, et al.* Activation of AMPK by berberine induces hepatic lipid accumulation by upregulation of fatty acid translocase CD36 in mice. *Toxicol Appl Pharmacol*. 2017;316:74-82.

342. Fernandez-Marcos PJ and Auwerx J. Regulation of PGC-1α, a nodal regulator of mitochondrial biogenesis. *Am J Clin Nutr*. 2011;93:884s-90.

343. Walton RG*, et al.* Metformin blunts muscle hypertrophy in response to progressive resistance exercise training in older adults: A randomized, double-blind, placebo-controlled, multicenter trial: The MASTERS trial. *Aging Cell*. 2019;18:e13039.

344. Chan AY*, et al.* Resveratrol inhibits cardiac hypertrophy via AMP-activated protein kinase and Akt. *J Biol Chem*. 2008;283:24194-201.

345. Kosuru R*, et al.* AMPK Contributes to Cardioprotective Effects of Pterostilbene Against Myocardial Ischemia- Reperfusion Injury in Diabetic Rats by Suppressing Cardiac Oxidative Stress and Apoptosis. *Cell Physiol Biochem*. 2018;46:1381-1397.

346. Chan SY and Rubin LJ. Metabolic dysfunction in pulmonary hypertension: from basic science to clinical practice. *Eur Respir Rev*. 2017;26.

347. Pal S*, et al.* The osteogenic effect of liraglutide involves enhanced mitochondrial biogenesis in osteoblasts. *Biochem Pharmacol*. 2019;164:34-44.

348. Zhou J*, et al.* Liraglutide induces beige fat development and promotes mitochondrial function in diet induced obesity mice partially through AMPK-SIRT-1-PGC1-α cell signaling pathway. *Endocrine*. 2019;64:271-283.

349. Prins KW*, et al.* Repurposing Medications for Treatment of Pulmonary Arterial Hypertension: What's Old Is New Again. *J Am Heart Assoc*. 2019;8:e011343.

350. Meng Q*, et al.* Development of a mouse model of metabolic syndrome, pulmonary hypertension, and heart failure with preserved ejection fraction. *American journal of respiratory cell and molecular biology*. 2017;56:497-505.